

ANALYSIS OF THE VORTICAL FLOW AROUND A 60 DEGREE


DELTA WING WITH VORTEX FLAP,

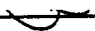
by

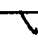
Bongzoo „Sung „,


Dissertation submitted to the Faculty of the
Virginia Polytechnic Institute and State University
in partial fulfillment of the requirements for the degree of
Doctor of Philosophy
in
Aerospace Engineering

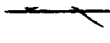
APPROVED:

 ~~_____~~
J. F. Marchman, III, Chairman

 _____
J. A. Schetz

 _____
B. Grossman

 _____
W. L. Neu

 _____
L. W. Rutland, II

December 1985

Blacksburg, Virginia

ANALYSIS OF THE VORTICAL FLOW AROUND A 60 DEGREE
DELTA WING WITH VORTEX FLAP

by

Bongzoo Sung

J. F. Marchman, III, Chairman

Aerospace Engineering

(ABSTRACT)

Subsonic wind tunnel investigations were conducted on a 60° swept, flat plate, delta wing with a leading edge vortex flap. The pressure distributions were measured over a range of angles of attack starting from zero to 40° in 5° interval and flap deflection angles from zero to 45° with 5° increments at a Reynolds number of about 2.14×10^6 based on the root chord. The flow visualization experiments were performed from zero degree to the stall angle, with ten different flap deflection angles at the same Reynolds number. The mean flow field was measured at angles of attack 10° and 15° with the flap deflection angles of 10° and 30° at a Reynolds number of about 1.50×10^6 . The experimental results shows that the leading edge vortex flap is an effective means to control the vortex flow over a delta wing. The optimum flap deflection angles were found where the primary vortex was confined to the leading edge vortex flap, thus producing a thrust on the flap. It was found that flap deflection could be used to restore a vortex flow from burst vortex condition.

A non-linear vortex lattice code with a new velocity jump formula was developed to predict the aerodynamic characteristics of plain and vortex flapped delta wings including the pressure distributions. The current method improved over other non-linear vortex lattice methods by predicting the pressure distributions, but the suction peak pressures were lower and the location of the suction peaks were predicted farther from the leading edge than the experimental results. The aerodynamic loads integrated from the pressure distributions also matched well with the experiments and with other "expensive" computational codes used by other researchers in similar studies. This current non-linear vortex lattice code appears to be a promising tool for vortex flap design.

ACKNOWLEDGEMENTS

I would like to express my sincere appreciation to Professor Marchman for his advice and encouragement during the course of this work. I am grateful to Professors Schetz, Grossman, Neu and Rutland for serving on my committee. Thanks also goes to Professor Mook for his advice on the computational matters.

I would also like to thank to all my friends at Virginia Tech for their help and advice, especially

I would like to express my gratitude to my parents and my wife. Their love, encouragement and support made it possible for me to complete my dissertation.

TABLE OF CONTENTS

I.	INTRODUCTION	1
1.1	General Aerodynamic Characteristics of the Delta Wing	1
1.2	Literature Review	5
1.2.a	Experimental Investigations	5
1.2.b	Analytical and Computational Investigation	8
1.3	Motivation for the Research	12
II.	EXPERIMENTAL APPROACH	15
2.1	Facility and Model	15
2.2	Instrumentation	17
2.3	Test Procedures	18
2.4	Uncertainty of the Experimental Results	22
III.	EXPERIMENTAL RESULTS	29
3.1	Flow Regime	29
3.2	Surface Streamlines	32
3.3	Pressure Distribution	37
3.4	Mean Flow Field	40
IV.	COMPUTATIONAL APPROACH	45
4.1	Basic Principle	45
4.2	Formulation of the Problem	52
4.3	Method of Solution	56

4.4	Aerodynamic Load Calculation	61
V.	COMPUTATIONAL RESULTS AND DISCUSSION	68
5.1	Effects of Various Parameters on the Computational Results.	68
5.2	Plain 60 Degree Delta wing	71
5.3	60 Degree Delta Wing with a Leading Edge Vortex Flap	74
5.4	Comparison of Current Computational Method with Others	78
VI.	CONCLUSIONS	80
	LIST OF REFERENCES	83
	APPENDX A. FLOW PROPERTY MEASUREMENT AND YAWHEAD CALIBRATION	91
A.1	Introduction	91
A.2	Calibration Theory	92
A.3	Calibration Experiment	99
A.4	Results and Discussions	101
VITA		243

LIST OF TABLES

Table A.1	Calibration coefficient of yawhead probe.	103
Table A.2	RMS error in flow field measurement.	106
Table 1	Location of pressure tabs.	111
Table 2	Free stream turbulence level.	112
Table 3	Cp distribution.	113
Table 4	Effect of various parameters in computation.	123

LIST OF ILLUSTRATIONS

Fig. A.1	Five hole yawhead probe.	107
Fig. A.2	Details of yawhead probe tip and flow angle definition.	108
Fig. A.3	Division of flow angularity zones.	109
Fig. A.4	Comparision of predicted flow angle with measured angle.	110
Fig. 1.	Sketch of flow field over a delta wing.	124
Fig. 2.	Effect of vortex on aerodynamic loads.	125
Fig. 3.	Effect of leading edge sweep angle on vortex bursting angle of attack, α_{VBTE}	126
Fig. 4.	Reduction of pressure gradient along the vortex core by leading edge vortex flap.	127
Fig. 5.	Leading edge camber effect.	128
Fig. 6.	Schematic of Virginia Tech Stability Wind Tunnel.	129
Fig. 7.	Geometry of the 60° delta wing model with leading edge vortex flap.	130
Fig. 8.	Schematic diagram of Instrumentation.	131
Fig. 9.	Test set-up for mean flow field measurement.	132
Fig. 10.	Effect of profile shape and leading edge on the aerodynamic characteristics of a 60° delta wing.	133
Fig. 11.	Effect of profile on aerodynamic performance of a delta wing with Aspect Ratio 2.31	135
Fig. 12.	Flow regime over a 60° delta wing with leading edge vortex flap.	136
Fig. 13.	Representative photograph of woolen tufts flow visualization experiment ($\alpha=10^\circ$ $\delta=10^\circ$).	137
Fig. 14.	Effect of tufts on pressure distribution.	138
Fig. 15.	Pressure distribution and surface streamlines at $\alpha=5^\circ$, $\delta=10^\circ$	139

Fig. 16.	Pressure distribution and surface streamlines at $\alpha=10^\circ$, $\delta=10^\circ$	140
Fig. 17.	Pressure distribution and surface streamlines at $\alpha=15^\circ$, $\delta=10^\circ$	141
Fig. 18.	Pressure distribution and surface streamlines at $\alpha=20^\circ$, $\delta=10^\circ$	142
Fig. 19.	Pressure distribution and surface streamlines at $\alpha=25^\circ$, $\delta=10^\circ$	143
Fig. 20.	Pressure distribution and surface streamlines at $\alpha=30^\circ$, $\delta=10^\circ$	144
Fig. 21.	Pressure distribution and surface streamlines at $\alpha=10^\circ$, $\delta=35^\circ$	145
Fig. 22.	Pressure distribution and surface streamlines at $\alpha=15^\circ$, $\delta=30^\circ$	146
Fig. 23.	58° delta wing model of Frink et al.(1983).	147
Fig. 24.	Comparison of reattachment line data with the result of Frink et al.(1983).	148
Fig. 25.	Effect of flap deflection at $\alpha=0^\circ$ (experiment).	149
Fig. 26.	Effect of flap deflection at $\alpha=5^\circ$ (experiment).	150
Fig. 27.	Effect of flap deflection at $\alpha=10^\circ$ (experiment).	151
Fig. 28.	Effect of flap deflection at $\alpha=15^\circ$ (experiment).	152
Fig. 29.	Effect of flap deflection at $\alpha=20^\circ$ (experiment).	153
Fig. 30.	Effect of flap deflection at $\alpha=25^\circ$ (experiment).	154
Fig. 31.	Effect of flap deflection at $\alpha=30^\circ$ (experiment).	155
Fig. 32.	Effect of flap deflection at $\alpha=35^\circ$ (experiment).	156
Fig. 33.	Effect of flap deflection at $\alpha=40^\circ$ (experiment).	157
Fig. 34.	Velocity jump across vortex sheet.	158
Fig. 35.	Location of vortex core in the X-Z plane.	159
Fig. 36.	Velocity vector plot at $\alpha=10^\circ$ with $\delta=10^\circ$	160
Fig. 37.	Static pressure distribution at $\alpha=10^\circ$ with $\delta=10^\circ$	163

Fig. 38.	Total pressure distribution at $\alpha=10^\circ$ with $\delta=10^\circ$.	166
Fig. 39.	Velocity vector plot at $\alpha=15^\circ$ with $\delta=10^\circ$.	169
Fig. 40.	Static pressure distribution at $\alpha=15^\circ$ with $\delta=10^\circ$.	172
Fig. 41.	Total pressure distribution at $\alpha=15^\circ$ with $\delta=10^\circ$.	175
Fig. 42.	Velocity vector plot at $\alpha=10^\circ$ with $\delta=30^\circ$.	178
Fig. 43.	Static pressure distribution at $\alpha=10^\circ$ with $\delta=30^\circ$.	181
Fig. 44.	Total pressure distribution at $\alpha=10^\circ$ with $\delta=30^\circ$.	184
Fig. 45.	Velocity vector plot at $\alpha=15^\circ$ with $\delta=30^\circ$.	187
Fig. 46.	Static pressure distribution at $\alpha=15^\circ$ with $\delta=30^\circ$.	190
Fig. 47.	Total pressure distribution at $\alpha=15^\circ$ with $\delta=30^\circ$.	193
Fig. 48.	Vortex loop panel arrangement and initial guess for free vortices (NW=7, NF=3).	196
Fig. 49.	Notation for Biot-Savart Law.	197
Fig. 50.	Flow chart of the program.	198
Fig. 51.	Notation for velocity jump formula.	199
Fig. 52.	Effect of number of panels.	200
Fig. 53.	Effect of number of panel columns on the flap.	201
Fig. 54.	Effect of initial free vortex shedding angle.	202
Fig. 55.	Effect of characteristic time step.	203
Fig. 56.	Effect of first shedding distance of free vortex from leading edge (FEDG).	207
Fig. 57.	Effect of free stream matching point.	211
Fig. 58.	Converged shape of free vortices for a plain 60° delta wing.	215
Fig. 59.	Comparison of total aerodynamic loads for a plain 60° delta wing with experimental data.	216
Fig. 60.	Comparison of pressure distribution on a plain 60° delta wing at $\alpha=20^\circ$.	218

Fig. 61.	Effect of leading edge flap deflection of a 60° delta wing with leading edge flap.	219
Fig. 62.	Effect of flap deflection at $\alpha=5^\circ$ (computed).	221
Fig. 63.	Effect of flap deflection at $\alpha=10^\circ$ (computed).	222
Fig. 64.	Effect of flap deflection at $\alpha=15^\circ$ (computed).	223
Fig. 65.	Effect of flap deflection at $\alpha=20^\circ$ (computed).	224
Fig. 66.	Converged shape of free vortices at $\alpha=10^\circ$ with $\delta=0^\circ$.	225
Fig. 67.	Converged shape of free vortices at $\alpha=10^\circ$ with $\delta=10^\circ$. .	226
Fig. 68.	Converged shape of free vortices at $\alpha=10^\circ$ with $\delta=20^\circ$. .	227
Fig. 69.	Converged shape of free vortices at $\alpha=10^\circ$ with $\delta=30^\circ$. .	228
Fig. 70.	Converged shape of free vortices at $\alpha=10^\circ$ with $\delta=40^\circ$. .	229
Fig. 71.	Converged shape of free vortices at $\alpha=5^\circ$ with $\delta=20^\circ$. .	230
Fig. 72.	Comparison of pressure distribution on a 60° delta wing with leading edge flap at $\alpha=10^\circ$ with $\delta=0^\circ$	231
Fig. 73.	Comparison of pressure distribution on a 60° delta wing with leading edge flap at $\alpha=10^\circ$ with $\delta=10^\circ$	232
Fig. 74.	Comparison of pressure distribution on a 60° delta wing with leading edge flap at $\alpha=10^\circ$ with $\delta=20^\circ$	233
Fig. 75.	Comparison of longitudinal aerodynamic load characteristics for a 74° delta wing.	234
Fig. 76.	Typical converged shape of free vortex filaments for a plain 74° delta wing.	236
Fig. 77.	Comparison of pressure distributions for a 74° delta wing.	237
Fig. 78.	Comparison of pressure difference distributions for a 74° delta wing.	238
Fig. 79.	Pressure distribution on a 74° delta wing with leading edge flap at $\alpha=14^\circ$ with $\delta=0^\circ$	239
Fig. 80.	Pressure distribution on a 74° delta wing with leading edge flap at $\alpha=14^\circ$ with $\delta=10^\circ$	240

- Fig. 81. Converged shape of free vortices for a 74° delta wing with leading edge flap at $\alpha=14^\circ$ with $\delta=0^\circ$ 241
- Fig. 82. Converged shape of free vortices for a 74° delta wing with leading edge flap at $\alpha=14^\circ$ with $\delta=10^\circ$ 242

NOMENCLATURE

A	: Influence coefficient
C	: Wing root chord
\bar{c}	: Mean aerodynamic chord
C_A	: Axial force coefficient
C_D	: Drag coefficient
C_{Di}	: Induced drag coefficient
C_{Do}	: Drag coefficient at zero lift
C_L	: Lift coefficient
C_M	: Pitching moment coefficient at $\frac{1}{4}\bar{c}$
C_N	: Normal force coefficient
C_P	: Pressure coefficient
G	: Strength of vortex loop
h_o	: Cutoff distance
\hat{i}	: Unit vector in X-axis
\hat{j}	: Unit vector in Y-axis
\hat{k}	: Unit vector in Z-axis
\hat{n}	: unit normal vector
NF	: Number of vortex loop panel columns on the flap
NW	: Number of vortex loop panel rows on the wing
M	: Total number of vortex loop panel
P	: Static pressure
P_t	: Total pressure
q	: Dynamic pressure

R : Normal component of the free stream velocity at the wing surface
 T : Temperature
 Δt_c : Characteristic time step
 \vec{V} : Velocity
 X : Axis along the wing center line
 Y : Axis perpendicular to X-axis in wing plane
 Z : Axis normal to X and Y
 X' : Axis along the wing-flap hinge line
 Y' : Axis perpendicular to X' -axis in wing plane
 \bar{Z} : Axis normal to free stream velocity V_∞ and Y axis

All distances are normalized w.r.t the wing root chord
 $x=0.0$: apex, $x=1.0$: trailing edge

u : Velocity component in X direction
 v : Velocity component in Y direction
 w : Velocity component in Z direction
 u' : Velocity component in X' direction
 v' : Velocity component in Y' direction
 \bar{w} : Velocity component in \bar{Z} direction

All velocities are normalized w.r.t the free stream velocity V_∞

Greek symbols

α	: Angle of attack
$\vec{\gamma}$: Strength of vortex sheet
$\vec{\Gamma}$: Strength of vortex filament
δ	: Flap deflection angle
ε	: Convergence criterion
Λ_{LE}	: Leading sweep back angle
μ	: Doublet strength
ρ	: Air density
σ	: Source strength
ϕ	: Perturbation velocity potential
Φ	: Total velocity potential
$\vec{\omega}$: Vorticity ($=\nabla \times \vec{V}$)

Subscripts

OPT	: Optimum flap deflection angle for an angle of attack or Optimum angle of attack for a flap deflection angle
STALL:	Stall angle
VBA	: Vortex bursting at the apex
VBTE	: Vortex bursting at the trailing edge
VS	: Vortex starting at the leading edge
∞	: Free stream condition

I. INTRODUCTION

1.1 GENERAL AERODYNAMIC CHARACTERISTICS OF THE DELTA WING

The sharp edged delta wing has been considered for supersonic aircraft because it has low wave drag in supersonic flight, sufficient structural stiffness and for military application, has small radar cross-section characteristics. Therefore delta winged aircraft are important in tactical supersonic fighter and supersonic cruise transport aircraft design. Although delta wings have have low drag characteristics at supersonic flight, they have relatively poor performance at low speeds encountered during landing, take-off and some maneuvers.

The flow field around a sharp edged delta wing is a complicated three dimensional flow and is very sensitive to disturbances since it has a low aspect ratio. At subsonic speeds, delta wings have aerodynamic characteristics which are substantially different from those of conventional moderate sweep, high aspect ratio wings.

The boundary layer flow on the lower surface of a delta wing tends to flow outward and separates at the leading edge, forming two free shear layers. The free shear layers curve upward and inboard, finally rolling up into two spiral shaped primary vortex sheets with an infinite number of turns above the upper surface of the delta wing. A sketch of the flow field is shown on Fig. 1. The rolled up vortex sheets over the wing induce an

additional velocity on the upper surface of the wing and the corresponding pressure distribution shows a negative peak pressure beneath the vortex core. At small angles of attack, the flow reattaches inboard of the vortex cores due to the pressure gradient generated by these vortex sheets. The flow is in the free stream direction inboard of the reattachment line. Between the reattachment line and the leading edge is a spiral flow caused by the vortex. The surface streamline shows that the flow has a spanwise component and has an inflection point just below the vortex core. A spanwise outflow is induced at the surface beneath the coiled vortex sheet and experiences an adverse pressure gradient as it approaches the leading edge. Thus the flow separates again and eventually forms a secondary vortex between the primary vortex and wing leading edge.

The size and strength of the coiled vortex sheet increase with angle of attack and they become a dominant feature of the flow around a delta wing. This flow field is basically independent of the Reynolds number. These vortices can be observed on a delta wing with a sweep back angle larger than about 57° and the two vortex sheets from each side of delta wing merge together at a larger sweep back angle around 79° (Poisson-Quinton (1978)). With increasing angle of attack, the lift increases nonlinearly due to the additional suction force caused by the vortex flow (Fig. 2). At higher angles of attack, tightly rolled-up vortices start to separate from the leading edge, resulting in a phenomenon called "breakdown" or "burst" of the vortices. The lift curve slope decreases and the pitching moment increases due to the loss of suction force associated with the vortex burst. The vortex breakdown starts from the

trailing edge and progresses to the apex with an increase in angle of attack or a decrease in the leading edge sweep back angle. Shown in Fig. 3 is the angle of attack at which vortex bursting occurs at the trailing edge, α_{VBTE} , at different leading edge sweep back angles for sharp edged, flat plate, delta wings. Due to the vortex breakdown, the vortex system on each side might become asymmetric and would generate a destabilizing rolling moment which could pose a serious problem in some part of the flight envelope. When vortex bursting appears above the wing, the velocity fluctuation as well as the pressure fluctuation on the wing become rapid. The exact mechanism of the vortex breakdown is not yet known and there are several approaches to explain the vortex breakdown (Lambourne and Bryer (1962), Ludwig (1962), Hall (1972), Hayashi and Nakaya (1975), and Leibovich (1984)). One of the mechanisms for the vortex breakdown is that the strong adverse pressure gradient along the vortex axis causes a strong dragging effect on the vortex flow and triggers vortex bursting. The vortex burst at high angles of attack is due to the increased adverse pressure gradient along the vortex core.

There are several methods to stabilize the vortex flow at a high angle of attack, such as vortex flaps, vortex generators, leading edge extensions, vortex lift strakes, and vortex augmentations (see Lamar and Campbell (1983)). Each method has an advantage and disadvantage over the others. The vortex flap uses a flap hinged at the leading edge of the delta wing and has two major benefits. One is to delay vortex breakdown by weakening the adverse pressure gradient along the vortex axis. The adverse pressure gradient could be reduced by deflecting the leading edge

of the wing downward because the path of the vortex core is not parallel to the leading edge of the delta wing but is always curved toward the center line of the wing (Fig. 4). Hence, by deflecting the leading edge, vortex breakdown can be delayed and prevented from progressing toward the wing apex.

The other benefit of leading edge deflection is the vectoring of the pressure force toward the thrust direction (Fig. 5). The low pressure produced by the vortices on the leading edge results not only in increasing the lift but also contributes to an increase in drag. The lift and drag increase non-linearly with the angle of attack. There was an attempt to overcome the drag penalty caused by the vortices by providing a permanent camber at the leading edge, thus preventing flow separation along the leading edge and preventing the formation of leading edge vortices (Coe and Huffman (1979), and Shoonover and Ohlson (1982)). The permanent leading edge camber reduces the lift as well as drag by providing an attached flow, and has a stabilizing effect on the pitching moment at high angles of attack. However these benefits may be outweighed by the reduction of the overall supersonic performance by the cambered leading edge.

A leading edge vortex flap (LEVF) controls the flow by causing vortex formation on the flap surface. Ideally the flow reattaches at the wing-flap hinge line and provides attached flow over the entire wing except the LEVF. The pressure force produced by the vortex could be oriented toward the flight direction to produce thrust instead of drag normally

produced by a leading edge vortex, with the downward deflection of the of the LEVF. The thrust will result in an increase in the lift/drag ratio for the wing and a significant improvement in performance. The upward deflection of the vortex flap could increase the lift with increased drag, which can be useful during landing. Another potential advantage of the LEVF is the generation of the rolling and yawing moments by asymmetric flap deflection which can be useful for lateral control at high angles of attack or in a yawed flight condition.

1.2 LITERATURE REVIEW

The literature review is divided into two subsections; experimental investigations and analytical and computational investigations.

1.2.A EXPERIMENTAL INVESTIGATIONS

Winter (1935) found the nonlinear characteristics of the lift of delta wings with respect to the angle of attack as early as 1935. Whittle and Lovell (1948) found that the nonlinear relationship is independent of Reynolds number for a sharp edged delta wing, and also found that the onset of the vortex flow could be delayed by deflecting the leading edge flap downward. Jacquet and Brewer (1949) found that profile shape has a significant effect on the static stability at high lift coefficients. Bartlett and Vidal (1955) investigated the effect of edge shapes, and found that the aerodynamic loads did not vary with Reynolds number for

delta wings with a sharp leading edge, while round edged delta wings showed a slight variation with Reynolds number.

Marsden et al. (1958) investigated the flow field and pressure distribution on a 70° delta wing. He found the secondary vortex between the primary vortex and leading edge with a sign opposite to the primary vortex, and also the non-conicity of the flow around a 70° delta wing. Harvey (1961) tested an 80° delta wing in a yawed position and observed tertiary separation between the secondary vortex and the leading edge. Peckham (1961) tested a wide range of delta and gothic wings with varying thickness. He found that the effect of increasing thickness or increasing aspect ratio was to move the reattachment line and suction peak further outboard on the wing. Earnshaw and Lawford (1966) tested a series of delta wings with sweep angles varying from 45° to 76° . They found the vortex breakdown angle of attack for each sweep angle. They also found that the vortex breakdown was delayed in a higher sweep delta wing and that vortex breakdown migrates to the apex with increase in angle of attack or decrease in sweep angle.

Earnshaw (1962) investigated the primary vortices generated by a delta wing of unit aspect ratio. He suggested that primary vortex flow can be divided into three regions: viscous sub-core, vortex core, and a region outside the vortex core. The behavior of the vortex core or the vortex breakdown phenomena and their effects were tested and investigated by many researchers such as Elle (1961), Lambourne and Bryer (1962), Lawson (1964), Hummel (1965), Hummel and Srinivasan (1967), Wentz and Kohlman

(1968), Werle (1971), Hayashi and Nakaya (1975), and Erickson (1982). The vortex flow field was mapped by Wentz and McMahon (1967), Hummel (1979), Brennenstuhl and Hummel (1982), and Verhaagen and Kruisbrink (1985).

Rao and Johnson (1981), Tingas and Rao (1982) and Rao (1983) tested various leading edge devices such as chordwise slots, fences, pylon vortex generators, sharp leading edge extensions, and vortex flaps and apex flaps to control the vortex flow over the delta wing. Seginer and Salomon (1983) tested spanwise blowing to energize the vortex flow. Double delta wings and leading edge strakes were investigated by Marchman and Terry (1983), Manor and Wentz (1985), and Verhaagen (1983).

Although the leading edge flap was tested on a delta wing as early as 1948, it has been tested recently as a means to improve delta wing performance. Coe and Weston (1979), Yip and Murri (1981), and Quinto and Paulson (1983) tested the vortex flaps on arrow wings. Marchman (1981a) investigated various constant-chord leading edge vortex flaps on 60° and 75° delta wings. He found that the drag reduced by up to 40 % with a small change in lift, thus increasing lift to drag ratio with flap deflection. Optimum results were obtained with a flap 38 % of wing area and deflected 30° . Pitching moment was adversely affected by the flap with both wings exhibiting unstable behavior at high angles of attack. Frink et al. (1983) tested vortex flaps on 50° to 74° swept delta wings. Erickson and McCann (1983) tested vortex flaps on a 65° cropped delta wing and a 70/50 cranked delta wing. Inverted vortex flaps were tested by Marchman

(1981b). Tabbed vortex flaps were investigated by Ruyan et al.(1980) and Hoffler and Rao (1985). More extensive references can be found from Timm (1967), Parker(1976) and Poisson-Quinton (1978) and Hoffman (1980).

1.2.B ANALYTICAL AND COMPUTATIONAL INVESTIGATION

In 1918 Prandtl presented his lifting-line theory (see Karamcheti, 1966). This is the earliest analytical method where the wing is replaced by a single bound vortex line with trailing vortices extending to infinity in the wing plane (horse-shoe vortex). This model is very simple and is limited to rectangular wings with a large aspect ratio and a low angle of attack. The first attempt at modeling the wing with a theory other than linear theory was made by Bollay (1937). He used a vortex model where the wing is represented by bound vortices and the trailing vortices no longer lie in the wing plane, but are shed downstream from the side edge of the wing at an angle $\alpha/2$ from the wing plane. Jones (1946) simplified the flow over a delta wing as a two dimensional flow in the transverse plane (slender body theory). Simple linear relationships between the aerodynamic loads and the angle of attack were found based on his theory.

The first attempt to model the separated flow over a thin, flat plate delta wing was by Legendre in 1952 (see Smith 1980). He used two concentrated line vortices to represent the vortex flow on each side of a delta wing. The position and strength of the vortices were determined by enforcing tangential flow over the wing and zero total force on each

isolated vortex. Brown and Michael (1954) improved Legendre's method by adding a feeding vortex sheet from the leading edge to the concentrated vortex. They used two boundary conditions: tangential velocity on the wing surface, and zero resultant force on the vortex plus feeding cut. The presence of the feeding cut, which makes a small angle to the local velocity, resulted in a pressure discontinuity in the flow field.

In an attempt to improve Brown and Michael's method, Mangler and Smith (1959) modeled the leading edge vortex flow as two parts, an inner part and an outer part. The outer part is the vortex sheet shed tangentially at the leading edge and rolled up spirally. The inner part is replaced by a concentrated vortex joined to the outer part by a feeding cut. The shape and strength of the vortex was found by enforcing zero resultant force on the line vortex and feeding cut, zero pressure jump across the vortex sheet, and tangential velocity on the wing surface. Later, Smith (1968) modified the previous method and adopted an iterative procedure to obtain a solution. Smith's method is based on the conical flow assumption, consequently this method is restricted to slender delta wings at small angles of attack or only in the vicinity of the apex.

Pohlhamus (1966) developed a method to predict the lift on a sharp edged delta wing which is called the leading edge suction analogy. This method estimated the overall lift from the sum of potential lift and vortex lift contribution. Total lift predicted by this method shows good agreement with the experimental results.

Falkner used discrete vortices for the numerical solution of the steady, subsonic, lifting surface problem by modeling the wing surface with straight horse-shoe vortices. He named this method as "Vortex Lattice Theory" (see DeYoung(1976)). Belotserkovskiy (1968) developed the first successful model of the wing tip wake. He modeled the wing surface by a system of discrete vortices, and the wake by a finite number of vortex filaments. Each vortex filament consists of a finite number of straight vortex segments. The positions of the vortex filaments representing the wake were found by aligning each straight segment with the velocity vector at its mid-point.

Rebach (see Rebach (1976)) applied the above non-linear vortex lattice method (NVLM) to the case of a slender delta delta wing in 1973. The solution is obtained by a geometry perturbation, where the case of a rectangular wing with side edge separation is solved first, then solutions are obtained by gradually decreasing the wing sweep angle until a delta wing is obtained. Mook and Maddox (1974) applied Belotserkovskiy's method to a delta wing and Kandil (1974) developed a generalized NVLM method for steady flow and Kostadinoupolus et al.(1985) extended the above method to the unsteady flow case. Recently Kandil and Balakrishnan (1981) improved the previous method by including a vortex core. A similar method was developed by Mehrotra and Lan (1978) and Pao and Lan (1982).

The above NVLM method predicts the total aerodynamic loads quite accurately, but none of the above methods can predict the pressure distribution. These methods can predict only the pressure differences across

the control points, and even the pressure differences are not as good as the total aerodynamic load predictions.

The higher order panel method developed at the Boeing Company (Weber et al.(1976) and Johnson et al.(1980)). solves the Prandtl-Glauert equation for three dimensional subsonic flow with leading edge vortex. The leading edge vortex flow was represented by a free vortex sheet, feeding cut and vortex core. The trailing edge wake was modeled as near wake and far wake. It is often called the Free Vortex Sheet (FVS) method and is the most elaborate and successful method. The pressure distributions can be predicted as accurately as the total aerodynamic loads.

A similar method was developed at the NLR of the Netherlands (Hoejimaakar and Bennekers (1979)). In the NLR method, a vortex system similar to the FVS is used, but the vortex system is mapped onto a rectangular computational domain and derivatives of the singularity are calculated as in the finite difference method. Both the FVS and NLR methods require a good initial guess on the position of the free vortex sheet and the vortex core to obtain a converged solution since both methods use a Quasi-Newton method for the iteration procedure. Some computational codes (Rao and Maskew (1982) and Nathman (1984)) were developed to provide an initial shape of the vortex sheet for the FVS code.

Recently some researchers (Hitzl and Schmidt (1984) and Rizzi (1985)) succeeded in computing the vortex flow over a delta wing by solving the Euler equations (Euler code). But there is a debate about the vorticity

generating mechanism in the Euler codes. Newsome (1985) tested the Euler code with a fine grid and a coarse grid, and concluded that the vorticity is generated by numerical errors in the Euler code. Fujii and Kutler (1983) obtained a solution for the flow over a round edged delta wing by solving the Reynolds-averaged, thin-Layer Navier-Stokes equations without modeling the trailing edge and trailing wake. They reported that it took one hour of CPU time on the Cray 1-S by using a vectorized version of the code.

1.3 MOTIVATION FOR THE RESEARCH

The leading edge vortex flap has received considerable attention recently as a device to improve the aerodynamic performance of highly swept delta wings. Most researchers to date have concentrated on the overall aerodynamic performance characteristics of the flaps such as forces and moments. In order to truly optimize the use of the vortex flap, or the optimal design of the vortex flap, more research is needed on the details of the flow over the wing-flap system and local pressure distributions on a delta wing with a vortex flap.

There has apparently been a problem in applying existing computational programs to a 60° sweep delta wing or a vortex flapped 60° sweep delta wing. Most literature to date has not computed the case of a 60° delta wing and some researchers (Kuhlman (1978) and Chaturvedi and Ghaffarri (1982)) reported that they could not obtain a converged solution or had difficulty in obtaining a solution.

FVS and NLR codes are the only currently available computational programs for predicting the pressure distribution on a delta wing. But it is still expensive to use such codes during the preliminary design phase of aircraft design where number of configurations are studied. For example, Erickson (1983) reported that FVS code took 500 - 1300 CPU seconds on the Cyber 175 computer to yield a converged solution for a flapped delta wing case using the converged solution of a similar case as a starting guess; therefore it would take more CPU time to run for different design cases.

Therefore, the purpose of the current study is to analyze the phenomena associated with a 60° delta wing with a flap, investigate the possibility of delaying the vortex breakdown using a vortex flap, and study the optimum angles of flap deflection at various angles of attack. Also, the present work attempts to develop an "inexpensive" computational code to predict the pressure distributions which can be used in the preliminary design phase of aircraft.

In Chapter II, the experimental approach is described together with the error analysis.

In Chapter III, flow regimes are defined according to the results obtained from flow visualization, surface streamlines and pressure distributions are discussed, and flow fields for different cases are analyzed including the flow field downstream of vortex bursting.

In Chapter IV, the computational formulation and developed velocity jump formula are presented.

In Chapter V, effects of certain parameters are discussed, the computational results for the flapped delta wing are compared with the experimental results and the results from the present computational code are compared with results from others.

In Chapter VI, some conclusions and recommendations for further extension of the current study are presented.

II. EXPERIMENTAL APPROACH

2.1 FACILITY AND MODEL

The experimental study was conducted in the 6ft x 6ft x 24ft (1.85m x 1.85m x 7.32m), straight test section of the Virginia Tech. Stability Wind Tunnel (Fig. 6). This wind tunnel was originally the NACA Stability Wind Tunnel at Langley Field and is a continuous, single return, subsonic facility. The tunnel is powered by a 600 hp DC motor, driving a 14 ft (4.27 m) diameter fixed pitch propeller, which can produce a stable, low turbulence flow in the test section up to the maximum speed of 220 ft/s (67 m/s).

The previous study (Reynolds (1982)) revealed that the facility has very good flow quality, that is, the turbulence level is less than 0.05 % of the free stream, and has a slight negative static pressure gradient of approximately $dC_p/dx = -0.003$ per meter because of constant area test section. The air exchanger is located downstream of the fan and motor assembly and uses a boundary layer bleed on the entry flow. The continuous air exchange prevents the excessive temperature increase during the test.

The model used for the wind tunnel test was a flat plate, half span, 60 degree sweep back delta wing with 4 segmented constant chord leading edge flaps and a 1.27 m root chord. The details of the delta wing model are

shown in Fig. 7. The model was designed to be mounted on a circular turntable of 1.78 m diameter, which was mounted on the wind tunnel floor. Since the turntable was raised 57.2 mm from the floor of the wind tunnel, additional wooden panels were installed on the tunnel floor to provide a even floor surface. The delta wing model was 38 mm thick, constructed of two sheets of 19 mm thick plywood glued together. Flaps were attached to the leading edge of the delta wing with a piano hinge, and heavy duty hinges were used to set the flaps at desired deflection angle. The flap apex angle was 30° . The flap chord to the wing root chord ratio was 0.095, which was based on the result of earlier tests by Marchman(1981a). 43 pressure taps were provided on the suction side of the wing and flaps, and 4 pressure taps were installed on the pressure side of the flaps.

In order to provide a smooth wing surface, 1.6 mm O.D. copper tubings were inlaid into grooves on the wing surface, and 0.5 mm pressure taps were drilled along a line perpendicular to the leading edge of the wing after final finishing of the wing surface. The location of the pressure taps are listed in Table. 1. All the pressure tubes connected to the pressure taps were buried inside the delta wing and connected to the pressure scanner which was located immediately outside the test section to reduce the time lag inherent in any pressure measuring system which may be caused by long leads from the pressure ports to the pressure transducer.

The maximum projected area of the model to the plane normal to the free stream was 12.5 % when the angle of attack was 40° with zero flap deflection.

2.2 INSTRUMENTATION

During the pressure distribution tests, 47 pressure taps from the wing model and from the static port of the tunnel pitot-static tube were connected to a pressure scanner (Scanivalve model D). A Setra model 237 pressure transducer was engaged with pressure scanner. This pressure scanner was capable of scanning 48 ports and was actuated by a scanner controller which received control signals from a relay actuator (Hewlett Packard 59306A). A small desk top computer (HP 9825) was used as a master controller and real time data processor and it was succeeded by a bigger desk desk top computer (HP 9836) during the later phase of the experiment. The desk top computer controlled a digital volt meter (HP 3455A), a scanner (HP 3495A) and a relay actuator (HP 59306A). A schematic diagram of the instrumentation is shown in Fig. 8. In addition to the above data acquisition system, a digital barometer (Validyne model DB 99) was used for barometric pressure measurement and a barocel electric manometer (Datametric model 1173) was used to read the tunnel dynamic pressure from a standard pitot-static tube of 7.9 mm diameter, which was mounted 0.3m from the tunnel wall. The free stream temperature was monitored by a thermistor type temperature sensing probe mounted on the tunnel wall and indicated on a digital thermometer (Instrulab model 1563). The temperature sensing probe was mounted on the tunnel wall using the wooden block to prevent the heat transfer from by the wind tunnel wall.

During the mean flow field survey, A 5-hole yawhead probe (United sensor model DC 125) was connected to the pressure scanner instead of the 47

pressure ports from the wing. The yawhead probe was mounted on a yawhead probe support which was fixed to the traverse system. A narrow L-shaped steel beam (25 mm wide, 1.4 m long) was fixed to the traverse system as a yawhead probe support. The traverse system was set 0.5 m behind the wing trailing edge to prevent the possible interference in the vortex flow. The traverse system was equipped with DC step motors, allowing a traverse of about 1.25 m in both horizontal and vertical directions. Therefore the flow field on the plane normal to the free stream could be mapped without difficulty. The least counts of the traverse in the vertical and horizontal direction was 1 mm and 0.25 mm respectively. The horizontal and the vertical travel of the traverse were independent and were controlled manually during the experiment.

The yawhead probe has a 0.61 m stem and probe tip has a blunt conical head. The probe tip was 3.2 mm diameter, and 50 mm long which was small enough not to interfere the vortex formation on the leading edge of the delta wing.

2.3 TEST PROCEDURES

The half span delta wing model was mounted vertically on the turntable within the accuracy of 0.5° . The angle of attack were set by rotating the turntable. The turntable was geared into a DC motor which could rotate the turntable in both clockwise or counter-clockwise directions. The rotation of the turntable was manually stopped when the counter showed the desired angle of attack. It was not a difficulty task to set the angle

of attack within 0.1° due to the slow movement of the turntable and a turntable indicator accuracy of 0.01° . Fig. 9 shows the test set up of the delta wing model in the test section for the mean flow field measurement.

Although the flaps were designed to allow setting at different individual flap deflection angles, all flaps were set at the same flap angle during these experiments. The flap deflection angle was adjusted manually with the precision inclinometer (Higler Watts model TB 121) with the error less than 0.3° . After setting the flap deflection angle, all the gaps between flaps and between flaps and wing were sealed with tape to prevent any leakage of the flow from the pressure side to suction side.

A data acquisition program was developed to control and read the data automatically from the various instruments. The data acquisition process was generally as follows. First, the desk top computer set the device at the desired position and the input channel of the scanner was selected to allow the output signal from the transducer to be read by the digital volt meter. Next, the digital volt meter read the output signal from the transducer and sent the results to the desk top computer. A certain number of readings were taken and averaged to prevent the random errors. Lastly, the averaged value of the readings was stored into the desk top computer. Above procedure was repeated for each output datum from the instrument. After all the data were taken, the results were printed out and recorded on the data cassettes or on the floppy diskettes of the desk top computer. The computer could also be used to send the experimental

data to the main computing facility (IBM 3084) for later data analysis. Throughout the tests, 25 readings were taken and averaged for each datum. The sampling rate of the digital volt meter was 24 readings per second.

The pressure distribution investigations were performed at a Reynolds number of about 2.14×10^6 based on the root chord of the delta wing, through a range of the angle of attack from zero to 40° with flap deflection angle from zero to 45° , both in 5° increments.

Smoke and tuft flow visualization tests were conducted in an attempt to correlate the flow pattern and pressure distributions, and to investigate the behavior of the vortex flow above the wing surface. Smoke tests proved inconclusive because the smoke stream being larger than the vortex, and therefore, covering the details of the flow. Two sets of the flow visualization experiments were done using woolen tufts. During the first set of flow visualization experiments, 12 rows of the woolen tufts were attached to the upper surface of the delta wing with flap, where each row of the woolen tufts was perpendicular to the flap hinge line. The average length of the tufts was about 51 mm. For the second set of the flow visualization experiment, 19 rows of woolen tufts were attached to the upper surface of the wing with flap. Each row of the tufts on the wing surface was perpendicular to the wing center line, while each row of the tufts on the flap surface was perpendicular to the flap hinge line. The average length of the tufts were about 19 mm. The flow pattern on the delta wing surface was recorded on a video cassette recorder for later analysis. The Reynolds number was kept the same for both pressure distribution ex-

periments and during the flow visualization experiments using woolen tufts.

The mean flow field surveys were performed for angles of attack of 10° and 15° with flap deflection angle of 10° and 30° . For each case, the flow fields were measured at 3 different planes over the wing surface which were perpendicular to the free stream and located at $X/C = 0.375$, 0.625 , and 0.875 each.

Previous calibrations of the yawhead probe (Lee (1983)) were based on the maximum flow angle of 42° . This was not enough to cover the highly complicated three dimensional vortex flow around a delta wing, and it also required a large amount of CPU time to compute flow properties from the yawhead output because two dimensional interpolation is needed to calculate each flow property (flow cone angle, flow bank angle, static pressure, and total pressure) for each data point. A new yawhead calibration was performed for a larger range of flow angle, and a simple method to determine the flow properties was developed based on the method of Gerner et al.(1984). The detailed procedures and the result of the yawhead calibration are listed in Appendix A

To measure the flow properties close to the leading edge flap surface, it was necessary to orient the yawhead probe at -10° pitch and -10° yaw from the free stream. These probe setting angles were calibrated in the free stream before measuring the flow field at each stream-wise station. After the flow field measurement, the flow angles were calculated to the

true flow angles w.r.t. the free stream using the pre-calibrated probe orientation angles.

To avoid the vibration of the yawhead probe support, the mean flow field measurements were done at the reduced free stream velocity and the Reynolds number was about 1.50×10^6 based on the root chord of the delta wing. The yawhead probe was also calibrated at the same free stream velocity as the mean flow field measurement, which resulted the Reynolds number of 3780 based on the probe tip diameter.

Sitaram et al.(1981) measured the wall vicinity effect for the yawhead probe which is similar to the one in present study. They found out that the errors in velocity and total pressure were less than 1 % of the actual value when the distance between probe and solid wall was more than 2.3 probe diameters. In the present study, the minimum distance between the wing surface and the yawhead probe was kept 2.88 probe diameter.

2.4 UNCERTAINTY OF THE EXPERIMENTAL RESULTS

An attempt has been made to identify the different sources and magnitude of the uncertainties associated with the various measurements and experimental methods throughout the experimental study.

The basis uncertainties introduced by the wind tunnel and model setting are as follows:

1. The average variation of the local dynamic pressure across the test section was less than 0.5 % of the free stream dynamic pressure (Reynolds (1982)).
2. Free stream turbulence levels were less than 0.05 % of the free stream velocity. Turbulence levels for several free stream velocities are listed in table 2.
3. The maximum temperature drift of the free stream was less than 0.4°F (0.22°C) for each run.
4. The maximum barometric pressure variation for each run was less than 1.0 lb/ft² (47.88 N/m²).
5. The error in model setting was less than 0.5°.
6. The angle of attack was set within the accuracy of 0.1°.
7. The probe positioning error was less than 3 mm during the mean flow measurement.

The uncertainties of the instruments which were used throughout the experiment are as follows:

1. The barometric pressure was measured within the accuracy of 0.01 inch Hg (33.86 N/m²)
2. The indicated dynamic pressure was accurate up to 0.05 % of reading.
3. The uncertainty of the free stream temperature measurement was less than 0.6°F (0.33°C).
4. The maximum uncertainty of the output from the pressure transducer used for the wing pressure distribution experiment and the mean flow field survey experiment was less than 0.009 lb/ft² (4.309 N/m²).

The uncertainties associated with the 5-hole yawhead probe were as follows:

1. The RMS (root mean square) error of the pitch angle was 3.93° .
2. The RMS error of the yaw angle was 2.36° .
3. The RMS error of the total pressure was 4.82 % of the actual total pressure.
4. The RMS error of the dynamic pressure was 5.33 % of the actual dynamic pressure.

The standard uncertainty equation (Eqn. (3.2) in Holman (1978)) was used to determine the uncertainty of the calculated value, which is,

$$\delta f = \left[\left(\frac{\partial f}{\partial x_1} \delta x_1 \right)^2 + \left(\frac{\partial f}{\partial x_2} \delta x_2 \right)^2 + \dots + \left(\frac{\partial f}{\partial x_n} \delta x_n \right)^2 \right]^{1/2} \quad (2. 1)$$

where $f = f(x_1, x_2, x_3, \dots, x_n)$

δf = uncertainty of the f

δx_i = uncertainty of the independent variables x_i

($i=1, 2, 3, \dots, n$)

ERROR IN DENSITY CALCULATION: The density of the air is given by (Eqn. (1) in Sung (1980))

$$\rho = \frac{1}{R_a T} \left(P_a - \frac{R_v - R_a}{R_v} P_v \right) \quad (2. 2)$$

where R_a = gas constant of the dry air

$$(1716 \text{ ft-lb/slug} \cdot ^\circ\text{R}, 286.90 \text{ m}^2/\text{sec}^2 \cdot ^\circ\text{K})$$

R_v = gas constant of the water vapor

$$(2760 \text{ ft-lb/slug} \cdot ^\circ\text{R}, 461.49 \text{ m}^2/\text{sec}^2 \cdot ^\circ\text{K})$$

P_a = barometric pressure

P_v = water vapor pressure

T = temperature.

using the uncertainty equation (2. 1) for the ρ ,

$$\delta\rho = \left[\left(\frac{\partial\rho}{\partial T} \delta T \right)^2 + \left(\frac{\partial\rho}{\partial P_a} \delta P_a \right)^2 + \left(\frac{\partial\rho}{\partial P_v} \delta P_v \right)^2 \right]^{1/2} \quad (2. 3)$$

$$\text{where } \left| \frac{\partial\rho}{\partial T} \delta T \right| = \frac{1}{R_a} \left(P_a - \frac{R_v - R_a}{R_v} P_v \right) \frac{\delta T}{T^2}$$

$$\left| \frac{\partial\rho}{\partial P_a} \delta P_a \right| = \frac{\delta P_a}{R_a T}$$

$$\left| \frac{\partial\rho}{\partial P_v} \delta P_v \right| = \left(\frac{R_v - R_a}{R_a R_v} \right) \frac{\delta P_v}{T}$$

The range of the each variables during the experiment was

$$T : 40.0 \sim 75.0^\circ\text{F} (4.4 \sim 23.9^\circ\text{C})$$

$$P_a : 1959 \sim 2005 \text{ lb/ft}^2 (9.38 \times 10^4 \sim 9.60 \times 10^4 \text{ N/m}^2)$$

Since the vapor pressure influence was not accounted for in the air density calculation, saturated vapor pressure at 75°F (62.0 lb/ft^2 , $2.967 \times 10^3 \text{ N/m}^2$) was used to calculate the uncertainty. Calculating the

maximum uncertainty value for each term using the above-mentioned uncertainty value from each measurement,

$$\left| \frac{\partial \rho}{\partial T} \delta T \right| = 2.81 \times 10^{-6} \text{ slug/ft}^3 \quad (1.45 \times 10^{-3} \text{ Kg/m}^3)$$

$$\left| \frac{\partial \rho}{\partial P_a} \delta P_a \right| = 8.25 \times 10^{-7} \text{ slug/ft}^3 \quad (4.25 \times 10^{-4} \text{ Kg/m}^3)$$

$$\left| \frac{\partial \rho}{\partial P_v} \delta P_v \right| = 2.56 \times 10^{-5} \text{ slug/ft}^3 \quad (2.32 \times 10^{-2} \text{ Kg/m}^3)$$

combining all three terms,

$$\delta \rho = 2.58 \times 10^{-5} \text{ slug/ft}^3 \quad (1.33 \times 10^{-2} \text{ Kg/m}^3)$$

using the air density at $T = 75^\circ\text{F}$ and $P_a = 1959 \text{ lb/ft}^2$, the maximum error in air density becomes,

$$\delta \rho / \rho = 0.0121$$

It is clear that the major portion of the uncertainty of the air density come from neglecting the vapor pressure.

ERROR IN DYNAMIC PRESSURE CALCULATION: For the dynamic pressure measurement, a standard pitot-static tube was used which has static pressure holes located at 8D from the tip and 16D from the stem, where D refers to the diameter of the pitot-static tube. In this case, the indicated dynamic pressure reads 0.5 % less than the actual dynamic pressure (Fig. 3.7 in Pope and Harper (1966)). Combining the uncertainty of the meas-

urement with the error from the dynamic pressure reading, the dynamic pressure error is,

$$\delta q/q = 0.0055$$

ERROR IN THE FREE STREAM VELOCITY CALCULATION: The free stream velocity is,

$$V = (2q/\rho)^{1/2} \quad (2.4)$$

then the equation for the free stream velocity become,

$$\delta V = \frac{V}{2} \left[\left(\frac{\delta q}{q} \right)^2 + \left(\frac{\delta \rho}{\rho} \right)^2 \right]^{1/2} \quad (2.5)$$

substituting the value for $\delta q/q$ and $\delta \rho/\rho$, the maximum error in free stream velocity is,

$$\delta V/V = 0.00665$$

For the velocity determined from the yawhead probe, using the RMS error in dynamic pressure measurement for $\delta q/q = 0.0533$, then the RMS error in velocity measurement is,

$$\delta V/V = 0.0273$$

ERROR IN THE PRESSURE COEFFICIENTS: Since the pressure coefficient is defined as,

$$C_p = \frac{P - P_\infty}{q} \quad (2.6)$$

then the error equation for the pressure coefficient is

$$\delta C_p = \left[\left(C_p \frac{\delta q}{q} \right)^2 + \left(\frac{\delta P}{q} \right)^2 + \left(\frac{\delta P_\infty}{q} \right)^2 \right]^{1/2} \quad (2.7)$$

Dynamic pressure ranged from 7.20 lb/ft² (344.8 N/m²) to 8.836 lb/ft² (423.1 N/m²). Using the $q = 7.20$ lb/ft², and $C_p = -3.57$ (minimum measured C_p on the wing) to get maximum δC_p , then the maximum error in pressure coefficient is

$$\delta C_p = 0.0198$$

III. EXPERIMENTAL RESULTS

3.1 FLOW REGIME

The results of the experimental study provide a detailed description of the flow and pressures on a delta wing with leading edge vortex flaps, over a wide range of angle of attack and flap deflection angle. The leading edge vortex flap will simply be called the flap for the rest of this text.

The flap deflection angle is defined as the angle between the flap upper surface and the surface parallel to the wing upper surface on a plane normal to the flap hinge line, rather than the angle between the wing camber line and flap camber line. This is because the vortex flow is affected more by the shape of the upper surface than the camber line shape. Results (Fig. 10) from other investigators (Campbell et al.(1955), Wentz and Kohlman (1968), Faery et al.(1981), and Marchman (1981a)) reveal the effect of the upper surface shape of the delta wing. From Fig. 10, one can find out that the delta wings with convex surface yield less lift coefficient than the flat plate delta wings at the same angle of attack, while the delta wings with sharp leading edge produce more induced drag than the delta wings with round leading edge at the same lift coefficient. The cause of the decrease in the drag coefficient after stall will be explained at section 3.2. A similar effect can be found from Fig. 11 which was taken from the result of Jaquet and Brewer (1949).

It was found that the flap deflection angle plays a decisive role in determining the flow pattern around a delta wing with flap, as expected. For each flap deflection angle, there is a range of angle of attack which has distinct flow characteristics. Generally, the vortex flow started on the leading edge of the flap at small angle of attack and only a small portion of the flap was affected by the vortex flow. With increasing angle of attack, the area affected by the vortex flow was increased. When the angle of attack at which a given flap angle was optimum was exceeded the vortex core moved inboard of the wing and then started to burst at the rear part of the wing. The vortex bursting point moved from the trailing edge to the apex with increasing angle of attack. A map of the flow regime (Fig. 12) corresponding to above-mentioned phenomena on a delta wing with flap, was made from the results of flow visualization experiments.

The vortex starting angle of attack, α_{VS} , is defined as angle of attack where the vortex flow starts on the leading edge of the flap upper surface at each flap deflection angle. α_{VS} increases as flap deflection angle is increased. A completely attached flow was observed on the upper surface of the wing and flap at angle of attack less than α_{VS} . In this case, flap deflection was large enough to make the flap surface face the incoming free stream. At large flap deflection angle ($\delta > 30^\circ$) with $\alpha < \alpha_{VS}$, a vortex flow (wing vortex) was developed inboard of the flap hinge line. This wing vortex was generated by the large flow turning angle between the flap upper surface and wing upper surface which caused flow separation at the flap hinge line and reattachment of the flow inboard of the flap

hinge line. It was not possible to define a boundary between the wing vortex and flow acceleration near the flap hinge line because it is a relatively slowly changing process, thus a flow regime with the wing vortex appearance was not included in Fig. 12.

As the angle of attack is increased above α_{VS} , the primary vortex was found on the flap surface and reattachment line was placed between the flap leading edge and the flap hinge line. The reattachment line moved continuously toward the flap hinge line as α increased.

The OPTIMUM ANGLE OF ATTACK, α_{OPT} , was defined as the angle of attack where the reattachment line at $x=0.75$ was placed on the flap hinge line at each flap deflection angle. At $\alpha=\alpha_{OPT}$, most of the primary vortex was above the flap, in other words, the primary vortex was confined to the leading edge flap, thus producing a thrust on the flap surface and increasing the lift/drag ratio due to the low pressure caused by the vortex flow.

A secondary vortex appeared outboard of the vortex core at around $\alpha=\alpha_{OPT}$ due to the adverse pressure gradient produced by the primary vortex driving the boundary layer flow under the vortex to flow toward the leading edge of the flap. At higher flap deflection angles ($\delta>30^\circ$), the secondary vortex flow was not found on the flap surface because the primary vortex and wing vortex already existed and these two vortices merged together to become a larger vortex with reduced influence on the boundary layer flow below the vortex. A streamwise attached flow was observed

between the primary vortex and the wing vortex at $\alpha_{VS} < \alpha < \alpha_{OPT}$ with higher flap deflection angle ($\delta > 30^\circ$).

As the angle of attack is increased from the α_{OPT} the rear portion of the vortex moved inboard of the wing and then started to burst from the wing trailing edge. The vortex bursting point progressed from the trailing edge to the apex of the wing with increasing angle of attack, thus producing a loss of suction effect on the upper surface and causing a loss of lift and increase in nose-up pitching moment. α_{VBA} is defined as an angle of attack where the vortex burst at the wing apex. Further increasing the angle of attack after α_{VBA} brought the delta wing into complete stall.

The vortex starting flap angle, δ_{VS} and the OPTIMUM FLAP ANGLE, δ_{OPT} are defined as the same manner as α_{VS} and α_{OPT} , respectively.

Increasing the flap angle at a fixed angle of attack caused a effect somewhat similar to the case of decreasing the angle of attack at a fixed flap angle.

3.2 SURFACE STREAMLINES

The surface streamlines were sketched based on flow visualization experiments using woolen tufts. A representative case is shown in Fig. 13. The streamlines near the wing center line are oriented toward the free stream direction and it begin diverge near the flap hinge line. The re-

attachment line for the primary vortex was found by tracing the points of diverging streamlines and the secondary separation line was found by tracing the points of the converging streamlines.

Prior to the tuft flow visualization experiment, the pressure distributions were compared for cases with and without tufts, to investigate the effect of the tufts on the flow. The results are shown on Fig. 14 for the case of $\alpha=15^\circ$ and $\alpha=25^\circ$ with zero flap deflection.

The pressure distributions were almost the same except that the suction pressure is reduced slightly for the case with the tufts. This occurred because the attached tufts increased the turbulence level inside the vortex flow which increased the displacement thickness of the turbulent boundary layer below the vortex core by small amount. The increased displacement thickness shifted the vortex core upward from the wing surface. For a constant circulation of the primary vortex, this upward shift of the vortex core leads to a reduction of the induced flow on the surface below the vortex core, and it will finally reduce the suction on the upper surface of the delta wing.

It was concluded that the results from the tuft flow visualization test could be used for comparison with the pressure distribution results since it was confirmed that no major change in flow occurred by attaching the tufts to the wing surface.

Typical cases of pressure distributions and corresponding sketches of the surface streamlines are shown on Fig. 15 - 22 for ranging angles of attack and $\delta=10^\circ$. Comparing the surface streamlines with the pressure distributions, one can see that the pressure distributions coincide exactly with the surface streamline patterns in such details as the primary vortex and the secondary separation line.

At small angle attack (Fig. 15 and 16) the flow near the wing apex separated from the apex edge (line OA in Fig. 7) and reattached to the flap surface, thus creating a closed bubble at the apex. The primary vortex started from the flap apex (point A in Fig. 7) and increased in strength as it flowed towards the trailing edge. The vortex core in Fig. 16.b was plotted based on the mean flow field measurement experiment and it shows the negative pressure peak beneath the vortex core. Below the closed bubble near the apex the pressure distribution become relatively smooth compared to the pressure distribution below the primary vortex. Inboard of the primary reattachment line the pressure distribution is almost constant due to the attached flow over a flat wing surface. There is a slight increase in suction pressure outboard of the secondary separation line due to the secondary vortex formed by the boundary separation below the vortex core. The combined effect of the increased suction in the region of decreasing the suction pressure resulted in the more or less even pressure distribution near the leading edge of the flap.

At moderate angles of attack (Fig. 17 and 18), the primary vortex merged with the separated flow from the apex edge, thus creating a strong primary

vortex from the wing apex and providing a strong negative pressure peak near the apex. The primary vortex become stronger as compared to the case of smaller angle of attack.

The primary vortex burst at $x=0.750$ ($x'=0.866$) for $\alpha=15^\circ$ with $\delta=10^\circ$ (midway between the 3rd and the 4th row of pressure taps). Bursting was characterized by the enlarged area of the vortex flow and flattened pressure distribution behind the bursting point instead of the negative pressure peak observed forward of the vortex bursting point (Fig. 17). The wool tufts fluctuated rapidly behind the vortex bursting point, and this was used to find the location of the primary vortex bursting point.

At $\alpha=20^\circ$ with $\delta=10^\circ$ (Fig. 18), the vortex bursting point progressed forward of the 3rd row of the pressure taps. The primary vortex reattachment line began at the wing apex along the flap hinge line near the apex for $\alpha=15^\circ$ and $\alpha=20^\circ$ with $\delta=10^\circ$. Further increasing the angle of attack, $\alpha=25^\circ$ with $\delta=10^\circ$, the reattachment line started from the point behind the wing apex on the wing center line and inboard of the flap hinge line (Fig. 19). After the vortex burst at the wing apex (Fig. 20), the reattachment line was started from the almost $X=0.5$ for the case of $\alpha=30^\circ$, $\delta=10^\circ$.

It was possible to define the mean surface streamlines after the vortex burst since the wool tufts fluctuated at high frequency with a small amplitude. After the complete stall, which is seen for the $\alpha \geq 35^\circ$ with $\delta=10^\circ$ case, the wool tufts were not fluctuating rapidly but fluctuating in low frequency with large amplitude. Therefore it was impossible to construct

the mean streamlines from the orientation of the tufts. At a slightly higher α than α_{VBA} , there is still a weak vortex flow on the upper surface of the delta wing which will wash away the flow. At higher α the vortex flow disappeared completely from the delta wing and the wing upper surface is placed in a dead air region, thus the delta wing behaves like the flat plate which is stalled in the free stream. This reduces the drag as well as lift. The transition from a weak vortex flow to fully separated flow, could explain the reduction in induced drag in Fig. 10.b.

Fig. 21 shows the streamwise attached flow between the primary vortex and wing vortex at $\alpha_{VS} < \alpha < \alpha_{OPT}$ with large flap deflection ($\delta > 30^\circ$). Comparing the location of the vortex core in Fig. 17 and Fig. 22, the vortex core was shifted toward the leading edge and the suction peak pressure reduced with an increase in flap deflection.

In order to confirm the accuracy of the experimental results, the results on the primary vortex reattachment lines were compared to the results of the Frink et al. (1983). Frink's results were based on a simple biconvex profile, 58° delta wing with a constant chord, sharp edged leading edge flap. The details of the Frink's model shown on Fig. 23, are quite close to the model in the current study. The flap chord to root chord ratio and the flap apex angle for Frink's model were 0.111 and 29° respectively, compared to 0.095 and 30° for the current study. From Frink's result, only the data for the case without the canard were compared with current study (Fig. 24). The flap deflection angle for the Frink's data was corrected to the surface deflection angle which was used in current study.

In Fig. 24 the abscissa represents the distance from the apex in fraction of the root chord and the ordinate corresponds the distance from the flap hinge line, also in fraction of the root chord. The zero value of the ordinate denotes the flap hinge line.

There is an excellent agreement in location of the reattachment line between Frink's results and the results from the current study, although Frink's results were based on pictures taken from an oil flow visualization experiment and the current data are based on the wool tuft flow visualization. When the reattachment line were occurred inboard of the flap hinge line, i.e. on the wing surface, there was a small deviation between the results which was due to the difference in wing profiles. A biconvex wing with 6.85% maximum thickness wing was used for Frink's study while a 3% flat plate wing was used for the current study. Using the same criteria to determine the optimum flap angles, the optimum flap angles fall onto the same curve for both cases (Fig. 12).

3.3 PRESSURE DISTRIBUTION

The pressure distribution results showing the effects of flap deflection at different angles of attack are shown on Fig. 25 - Fig. 33. Pressure distributions are plotted on a rotated axis where X' represents the distance along the flap hinge line from the wing apex, and Y' corresponds to the distance from the flap hinge line. Therefore, $Y' > 0$ on the flap surface and $Y' < 0$ on the wing surface, i.e. inboard of the flap hinge line.

There is no considerable effect of the flap deflection at $\alpha=0^\circ$, since the primary vortex had not started at $\alpha=0^\circ$ with $\delta=0^\circ$ (Fig. 25). The pressure distribution on the flap upper surface increased with increased flap deflection angle, and a small negative pressure peak was occurred immediately inboard of the flap hinge line for large flap deflections because of the flow acceleration around the flap hinge.

The effect of the flap deflection on a pressure distribution started to appear at $\alpha=5^\circ$ (Fig. 26), although it is still a weak vortex flow. The vortex flow was weakened by small flap deflection. With large flap deflection, the pressure distributions look similar to the $\alpha=0^\circ$ case because the vortex did not occur at $\alpha=5^\circ$ with $\delta\geq 15^\circ$. Since the vortex flow was well developed at $\alpha=10^\circ$ with $\delta=0^\circ$, the flap deflection effect became evident from $\alpha=10^\circ$ (Fig. 27). Generally, increasing the flap deflection at a fixed angle of attack reduce the strength of the vortex flow and the vortex core moved close to the leading edge of the flap.

At $\alpha=15^\circ$ (Fig. 28), small flap deflection ($\delta<15^\circ$) weakened the vortex flow so the negative pressure peak is reduced, which is similar to the case of $\alpha=10^\circ$. But at moderate flap deflection ($15^\circ\leq\delta<30^\circ$), not only did the negative pressure peak move outward from the wing center line, but also the negative pressure peak is increased. The small flap deflection weakened the strength of the primary vortex and the primary vortex remains in merged vortex flow with the separated flow from the apex edge. With moderate flap deflection, the separated bubble on the apex detached from the primary vortex which resulted in a weaker and smoother negative

pressure distribution near the apex. The weak primary vortex generated a weak adverse pressure gradient below the vortex core, therefore the secondary vortex region was reduced. As the secondary vortex region was reduced, the primary vortex core moved closer to the leading edge (downward and outboard shift), and this shift of the vortex core induced a higher velocity on the flap surface resulting in a strong negative pressure peak near the leading edge. A large flap deflection ($\delta \geq 30^\circ$) weakened the primary vortex so much that the secondary vortex disappeared and the negative pressure peak decreased as flap deflection increased above a moderate flap angle.

Another benefit of the flap deflection shown in Fig. 28 is the restoration of the vortex flow where bursting had occurred at lower flap deflection. The primary vortex flow is restored at $\alpha = 15^\circ$ with a flap deflection $\delta > 20^\circ$ at $x' = 1.011$, where the primary vortex had burst with $\delta = 0^\circ$. The restoration of the vortex flow is due to the decreased adverse pressure gradient along the vortex core with flap deflection. The restoration of the vortex flow (or suppression of the vortex bursting) is clear at $\alpha = 20^\circ$ (Fig. 29), where flap deflection of $\delta \geq 25^\circ$ restored the vortex bursting at $x' = 0.722$.

The shift of the vortex core and increased suction peak are also seen at $\alpha = 20^\circ, 25^\circ$ (Fig. 29 and 30). The burst vortex near the trailing edge can not be suppressed at high angle of attack (Fig. 30). At high angle of attack where the vortex burst from the apex, flap deflection can restore the vortex flow only near the apex. One can see that the vortex is restored only up to $x' = 0.433$ at $\alpha = 30^\circ$, by a flap deflection of $\delta = 45^\circ$ (Fig.

31). At $\alpha=35^\circ$ (Fig. 32), It was not possible to suppress the vortex bursting from the apex, but the burst weak vortex flow is obtained by large flap deflection ($\delta=45^\circ$). Further increasing the angle of attack up to $\alpha=40^\circ$, the flow was completely stalled, therefore the flap was ineffective as a means of aerodynamic performance improvement (Fig. 33).

It might be possible to restore the vortex flow near the apex at $\alpha=35^\circ$ by large flap deflection ($\delta>45^\circ$), but deflecting the leading edge flap more than 45° does not appeared to be a practical way to improve aerodynamic performance, when one compares the gain in lift in light of the structural requirement of the flap and increased drag.

If one assumes that the operating range of the delta wing is determined by the criteria of the presence of a well established vortex flow up to 50% of the wing chord, then the operating range of this type delta wing will be $\alpha=5^\circ - 30^\circ$. Tabulated data for the pressure distributions are listed in Table 3. Some of the data in Table 3 are missing due to the error in positioning the pressure scanner selector and clogged pressure taps in the later phases of the experiment.

3.4 MEAN FLOW FIELD

Prior to discussing the results of the mean flow field experiment, consider the criteria to determine the location of the vortex sheet. Referring to Fig. 34, let V_s be the velocity at an arbitrary point P on the

vortex sheet. From Eqn.(18.36) in Karamcheti (1966), the velocity jump across the vortex sheet is,

$$\Delta \vec{V} = \gamma \times \hat{n} \quad (3. 1)$$

where \hat{n} is the unit normal vector at the vortex sheet and γ is the strength of the vortex sheet. Then the velocities on both sides of the vortex sheet become,

$$\vec{V}_e = \vec{V}_s + \frac{1}{2}\Delta \vec{V} \quad (3. 2)$$

$$\vec{V}_i = \vec{V}_s - \frac{1}{2}\Delta \vec{V} \quad (3. 3)$$

where the subscript e and i refer to the outside and inside of the vortex sheet. Bernoulli's equation for steady flow can be written as ,

$$P_{te} = P_e + \frac{1}{2}\rho V_e^2 = P_e + \frac{1}{2}\rho(V_s^2 + \frac{1}{4}\Delta V^2)$$

$$P_{ti} = P_i + \frac{1}{2}\rho V_i^2 = P_i + \frac{1}{2}\rho(V_s^2 + \frac{1}{4}\Delta V^2)$$

$$P_{ts} = P_s + \frac{1}{2}\rho V_s^2$$

where the subscript s refers to the vortex sheet. The scalar product of \vec{V}_s with $\Delta \vec{V}$ is zero because \vec{V}_s is perpendicular to $\Delta \vec{V}$. Since there is no pressure difference across the free vortex sheet,

$$P_{te} = P_{ti} = \frac{1}{2}\rho(V_s^2 + \frac{1}{4}\Delta V^2) + P \quad (3. 4)$$

$$P_{ts} = P + \frac{1}{2}\rho V_s^2 \quad (3. 5)$$

The total pressure becomes minimum at the vortex sheet, therefore this can be used as a criterion to find the vortex sheet. Since the velocity jump is proportional to the inverse of the distance from the vortex sheet, the total velocity becomes maximum just outside the vortex sheet. Therefore the local maximum velocity can also be used to determine the location of the vortex sheet.

For the current study, vortex sheet location was determined from the local maximum velocity and not from the local minimum P_t for two reasons. The first reason is that a large amount of data are needed to find the local minimum of P_t because minimum P_t occurs only at the vortex sheet. The other reason is that the measurement error in velocity is about one half of the the measurement error in the total pressure. From section 2.4., the error in the velocity measurement is 2.73% while that of the total pressure is 4.82% .

The velocity vector plots, the static pressure contour plots and the total pressure contour plots are made from the results of the mean flow field measurement and are shown in Fig. 36 - 47. In the static pressure contour plots and the total pressure contour plots, each contour represents the static pressure coefficient, $C_{ps} = (P_s - P_\infty)/q_\infty$ and total pressure coefficient, $C_{pt} = (P_t - P_\infty)/q_\infty$, respectively. In Fig. 36 - 47, the flow properties were plotted on the plane perpendicular to the free stream. Z and \bar{w} represent the axis perpendicular to the free stream and Y-axis, and the velocity in Z direction, respectively. The vortex sheet location was determined by tracing the local maximum of the velocity which is plotted

as dashed line. The cross sectional shapes of the vortex sheet are elliptical for the 60° delta wing rather than the circular shape usually found on higher sweep delta wings. The general shape of the static pressure contour is spiral compared to the concentric ellipse for the total pressure contour.

The positions of the vortex core were determined by examining the point where the velocity changes the sign in both Y and Z direction, and it coincided well with the location of the minimum total pressure and the minimum static pressure. The trajectories of the vortex core on the X-Z plane are plotted on the Fig. 35.

The velocity vector plots in the Y-Z plane for the case of $\alpha=10^\circ$ with $\delta=10^\circ$ are shown in Fig. 36, and the corresponding static pressure and total pressure isobars are shown in Fig. 37 and 38, respectively. The shape of the vortex sheet did not change much at different X stations for this case. The effect of the secondary vortex on the velocity vector plot was so small that it can only be recognized from the slight upward inclination of the velocity vector, since the secondary vortex is a separation bubble inside the boundary layer. If measurements had been taken close to the flap surface, the secondary vortex might be seen clearly. The secondary vortex can be seen clearly in the total pressure plot, where the region containing the secondary vortex is shown by the closed region of reduced total pressure.

The effect of the vortex bursting is shown on Fig. 39 - 41 for the case of $\alpha=15^\circ$ with $\delta=10^\circ$ where the vortex had burst at $x=0.75$. The first effects are the enlarged shape of the vortex sheet and reduced gradient of the tangential velocity in radial direction at the station downstream of the bursting point. The next effects are the large decreases in the gradients of the static pressure and total pressure in the radial direction. Also the region of minimum total pressure and minimum static pressure are widened after vortex bursting. All the above phenomena were caused by the resulting turbulent mixing process inside the burst vortex flow which has the effect of smoothing the gradient of any properties.

At $\alpha=10^\circ$ with $\delta=30^\circ$, a weak vortex was developed and flow reattachment occurred on the flap surface, as shown in Fig. 42 - 44. The wing vortex is shown clearly, having been generated by flow separation at the flap hinge line due to the large flow turning angle. Subsequently there is flow reattachment inboard of the hinge line.

The case close to optimum flap deflection is shown on Fig. 45 - 47, where the vortex is attached near to the flap hinge line, thus producing a thrust force on the flap. The second vortex did not start at $x=0.375$, therefore there was neither an upward inclination of the velocity vector, nor a closed region of reduced total pressure.

IV. COMPUTATIONAL APPROACH

4.1 BASIC PRINCIPLE

For an incompressible flow over a solid body, the continuity equation for the flow field is,

$$\nabla \cdot \vec{V} = 0 \quad (4.1)$$

If the flow is also irrotational, there exists a scalar function $\phi(x,y,z)$ which has a gradient equal to the velocity at each field point in the flow field such that $\vec{V} = \nabla \phi$. Then the continuity equation becomes the governing Laplace equation,

$$\nabla^2 \phi = 0 \quad (4.2)$$

The boundary conditions for this case can be written as,

$$\begin{aligned} \nabla \phi &= \vec{V}_{\infty} && \text{at infinity} \\ \nabla \phi \cdot \hat{n} &= 0 && \text{on body surface} \end{aligned} \quad (4.3)$$

where \vec{V}_{∞} = free stream velocity
 \hat{n} = unit normal vector on the body surface

Without a solid body in the flow field, the solution of the equation (4.2) becomes $\phi = V_{\infty} x$, if an axes system is chosen such that \vec{V}_{∞} is par-

allel to the X-axis. Separating the free stream solution $\phi_{\infty} = V_{\infty}x$ from the influence of a solid body, the velocity potential can be written as,

$$\Phi = \phi_{\infty} + \phi \quad (4.4)$$

where ϕ is the perturbation velocity potential due to the presence of a solid body in the flow field. This superposition is possible because the governing equation (4.2) is a linear differential equation. Since ϕ_{∞} is known, rewriting the governing equation w.r.t. ϕ alone,

$$\nabla^2 \phi = 0 \quad (4.5)$$

with the boundary conditions,

$$\left. \begin{array}{l} \phi = 0 \\ \nabla \phi = 0 \end{array} \right\} \quad \text{at infinity}$$

$$\nabla \Phi \cdot \hat{n} = \nabla(\phi_{\infty} + \phi) \cdot \hat{n} = 0 \quad \text{on body surface} \quad (4.6)$$

To find the solution for the Laplace equation, one starts from the divergence theorem. For any continuous vector field \vec{A} , in a domain D enclosed by the body surface S and outer boundary Σ which is located at an infinite distance from the body, the divergence theorem can be written as,

$$\iiint_D \nabla \cdot \vec{A} \, dD = \iint_{S+\Sigma} \vec{A} \cdot \hat{n} \, dS \quad (4.7)$$

Let

$$\vec{A} = \psi \nabla \psi' \quad (4.8)$$

Then Green's second theorem is obtained by substituting for A in equation (4. 7),

$$\iiint_D [\psi \nabla^2 \psi' - \psi' \nabla^2 \psi] dD = \iint_{S+\Sigma} [\psi \partial \psi' / \partial n - \psi' \partial \psi / \partial n] dS \quad (4. 9)$$

The solution for the Laplace equation (4. 5) can be obtained, if the proper function ψ' in equation (4. 9) is found. For this purpose, introduce the singularity functions that have a picking-out property. They are $1/r$ for the three-dimensional problem and $\ln r$ for the two-dimensional problem, where r is the distance of any point from a fixed point $P(x,y,z)$, where both points are in the same domain D . The singularity function is harmonic except at $r=0$ and can be expressed as,

$$\nabla^2(1/r) = -4\pi\delta(r) \quad (4.10)$$

where $\delta(r)$ is the Dirac delta function. Substituting ϕ and $1/r$ for ψ and ψ' respectively in equation (4. 9), the integration over the outer boundary Σ will yield zero because of the boundary conditions (4. 6) at infinity. Equation (4. 9) becomes,

$$\phi(P,t) = -\frac{1}{4\pi} \iint_S \frac{1}{r} \frac{\partial \phi}{\partial n} dS + \frac{1}{4\pi} \iint_S \phi \frac{\partial}{\partial n} \left(\frac{1}{r} \right) dS \quad (4.11)$$

where $P = P(x,y,z)$

This gives the value of ϕ at any point P in the flow field in terms of the value of ϕ and $\partial\phi/\partial n$ at the boundary. The first term in equation (4.11) has the same form as the velocity potential due to the source distributed on the body surface with source density $\partial\phi/\partial n$ per unit area. The second term is the same as the velocity potential due to the surface distribution of the doublet with doublet density ϕ . Replacing $\partial\phi/\partial n$ and ϕ with source density σ and doublet density μ , equation (4.11) becomes,

$$\phi = \underbrace{\iint_S \sigma \left(-\frac{1}{4\pi r} \right) dS}_{\text{source sheet}} + \underbrace{\iint_S \mu \left(-\frac{\partial}{\partial n} \frac{1}{4\pi r} \right) dS}_{\text{doublet sheet}} \quad (4.12)$$

where $\phi=\phi(P,t)$ velocity potential

$\sigma=\sigma(Q,t)$ source density

$\mu=\mu(Q,t)$ doublet density

P : point in flow field D

Q : point on the body surface S

r : distance between P and Q

n : normal to S at Q, positive into the flow

doublet axis direction is normal to S

There exists an infinite number of $\sigma(Q,t)$ and $\mu(Q,t)$ distributions producing the same solution in flow field D, but they will produce different solutions on surface S. The key is to find $\sigma(q,t)$ and $\mu(Q,t)$ that yields a solution satisfying the boundary conditions.

Generally, source distributions provide the shape of the body and doublet distributions provide load characteristics. Since solutions for thin lifting surfaces such as delta wings are desired, only the doublet distributions will be considered. Then equation (4.12) becomes,

$$\phi = \iint_S \mu \frac{\partial}{\partial n} \left(\frac{1}{4\pi r} \right) dS \quad (4.13)$$

Since the boundary conditions enforce zero normal velocity on the body surface (Neumann type B.C.), the solution ϕ can be obtained uniquely with the difference in additive constant. Hence, if the solution is found in terms of velocity, then it will be unique since the velocity is the gradient of the velocity potential. The boundary condition (4.6) at an arbitrary point on the body surface can be written as,

$$-V_{\infty n} = \nabla \phi \cdot \hat{n} \quad (4.14)$$

$$\text{where } V_{\infty n} = \nabla \phi_{\infty} \cdot \hat{n}$$

since ϕ is defined in D,

$$\begin{aligned} -V_{\infty n} &= \nabla_Q \phi \cdot \hat{n}_Q \\ &= \lim_{P \rightarrow Q} (\nabla_P \phi \cdot \hat{n}_P) \end{aligned} \quad (4.15)$$

where the subscripts P and Q refer the points where the gradient is evaluated. Substituting equation (4.13) in equation (4.15),

$$-V_{\infty n} = \lim_{P \rightarrow Q} \left\{ \iint_S \mu(Q) \hat{n}_P \cdot \nabla_P \left[\frac{\partial}{\partial n} \left(\frac{1}{4\pi r} \right) \right] dS \right\} \quad (4.16)$$

the above equation can be abbreviated as,

$$-V_{\infty n} = \iint_S \mu(Q) \hat{n}_Q \cdot V(P;Q) dS \quad (4.17)$$

where $V_{\mu}(P;Q)$: induced velocity at P by a unit doublet strength at Q

The governing equation (4. 5) with boundary conditions (4. 6) is changed to the integral equation (4.17).

Dividing the body surface S into an infinite number of small surface elements, equation (4.17) becomes,

$$-V_{\infty ni} = \sum_j \mu_j A_{ij} \quad (4.18)$$

for $i, j = 1, 2, 3, \dots, \infty$

where $V_{\infty ni}$: normal component of free stream velocity at i-th surface element

μ_j : doublet strength of j-th surface element

A_{ij} : normal component of induced velocity at i-th surface element by a unit strength doublet at j-th surface element

An approximate solution to the above equation can be obtained by dividing the surface into a finite number of surface elements. If the surface is divided into M panels, then equation (4.18) is applied at only M discrete

points on the surface, which are usually called control points. Then equation (4.18) becomes,

$$[A]\{\mu\} = \{R\} \quad (4.19)$$

where

$$[A] = \begin{bmatrix} A_{11} & A_{12} & \dots & A_{1M} \\ A_{21} & A_{22} & \dots & A_{2M} \\ \vdots & \vdots & \ddots & \vdots \\ \vdots & \vdots & \ddots & \vdots \\ \vdots & \vdots & \ddots & \vdots \\ A_{M1} & A_{M2} & \dots & A_{MM} \end{bmatrix}$$

$$\{\mu\} = (\mu_1, \mu_2, \dots, \mu_j, \dots, \mu_M)^T$$

$$\{R\} = (-V_{\infty 1}, -V_{\infty 2}, \dots, -V_{\infty i}, \dots, -V_{\infty M})^T$$

A_{ij} is the normal component of the induced velocity at the i -th control point by a unit strength doublet at the j -th panel. They are functions of geometry and are calculated before solving for μ 's. After μ 's are obtained, all other desired flow properties can be calculated using the discrete form of equation (4.13).

A surface doublet distribution of density μ can be replaced by an equivalent surface vortex distribution (Hess (1972)) where the vortex sheet strength $\vec{\gamma}$ at each surface points satisfies the relation,

$$\vec{\gamma} = -\hat{n} \times \nabla \mu \quad (4.20)$$

A doublet panel with constant positive strength μ induces the same velocity field at every field point as a counter-clockwise vortex loop with

strength μ , provided that the edges of the doublet panel coincide with the vortex loop. In the current study, vortex loop panels were used rather than doublet panels for easy handling of the leading edge vortex flow and trailing edge wake.

For a flow over a wing at a high Reynolds number, the viscosity effects are limited to the boundary layer on the surface. Vorticity is created in the boundary layer and vortices are formed along sharp edges. These vortices are shed from the wing and constitute the wake. Therefore, flow over a thin wing can be modelled as a potential flow with vortex sheets representing the wing and wake.

4.2 FORMULATION OF THE PROBLEM

Two types of vortex sheets were used for the current study; a bound vortex sheet which represents the wing surface, and a free vortex sheet which represents the wake flow. There is a pressure jump across the bound vortex sheet, while across the free vortex sheet there is no pressure difference. Hence they are allowed to deform to a position where the net force is zero. The wing surface was divided into a finite number of surface panels. Each surface panel was made up of straight vortex filaments fixed at the edge of the panel, forming a closed vortex loop with constant circulation. Free vortex sheets were represented by free vortex filaments starting from the edge of the wing and extending to infinity. Each free vortex filament consisted of a series of short straight vortex segments and one final semi-infinite segment. To satisfy the Kutta con-

dition, no vortex filaments were placed along the edge of the wing, but vortex filaments were placed perpendicular to the edge of the wing. The panels on the edge of the wing formed closed vortex loops by including the vortex filaments at infinity which were starting vortices. The control points were located at the geometric centers of the surface elements.

Fig. 48 shows the panel arrangement which includes the initial guess for the free vortex filaments. The solid lines represent the vortex loop panel and dashed lines represent the free vortex filaments. The edge of the wing is represented by a dotted line and the control points are denoted by (+) symbols. By using the vortex loop panels the number of the unknowns are reduced and the influence coefficient matrix becomes diagonally dominant.

For the current study, the vortex loop panel was not shifted one quarter of the local panel chord, while most other researchers (Rebach (1976), Mook and Maddox (1974), Kandil (1974), Mehrotra and Lan (1978), Pao and Lan (1982), Kandil and Balakrishnan (1981), and Konstadinoupolus et al.(1985)) put the vortex filaments shifted back one quarter-chord length from the edge of the panel ($c/4$ rule) where c refers to the local panel chord. Since the $c/4$ rule was developed for the two-dimensional lifting problem to provide a good estimation on the pitching moment coefficient, there was no obvious reason to use this rule for three-dimensional problems like delta wings. It was also impossible to model the delta wing with flaps using a $c/4$ rule because the flap hinge line would have to be placed at the middle of the vortex panel.

The Biot-Savart law (Eqn. 6.36 in Bertin and Smith (1979)) was used to calculate the induced velocity due to the segments of vortex filaments. Referring to Fig. 49, induced velocity due to the vortex segment AB is

$$v = \frac{\Gamma}{4\pi h} \frac{\vec{r}_1 \times \vec{r}_2}{|\vec{r}_1 \times \vec{r}_2|} \left[\frac{\vec{r}_o \cdot \vec{r}_1}{r_o r_1} - \frac{\vec{r}_o \cdot \vec{r}_2}{r_o r_2} \right] \quad (4.21)$$

where $h = |\vec{r}_1 \times \vec{r}_2| / r_o$

Γ = strength of the vortex filament

Using the vortex loop panels, the governing equation (4.19) for a M paneled wing can be written as,

$$[A]\{G\} = \{R\} \quad (4.22)$$

where

$$[A] = \begin{bmatrix} A_{11} & A_{12} & \dots & A_{1M} \\ A_{21} & A_{22} & \dots & A_{2M} \\ \vdots & \vdots & \ddots & \vdots \\ \vdots & \vdots & \ddots & \vdots \\ \vdots & \vdots & \ddots & \vdots \\ \vdots & \vdots & \ddots & \vdots \\ A_{M1} & A_{M2} & \dots & A_{MM} \end{bmatrix}$$

$$\{G\} = (G_1, G_2, \dots, G_j, \dots, G_M)^T$$

$$\{R\} = (R_1, R_2, \dots, R_i, \dots, R_M)^T$$

A_{ij} is an element of the influence coefficient matrix and is the normal component of the induced velocity at the i-th control point by a vortex loop with unit strength at the j-th panel, G_j is the strength of the vortex loop at the j-th panel, and $R_i = -V_{\infty n_i}$ is the normal component of the free stream velocity at the i-th control point. G_j was taken positive

for the clockwise vortex loop which induced a velocity in the negative z direction in Fig. 48.a.

The boundary conditions for the current problem are;

1. Flow must be tangential to the wing surface. (No normal velocity)
2. The Kutta condition should be satisfied at the leading edge and trailing edge of the wing.
3. Free vortex sheets are force-free.
4. Spatial conservation of the vorticity should be enforced at the vortex sheet.

This is a non-linear problem because the strength of the vortex loops and the location of the free vortices are unknown. Thus the problem can be solved by an iterative method.

The first boundary condition was used to construct the governing algebraic equation (4.22) for the strength of the vortex loop. The vortex filaments were not placed on the leading edge and trailing edge of the wing except the apex edge to satisfy the second boundary condition. The third boundary condition was used to relax the position of the free vortices to a force-free position after the strengths of the vortex loops were obtained. The fourth boundary condition came from the vector identity, $\nabla \cdot \vec{\omega} = \nabla \cdot (\nabla \times \vec{V}) = 0$ which means that there is no net production of vorticity in the flow field. This can be interpreted as, the sum of the circulation at each corner point of the vortex loop (intersecting point of the vortex

lattice) should be zero. This was satisfied automatically by adopting the vortex loop panels, otherwise additional equations are needed at each corner of the vortex loop panels.

4.3 METHOD OF SOLUTION

Initial guesses for the positions of the vortices were needed at the beginning, since the vortex filament positions were a part of the solution. At first iteration step, all the free vortices were set to shed parallel to the free stream from the edge of the wing and all A_{ij} 's in equation (4.22) were calculated according to the Biot-Savart law in equation (4.21) using unit circulation for all vortex loop panels. Equation (4.22) was used for only half of the wing, since the computation was done for the symmetric flight case (zero yaw). Thus each A_{ij} consisted of the influence of the j -th vortex loop and the image of the j -th vortex loop on the i -th control point. The image of the j -th vortex loop was on the port side of the wing if the computation was done on the starboard side of the wing. Free vortex filaments were included in the calculation of the induced velocity by the panels on the edge of the wing.

After the influence coefficient matrix $[A]$ is formed, the solution vector $\{G\}$ was obtained by using the Gauss-Seidel iterative method (Carnahan et al. (1969)). Since Gauss-Seidel method needs an initial guess, the strengths of all the vortex loops were set to 0.1 at the first iteration step. The Gauss-Seidel method assures the convergence of the solution only if:

$$|A_{ii}| > \sum A_{ij} \quad (4.23)$$

for $i=1,2, \dots, M$

$j=1,2, \dots, M$, except $i=j$

The matrix $[A]$ was sufficiently strongly diagonal to use the Gauss-Seidel method because A_{ij} 's were calculated using the Biot-Savart law.

The position of the free vortices were relaxed to satisfy a force-free condition by aligning the segments of the vortex filament in the local velocity direction. In determining the positions of the vortex filaments, a constant characteristic time step was used rather than a constant vortex segment length. The new position can be expressed as,

$$\vec{r}_{i\ j+1} = \vec{r}_{ij} + \vec{V}(\vec{r}_{ij})\Delta t_c \quad (4.24)$$

where $\vec{V}(\vec{r}_{ij}) = \vec{V}_\infty + \vec{V}_i(\vec{r}_{ij})$

\vec{r}_{ij} : j -th nodal point of the i -th free vortex

$\vec{r}_{i\ j+1}$: $j+1$ th nodal point of the i -th free vortex

Δt_c : characteristic time step

$\vec{V}(\vec{r}_{ij})$: local velocity at \vec{r}_{ij}

$\vec{V}_i(\vec{r}_{ij})$: induced velocity at \vec{r}_{ij}

One unit of the characteristic time step corresponds to the required time to pass the delta wing from apex to trailing edge with free stream velocity. When the i -th free vortex was relaxed, the influence of the i -th free vortex itself was not counted in the calculation of the induced velocity \vec{V}_i . Equation (4.24) was used to find the next nodal point of the

vortex segment except for the case of either the free vortex filament tending to go through the wing surface, or the vortex filament coming too close to the wing surface. If the free vortex filament was going to be placed within the minimum distance z_{\min} from the wing or flap surface, $x_{i,j+1}$ and $y_{i,j+1}$ were calculated by equation (4.24) while $z_{i,j+1}$ was set as z_{ij} . The relaxation began at the first nodal points of the free vortices from the trailing edge and at the second nodal points of the free vortex filaments from the leading edge. The first segments of the vortices from the leading edge were fixed to prevent numerical instability and to maintain the diagonal dominance of the influence coefficient matrix. If the free vortices from the leading edge were allowed to be relaxed from the first nodal points, they were usually placed inboard of the first control point from the leading edge and close to the wing surface due to the small aspect ratio of the vortex loop panels on the leading edge, thus producing a strong induced velocity in the positive z direction at the control point on the leading edge. Therefore at the control point of the panel on the leading edge, the induced velocities due to the other edges of the vortex loop panel are canceled out by those of the free vortex. Thus A_{ii} is reduced to a small value while $A_{i-1,i}$ is increased, where i refers the panel on the leading edge and $i-1$ refers the panel just inboard of the i -th panel. This will happen at all the panels along the leading edge and leads to an ill-conditioned influence coefficient matrix for use in the Gauss-Seidel method. For the current study, the vortex filaments from the leading edge of the wing were forced to shed perpendicular to the flap surface up to a certain distance from

the wing to avoid the above-mentioned difficulties. The forced shedding of free vortices is an inevitable error in this computation.

In order to prevent excessive induced velocity by closely located vortex filaments, a cut-off distance h_0 was used to set the induced velocity \vec{V}_i to zero in equation (4.21) when the distance h between the vortex filament and field point was less than h_0 . The cut-off distance was selected as 0.9 times the minimum distance of the bound vortex from the nearest control point. The cut-off distance h_0 was also used as minimum distance z_{\min} .

The matrix $[A]$ is a function of the geometry of the vortex loop panels, and the position of the panels and free vortices. The positions of the free vortices are dependent on the strength of the vortex loop $\{G\}$. Hence $[A]$ is a function of $\{G\}$. The governing equation (4.22) becomes,

$$[A(G)]\{G\} = \{R\} \quad (4.25)$$

Equation (4.25) is a non-linear equation, and solved iteratively,

$$\{G^{k+1}\} = [A(G^k)]^{-1}\{R\} \quad (4.26)$$

where the superscript k refers to the iteration step number.

Every iteration step consists of calculating $[A(G^k)]$, solving for $\{G^{k+1}\}$, and relaxing the free vortex to a force-free position. This procedure was repeated until both $\{G\}$ and the positions of the free vortices con-

verged within the pre-set convergence criteria. The aerodynamic loads were computed after the convergences were achieved for both the positions of the free vortices and the strength of the vortex loop {G}. The flow chart for the computation program is shown in Fig. 50.

During the calculation of the updated influence coefficient matrix [A] after the free vortices were relaxed, most of the elements were unchanged. The elements of the matrix [A] updated at each iteration step were A_{ij} 's for all the j-th panels at the edge of the wing having free vortex filaments. The advantage of the Gauss-Seidel method was that after relaxing the free vortices, previous set of the solution vector {G} was used as an initial guess for the next iteration. As the free vortices approached convergence, the strength of the vortex loop was not changed much. Hence after a few iteration steps, the inner iteration step to compute the converged {G} were reduced greatly.

The convergence of the strength of the vortex loop {G} was checked by,

$$\max \left[\frac{|G_i^{k+1} - G_i^k|}{G_i} \right] \leq \epsilon_G \quad \text{for } i=1,2,3,\dots,M \quad (4.27)$$

where ϵ_G is the convergence criterion for {G}

The convergence of the free vortex positions was examined by,

$$\max \left[\frac{|r_{ij}^{k+1} - r_{ij}^k|}{V_\infty \Delta t_c} \right] \leq \epsilon_F \quad \begin{matrix} \text{for } i=1,2, \dots, NV \\ j=1,2, \dots, NS \end{matrix} \quad (4.28)$$

where ϵ_F is the convergence tolerance for the free vortices

NV is the number of free vortices

NS is the number of vortex segments in a free vortex

Usually during the last 2 - 3 iteration steps, the strength of the vortex loop {G} was changed by a very small amount. Hence the smaller value of ϵ_G was used compared to the ϵ_F . The convergence criteria for the strength of the vortex loop and the positions of the free vortex were 0.25×10^{-4} and 0.02 respectively and these were selected such that the maximum error in normal velocity component at each control point was less than 0.1 % of the free stream velocity after the converged solution is obtained.

4.4 AERODYNAMIC LOAD CALCULATION

The velocity jump across the vortex sheet is,

$$\Delta \vec{V} = \vec{\gamma} \times \hat{n} \quad (4.29)$$

The velocity discontinuity can not be obtained at the control point in a strict sense because the wing was modeled with vortex loop panels. The purpose of this computational program was not to find an exact solution, but an approximate solution was desired. Therefore the same order of approximation was required to obtain the velocity jump as the wing was modeled.

To obtain a velocity jump, the vortex loop panel was considered as a constant doublet strength panel since both panels produce the same induced velocity (Hess (1972)). Substituting the doublet-vortex relation (4.20) into the velocity jump-vortex strength relation (4.29), the velocity jump across a doublet panel is,

$$\begin{aligned}\vec{\Delta V} &= (-\hat{n} \times \nabla \mu) \times \hat{n} \\ &= -\nabla \mu\end{aligned}\tag{4.30}$$

Since the vortex loop panel is the same as the constant strength doublet panel, the velocity jump at the control point of the panel can be obtained by a mean slope of the doublet strength on a panel. Referring to Fig. 51.a the mean slope of the doublet strength at the i -th panel is

$$\begin{aligned}-\mu_x &= \frac{\frac{1}{2}(G_{i+1} + G_i) - \frac{1}{2}(G_{i-1} + G_i)}{l_x} \\ &= \frac{G_{i+1} - G_{i-1}}{2l_x}\end{aligned}\tag{4.31.a}$$

$$\begin{aligned}-\mu_y &= \frac{\frac{1}{2}(G_{i+n} + G_i) - \frac{1}{2}(G_{i-n} + G_i)}{l_y} \\ &= \frac{G_{i+n} - G_{i-n}}{2l_y}\end{aligned}\tag{4.31.b}$$

Hence the velocity jump can be obtained directly from the strength of the vortex loop.

$$\Delta \vec{V} = -\nabla \mu = \nabla G \quad (4.32)$$

A mean vortex strength can be obtained using equation (4.29) and equation (4.31)

$$\begin{aligned} \vec{\gamma} &= \hat{n} \times \Delta \vec{V} \\ &= \hat{n} \times \nabla G \\ &= \frac{G_{i+1} - G_{i-1}}{2l_x} \hat{j} - \frac{G_{i+n} - G_{i-n}}{2l_y} \hat{i} \\ &= [-G_{i+n} l_x \hat{i} + G_{i+1} l_y \hat{j} + G_{i-n} l_x \hat{i} - G_{i-1} l_y \hat{j}] / (2l_x l_y) \end{aligned}$$

$$\begin{aligned} \text{choosing } \Gamma_1 &= G_{i+n}, \Gamma_2 = G_{i+1}, \Gamma_3 = G_{i-n}, \Gamma_4 = G_{i-1}, \\ \vec{l}_1 &= l_x \hat{i}, \vec{l}_2 = -l_y \hat{j}, \vec{l}_3 = -l_x \hat{i}, \vec{l}_4 = l_y \hat{j}, \\ \text{and } A &= l_x l_y, \end{aligned}$$

then

$$\vec{\gamma} = -\sum_{i=1,2,3,4} \Gamma_i \vec{l}_i / (2A) \quad (4.33)$$

Since there are no panels ahead of the apex edge (leading edge for the rectangular wing), G_{i+n} is zero when i -th panel is on the apex edge. Hence the velocity jump and mean vortex strength become,

$$\Delta \vec{V} = \frac{G_{i+1} - G_{i-1}}{2l_x} \hat{j} - \frac{G_{i-n}}{2l_y} \hat{i} \quad (4.34)$$

$$\vec{\gamma} = -\sum_{i=2,3,4} \Gamma_i \vec{l}_i / (2A) \quad (4.35)$$

One can think that the doublet sheet is stretched to infinity from the trailing edge because the vortices are being shed from the trailing edge to infinity. If the i -th panel is on the trailing edge then G_{i-n} becomes G_i and the velocity jump and the mean vortex strength are,

$$\Delta \vec{V} = \frac{G_{i+1} - G_{i-1}}{2l_x} \hat{i} + \frac{G_{i+n} - G_i}{2l_y} \hat{j} \quad (4.36)$$

$$\vec{\Gamma} = -\sum_{i=1,2,3,4} \Gamma_i \vec{l}_i / (2A) \quad (4.37)$$

where $\Gamma_3 = G_i$

A similar relation can be applied to the leading edge of a delta wing and side edge of a rectangular wing.

For a triangular panel ABC in Fig. 51.b, the velocity jump in the x -direction is,

$$\Delta u = \frac{\frac{1}{2}(G_{i+1} + G_i) - \frac{1}{2}(G_{i-1} + G_i)}{\frac{1}{2}l_x} = \frac{G_{i+1} - G_{i-1}}{l_x}$$

The velocity jump in the y -direction can be expressed as a weighted average of the velocity jumps in two zones. If Δv_1 and Δv_2 represent the velocity jumps in the y -direction in zone #1 and #2 respectively,

$$\Delta v_1 = \frac{\frac{1}{2}(G_{i+1} + G_i) - \frac{1}{2}(G_{i-n} + G_i)}{\frac{1}{2}l_m} = \frac{G_{i+1} - G_{i-1}}{l_m}$$

Similarly

$$\Delta v_2 = \frac{G_{i+1} - G_{i-1}}{l_m}$$

$$\text{where } l_m = \frac{l_x l_y}{1 + l_x}$$

Thus the velocity jump in the y-direction is,

$$\begin{aligned} \Delta v &= \frac{\Delta v_1 l_x + \Delta v_2 l}{l_x + 1} \\ &= \frac{(G_{i+1} - G_{i-n}) l_x + (G_{i+1} - G_{i-1}) l}{l_m (1 + l_x)} \end{aligned}$$

Hence the total velocity jump becomes,

$$\Delta \vec{V} = \frac{G_{i+1} - G_{i-1}}{l_x} \hat{i} + \frac{(G_{i+1} - G_{i-n}) l_x + (G_{i+1} - G_{i-1}) l}{l_x l_y} \hat{j} \quad (4.38)$$

The mean vortex strength becomes,

$$\begin{aligned} \vec{\zeta} &= \hat{n} \times \Delta \vec{V} \\ &= \frac{-1}{l_x l_y} [G_{i+1} (l_x + 1) \hat{i} - G_{i+1} l_y \hat{j} - G_{i-n} l_x \hat{i} - G_{i-1} l \hat{i} + G_{i-1} l_y \hat{j}] \\ \text{choosing } \Gamma_1 &= G_{i+1}, \Gamma_2 = G_{i-n}, \Gamma_3 = G_{i-1}, \\ \text{and } \vec{l}_1 &= (l_x + 1) \hat{i} - l_y \hat{j} \\ \vec{l}_2 &= -l_x \hat{i} \\ \vec{l}_3 &= -l \hat{i} + l_y \hat{j} \end{aligned}$$

The mean vortex strength can be written in the same way,

$$\vec{\gamma} = -\sum_{i=1,2,3} \Gamma_i \vec{l}_i / (2A) \quad (4.39)$$

It is convenient to find the mean vortex strength rather than the velocity jump directly because the same formula can be applied to any triangular and rectangular panels. The velocity jump can be calculated using equation (4.29).

After the velocity jump is obtained, the pressure can be found by using Bernoulli's equation. The total pressure was assumed to be constant in the flow field. Since only steady cases were considered,

$$P + \frac{1}{2}\rho V^2 = P_{\infty} + \frac{1}{2}\rho V_{\infty}^2 \quad (4.40)$$

The velocities on the upper surface and lower surface at the control point are,

$$\begin{aligned} \vec{V}_u &= \vec{V}_{\infty} + \vec{V}_i + \frac{1}{2}\Delta\vec{V} \\ \vec{V}_l &= \vec{V}_{\infty} + \vec{V}_i - \frac{1}{2}\Delta\vec{V} \end{aligned} \quad (4.41)$$

The pressure coefficients for both surfaces become,

$$\begin{aligned} C_{pu} &= 1 - (V_u/V_{\infty})^2 \\ C_{pl} &= 1 - (V_l/V_{\infty})^2 \end{aligned} \quad (4.42)$$

The normal force coefficient and axial force coefficient are obtained by summing up the pressure differences multiplied by each panel area. The pitching moment was calculated for a half chord point of the root chord which is the quarter chord point from the leading edge of the mean aerodynamic chord.

$$\begin{aligned}
 C_N &= \sum (C_{p1} - C_{pu})_i n_z A_i / A \\
 C_A &= \sum (C_{p1} - C_{pu})_i n_x A_i / A \\
 C_M &= [\sum (C_{p1} - C_{pu})_i \{n_z (x_{ac} - x) + n_x z\} A_i] / A \bar{c} \quad (4.43) \\
 &\quad i=1,2, \dots, M
 \end{aligned}$$

where A_i : area of the i th panel

A : total area of the wing projected on the x-y plane

\bar{c} : mean aerodynamic chord

x, z : x and z coordinate of the i th control point

n_x, n_z : x, z component of the i th unit normal vector

Then the lift coefficient and induced drag coefficient are,

$$\begin{aligned}
 C_L &= C_N \cos \alpha - C_A \sin \alpha \\
 C_{Di} &= C_N \sin \alpha + C_A \cos \alpha \quad (4.44)
 \end{aligned}$$

V. COMPUTATIONAL RESULTS AND DISCUSSION

5.1 EFFECTS OF VARIOUS PARAMETERS ON THE COMPUTATIONAL RESULTS.

Prior to running the computational program for various cases, the effects of the certain parameters on the computational results were tested, and proper values were selected for each parameter based on the quality of the result, numerical stability, and required execution time to get the converged result. The main wing was divided into $NW \times (NW + 1)/2$ panels and $NW \times NF$ panels were used to represent the flap, where NW refers to the number of the vortex loop panel rows on a wing and NF is the number of vortex loop panel columns on a flap (see Fig. 48).

The effects of each parameter on the pressure distributions and converged shapes of the free vortex filaments at $\alpha=10^\circ$ with $\delta=0^\circ$ are shown in Fig. 52 - 57 and listed in Table 4.

The first parameter considered was the number of the panels. Fig. 52 shows the effect of the number of vortex loop panels on the pressure distributions at 4 different stations perpendicular to the leading edge where the experimental pressures were measured. The cases tested are represented by $NW \times NF$ which are 6×2 , 7×3 , and 9×4 ; the total number of panels are 33, 49, and 81 respectively. The general shapes of the pressure distribution were the same but the suction pressure increased with an increase in number of panels, and the resulting aerodynamic loads

were also increased slightly. The unusual dip in the pressure distribution at $x' = 0.722$ for the 6×2 case is caused by the interpolation procedure used in the plotting program.

The effects of the number of vortex loop panel columns on the flap are shown in Fig. 53. Comparison was made for $NW = 7$ with $NF = 2 - 5$ which resulted in the aspect ratio of the panel on the flap ranging from 0.115 - 0.288. The results show that there were no significant effect of NF on the pressure distributions, in other words the density of the vortex loop panels on the flap does not affect the flow around a delta wing. The shapes of the converged free vortices were unchanged for different values of NF .

Fig. 54 shows that the initial free vortex shedding angle has no effect on the final pressure distributions, if the initial shedding angle is between 0.5 - 1.5 times the angle of attack. The total aerodynamic loads and the shape of free vortices also unchanged. Here $AFACT$ is the factor multiplied to the angle of attack to get the initial shedding angle.

The characteristic time step Δt_c has considerable influence on the pressure distributions and the shape of the free vortices (Fig. 55). Compared to the larger time step, using a small time step yielded a better result closer to the experimental result as it rendered a tighter rolled-up leading edge vortex thus resulting in a suction peak placed closer to the leading edge of the flap. But it required more CPU time to relax a single vortex filament and also more iteration steps to result

in a converged shape of the free vortices, and sometimes free vortices were not converged into the force-free positions. The amount of CPU time to obtain the converged solution increased approximately 2.7 times for the case of $\Delta t_c = 0.05$ compared to $\Delta t_c = 0.09$. Therefore, one needs a compromise between the quality of the result, CPU time and the risk of non-convergence. After considering several cases, $\Delta t_c = 0.07$ was chosen for the current study.

The effects of the first shedding distance (FEDG) of the free vortices from the leading edge are shown on Fig. 56. It has a more significant effect than the characteristic time step. A shorter shedding distance would simulate the vortex flow closer to the real flow, but sometimes the free vortices tended to penetrate the wing or flap surface during the relaxation and this resulted in a numerical instability of the program and also required more iteration steps for convergence. Therefore, one needs another compromise between the quality of the result and the stability of the numerical procedure. After testing several cases, $FEDG = 0.03$ was chosen which is approximately 32% of the flap chord.

Fig. 57 shows the effect of the free stream matching point. The free vortices were relaxed to a force-free position up to the free stream matching point which is at $x = FVEND$ and the free vortices were aligned with the free stream after $x = FVEND$. Three different value of $FVEND$ were tested namely 1.2, 1.6, and 2.0. The pressure distributions coincided perfectly with each other and so did the total aerodynamic loads. From Fig. 57.b - 57.d, one can also see that the positions of the free vortices were

not affected by FVEND. The free vortices were plotted only up to $x=1.4$ in Fig. 57.b - 57.d. It was considered safe enough to use FVEND=1.2 to get the same quality of the result compared to the higher value of FVEND.

Generally, the current computational program predicted the suction peak located farther from the leading edge, a lower suction peak pressure and higher C_L than the experimental result. A smaller Δt_c resulted in a suction peak closer to the leading edge (Fig. 55.a), and a smaller value of FEDG gives a lower C_L and higher suction peak pressure which is closer to the experimental result (Fig 56.a and Table 4). Hence a certain value of FEDG and Δt_c other than an infinitely small value will result an inevitable error in the computational result and it can be reduced by using smaller values.

Although much effort was spent on selecting the proper values of various parameters, free vortex filaments were oscillatory and tended to go through the wing surface during the relaxation to a force-free position in some cases. If this happened, a converged solution was obtained by changing the characteristic time step slightly.

5.2 PLAIN 60 DEGREE DELTA WING

The cases for a 60° sweep delta wing without leading edge flaps were computed and compared with the experimental results. A similar panel arrangement was used for the simple delta wing as in the case of delta wing with flaps. For the plain delta wing, it was possible to obtain the

solutions with smaller values of first shedding distance (FEDG) than for the flapped delta wing, therefore $FEDG = 0.02$ was used while all other parameters remained the same.

Fig. 58 shows the typical shape of the converged free vortex filaments with panel arrangement at a 20° angle of attack. As can be seen from Fig. 58, the first free vortex filament was shed to the free stream not from the apex but from the leading edge downstream of the apex. In actual flow the leading edge vortex flow starts from the apex of the delta wing, but in the vortex lattice method free vortices can not be shed from the apex. If the first vortex filament was allowed to be shed very close to the apex, the vortex filament would be placed parallel to the free stream and would create a higher suction pressure near the wing center line. This results from the fact that the vortex flow is not well developed and only a small portion of the flow field is a vortex flow near the apex while most of the flow is in the free stream direction.

Fig. 59 shows the comparison of the current computational result with the experimental results. Since the upper surface shape of the delta wing has a significant effect on total aerodynamic load characteristics as already mentioned in section 3.1, current results were compared with experiments only for the flat plate delta wing cases. The leading edge of both models (Wentz and Kohlman (1968) and Faery et al.(1981)) was beveled 7.5° , therefore two computational results were included. One is the delta wing with flat surface, the other is the beveled leading edge according to Faery's model. The total aerodynamic load predictions matched well

up to around $\alpha = 12^\circ$, and the deviation between the experimental result and computational result became larger from $\alpha = 12^\circ$. This correspond to the vortex bursting angle of attack at the trailing edge, α_{VBTE} . From Fig. 3, α_{VBTE} ranged from 11° to 14° for a 60° sweep delta wing. In actual flow, increasing angle of attack above α_{VBTE} , vortex bursting progressed to the apex, but the vortex bursting was not counted in the computational model which resulted in a larger deviation in aerodynamic loads between the current computational result and experimental result.

There is no available experimental pressure data with which to compare the current computational result. Also no other researcher reported the computation of flow around a 60° delta wing including leading edge separation except Fujii and Kutler (1983). Some researchers (Kuhlman (1978), and Chaturvedi and Ghaffari (1982)) reported that they did not get a converged solution or had difficulty in obtaining a solution using the Free Vortex Sheet method (Weber et al.(1976) and Johnson et al.(1980)). The author also experienced convergence problems when he tried to model the leading edge vortex flow with vortex loop panels. These were caused by excessive twist of the panel during the relaxation of the free vortex sheet to a force-free position, and probably came from the non-conical flow characteristics of the flow around a 60° delta wing.

Recently, Fujii and Kutler (1983) succeeded in computing the flow around a 60° delta wing by solving the Reynolds-Averaged Thin Layer Navier-Stokes Equation (N-S code) with the wing trailing edge extended to the outflow boundary. Fujii and Kutler used a 9.24 % thick delta wing with rounded

leading edge and computed the flow at $M = 0.5$. Since Fujii's model was not a sharp-edged delta wing, the pressure distributions from the current method were compared to a $\alpha = 20^\circ$ case of Fujii's result where the vortex is fully developed (Fig. 60). Fujii's model has a blunt nose and smoothly cropped tip, therefore the comparison was made for stations with the same local span. The general shape of the pressure distribution matched well for both cases (Fig. 60), while the present method predicted a higher suction peak and its location was placed farther from the leading edge than the N-S code at $x/C = 0.56$. This is because the N-S code used a round leading edged delta wing thus the vortex strength might be weaker than the sharp-edged delta wing ; and the inner location of the suction peak is an inherent error of the current method as already mentioned in section 5.1. A sharp suction peak occurred on the leading edge of the Fujii model because of the rapid flow acceleration as mentioned in their paper (Fujii and Kutler (1983)). Since Fujii's model did not include a trailing edge, flow can not sense the trailing edge, and therefore the N-S code predicts a higher pressure on the lower surface and higher suction pressure on the upper surface than the current method at $x/C = 0.90$.

5.3 60 DEGREE DELTA WING WITH A LEADING EDGE VORTEX FLAP

The cases for the 60° delta wing with leading edge vortex flap were computed using the parameters determined in Section 5.1 and compared with the experimental result. The pressure distributions were computed at the same stations where the pressure tabs were located in experiment. The flap deflection angle used in computation is the same as that in

experiment; a surface deflection angle and not a mean camber line deflection angle. Computation was performed at four different angles of attack, $\alpha = 5^\circ, 10^\circ, 15^\circ$, and 20° with five different flap deflection angles, $\delta = 0^\circ, 10^\circ, 20^\circ, 30^\circ$, and 40° .

The effect of the flap deflection angle on the longitudinal aerodynamic load characteristics is shown on Fig. 61. The plain delta wing cases were also included in Fig. 61 for comparison. The plain delta wing cases were computed with the same parameters mentioned in Section 5.1, therefore the aerodynamic load characteristics are slightly different from the plain delta wing case in section 5.2. The reference area used in the calculation of C_L , C_D and C_M is based on the total projection area onto the wing plane. Comparing the cases of a flapped delta wing with zero flap deflection angle to the cases of a plain delta wing, the lift coefficient was decreased because the area near the apex is reduced in flapped delta wing where the highest suction pressure is applied. The pitching moment was also higher in the plain wing cases which is due to using the same mean aerodynamic chord as the cases of plain delta wing. The drag coefficient came out as almost the same for the plain and flapped delta wing with zero flap deflection.

Increasing the flap deflection angle resulted in a decrease in lift coefficient, and an increase in pitching moment at the same angle attack. The induced drag coefficient decreased with increase in the flap deflection angle at the same lift coefficient. This trend matched well with the experimental results of Marchman (1981a) and Erickson and McCann

(1983) except near the α_{STALL} where experimental results showed increase in $C_{L\ max}$. The strength of free vortex filaments is weakened by an increase in flap deflection, thus resulting in a smaller induced velocity on the wing surface which produces a lower suction pressure and therefore lift is decreased. Rotating the suction force forward from the wing normal direction increased the pitching moment. The combined effect of forward vectoring the suction force and weakened vortex strength decreased the induced drag.

The pressure distribution plots (Fig. 62 - 65) clearly show the effect of the flap deflection. The suction peak was reduced gradually as the flap deflection angle was increased. As already discussed in Section 3.3, the major effects of the flap deflection are a reduction in suction peak and shift of the suction peak closer to the leading edge. From the computational result, the reduction of the suction peak effect showed up well but the suction peak did not move closer to the leading edge with increase in flap deflection angle. It was impossible to get a converged solution at low angles of attack with larger flap deflection angle because the flow over the flap surface is an attached flow and experiences a positive pressure hence the vortex filament always tended to penetrate the wing.

Converged shapes of the free vortex filaments are shown on Fig. 66 - 71. One interesting phenomenon was that the first free vortex filament shed from the flap apex behaved like a vortex core when the vortex flow was well developed. One can notice the shift of the first vortex filament toward the leading edge of the flap in Fig. 67 compared to Fig. 66, but

this shift was so small that the location of the suction peak did not change. With increase in flap deflection, the coiled free vortex filaments started to unwind because the vortex strength was decreased and the pressure distributions became flatter (Fig. 63, 68 and 69). With large flap deflection angle and small angle of attack, which correspond to the vortex starting angle of attack α_{VS} in experiment (Fig. 12), free vortex filaments were placed parallel to the free stream shown on Fig. 70 and Fig. 71 because the vortex strength was so small that velocity induced by the vortex was much less than the free stream velocity. The location of the suction pressure did not shift toward the leading edge because of the uncoiling of the free vortex filaments. The pressure distributions obtained from the current computational method are compared with the experimental results in Fig. 72 - 74.

In actual flow the leading edge free vortex sheet is rolled up tightly due to the negative radial pressure gradient, while in computation there was no mechanism to roll up the vortex filaments tightly. This effect combined with the finite length of the vortex segments resulted in a loosely rolled-up leading edge vortex filament and a smaller suction peak near the leading edge. Another aspect worth mentioning is that near the trailing edge, vortex filament are spread wide due to the loose roll-up of vortex filaments together with the increased local wing span thus resulting in a pressure distribution similar to the burst vortex flow.

5.4 COMPARISON OF CURRENT COMPUTATIONAL METHOD WITH OTHERS

The current computational method was compared with two other methods for the 74° plain delta wing cases and 74° delta wing with leading edge flap to verify the pressure formula developed in Section 4.4. The Free Vortex Sheet (FVS) method (Weber et al. (1976) and Johnson et al. (1980)) and Mehrotra's method (Mehrotra and Lan (1978)) were compared with the current method because both methods had been compared with the same experiment (Wentz (1972a,b)) where a flat plate delta wing was used. FVS code used higher order panels with leading edge vortex core and Mehrotra's method was a typical Non-linear Vortex Lattice Method (NVLM) using the c/4 rule.

The results for the longitudinal aerodynamic loads are compared in Fig. 75 for angles of attack up to 40° . The current method predicts the total aerodynamic loads quite accurately up to stall angle because α_{VBTE} is higher than the 60° delta wing case and is in the range of $28^\circ - 35^\circ$ in Fig. 3. Mehrotra's method predicts the lift coefficient and pitching moment quite close to the experimental result. The FVS code predicts the lift coefficient very close to the experimental result while pitching moment and induced drag predictions were not as good as the current method. A typical converged shape of the free vortex filaments is shown on Fig. 76.

The pressure distributions and pressure difference distributions are compared in Fig. 77 and Fig. 78 respectively. The current method predicts the suction peak lower than the experiment and predicts the location of

the suction peak correctly. In prediction of the pressure difference distribution, the current method predicts the peak pressure difference lower than the FVS code and experiment, and a higher pressure difference near the wing center line. Mehrotra's method did not predict the pressure difference as well as it did on the total loads prediction. A typical execution time was approximately 70 seconds in 12 iteration using the current method on IBM 3084, while Mehrotra's method took 4540 seconds in 10 iteration on the Cyber 175 (Pao and Lan (1982)). The computational speeds of IBM 3084 and Cyber 175 are comparable.

The cases for a 74° delta wing with a leading edge flap at an angle of attack 14° , were computed and compared with the experimental data and FVS code (Luckring et al. (1982)). The experimental data used in Fig. 79 and Fig. 80 were not published and were taken from Luckring et al. (1982). The current method predicts the pressure distribution with reasonable accuracy at $x/C = 0.53$ for both $\delta = 0^\circ$ and 10° cases, but at the downstream stations the suction peaks were lower than the experiments and a higher suction pressure was predicted near the wing center line. The converged shape of the free vortex filaments is shown in Fig. 81 and 82. The execution time of the FVS code is not known for this case. Generally, the FVS code is known to need a large amount of CPU time. For example, the FVS code took 22450 seconds in 8 iteration to compute the double delta wing cases on the Cyber 175 computer, while a method similar to Mehrotra and Lan (1978) with vortex core took 5620 seconds in 8 iteration for the same case (Pao and Lan (1982)).

VI. CONCLUSIONS

An experimental study was undertaken to investigate the details of the flow phenomena over a delta wing with leading edge vortex flap. Also a non-linear vortex lattice method was developed as a cost-effective prediction tool for the plain or vortex flapped delta wing aerodynamics.

The experimental research was conducted on a semi-span model of 60° swept, flat plate, delta wing with constant-chord leading edge flap. The pressure distributions were measured over a range of angles of attack starting from zero to 40° with 5° interval and flap deflection angles from zero to 45° with 5° increments, at a Reynolds number of about 2.14×10^6 based on the root chord of the wing. The flow visualization experiments were performed over the range of zero to stall angle with ten different flap deflection angles at the same Reynolds number. The mean flow fields were measured at angles of attack 10° and 15° with flap deflection angles of 10° and 30° at a Reynolds number of about 1.50×10^6 .

For computational study, the velocity jump formula was developed for the vortex loop panel to predict the pressure distributions on a delta wing surface. A parametric study was also done to find the characteristics of the non-linear vortex lattice method and the results from the current methods were compared with other "expensive" codes.

Following are the conclusions drawn from the current research.

From the experimental study,

1. The leading edge vortex flap was found to be an effective means to control the leading edge vortex flow over a delta wing.
2. The optimum flap deflection angles were found for angles of attack at which most of the leading edge vortex could be placed on the flap: i.e., the reattachment line is on the wing-flap hinge line, thus producing a thrust on the flap by low pressure caused by the vortex flow.
3. The flap deflection reduces the strength of the leading edge vortex over a delta wing thus reducing the suction peak pressure and shifting the location of the suction peak closer to the leading edge.
4. It was possible to restore vortex flow from a burst vortex flow with proper flap deflection .

From the computational study,

1. The total aerodynamic loads obtained by integration of the pressure distributions over the wing matched well with the experimental data except at high angles of attack where leading edge vortex bursting occurred in actual flow. The current result also matched well with the results from the other codes.
2. The first shedding distance of the free vortex filaments has the strongest effect on the converged solutions.

3. The current method under-predicts the suction peak pressures and predicts the location of the suction peak farther from the leading edge than the experimental results.
4. The current method improved over other non-linear vortex lattice methods by predicting the actual pressures. It should be noted that the FVS did not converged for 60° delta wings where as the present method gave good results for the forces and moments.

In closing a few recommendations are made based on the experiences gained during this study.

1. A study on a full model with a generic fuselage is suggested to investigate the interaction of the leading edge vortex flow with the body or the vortex flow generated from the nose cone of the body.
2. A flow field measurement using a seven hole yawhead probe and hot wire anemometer is suggested to study the vortex core and unsteady flow characteristics after vortex bursting.
3. A modelling of the vortex core combined with the sink is suggested to yield a tightly rolled-up vortex flow for the computational study. It is anticipated that the vortex core and sink combination will result in higher suction peaks and will locate the suction peak closer to the leading edge by allowing the free vortex filaments to roll-up tightly. If a proper relationship between the strength of the sink and the strength of the free vortices is established, the vortex bursting effect might also be simulated.

LIST OF REFERENCES

1. Bartlett, G.E. and Vidal, R.J., "Experimental Investigation of Influence of Edge Shape on the Aerodynamic Characteristics of Low Aspect Ratio Wings at Low Speeds", J. Aeronautical Sciences, Vol.22, No.8, Aug. 1955, pp.517-533, 588.
2. Belotserkovsky, S.M., "Calculation of the Flow around Wings of Arbitrary Planform over a Wide Range of Angle of Attack", Fluid Dynamics, Vol.3, No.4, 1968, pp.20-27.
3. Bertin, J.J. and Smith, M.L., Aerodynamics for Engineers, Printice-Hall, Englewood Cliff, N.J., 1979.
4. Bolly, W., "A Non-Linear Wing Theory and Its Application to Rectangular Wings of Small Aspect Ratio", J. Aeronautical Sciences, Vol.4, 1937, pp.294-296.
5. Brennenstuhl, U. and Hummel, D., "Vortex Formation over Double-Delta Wings", ICAS-82-6.6.3, 1982, pp.1133-1146.
6. Brown, C.E. and Michael, W.H., "Effect of Leading-Edge Separation on the Lift of a Delta Wing", J. Aeronautical Sciences, Vol.21, Oct. 1954, pp.690-694, 706.
7. Campbell, J.P., Johnson, J.L., and Hewes, D.E., "Low-Speed Study of the Effect of Frequency on the Stability Derivatives of Wings Oscillating in Yaw with Particular reference to High Angle-of-Attack Conditions", NACA RM L55H05, 1955.
8. Carnahan, B., Luther, H.A., and Wilkes, J.O., Applied Numerical Methods, John Wiley and Sons, New York, N.Y., 1969.
9. Chaturvedi, S.K. and Ghaffari, F., "Study of Highly Sweptback Wings by the Free Vortex Sheet Method", NASA CR 169559, 1982.
10. Coe, P.L. and Huffman, J.K., "Influence of Optimized Leading-Edge Deflection and Geometric Anhedral on the Low-Speed Aerodynamic Characteristics of a Low-Aspect-Ratio Highly Swept Arrow-Wing Configuration", NASA TM 80083, 1979.
11. Coe, P.L. and Weston, R.P., "Effects of Wing Leading-Edge Deflection on Low-Speed Aerodynamic Characteristics of a Low-Aspect-Ratio Highly Swept Arrow-Wing Configuration", NASA TP 1434, 1979.

12. Dau, A., McLeod, M., and Surry, D., "Two Probes for the Measurement of the Complete Velocity Vector in Subsonic Flow", Aeronautical J. RAS, Vol.72, Dec. 1968, pp.1066-1068.
13. DeYoung, J., "Historical Evolution of Vortex-Lattice Methods", Vortex-Lattice Utilization, NASA SP 405, 1976, pp.1-9.
14. Earnshaw, P.B., "An Experimental Investigation of the Structure of a Leading Edge Vortex", ARC RM 3281, 1962.
15. Earnshaw, P.B. and Lawford, J.A., "Low Speed Wind-Tunnel Experiments on a Series of Sharp-Edged Delta Wings", ARC RM 3424, 1966.
16. Elle, B.J., "An Investigation at Low Speed of the flow near the Apex of Thin Delta Wings with Sharp Leading Edges", ARC RM 3176, 1961.
17. Erickson, G.E., "Water-Tunnel Studies of Leading-Edge Vortices", J. Aircraft, Vol.19, No.6, June 1982, pp.442-448.
18. Erickson, G.E., "Application of Free Vortex Sheet Theory to Slender Wings with Leading-Edge Vortex Flaps", AIAA Paper 83-1813, 1983.
19. Erickson, G.E. and McCann, M.K., "Experimental and Analytical Investigation of the Subsonic Aerodynamics of Slender Wings with Leading-Edge Vortex Flaps", AIAA Paper 83-2113, 1983.
20. Faery, H.F., Stozier, J.K., and Ham, J.A., "Experimental and Theoretical Study of Three Interacting, Close-Spaced Sharp-Edged 60° Delta Wings at Low Speeds", NASA CR 3460, 1981.
21. Frink, N.T., Huffman, J.K., and Johnson, T.D., "Vortex Flap Flow Reattachment Line and Subsonic Longitudinal Aerodynamic Data on 50° to 74° Delta Wings on Common Fuselage", NASA TM 84618, 1983.
22. Fujii, K. and Kutler, P., "Numerical Simulation of the Leading-Edge Separation Vortex for a Wing and Strake-Wing Configuration", AIAA Paper 83-1908, 1983.
23. Gerner, A.A., Maurer, C.L., and Gallington, R.W., "Non-Nulling Seven-Hole Probes for High Angle Flow Measurement", Experiments in Fluids, Vol.2, 1984, pp.95-103.
24. Hall, M.G., "Vortex Breakdown", Ann. Rev. Fluid Mech., Vol.4, 1972, pp.195-218.
25. Harvey, J.K., "Some Measurements on a Yawed Slender Delta Wing with Leading-Edge Separation", ARC RM 3160, 1961.

26. Hayashi, Y. and Nakaya, T., "Flow Field in a Vortex with Breakdown above Sharp Edged Delta Wings" , Japan Natl. Aerosp. Lab., NAL-TR-423, Aug. 1975, translated as: NASA TM 75339, Nov. 1978.
27. Hess, J.L., "Calculation of Potential Flow about Arbitrary Three-Dimensional Lifting Bodies", MDC J5679-01, Oct. 1972, McDonnell Douglas.
28. Hitzel, S.M. and Schmidt, W., "Slender Wings with Leading-Edge Vortex Separation: A Challenge for Panel Methods and Euler Solvers", J. Aircraft, Vol. 21, No.10, Oct. 1984, pp.751-759
29. Hoeijmakers, H.W.M. and Bennekers, B., "A Computational Model for the Calculation of the Flow about Wings with Leading-Edge Vortices", High Angle of Attack Aerodynamics, AGARD CP 247, 1979.
30. Hoffler, K.D. and Rao, D.M., "An Investigation of the Tabbed Vortex Flap", J. Aircraft, Vol.22, No.6, June 1985, pp.490-497.
31. Hoffman, S., "Bibliograph of Supersonic Cruise Research (SCR) Program From 1977 to Mid-1980", NASA RP 1063, 1980.
32. Holman, J.P., Experimental Methods for Engineers, 3rd ed., McGraw Hill, New York, N.Y., 1978.
33. Hummel, D., "Experimentelle Untersuchung der Strömung auf der Saugseite eines schlanken Deltaflügels", Z. Flugwiss., Vol. 13, July 1965, pp.247-252, translated as: "Experimental Investigation of the Flow on the Suction Side of a Thin Delta Wing", NASA TM 75897, March 1981.
34. Hummel, D., "On the Vortex Formation over a Slender Wing at Large Angles of Incidence", High Angle of Attack Aerodynamics, AGARD CP 247, 1979.
35. Hummel, D., and Srinivasan, P.S. "Vortex Breakdown Effects on the Low-Speed Aerodynamic Characteristics of Slender Delta Wings in Symmetrical Flow", J. RAS, Vol.71, April 1967, pp.319-322.
36. Jaquet, B.M. and Brewer, J.D., "Low Speed Static Stability and Rolling Characteristics of Low-Aspect-Ratio Wing of Triangular and Modified Triangular Planforms", NACA RM L8L29, March 1949.
37. Johnson, F.T., Lu, P., Ticono, E.N., and Epton, M.A., "An Improved Panel Method for the Solution of Three-Dimensional Leading-Edge Vortex Flows; Vol.1-Theory Document", NASA CR 3278, July 1980.
38. Jones, R.T., "Properties of Low-Aspect-Ratio Pointed wings at Speeds Below and Above the Speed of Sound", NACA Report 835, 1946.

39. Kandil, O.A., "Prediction of the Steady Aerodynamic Loads on Lifting Surfaces having Sharp-Edge Separation", Ph.D. Dissertation, VPI&SU, Blacksburg, Va., 1974.
40. Kandil, O.A. and Balakrishnan, L., "Recent Improvements in the Prediction of the Leading and Trailing Edge Vortex Cores of Delta Wings", AIAA Paper 81-1263, 1981.
41. Karamcheti, K., Principles of Ideal Fluid Aerodynamics, John Wiley and Sons, New York, N.Y., 1966.
42. Konstadinopoulous, P., Thrasher, D.F., Mook, D.T., Nayfeh, A.H., and Watson, L., "A Vortex Lattice Method for General Unsteady Aerodynamics", J. Aircraft, Vol.22, No.1, Jan. 1985, pp.43-49.
43. Küchemann, D., The Aerodynamic Design of Aircraft, Pergamon, Oxford, 1978.
44. Kuhlman, J., "Load Distributions on Slender Delta Wings Having Vortex Flow", J. Aircraft, Vol.14, No.4, July 1977, pp.699-702
45. Kuhlman, J.M., "Analytical Studies of Separated Vortex Flow on Highly Swept Wings", NASA CR 3022, 1978.
46. Lambourne, N.C. and Bryer, D.W., "The Bursting of Leading-Edge Vortices - Some Observations and Discussion of the Phenomenon", ARC RM 3282, 1962.
47. Larmar. J.E. and Campbell, J.F., "Recent Studies at NASA-Langley of Vortical Flows Interacting with Neighboring Surfaces", Aerodynamics of Vortical Type Flows in Three Dimensions, AGARD CP 342, 1983.
48. Lowson, M.V., "Some Experiments with Vortex Breakdown", J. RAS, Vol. 68, May 1964, pp.343-346.
49. Lee, H., "Computational and Experimental Study of Trailing Vortices", Ph.D. Dissertation, VPI&SU, Blacksburg, Va., 1983.
50. Leibovich, S, "Vortex Stability and Breakdown; Survey and Extension", AIAA J., Vol.22, No.9, Sept. 1984, pp.1192-1206.
51. Luckring, J.M., Schoonover, W.E., and Frink, N.T., "Recent Advances in Applying Free Vortex Sheet Theory for the Estimation of Vortex Flow Aerodynamics", AIAA Paper 82-0095, 1982.
52. Ludwig, H., "Zur Erklärung der Instabilität der über angestellten Deltaflügeln auftretenden freien Wirbelkerne", Z. Flugwiss., Vol.10, No.6, June 1962, pp.242-249, translated as: "An Explanation of the Instability of the Free Vortex Cores Occurring over Delta Wings with Raised Edges", NASA TM 75861, Sept. 1980.

53. Marchman, J.F., "Effectiveness of Leading-Edge Vortex Flaps on 60 and 75 degree Delta Wings", J. Aircraft, Vol.18, No.4, April 1981, pp.280-286.
54. Marchman, J.F., "Aerodynamics of Inverted Leading-Edge Flaps on Delta Wings", J. Aircraft, Vol.18, No.12, Dec. 1981, pp.1051-1056.
55. Marchman, J.F. and Terry, J.E., "The Impact of Strakes on a Vortex-Flapped Delta Wing", AIAA Paper 83-1814, 1984.
56. Mangler, K.W. and Smith, J.H.B., "A Theory of the Flow past a Slender Delta Wing with Leading Edge Separation", Proc. Roy. Soc. A, Vol. 251, Oct. 1959, pp.200-217.
57. Manor, D. and Wentz, W.H., "Flow over Double Delta Wing and Wing Body at high α ", J. Aircraft, Vol.22, No.1, Jan. 1985, pp.78-82.
58. Marsden, D.J., Simpson, R.W., and Rainbird, W.J., "An Investigation into the Flow over Delta Wings at Low Speeds with Leading Edge Separation", College of Aeronautics, Cranfield, Report 114, Feb. 1958.
59. Mehrotra, S.C. and Lan, C.E., "A Theoretical Investigation of the Aerodynamics of Low-Aspect-Ratio Wings with Partial Leading-Edge Separation ", NASA CR 145304, Jan. 1978.
60. Mook, D.T. and Maddox, S.A. "Extension of a Vortex-Lattice Method to include the Effects of Leading-Edge Separation", J. Aircraft, Vol.11, No.2, Feb. 1974, pp.127-128.
61. Nathman, J.K., "Estimation of Wake Rollup Over Swept Wings", AIAA Paper 84-2174, 1984.
62. Newsome, R.W., "A Comparison of Euler and Navier-Stokes Solutions for Supersonic Flow over a Conical Delta Wing", AIAA Paper 85-0111, 1985
63. Ostowari, C., and Wentz, W.H., "Modified Calibration Technique of a Five-Hole Probes for High Flow Angles", Experiments in Fluids, Vol.1, 1963, pp.166-168.
64. Pao, J-L, and Lan, E.C., "A Vortex-Filaments and Core Model for Wings with Edge Vortex Separation", NASA CR 165847, Feb. 1982.
65. Parker, A.G., "Aerodynamic Characteristics of Slender Wings with Sharp Leading-Edges - A Review", J. Aircraft, Vol.13, No.3, March 1976, pp.161-168.
66. Peckham, D.H., "Low-Speed Wind-Tunnel Tests on a Series of Uncambered Slender Pointed Wings with Sharp Edges", ARC RM 3186, 1961.

67. Pohlhamus, E.C., "A concept of the Vortex Lift of Sharp-Edged Delta Wings based on a Leading-Edge-Suction Analogy", NASA TN D-3767, Dec. 1966
68. Poisson-Quinton, Ph., "Slender Wings for Civil and Military Aircraft", Israel J. Technology, Vol.16, 1978, pp.97-131.
69. Pope, A. and Harper, J.J., Low Speed Wind Tunnel Testing, John Wiley and Sons, New York, N.Y., 1966.
70. Quinto, P.F. and Paulson, J.W., "Flap Effectiveness on Subsonic Longitudinal Aerodynamic Characteristics of a Modified Arrow Wing", NASA TM 84582, 1983.
71. Rao, B.M. and Maskew, B., "Flows over Wings with Leading Edge Vortex Separation", NASA CR 165858, 1982.
72. Rao, D.M. and Johnson, T.D., "Investigation of Delta Wing Leading-Edge Devices", J. Aircraft, Vol.18, No.3, March 1981, pp.161-167.
73. Rao, D.M., "Vortical Flow Management for Improved Configuration Aerodynamics - Recent Experiences", Aerodynamics of Vortical Type Flows in Three Dimensions, AGARD CP 342, 1983.
74. Rebach, C, "Numerical Investigation of Leading Edge Vortex for Low-Aspect Ratio Thin Wings", J. Aircraft, Vol.14, No.2, Feb. 1976, pp.253-255.
75. Reynolds, G.A., "Experiments on the Stability of the Flat-Plate Boundary Layer with Suction", Ph.D. Dissertation, VPI&SU, Blacksburg, VA., 1982.
76. Rizzi, A., "Euler Solution of Transonic Vortex Flow around the Dilliner Wing", J. Aircraft, Vol.22, No.4, April 1985, pp.325-328
77. Runyan, L.J., Middleton, W.D. and Paulson, J.A., "Wind Tunnel Test Results of a New Leading Edge Flap Design for Highly Swept Wings - A Vortex Flap", Supersonic Cruise Research '79, NASA CP 2108, 1980, pp.131-147.
78. Schoonover, W.E. and Ohlson, W.E., "Wind-Tunnel Investigation of Vortex Flaps on a Highly Swept Interceptor Configuration", ICAS proc., ICAS-82-6.7.3, Aug. 1982, pp.1276-1290.
79. Seginer, A and Salomon, M, "Augmentation of Fighter - Aircraft Performance by Spanwise Blowing over the Wing Leading Edge", Aerodynamics of Vortical Type Flows in Three Dimensions, AGARD CP 342, 1983.

80. Sitaram, N., Lakshminarayana, B., and Ravindranath, A., "Conventional Probes for the Relative Flow Measurement in a Turbomachinery Rotor Blade Passage", Trans. ASME, Vol.103, April 1981, pp.406-414
81. Smith, J.H.B., "Improved Calculation of Leading-Edge Separation from Slender, Thin, Delta Wings", Proc. Roy. Soc. A, Vol.306, 1968, pp.67-90
82. Smith, J.H.B., "Vortical Flows and Their Computation", Computational Fluid Dynamics, VKI Lecture Series 1980-5, 1980.
83. Stanbrook, A. and Squire, L.C., "Possible Types of Flow at Swept Leading Edges", Aeronautical Quarterly, Feb. 1964, pp.72-82.
84. Sung, B., "Determination of Air Density with Water Vapor", J. Korean Soc. Aero. Space Sci., Vol.8, No.2, 1980, pp.49-52.
85. Timm, G.K., "Survey of Experimental Velocity Distribution in Vortex Flow with Bibliography", DI-82-0683, Boeing Scientific Research Lab., Nov. 1967.
86. Tingas, S.A. and Rao, D.M., "Subsonic Balance and Pressure Investigation of a 60-Degree Delta Wing with Leading-Edge Devices", NASA CR 165923, May 1982.
87. Treaster, A.L. and Yocum, A.M., "The Calibration and Application of Five-Hole Probes", Proc. ISA, Vol.18, 1978, pp.255-266.
88. Verhaagen, N.G., "An Experimental Investigation of the Vortex Flow over Delta and Double Delta Wings at Low Speed", Aerodynamics of Vortical Type Flows in Three Dimensions, AGARD CP 342, 1983
89. Verhaagen, N.G. and Kruisbrink, A.C.H., "The Entrainment Effect of a Leading-Edge Vortex", AIAA Paper 85-1584, 1985.
90. Weber, J.A., Brune, G.W., Johnson, F.T., Lu, P., and Rubbert, P.E. "The Three Dimensional Solution of Flows over Wings with Leading-Edge Vortex Separation", AIAA J, Vol.14, No.4, April 1976, pp.519-525.
91. Wentz, W.H., "Effect of Leading Edge Camber on Low Speed Characteristics of Slender Delta Wings", NASA CR 2002, Oct. 1972.
92. Wentz, W.H., "Effect of Leading Edge Camber on Low Speed Characteristics of Slender Delta Wings - Technique and Tabulated data", NASA CR 112016, 1972.
93. Wentz, W.H. and Kohlman, D.L., "Wind Tunnel Investigations of Vortex Breakdown on Slender Sharp-Edged Wings", NASA CR 98737, Nov. 1968.

94. Wentz, W.H. and McMahon, M.C., "Further Experimental Investigations of Delta and Double-Delta Wing Flow fields at Low Speeds.", NASA CR 714, Feb. 1967.
95. Werle, H., "Sur l'eclatement des tourbillons", ONERA TN 175, 1971, translated as: "On Vortex Bursting", NASA TM 77587, June 1984.
96. Whittle, E.F. and Lovell, J.C., "Full Scale Investigation of an Equilateral Triangular Wing Having 10-Percent-Thick Biconvex Airfoil Section", NASA RM L8G05, Sept. 1948.
97. Winter, H., "Strömungsvorgänge an Platten und profilierten Körpern bei kleinen Spannweiten", Forsch. Ing.-Wes., Vol. 6, 1935, pp.67-71, translated as: "Flow Phenomena on Plates and Airfoil of Short Span", NACA TM 798, 1937.
98. Wright, M.A., "The Evaluation of a Simplified Form of Presentation for Five-Hole Spherical and Hemispherical Pitometer Calibration Data", J. Physics E, Scientific Instrument, Vol.3, 1970, pp.356-362.
99. Yip, L.P. and Murri, D.G., "Effect of Vortex Flaps on the Low Speed Aerodynamic Characteristics of an Arrow Wing", NASA TP 1914 1981.

APPENDX A. FLOW PROPERTY MEASUREMENT AND YAWHEAD CALIBRATION

A.1 INTRODUCTION

Modern methods of flow field measurement such as the use of the laser doppler velocimeter are good for a wide range of velocity measurement including separated flow and rapidly changing flow fields, and the hot wire anemometer is good for measurement in and near the boundary layer. But neither methods can be used to measure the flow parameters such as pressure in a flow field of varying total pressure. The only possible way to measure a complicated flow field with non-constant total pressure such as vortex flow around a delta wing, is the non-nulling pressure hole type probe where the flow properties can be determined from the pressure readings using pre-calibrated data for each flow properties such as flow pitch angle, flow yaw angle, total pressure, and static pressure. One commercially available probe of this type is the 5-hole yawhead probe with conical tip such as United Sensor DC-125 probe which was used in this research (Fig. A.1)

A previous calibration (Lee (1983)) of the probe used in the current experiment was based on a maximum flow angle of 42° , which was not enough to cover the complex flow field around a delta wing, and it can not be used in real time calculation of the flow properties because a two dimensional interpolation technique is employed to determine the flow

properties, requiring a large amount of CPU time in the mainframe computer.

Several calibration methods (Dau et al. (1968), Wright (1970), Treaster and Yocum (1978), Ostowari and Wentz (1983), and Gerner et al. (1984)) were tried in order to develop a new method to measure the flow properties in complex flow field. The new method should have a sufficient accuracy, allow a wide range of the flow angles, and must be a simple procedure to allow real time calculation of the flow properties using the wind tunnel computer during the experiment. The method of Gerner et al. (1984) was used to develop the new method for flow property measurement.

A.2 CALIBRATION THEORY

The basic ideas of this method are that flow angularity is grouped into several zones according to the orientation of the flow w.r.t the yawhead probe and the flow properties (flow pitch angle, flow yaw angle, total pressure, and static pressure) can be expressed as a polynomial function of two angular variables (pitch coefficient, roll coefficient). Since a 5-hole yawhead probe was used for the present study, flow angularity was divided into 5 zones. Let P_i denote the pressure on the i -th pressure port in Fig. A.2.a. At the i -th zone, the i -th pressure port indicates the highest pressure and also indicates the general direction from which the incoming velocity vector is approaching (Fig. A.2 and A.3). For example, at zone 2 flow is approaching the probe from the negative Y direction and P_2 is the highest pressure from P_1 to P_5 .

LOW FLOW ANGLES: At low flow angles, flow over the probe tip is attached and P_1 is the highest pressure, hence the flow angularity is in zone 1. The flow pitch angle α and the flow yaw angle β are nearly linear to the pressure difference ΔP_p and ΔP_y respectively where,

$$\Delta P_p = P_4 - P_5, \text{ and } \Delta P_y = P_2 - P_3,$$

therefore the conventional pitch and yaw reference system is used (Fig. A.2.b) at low angle. Since P_1 is the closest value to the total pressure, P_1 is used as an approximate total pressure and the average of the P_2 through P_5 assumed as an approximate static pressure. Hence an approximate dynamic pressure q' can be defined as,

$$q' = P_1 - (P_2 + P_3 + P_4 + P_5)/4 \quad (\text{A. 1})$$

Let P_t and P_s denote the true total pressure and true static pressure respectively, then the total pressure coefficient A_t and static pressure coefficient A_s can be written as,

$$A_t = (P_1 - P_t)/q' \quad (\text{A. 2})$$

$$A_s = (P_1 - P_s)/q' \quad (\text{A. 3})$$

Since the flow pitch angle and flow yaw angle are varying proportional to ΔP_p and ΔP_y , the two flow angular variables are defined as pitch coefficient B_p , and yaw coefficient B_y respectively,

$$B_p = (P_4 - P_5)/q' \quad (\text{A. 4})$$

$$B_y = (P_2 - P_3)/q' \quad (\text{A. 5})$$

HIGH FLOW ANGLES: The polar reference system (Fig. A.2.b) is better suited than the conventional pitch-yaw system for the high flow angles. The flow cone angle θ is defined as an angle between the velocity vector and probe axis, hence it is always positive. The flow roll angle ϕ is defined as an angle between the Y-axis and the projection of the velocity vector onto the Y-Z plane. The roll angle is measured positive from the negative Y-axis in a clockwise direction as viewed from upstream when the velocity vector is approaching the probe tip.

Since the flow tends to separate over the leeward side of the probe at the high flow angles, pressure ports lying in separated flow region are insensitive to the flow angularity. Hence a maximum of 4 pressure ports can be used to determine the flow parameter. The highest pressure from P_2 to P_5 is used as an approximate total pressure P_i and flow angularity zone is also determined by the port number of the highest pressure (zone i). The average of two pressures from the ports adjacent to the highest pressure port is defined as an approximate static pressure. Therefore the approximate dynamic pressure q' can be defined as

$$q' = P_i - (P_{ic} + P_{icc})/2 \quad (\text{A. 6})$$

where P_i : highest pressure from P_2 to P_5

P_{ic} : pressure from the port next to the P_i
in clockwise

P_{icc} : pressure from the port next to the P_i
in counter clockwise

the total pressure coefficient A_t and static pressure coefficient A_s can be defined as,

$$A_t = (P_i - P_t)/q' \quad (\text{A. 7})$$

$$A_s = (P_i - P_s)/q' \quad (\text{A. 8})$$

Since the flow cone angle is proportional to the pressure difference between P_i and P_1 , and flow roll angle is varying with the pressure difference between P_{ic} and P_{icc} , the two flow angular variables are defined as cone angle coefficient B_c , and roll angle coefficient B_r respectively,

$$B_c = (P_i - P_1)/q' \quad (\text{A. 9})$$

$$B_r = (P_{icc} - P_{ic})/q' \quad (\text{A.10})$$

POLYNOMIAL FUNCTION AND CALIBRATION CONSTANT.: Assuming the each flow property can be expressed as a polynomial expansions of two flow angular variables, then the flow property A can be written as,

$$\begin{aligned} A = & K_1 + K_2 B_c + K_3 B_r + K_4 B_c^2 + K_5 B_c B_r + K_6 B_r^2 + K_7 B_c^3 \\ & + K_8 B_c^2 B_r + K_9 B_c B_r^2 + K_{10} B_r^3 + K_{11} B_c^4 + K_{12} B_c^3 B_r \\ & + K_{13} B_c^2 B_r^2 + K_{14} B_c B_r^3 + K_{15} B_r^4 + K_{16} B_c^5 + \dots \quad (\text{A.11}) \end{aligned}$$

If the terms higher than the 4-th order are neglected.

$$A = K_1 + K_2 B_c + K_3 B_r + \dots + K_{15} B_r^4 \quad (\text{A.12})$$

Also assuming the m set of data points are obtained from the calibration experiment (at least 15 different data points are required for the 4-th order polynomial equation to determine the 15 K 's uniquely for this case), then the m different equations can be written for m calibration points, which is

$$\begin{Bmatrix} A_1 \\ A_2 \\ \vdots \\ \vdots \\ \vdots \\ \vdots \\ A_m \end{Bmatrix} = \begin{bmatrix} 1 & B_{c1} & B_{r1} & \dots & B_{r1}^4 \\ 1 & B_{c2} & B_{r2} & \dots & B_{r2}^4 \\ \vdots & \vdots & \vdots & \dots & \vdots \\ \vdots & \vdots & \vdots & \dots & \vdots \\ \vdots & \vdots & \vdots & \dots & \vdots \\ \vdots & \vdots & \vdots & \dots & \vdots \\ 1 & B_{cm} & B_{rm} & \dots & B_{rm}^4 \end{bmatrix} \begin{Bmatrix} K_1 \\ K_2 \\ \vdots \\ \vdots \\ \vdots \\ \vdots \\ K_{15} \end{Bmatrix}$$

Above equation can be abbreviated as,

$$\{A\} = [B]\{K\} \quad (A.13)$$

$$\text{where } \{A\} = (A_1, A_2, A_3, \dots, A_m)^T$$

$$\{K\} = (K_1, K_2, K_3, \dots, K_{15})^T$$

$$[B] = \begin{bmatrix} 1 & b_{c1} & b_{r1} & \dots & b_{c1}^4 \\ \vdots & \vdots & \vdots & \dots & \vdots \\ \vdots & \vdots & \vdots & \dots & \vdots \\ \vdots & \vdots & \vdots & \dots & \vdots \\ \vdots & \vdots & \vdots & \dots & \vdots \\ \vdots & \vdots & \vdots & \dots & \vdots \\ 1 & b_{cm} & b_{rm} & \dots & b_{cm}^4 \end{bmatrix}$$

During the calibration experiment, the elements in the vector $\{A\}$ are set by the experimenter, and the matrix $[B]$ can be constructed by using B_c and B_r (or B_p and B_y) calculated from the pressure readings of the yawhead

probe. The unknown calibration coefficient $\{K\}$ can be found uniquely. Multiplying the $[B]^T$ to the both side of the equation(A.13),

$$\{Y\} = [C]\{K\} \quad (A.14)$$

where $\{Y\} = [B]^T\{A\}$, vector with 15 elements

$[C] = [B]^T[B]$, 15 x 15 matrix

$\{K\}$, vector with 15 elements.

hence the $\{K\}$ is

$$\begin{aligned} \{K\} &= [C]^{-1}\{Y\} \\ &= ([B]^T[B])^{-1}[B]^T\{A\} \end{aligned} \quad (A.15)$$

This turns out to a 4-th order least square curve fitted to the experimental data.

Four sets of equations like (A.13) can be constructed at each flow angularity zone, which are

$$\begin{aligned} \{\theta\} &= [B]\{K^\theta\} \quad \text{or} \quad \left\{ \begin{aligned} \{\alpha\} &= [B]\{K^\alpha\} \\ \{\beta\} &= [B]\{K^\beta\} \end{aligned} \right\} \text{ for zone 1} \\ \{\phi\} &= [B]\{K^\phi\} \\ \{A_t\} &= [B]\{K^t\} \\ \{A_s\} &= [B]\{K^s\} \end{aligned} \quad (A.16)$$

Having determined the all calibration constant {K}'s, the calibration process is completed, and the yawhead probe is ready to use in an unknown flow field.

FLOW PROPERTIES IN UNKNOWN FLOW FIELD: When the yawhead probe is being used in an unknown flow field, the flow angularity zone can be determined from the highest pressure from port 1 to 5 of the probe. The intermediate variable V's are calculated using the two flow angular variables B_c and B_r (or B_p and B_y).

$$V_1 = 1.0$$

$$V_2 = B_c$$

$$V_3 = B_r$$

$$V_4 = B_c^2$$

$$V_5 = B_c B_r$$

$$V_6 = B_r^2$$

$$V_7 = B_c^3$$

$$V_8 = B_c^2 B_r$$

$$V_9 = B_c B_r^2$$

$$V_{10} = B_r^3$$

$$V_{11} = B_c^4$$

$$V_{12} = B_c^3 B_r$$

$$V_{13} = B_c^2 B_r^2$$

$$V_{14} = B_c B_r^3$$

$$V_{15} = B_r^4$$

Flow properties can be obtained by taking the scalar product of $\{V\}$ with the calibration coefficient $\{K\}$

$$\begin{aligned}\theta &= \{V\}^T \{K^\theta\} \quad \text{or } \alpha = \{V\}^T \{K^\alpha\} \\ \phi &= \{V\}^T \{K^\phi\} \quad \beta = \{V\}^T \{K^\beta\} \\ A_t &= \{V\}^T \{K^t\} \\ A_s &= \{V\}^T \{K^s\}\end{aligned}\tag{A. 17}$$

From the θ , ϕ , A_t , and A_s , the following physical flow parameters can be obtained

$$\begin{aligned}P_t &= P_i - A_t q' \\ P_s &= P_i - A_s q' \\ q &= P_t - P_s \\ V_\infty &= (2q/\rho)^{\frac{1}{2}} \\ u &= V_\infty \cos\theta \quad \text{or } u = V_\infty \cos\alpha \cos\beta \\ v &= V_\infty \sin\theta \cos\phi \quad v = V_\infty \sin\beta \\ w &= V_\infty \sin\theta \sin\phi \quad w = V_\infty \sin\alpha \cos\beta\end{aligned}$$

A.3 CALIBRATION EXPERIMENT

A 5-hole yawhead probe (United Sensor DC-125) was calibrated in the Virginia Tech. Stability Wind Tunnel. The yawhead probe and details are shown in Fig. A.1 and Fig. A.2.a respectively. The yawhead probe was mounted on the strut which was installed on the turntable in the test

section. The Reynolds number of the calibration test was 3780 based on the probe tip diameter, which is $Re=1.19 \times 10^6$ per meter of the characteristic length. During the test, the flow cone angles and the flow roll angles were set by rotating the turntable from -70° to 70° with 10° interval, and by rolling the yawhead probe w.r.t the probe axis from -90° to 90° in 10° increments, which resulted in flow angles ranging from 0° to 70° in flow cone angle and flow roll angles ranged from -180° to 180° . The relation between the probe setting angle and flow angle are,

$$\theta = |\theta_t|$$

$$\phi = \phi_t + \text{sgn}(\theta_t).90^\circ$$

where the subscript t denotes the probe setting angle.

The relations between α , β with θ , ϕ are

$$\alpha = \tan^{-1}(\tan\theta.\sin\phi)$$

$$\beta = \sin^{-1}(\sin\theta.\cos\phi)$$

or

$$\theta = \cos^{-1}(\cos\alpha.\cos\beta)$$

$$\phi = \tan^{-1}(\sin\alpha/\tan\beta)$$

The same instruments were used for the mean flow field measurement.

A.4 RESULTS AND DISCUSSIONS

The calibration coefficients were obtained using the calibration theory mentioned in section A.2., and shown in Table A.1. The calibration data for the case of $\theta=70^\circ$ were not used for the calculation of the calibration coefficients because of the poor characteristics of the probe at $\theta=70^\circ$.

After obtained the calibration coefficients, the data were substituted back into equation (A.16) to produce the predicted value at each calibration point. The predicted flow angles are compared with the measured flow angles in Fig. A.4. The root mean square (RMS) errors were calculated using the differences between the measured values and the predicted values for the corresponding calibration points to predict the accuracy of the method, and the RMS errors are listed in Table A.2.

From Table A.2. and Fig. A.4., the flow properties can be predicted quite accurately in low flow angles (zone 1). At high flow angles (zone 2 to zone 5), flow cone angles were predicted with reasonable accuracy, while there are large deviations in flow roll angles between the measured value and predicted value at the high flow cone angles. The major portions of the error in the overall flow regime came from the errors in flow roll angle predictions at different flow angularity zones.

The cause of the poor prediction of the roll angle is flow separation on the yawhead probe. Flow over a circular cylinder separates at around 80°

for laminar flow. At high flow cone angles, flow over the probe tip will separate near 80° , since the probe tip behaves like a circular cylinder and at the Reynolds number of 3780, the boundary layer over the probe tip is laminar. If the flow roll angle is in the range of $\pm 20^\circ$ from the location of the pressure port 2 to 5 ($\pm 20^\circ$ from $\phi = 0^\circ, 90^\circ, 180^\circ$, and -90°), pressure on the adjacent pressure ports can not be distinguished for different flow roll angles, and this fact resulted a poor prediction in flow roll angles at the high cone angles. This situation can be improved only by using a yawhead probe which has pressure ports at less than 70° intervals such as 7-hole yawhead probe.

From Fig. A.4, it is seen that the flow yaw angles were predicted higher than the measured values at $\alpha < 0^\circ$. This can be the result of a slight bend in the stem of the probe or if the pressure ports on the periphery of the nose (port 2 to port 5) are not an equal distance from port 1.

Table A.1 Calibration coefficient of yawhead probe.

Zone 1				
I	K^{α}	K^{β}	K^t	K^s
1	0.3642E-02	0.1072E-02	0.1561E-01	0.9104E+00
2	0.5251E+00	-0.2356E-01	-0.4406E-02	-0.2230E-02
3	0.2744E-01	0.5131E+00	0.4229E-02	-0.4222E-03
4	-0.3872E-02	0.1183E-01	-0.3573E+00	-0.5179E-01
5	-0.3940E-01	-0.6946E-02	0.9495E-02	0.1103E-01
6	-0.5503E-02	-0.1281E-01	-0.3487E+00	-0.6321E-01
7	-0.7993E-01	0.5252E-02	-0.8305E-03	0.1804E-02
8	-0.5668E-02	-0.7291E-01	0.1164E-01	0.6131E-02
9	-0.4465E-01	0.7837E-03	0.2070E-01	0.1282E-01
10	-0.2779E-02	-0.7375E-01	-0.1401E-02	0.2900E-02
11	0.1136E-02	-0.5432E-02	0.4194E-01	-0.2710E-01
12	0.1958E-01	-0.8177E-02	-0.1235E-01	-0.7705E-02
13	0.7114E-02	0.1531E-02	0.1637E-01	-0.2815E-01
14	0.1435E-01	0.5761E-02	-0.2938E-02	-0.1242E-01
15	0.2623E-02	0.5878E-02	0.3750E-01	-0.2310E-01

Zone 2				
I	K^{θ}	K^{ϕ}	K^t	K^s
1	0.5064E+00	0.3501E-01	-0.3867E+00	0.5379E+00
2	0.5483E+00	0.2019E-01	0.8385E+00	-0.8273E-01
3	-0.5038E-01	-0.1033E+01	-0.2787E-01	-0.1460E-01
4	-0.6723E+00	0.2258E+00	-0.8212E+00	-0.1026E+00
5	-0.9242E-01	-0.5895E-01	-0.1537E+00	-0.3444E-01
6	0.2024E+00	0.2012E+00	-0.5677E+00	-0.5246E-01
7	0.2090E+01	-0.4628E+00	0.9651E+00	-0.5082E-01
8	0.4280E+00	-0.1617E+00	0.3252E+00	0.8825E-02
9	-0.7299E+00	0.2114E-01	-0.7118E+00	-0.4804E-01
10	-0.2990E-01	0.4575E+00	-0.2809E-01	0.8332E-02
11	-0.1343E+01	0.2005E+00	-0.6718E+00	0.4864E-01
12	-0.3352E+00	0.8534E-01	-0.1234E+00	0.3299E-02
13	0.3565E+00	-0.2461E-01	0.1786E+00	-0.9281E-02
14	0.1553E+00	0.6361E-01	0.2133E+00	0.2471E-01
15	-0.1518E-01	-0.2033E+00	0.7636E-01	-0.4235E-02

Table A.1 Continued.

Zone 3				
I	K^{θ}	K^{ϕ}	K^t	K^s
1	0.5133E+00	0.3162E+01	-0.3715E+00	0.5287E+00
2	0.1240E+01	0.1289E+01	0.1647E+01	-0.1583E+00
3	0.4873E-02	-0.1103E+01	0.6764E-01	0.2708E-01
4	-0.4891E+01	-0.6169E+01	-0.5381E+01	0.2897E+00
5	-0.1253E-01	-0.7158E+00	-0.1778E+00	0.4048E-01
6	0.7873E+00	0.9508E+00	-0.1874E+00	-0.9815E-01
7	0.9928E+01	0.1047E+02	0.8840E+01	-0.6506E+00
8	-0.1890E+00	0.1484E+00	0.3724E-01	0.2627E-01
9	-0.3008E+01	-0.3694E+01	-0.3161E+01	0.1511E+00
10	-0.1269E-01	0.4425E+00	-0.6315E-01	0.1638E-02
11	-0.5847E+01	-0.5795E+01	-0.5106E+01	0.3417E+00
12	0.1324E+00	-0.2106E+00	0.1159E+00	0.9177E-02
13	0.2585E+01	0.3281E+01	0.2545E+01	-0.1909E+00
14	0.2241E+00	0.1026E+01	0.5082E+00	-0.3909E-01
15	-0.1979E+00	-0.4402E+00	0.2860E-01	0.2978E-02

Zone 4				
I	K^{θ}	K^{ϕ}	K^t	K^s
1	0.5264E+00	0.1623E+01	-0.3943E+00	0.5435E+00
2	0.4030E+00	-0.1925E+00	0.7672E+00	-0.1132E+00
3	0.6847E-02	-0.8197E+00	-0.6261E-01	-0.5256E-02
4	0.1130E+00	0.1568E+00	-0.6351E+00	-0.6261E-01
5	0.9966E-02	-0.2066E+00	0.7795E-01	-0.1086E-02
6	0.7237E-01	-0.9876E-01	-0.4931E+00	-0.6780E-01
7	0.6824E+00	0.1206E+00	0.6843E+00	-0.3451E-01
8	-0.1558E+00	0.1056E-01	-0.8449E-01	0.4882E-02
9	-0.2455E+00	0.1434E+00	-0.4372E+00	-0.5980E-02
10	0.1465E-01	0.1475E+00	0.6047E-01	0.3694E-02
11	-0.5934E+00	-0.1874E+00	-0.5154E+00	0.5536E-02
12	0.1923E+00	0.1967E-02	0.1775E+00	-0.8814E-02
13	0.8645E-01	0.6915E-01	0.1243E+00	0.3067E-02
14	-0.5333E-01	0.7387E-01	-0.6669E-01	0.3007E-02
15	-0.2985E-02	0.3539E-01	0.3419E-01	0.3261E-02

Table A.1 Concluded.

Zone 5				
I	K^{θ}	K^{ϕ}	K^t	K^s
1	0.5276E+00	-0.1513E+01	-0.3384E+00	0.5474E+00
2	0.4877E+00	-0.9350E-01	0.7448E+00	-0.1509E+00
3	0.3105E-01	-0.9267E+00	-0.4355E-01	-0.1935E-01
4	-0.5375E+00	0.2393E+00	-0.1572E+01	-0.5384E-02
5	0.3151E-01	-0.2999E+00	0.1338E+00	-0.1078E-01
6	0.1602E+00	-0.7788E-01	-0.6936E+00	-0.1302E+00
7	0.1956E+01	-0.4458E-01	0.2952E+01	-0.4740E-01
8	-0.2327E-01	0.6242E-01	-0.3751E-01	0.1793E-02
9	-0.6548E+00	0.1351E+00	-0.1020E+01	0.1071E-01
10	-0.5486E-02	0.1766E+00	0.5038E-01	0.5114E-02
11	-0.1361E+01	-0.3463E-01	-0.2014E+01	-0.5160E-02
12	-0.1487E-01	-0.3652E-01	-0.1936E-01	-0.2880E-01
13	0.5613E+00	-0.4357E-01	0.9837E+00	-0.5721E-02
14	-0.2920E-01	0.1384E+00	-0.9753E-01	0.1052E-01
15	-0.2856E-01	0.4334E-01	0.9214E-01	0.1658E-01

Table A.2 RMS error in flow field measurement.

zone	$\delta\alpha(\text{deg})$	$\delta\beta(\text{deg})$	$\delta\theta(\text{deg})$	$\delta\phi(\text{deg})$	$\delta P_t(\%)$	$\delta q(\%)$
1	0.51	0.56	-	-	1.33	1.34
2	-	-	1.38	4.52	4.99	6.08
3	-	-	1.33	6.01	7.78	8.68
4	-	-	1.57	5.04	5.66	6.38
5	-	-	1.64	3.95	6.48	6.62
total	3.93	2.36	-	-	4.82	5.33

maximum cone angle was 60 degree

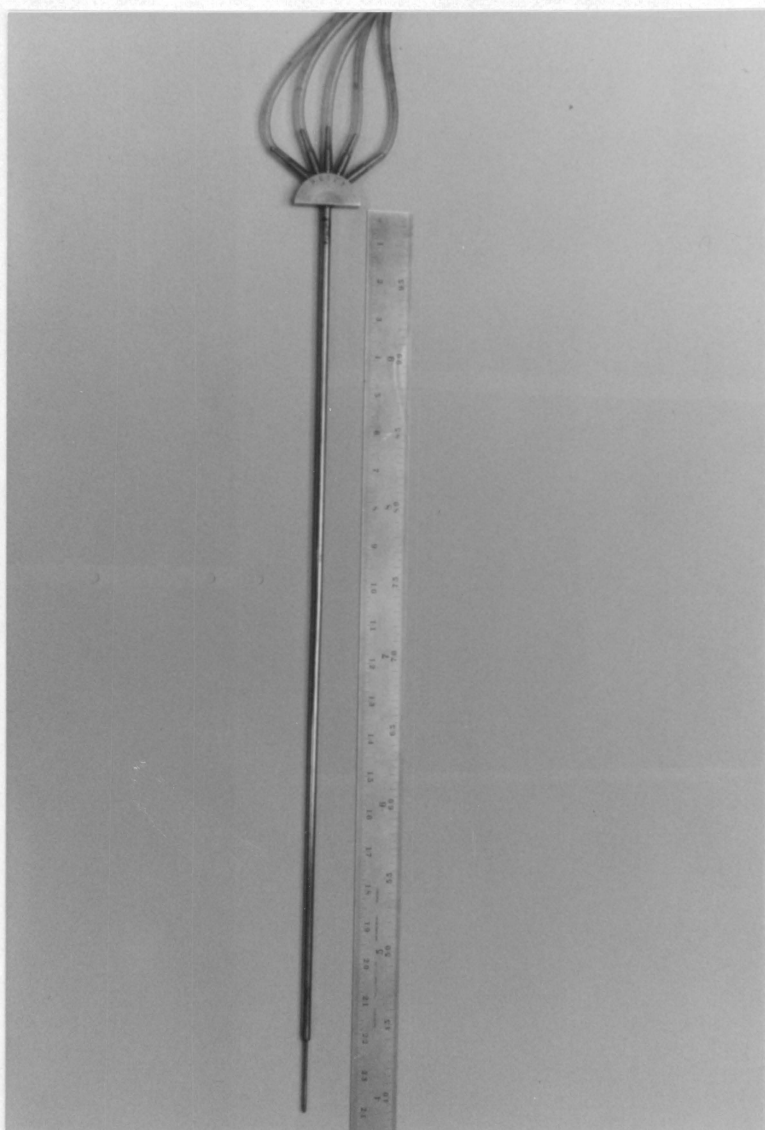
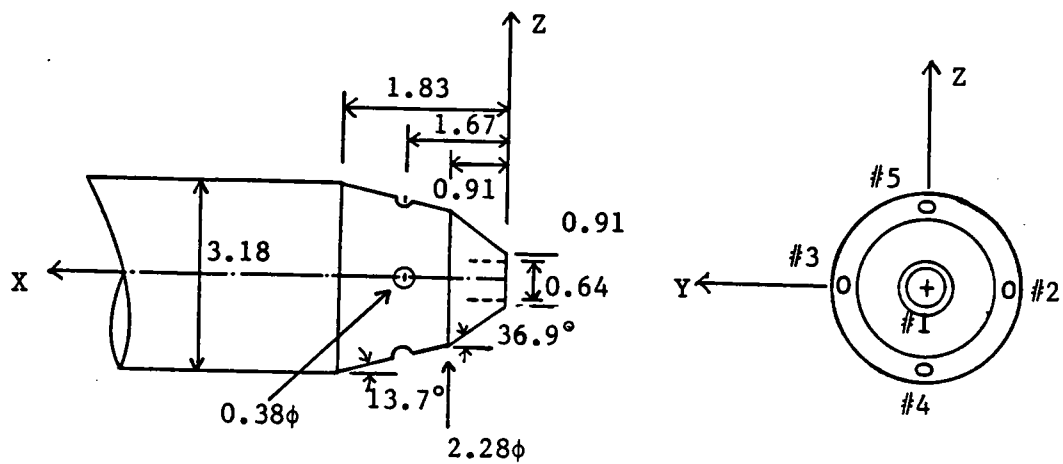
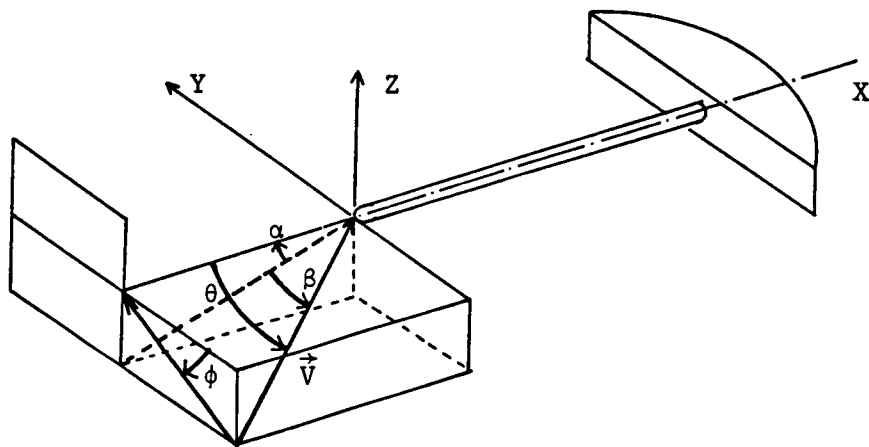


Fig. A.1. Five hole yawhead probe.



(a) DETAILS of THE FIVE-HOLE YAWHEAD PROBE TIP.
DIMENSIONS IN millimeters



(b) FLOW ANGLE DEFINITION.

Fig. A.2. Details of yawhead probe tip and flow angle definition.

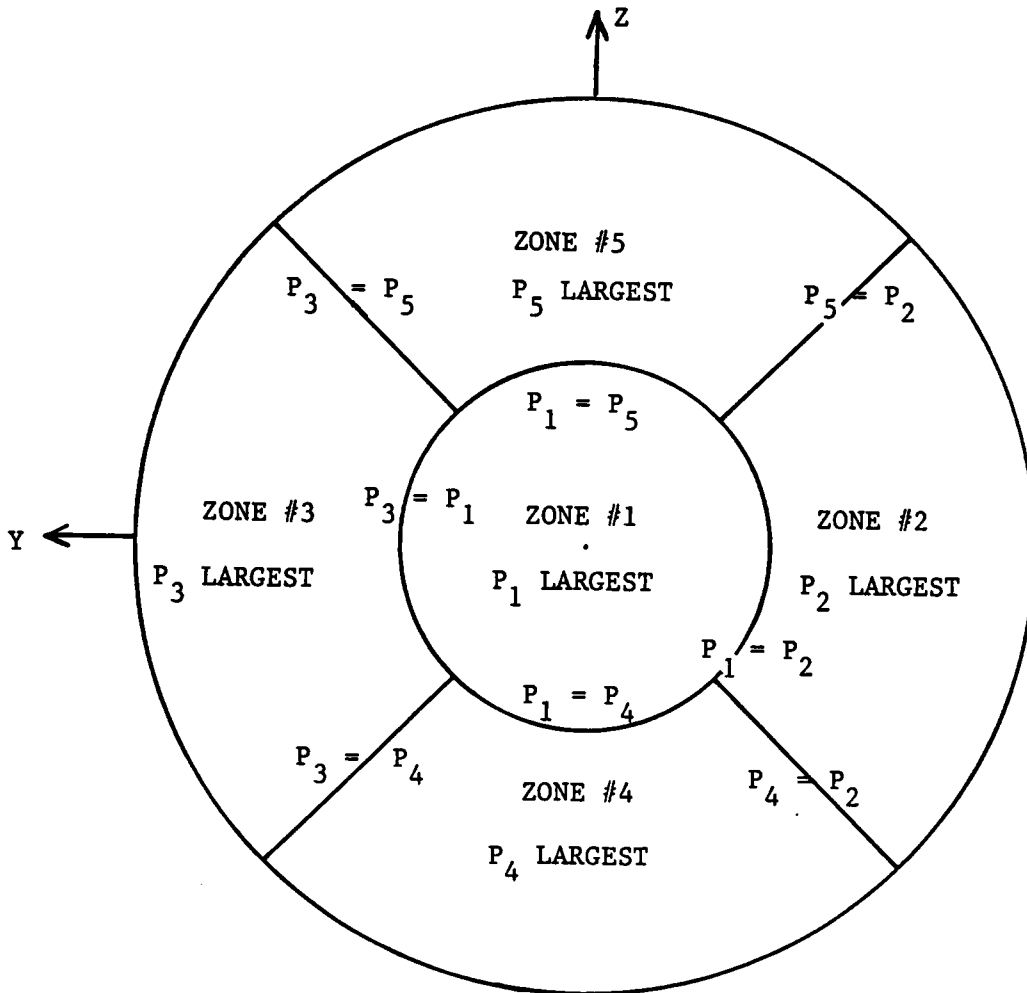


Fig. A.3. Division of flow angularity zones.

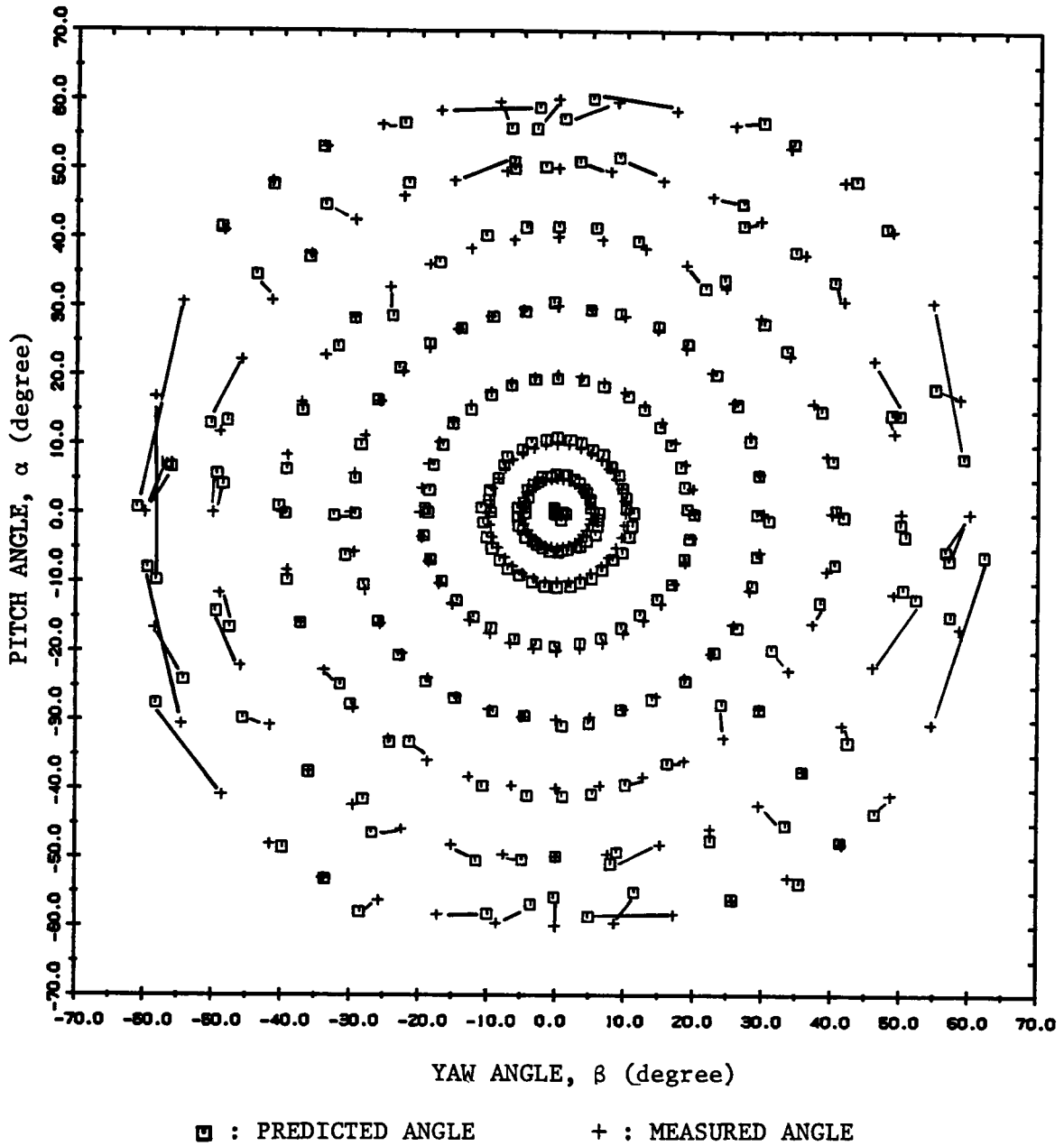
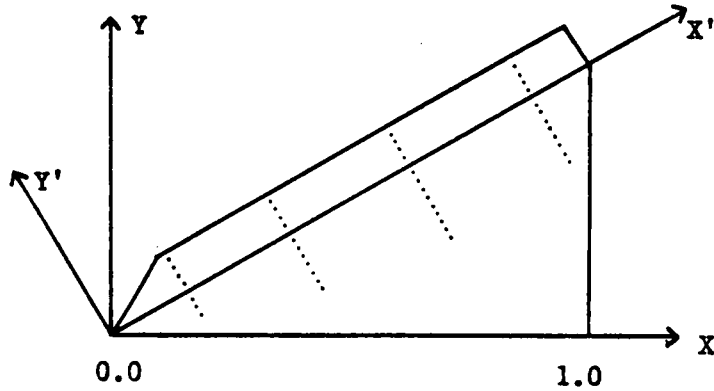


Fig. A.4. Comparison of predicted flow angle with measured angle.

Table 1 Location of pressure taps.



No.	X	Y	X'	Y'	No.	X	Y	X'	Y'
1*	0.125	0.159	0.188	0.075	25	0.618	0.374	0.722	0.015
2	0.125	0.159	0.188	0.075	26	0.635	0.344	0.722	-0.020
3	0.135	0.142	0.188	0.055	27	0.645	0.326	0.722	-0.040
4	0.145	0.124	0.188	0.035	28	0.655	0.309	0.722	-0.060
5	0.155	0.107	0.188	0.015	29	0.665	0.292	0.722	-0.080
6	0.173	0.077	0.188	-0.020	30	0.675	0.274	0.722	-0.100
7	0.183	0.059	0.188	-0.040	31	0.685	0.257	0.722	-0.120
8	0.193	0.042	0.188	-0.060	32	0.695	0.240	0.722	-0.140
9*	0.338	0.282	0.433	0.075	33	0.705	0.222	0.722	-0.160
10	0.338	0.282	0.433	0.075	34	0.715	0.205	0.722	-0.180
11	0.348	0.264	0.433	0.055	35*	0.838	0.570	1.011	0.075
12	0.358	0.247	0.433	0.035	36	0.838	0.570	1.011	0.075
13	0.368	0.230	0.433	0.015	37	0.848	0.553	1.011	0.055
14	0.385	0.199	0.433	-0.020	38	0.858	0.536	1.011	0.035
15	0.395	0.182	0.433	-0.040	39	0.868	0.518	1.011	0.015
16	0.405	0.165	0.433	-0.060	40	0.885	0.488	1.011	-0.020
17	0.415	0.147	0.433	-0.080	41	0.895	0.471	1.011	-0.040
18	0.425	0.130	0.433	-0.100	42	0.905	0.453	1.011	-0.060
19	0.435	0.113	0.433	-0.120	43	0.915	0.436	1.011	-0.080
20	0.445	0.095	0.433	-0.140	44	0.925	0.419	1.011	-0.100
21*	0.588	0.426	0.722	0.075	45	0.935	0.401	1.011	-0.120
22	0.588	0.426	0.722	0.075	46	0.945	0.384	1.011	-0.140
23	0.598	0.409	0.722	0.055	47	0.955	0.367	1.011	-0.160
24	0.608	0.391	0.722	0.035					

* : Pressure tabs on the pressure side of the flap

Table 2 Free stream turbulence level.(from Reynolds (1982))

V_{∞} (m/s)	$ u' /V_{\infty} $ (%)
9.0	0.018
10.0	0.018
15.0	0.022
20.0	0.028
30.0	0.045

Table 3 Cp distribution.

$\alpha(\text{deg})$	0.0	5.0	10.0	15.0	20.0	25.0	30.0	35.0	40.0
$\delta(\text{deg})$	0.0	0.0	0.0	0.0	0.0	0.0	0.0	0.0	0.0
Re(+6)	2.22	2.21	2.21	2.20	2.19	2.19	2.20	2.18	2.19
Cp(1)	0.245	0.371	0.459	0.498	0.503	0.602	0.626	0.633
Cp(2)	-0.101	-0.756	-1.266	-1.935	-2.318	-2.338	-0.734	-0.669	-0.653
Cp(3)	-0.089	-0.663	-1.525	-2.963	-2.956	-2.613	-0.755	-0.668	-0.655
Cp(4)	-0.069	-0.566	-1.798	-2.917	-3.573	-2.750	-0.751	-0.684	-0.657
Cp(5)	-0.050	-0.410	-0.891	-0.809	-2.454	-2.820	-0.743	-0.679	-0.654
Cp(6)	-0.040	-0.129	-0.187	-0.331	-0.514	-2.361	-0.749	-0.686	-0.655
Cp(7)	-0.028	-0.136	-0.252	-0.399	-0.550	-1.459	-0.767	-0.663	-0.670
Cp(8)	-0.028	-0.148	-0.277	-0.429	-0.608	-1.023	-0.780	-0.676	-0.656
Cp(9)	0.122	0.254	0.320	0.347	0.352	0.327	0.405	0.425	0.429
Cp(10)	-0.136	-0.849	-1.166	-1.391	-1.584	-1.695	-0.756	-0.683	-0.679
Cp(11)	-0.045	-1.214	-1.696	-1.927	-2.011	-1.911	-0.762	-0.698	-0.661
Cp(12)	-0.041	-0.377	-2.236	-2.318	-2.227	-2.075	-0.737	-0.684	-0.683
Cp(13)	-0.042	-0.086	-1.013	-1.860	-2.196	-2.018	-0.757	-0.686	-0.673
Cp(14)	-0.035	-0.136	-0.100	-0.647	-1.538	-2.059	-0.735	-0.690	-0.684
Cp(15)	-0.037	-0.152	-0.120	-0.398	-1.045	-1.818	-0.768	-0.691	-0.675
Cp(16)	-0.040	-0.147	-0.147	-0.329	-0.671	-1.415	-0.787	-0.720	-0.700
Cp(17)	-0.065	-0.174	-0.223	-0.383	-0.607	-1.159	-0.761	-0.682	-0.686
Cp(18)	-0.055	-0.157	-0.221	-0.362	-0.539	-0.843	-0.760	-0.702	-0.680
Cp(19)	-0.047	-0.139	-0.214	-0.347	-0.502	-0.745	-0.747	-0.686	-0.659
Cp(20)	-0.044	-0.133	-0.217	-0.342	-0.490	-0.673	-0.749	-0.693	-0.680
Cp(21)	0.105	0.228	0.283	0.303	0.299	0.275	0.283	0.292	0.277
Cp(22)	-0.292	-0.579	-0.789	-0.919	-1.035	-1.092	-0.736	-0.688	-0.666
Cp(23)	-0.032	-0.682	-0.821	-0.961	-1.091	-1.133	-0.720	-0.689	-0.694
Cp(24)	-0.042	-0.937	-0.871	-1.031	-1.153	-1.235	-0.722	-0.695	-0.700
Cp(25)	-0.084	-0.847	-1.296	-1.196	-1.272	-1.353	-0.732	-0.694	-0.704
Cp(26)	-0.054	-0.121	-1.097	-1.317	-1.371	-1.446	-0.731	-0.711	-0.717
Cp(27)	-0.053	-0.046	-0.614	-1.196	-1.314	-1.449	-0.748	-0.708	-0.697
Cp(28)	-0.051	-0.064	-0.301	-0.981	-1.229	-1.415	-0.732	-0.712	-0.706
Cp(29)	-0.065	-0.104	-0.200	-0.761	-1.136	-1.382	-0.736	-0.707	-0.708
Cp(30)	-0.049	-0.096	-0.143	-0.535	-0.985	-1.285	-0.746	-0.703	-0.706
Cp(31)	-0.061	-0.115	-0.145	-0.379	-0.825	-1.169	-0.727	-0.699	-0.694
Cp(32)	-0.054	-0.111	-0.140	-0.295	-0.660	-1.019	-0.726	-0.701	-0.702
Cp(33)	-0.071	-0.134	-0.168	-0.274	-0.538	-0.908	-0.746	-0.696	-0.715
Cp(34)	-0.059	-0.122	-0.155	-0.252	-0.480	-0.742	-0.749	-0.704	-0.718
Cp(35)	0.093	0.200	0.233	0.235	0.222	0.193	0.172	0.169	0.158
Cp(36)	-0.371	-0.440	-0.427	-0.528	-0.631	-0.703	-0.670	-0.642	-0.634
Cp(37)	-0.063	-0.467	-0.484	-0.608	-0.682	-0.750	-0.651	-0.635	-0.617
Cp(38)	-0.086	-0.456	-0.501	-0.633	-0.706	-0.769	-0.669	-0.643	-0.633
Cp(39)	-0.108	-0.531	-0.513	-0.652	-0.734	-0.804	-0.676	-0.654	-0.636
Cp(40)	-0.061	-0.652	-0.656	-0.711	-0.795	-0.886	-0.680	-0.663	-0.646
Cp(41)	-0.074	-0.489	-0.744	-0.744	-0.829	-0.931	-0.685	-0.647	-0.651
Cp(42)	-0.091	-0.247	-0.714	-0.756	-0.865	-0.977	-0.702	-0.652	-0.641
Cp(43)	-0.082	-0.050	-0.624	-0.739	-0.850	-0.986	-0.694	-0.664	-0.656
Cp(44)	-0.099	-0.028	-0.523	-0.704	-0.841	-0.995	-0.694	-0.675	-0.654
Cp(45)	-0.113	-0.052	-0.373	-0.646	-0.805	-0.999	-0.709	-0.677	-0.667
Cp(46)	-0.130	-0.097	-0.285	-0.625	-0.802	-1.006	-0.706	-0.672	-0.664
Cp(47)	-0.131	-0.123	-0.211	-0.541	-0.756	-0.967	-0.715	-0.687	-0.657

Table 3 Continued.

$\alpha(\text{deg})$	0.0	5.0	10.0	15.0	20.0	25.0	30.0	35.0	40.0
$\delta(\text{deg})$	5.0	5.0	5.0	5.0	5.0	5.0	5.0	5.0	5.0
Re(+6)	2.06	2.06	2.03	2.02	2.02	2.02	2.01	2.02	2.02
Cp(1)	0.052	0.210	0.336	0.434	0.495	0.509	0.581	0.608	0.618
Cp(2)	-0.042	-0.680	-1.160	-1.860	-2.330	-2.420	-1.010	-0.870	-0.833
Cp(3)	-0.050	-0.538	-1.230	-2.530	-2.840	-2.780	-0.988	-0.870	-0.837
Cp(4)	-0.057	-0.427	-1.320	-2.780	-3.550	-2.980	-1.030	-0.855	-0.859
Cp(5)	-0.061	-0.331	-1.050	-1.100	-2.720	-3.250	-1.040	-0.891	-0.829
Cp(6)	-0.034	-0.134	-0.151	-0.246	-0.425	-1.980	-0.983	-0.884	-0.840
Cp(7)
Cp(8)	-0.042	-0.151	-0.271	-0.412	-0.607	-0.778	-1.010	-0.850	-0.862
Cp(9)	0.057	0.217	0.294	0.336	0.349	0.344	0.388	0.405	0.418
Cp(10)	-0.031	-0.738	-1.110	-1.390	-1.650	-1.720	-0.942	-0.860	-0.822
Cp(11)	-0.041	-0.988	-1.330	-1.840	-2.030	-1.980	-0.976	-0.858	-0.845
Cp(12)	-0.053	-0.195	-1.570	-2.260	-2.300	-2.150	-0.951	-0.853	-0.852
Cp(13)	-0.077	-0.138	-1.110	-1.880	-2.320	-2.340	-1.020	-0.876	-0.836
Cp(14)	-0.057	-0.166	-0.216	-0.555	-1.590	-2.030	-0.996	-0.853	-0.850
Cp(15)	-0.056	-0.176	-0.222	-0.367	-1.060	-1.750	-0.953	-0.868	-0.847
Cp(16)	-0.051	-0.165	-0.191	-0.327	-0.673	-1.290	-0.992	-0.860	-0.863
Cp(17)	-0.062	-0.174	-0.212	-0.355	-0.574	-1.030	-0.993	-0.860	-0.851
Cp(18)	-0.058	-0.166	-0.209	-0.351	-0.530	-0.823	-0.999	-0.851	-0.847
Cp(19)	-0.059	-0.158	-0.217	-0.352	-0.518	-0.723	-0.975	-0.854	-0.856
Cp(20)	-0.050	-0.143	-0.211	-0.337	-0.498	-0.663	-0.981	-0.883	-0.859
Cp(21)	0.058	0.194	0.251	0.277	0.273	0.263	0.225	0.228	0.241
Cp(22)	-0.059	-0.588	-0.800	-0.898	-1.130	-1.160	-0.903	-0.865	-0.862
Cp(23)	-0.067	-0.686	-0.885	-0.983	-1.200	-1.250	-0.950	-0.847	-0.844
Cp(24)	-0.058	-0.690	-1.120	-1.070	-1.210	-1.230	-0.929	-0.832	-0.858
Cp(25)	-0.093	-0.571	-1.290	-1.250	-1.330	-1.340	-0.910	-0.868	-0.853
Cp(26)	-0.082	-0.175	-0.984	-1.320	-1.400	-1.480	-0.950	-0.865	-0.852
Cp(27)	-0.062	-0.081	-0.588	-1.190	-1.350	-1.500	-0.984	-0.849	-0.852
Cp(28)	-0.085	-0.132	-0.333	-0.997	-1.340	-1.560	-0.934	-0.846	-0.859
Cp(29)	-0.079	-0.134	-0.192	-0.696	-1.190	-1.440	-0.929	-0.844	-0.864
Cp(30)	-0.073	-0.134	-0.153	-0.484	-1.060	-1.350	-0.941	-0.862	-0.847
Cp(31)	-0.081	-0.148	-0.160	-0.360	-0.872	-1.190	-0.949	-0.861	-0.869
Cp(32)
Cp(33)	-0.058	-0.122	-0.145	-0.227	-0.518	-0.876	-0.937	-0.837	-0.859
Cp(34)	-0.058	-0.124	-0.140	-0.214	-0.454	-0.733	-0.969	-0.845	-0.849
Cp(35)	0.019	0.155	0.195	0.206	0.201	0.187	0.139	0.135	0.127
Cp(36)	-0.076	-0.609	-0.396	-0.526	-0.679	-0.731	-0.812	-0.783	-0.797
Cp(37)	-0.094	-0.498	-0.469	-0.593	-0.709	-0.787	-0.818	-0.776	-0.788
Cp(38)	-0.112	-0.303	-0.516	-0.632	-0.738	-0.797	-0.803	-0.760	-0.798
Cp(39)	-0.121	-0.339	-0.521	-0.667	-0.764	-0.821	-0.837	-0.801	-0.808
Cp(40)
Cp(41)	-0.089	-0.381	-0.745	-0.743	-0.846	-0.966	-0.833	-0.796	-0.816
Cp(42)	-0.097	-0.150	-0.664	-0.744	-0.864	-0.952	-0.851	-0.822	-0.827
Cp(43)	-0.105	-0.094	-0.566	-0.735	-0.934	-1.030	-0.842	-0.803	-0.829
Cp(44)	-0.111	-0.093	-0.375	-0.697	-0.877	-1.030	-0.864	-0.810	-0.803
Cp(45)	-0.128	-0.122	-0.217	-0.650	-0.842	-1.020	-0.882	-0.820	-0.834
Cp(46)	-0.147	-0.151	-0.157	-0.627	-0.891	-1.090	-0.901	-0.819	-0.827
Cp(47)	-0.147	-0.152	-0.143	-0.539	-0.794	-0.950	-0.878	-0.820	-0.812

Table 3 Continued.

$\alpha(\text{deg})$	0.0	5.0	10.0	15.0	20.0	25.0	30.0	35.0	40.0
$\delta(\text{deg})$	10.0	10.0	10.0	10.0	10.0	10.0	10.0	10.0	10.0
Re(+6)	2.13	2.15	2.16	2.16	2.15	2.15	2.16	2.16	2.14
Cp(1)	0.195	0.396	0.444	0.517	0.560	0.629	0.673	0.706
Cp(2)	0.027	-0.388	-1.067	-1.717	-2.085	-2.378	-0.850	-0.690	-0.652
Cp(3)	0.001	-0.291	-1.078	-2.093	-2.680	-2.546	-0.809	-0.698	-0.670
Cp(4)	-0.024	-0.230	-0.990	-2.571	-3.374	-2.883	-0.832	-0.676	-0.676
Cp(5)	-0.050	-0.200	-0.738	-1.267	-2.295	-3.148	-0.847	-0.701	-0.668
Cp(6)	-0.062	-0.173	-0.193	-0.234	-0.348	-1.900	-0.877	-0.701	-0.677
Cp(7)	-0.036	-0.137	-0.150	-0.335	-0.461	-0.761	-0.877	-0.704	-0.683
Cp(8)	-0.024	-0.131	-0.185	-0.373	-0.526	-0.652	-0.850	-0.698	-0.659
Cp(9)	0.025	0.204	0.367	0.356	0.386	0.401	0.449	0.487	0.514
Cp(10)	0.029	-0.626	-1.090	-1.346	-1.571	-1.701	-0.817	-0.698	-0.680
Cp(11)	0.000	-0.544	-1.829	-1.801	-1.968	-1.837	-0.823	-0.696	-0.692
Cp(12)	-0.029	-0.154	-1.266	-2.431	-2.254	-2.061	-0.795	-0.697	-0.695
Cp(13)	-0.061	-0.168	-0.222	-1.695	-2.281	-2.169	-0.803	-0.700	-0.678
Cp(14)	-0.100	-0.177	-0.165	-0.324	-1.346	-2.010	-0.818	-0.702	-0.697
Cp(15)	-0.045	-0.155	-0.194	-0.290	-0.769	-1.637	-0.790	-0.698	-0.698
Cp(16)	-0.058	-0.146	-0.193	-0.289	-0.480	-1.149	-0.792	-0.702	-0.686
Cp(17)	-0.064	-0.173	-0.217	-0.364	-0.498	-0.934	-0.808	-0.680	-0.689
Cp(18)	-0.056	-0.155	-0.202	-0.343	-0.465	-0.724	-0.818	-0.684	-0.684
Cp(19)	-0.047	-0.141	-0.166	-0.323	-0.444	-0.623	-0.815	-0.700	-0.693
Cp(20)	-0.044	-0.135	-0.154	-0.313	-0.438	-0.595	-0.801	-0.712	-0.691
Cp(21)	0.003	0.191	0.336	0.318	0.329	0.331	0.332	0.358	0.371
Cp(22)	0.008	-0.991	-0.840	-0.933	-1.085	-1.093	-0.772	-0.694	-0.696
Cp(23)	-0.016	-0.126	-0.924	-0.997	-1.141	-1.152	-0.776	-0.687	-0.694
Cp(24)	-0.038	-0.234	-1.123	-1.065	-1.188	-1.181	-0.787	-0.689	-0.702
Cp(25)	-0.090	-0.330	-1.250	-1.344	-1.307	-1.247	-0.785	-0.709	-0.702
Cp(26)	-0.084	-0.192	-0.607	-1.369	-1.368	-1.409	-0.768	-0.710	-0.697
Cp(27)	-0.072	-0.163	-0.193	-1.120	-1.309	-1.403	-0.787	-0.688	-0.714
Cp(28)	-0.061	-0.154	-0.072	-0.798	-1.191	-1.401	-0.790	-0.695	-0.718
Cp(29)	-0.071	-0.163	-0.093	-0.508	-1.036	-1.245	-0.797	-0.705	-0.701
Cp(30)	-0.053	-0.139	-0.090	-0.296	-0.864	-1.203	-0.801	-0.700	-0.705
Cp(31)	-0.064	-0.141	-0.111	-0.232	-0.696	-1.091	-0.776	-0.706	-0.713
Cp(32)	-0.055	-0.127	-0.107	-0.206	-0.529	-0.945	-0.806	-0.712	-0.711
Cp(33)	-0.070	-0.139	-0.130	-0.232	-0.455	-0.818	-0.793	-0.707	-0.713
Cp(34)	-0.057	-0.124	-0.119	-0.218	-0.391	-0.702	-0.786	-0.686	-0.710
Cp(35)	-0.019	0.160	0.291	0.242	0.246	0.234	0.220	0.229	0.239
Cp(36)	-0.007	-1.034	-0.457	-0.551	-0.622	-0.707	-0.679	-0.626	-0.641
Cp(37)	-0.046	-0.122	-0.512	-0.621	-0.684	-0.737	-0.680	-0.600	-0.643
Cp(38)	-0.082	-0.257	-0.559	-0.631	-0.707	-0.754	-0.701	-0.632	-0.650
Cp(39)	-0.129	-0.313	-0.600	-0.650	-0.714	-0.746	-0.705	-0.645	-0.631
Cp(40)	-0.098	-0.176	-0.777	-0.720	-0.778	-0.826	-0.717	-0.646	-0.652
Cp(41)	-0.089	-0.138	-0.756	-0.736	-0.813	-0.841	-0.723	-0.658	-0.666
Cp(42)	-0.105	-0.152	-0.618	-0.748	-0.834	-0.930	-0.731	-0.664	-0.676
Cp(43)	-0.093	-0.141	-0.355	-0.706	-0.822	-0.922	-0.720	-0.662	-0.661
Cp(44)	-0.105	-0.160	-0.150	-0.663	-0.814	-0.943	-0.743	-0.669	-0.671
Cp(45)	-0.111	-0.166	-0.048	-0.586	-0.762	-0.912	-0.747	-0.668	-0.661
Cp(46)	-0.127	-0.189	-0.031	-0.538	-0.756	-0.920	-0.749	-0.679	-0.667
Cp(47)	-0.136	-0.184	-0.060	-0.447	-0.694	-0.907	-0.741	-0.683	-0.667

Table 3 Continued.

$\alpha(\text{deg})$	0.0	5.0	10.0	15.0	20.0	25.0	30.0	35.0	40.0
$\delta(\text{deg})$	15.0	15.0	15.0	15.0	15.0	15.0	15.0	15.0	15.0
Re(+6)	2.01	2.00	2.00	2.00	2.00	2.00	2.00	2.00	2.00
Cp(1)	-0.037	0.160	0.288	0.410	0.504	0.564	0.596	0.666	0.707
Cp(2)	0.071	-0.187	-1.210	-1.580	-2.200	-2.490	-2.340	-0.885	-0.855
Cp(3)	0.024	-0.168	-0.983	-1.680	-2.690	-2.650	-2.370	-0.888	-0.852
Cp(4)	-0.017	-0.186	-0.710	-1.750	-3.290	-3.310	-2.620	-0.891	-0.871
Cp(5)	-0.083	-0.225	-0.498	-1.490	-1.950	-3.330	-2.410	-0.911	-0.879
Cp(6)	-0.053	-0.187	-0.312	-0.246	-0.296	-0.789	-2.590	-0.908	-0.845
Cp(7)
Cp(8)	-0.037	-0.161	-0.255	-0.353	-0.507	-0.653	-1.750	-0.870	-0.850
Cp(9)	-0.035	0.168	0.280	0.343	0.380	0.400	0.405	0.467	0.495
Cp(10)	0.066	-0.548	-1.160	-1.550	-1.750	-1.810	-1.920	-0.908	-0.857
Cp(11)	0.014	-0.249	-1.750	-2.260	-2.160	-1.960	-1.900	-0.872	-0.845
Cp(12)	-0.024	-0.184	-0.543	-2.430	-2.410	-2.300	-1.930	-0.876	-0.856
Cp(13)	-0.083	-0.249	-0.222	-1.100	-2.330	-2.410	-2.140	-0.883	-0.860
Cp(14)	-0.077	-0.214	-0.301	-0.287	-1.120	-2.010	-2.000	-0.878	-0.869
Cp(15)	-0.063	-0.185	-0.286	-0.323	-0.586	-1.540	-2.010	-0.854	-0.820
Cp(16)	-0.054	-0.161	-0.277	-0.321	-0.455	-1.070	-1.890	-0.902	-0.860
Cp(17)	-0.061	-0.169	-0.284	-0.345	-0.477	-0.795	-1.600	-0.901	-0.853
Cp(18)	-0.057	-0.159	-0.270	-0.318	-0.465	-0.674	-1.610	-0.862	-0.828
Cp(19)	-0.056	-0.153	-0.258	-0.312	-0.457	-0.632	-1.120	-0.864	-0.859
Cp(20)	-0.050	-0.141	-0.236	-0.293	-0.438	-0.605	-1.080	-0.900	-0.855
Cp(21)	-0.034	0.162	0.243	0.296	0.314	0.315	0.286	0.307	0.320
Cp(22)	0.044	-0.764	-0.943	-1.080	-1.120	-1.150	-1.320	-0.847	-0.842
Cp(23)	-0.001	-0.117	-1.090	-1.150	-1.180	-1.280	-1.280	-0.852	-0.852
Cp(24)	-0.037	-0.211	-1.090	-1.290	-1.270	-1.340	-1.350	-0.861	-0.840
Cp(25)	-0.114	-0.297	-0.981	-1.580	-1.390	-1.380	-1.410	-0.869	-0.826
Cp(26)	-0.098	-0.249	-0.479	-1.300	-1.440	-1.470	-1.510	-0.870	-0.849
Cp(27)	-0.074	-0.199	-0.229	-0.876	-1.370	-1.490	-1.560	-0.843	-0.843
Cp(28)	-0.090	-0.200	-0.226	-0.558	-1.310	-1.490	-1.570	-0.850	-0.858
Cp(29)	-0.081	-0.176	-0.217	-0.289	-1.020	-1.400	-1.540	-0.868	-0.858
Cp(30)	-0.073	-0.165	-0.211	-0.233	-0.845	-1.300	-1.530	-0.870	-0.866
Cp(31)	-0.084	-0.174	-0.220	-0.235	-0.645	-1.170	-1.490	-0.874	-0.857
Cp(32)
Cp(33)	-0.058	-0.126	-0.181	-0.214	-0.372	-0.752	-1.280	-0.857	-0.857
Cp(34)	-0.054	-0.121	-0.180	-0.216	-0.349	-0.670	-1.140	-0.865	-0.849
Cp(35)	-0.100	0.117	0.187	0.209	0.221	0.217	0.210	0.188	0.188
Cp(36)	0.025	-0.738	-0.634	-0.566	-0.648	-0.750	-0.888	-0.771	-0.785
Cp(37)	-0.034	-0.154	-0.709	-0.624	-0.721	-0.808	-0.859	-0.787	-0.790
Cp(38)	-0.083	-0.249	-0.706	-0.647	-0.718	-0.798	-0.905	-0.787	-0.803
Cp(39)	-0.140	-0.294	-0.639	-0.675	-0.788	-0.829	-0.915	-0.790	-0.811
Cp(40)
Cp(41)	-0.100	-0.190	-0.677	-0.765	-0.829	-0.905	-1.010	-0.789	-0.810
Cp(42)	-0.101	-0.177	-0.543	-0.729	-0.816	-0.905	-1.110	-0.816	-0.831
Cp(43)	-0.109	-0.175	-0.380	-0.722	-0.825	-0.981	-1.120	-0.826	-0.821
Cp(44)	-0.113	-0.166	-0.185	-0.628	-0.835	-0.962	-1.150	-0.799	-0.809
Cp(45)	-0.129	-0.181	-0.127	-0.559	-0.776	-0.962	-1.160	-0.821	-0.837
Cp(46)	-0.145	-0.193	-0.144	-0.494	-0.784	-0.967	-1.210	-0.823	-0.823
Cp(47)	-0.144	-0.196	-0.155	-0.342	-0.682	-0.889	-1.130	-0.823	-0.828

Table 3 Continued.

$\alpha(\text{deg})$	0.0	5.0	10.0	15.0	20.0	25.0	30.0	35.0	40.0
$\delta(\text{deg})$	20.0	20.0	20.0	20.0	20.0	20.0	20.0	20.0	20.0
Re(+6)	2.15	2.17	2.17	2.18	2.17	2.17	2.17	2.16	2.16
Cp(1)	-0.091	0.141	0.281	0.407	0.515	0.597	0.645	0.720	0.767
Cp(2)	0.114	-0.109	-0.910	-1.497	-1.989	-2.245	-1.899	-0.721	-0.665
Cp(3)	0.057	-0.124	-0.594	-1.542	-2.168	-2.442	-1.903	-0.727	-0.682
Cp(4)	0.009	-0.155	-0.453	-1.411	-2.524	-2.734	-1.704	-0.721	-0.662
Cp(5)	-0.065	-0.217	-0.384	-1.122	-2.415	-3.149	-1.916	-0.738	-0.671
Cp(6)	-0.071	-0.205	-0.372	-0.549	-0.346	-1.241	-2.303	-0.734	-0.678
Cp(7)	-0.038	-0.162	-0.279	-0.272	-0.283	-0.427	-1.981	-0.748	-0.674
Cp(8)	-0.025	-0.141	-0.229	-0.291	-0.383	-0.501	-1.636	-0.724	-0.666
Cp(9)	-0.171	0.156	0.281	0.352	0.405	0.439	0.467	0.530	0.572
Cp(10)	0.114	-0.150	-1.054	-1.573	-1.695	-1.683	-1.594	-0.729	-0.676
Cp(11)	0.054	-0.153	-1.457	-2.627	-1.912	-1.808	-1.544	-0.714	-0.683
Cp(12)	0.002	-0.190	-0.382	-1.893	-2.283	-2.049	-1.486	-0.717	-0.691
Cp(13)	-0.075	-0.259	-0.274	-0.489	-2.287	-2.231	-1.489	-0.720	-0.686
Cp(14)	-0.081	-0.229	-0.328	-0.355	-1.066	-1.949	-1.713	-0.731	-0.672
Cp(15)	-0.055	-0.179	-0.279	-0.374	-0.527	-1.586	-1.549	-0.715	-0.686
Cp(16)	-0.046	-0.152	-0.254	-0.379	-0.377	-1.053	-1.438	-0.747	-0.703
Cp(17)	-0.076	-0.182	-0.290	-0.392	-0.442	-0.803	-1.442	-0.735	-0.675
Cp(18)	-0.059	-0.157	-0.264	-0.367	-0.421	-0.632	-1.335	-0.717	-0.674
Cp(19)	-0.049	-0.142	-0.247	-0.333	-0.399	-0.562	-1.288	-0.731	-0.680
Cp(20)	-0.045	-0.135	-0.234	-0.306	-0.393	-0.543	-1.096	-0.715	-0.695
Cp(21)	-0.086	0.147	0.253	0.316	0.350	0.366	0.363	0.406	0.431
Cp(22)	0.093	-0.462	-1.012	-1.158	-1.081	-1.092	-1.181	-0.710	-0.680
Cp(23)	0.036	-0.140	-1.140	-1.252	-1.124	-1.178	-1.156	-0.700	-0.684
Cp(24)	-0.012	-0.196	-0.766	-1.416	-1.195	-1.186	-1.144	-0.715	-0.710
Cp(25)	-0.105	-0.317	-0.610	-1.623	-1.308	-1.270	-1.208	-0.711	-0.683
Cp(26)	-0.109	-0.260	-0.482	-1.160	-1.393	-1.380	-1.206	-0.719	-0.704
Cp(27)	-0.083	-0.216	-0.284	-0.599	-1.302	-1.347	-1.291	-0.711	-0.696
Cp(28)	-0.069	-0.177	-0.231	-0.277	-1.215	-1.321	-1.356	-0.706	-0.708
Cp(29)	-0.078	-0.175	-0.241	-0.214	-1.042	-1.263	-1.230	-0.711	-0.707
Cp(30)	-0.058	-0.150	-0.211	-0.197	-0.805	-1.188	-1.212	-0.715	-0.697
Cp(31)	-0.067	-0.152	-0.214	-0.224	-0.597	-1.052	-1.214	-0.713	-0.683
Cp(32)	-0.057	-0.137	-0.193	-0.223	-0.443	-0.884	-1.146	-0.721	-0.692
Cp(33)	-0.071	-0.145	-0.201	-0.246	-0.388	-0.752	-1.156	-0.731	-0.703
Cp(34)	-0.056	-0.129	-0.189	-0.239	-0.336	-0.631	-1.092	-0.706	-0.704
Cp(35)	-0.095	0.110	0.208	0.240	0.253	0.253	0.251	0.267	0.289
Cp(36)	0.081	-0.392	-0.770	-0.566	-0.614	-0.705	-0.787	-0.648	-0.630
Cp(37)	0.007	-0.154	-0.943	-0.611	-0.664	-0.735	-0.823	-0.636	-0.621
Cp(38)	-0.059	-0.235	-0.701	-0.643	-0.687	-0.736	-0.823	-0.657	-0.632
Cp(39)	-0.149	-0.328	-0.497	-0.676	-0.696	-0.759	-0.823	-0.654	-0.646
Cp(40)	-0.123	-0.248	-0.559	-0.759	-0.741	-0.799	-0.867	-0.664	-0.654
Cp(41)	-0.103	-0.204	-0.475	-0.761	-0.793	-0.834	-0.913	-0.663	-0.648
Cp(42)	-0.111	-0.191	-0.317	-0.732	-0.808	-0.876	-0.931	-0.679	-0.656
Cp(43)	-0.097	-0.171	-0.215	-0.669	-0.784	-0.866	-1.031	-0.672	-0.653
Cp(44)	-0.107	-0.169	-0.216	-0.599	-0.775	-0.898	-0.997	-0.669	-0.669
Cp(45)	-0.112	-0.166	-0.214	-0.461	-0.743	-0.865	-0.991	-0.672	-0.667
Cp(46)	-0.128	-0.177	-0.229	-0.372	-0.733	-0.871	-0.988	-0.687	-0.669
Cp(47)	-0.136	-0.183	-0.215	-0.308	-0.671	-0.842	-1.014	-0.671	-0.657

Table 3 Continued.

$\alpha(\text{deg})$	0.0	5.0	10.0	15.0	20.0	25.0	30.0	35.0	40.0
$\delta(\text{deg})$	25.0	25.0	25.0	25.0	25.0	25.0	25.0	25.0	25.0
Re(+6)	2.24	2.24	2.23	2.22	2.22	2.21	2.20	2.21	2.20
Cp(1)	-0.237	0.256	0.381	0.498	0.606	0.670	0.736	0.786
Cp(2)	0.163	-0.028	-0.317	-1.613	-1.889	-2.201	-2.153	-0.780	-0.660
Cp(3)	0.101	-0.079	-0.281	-1.383	-2.096	-2.401	-2.306	-0.800	-0.661
Cp(4)	0.041	-0.132	-0.300	-1.030	-1.987	-2.635	-2.311	-0.770	-0.679
Cp(5)	-0.056	-0.234	-0.368	-0.726	-1.686	-2.882	-2.304	-0.796	-0.699
Cp(6)	-0.102	-0.211	-0.372	-0.619	-0.907	-1.190	-2.328	-0.779	-0.678
Cp(7)	-0.034	-0.167	-0.321	-0.418	-0.390	-0.375	-1.913	-0.779	-0.672
Cp(8)	-0.023	-0.148	-0.260	-0.299	-0.326	-0.411	-1.160	-0.787	-0.684
Cp(9)	-0.544	0.123	0.267	0.351	0.407	0.460	0.491	0.557	0.606
Cp(10)	0.156	-0.065	-0.949	-1.602	-1.971	-1.748	-1.614	-0.754	-0.689
Cp(11)	0.088	-0.101	-0.905	-2.514	-2.793	-1.776	-1.662	-0.759	-0.691
Cp(12)	0.022	-0.167	-0.270	-1.248	-2.717	-1.901	-1.705	-0.798	-0.697
Cp(13)	-0.075	-0.280	-0.383	-0.287	-1.616	-2.087	-1.704	-0.774	-0.708
Cp(14)	-0.092	-0.255	-0.393	-0.432	-0.514	-1.941	-1.818	-0.788	-0.682
Cp(15)	-0.055	-0.182	-0.292	-0.379	-0.530	-1.567	-1.756	-0.772	-0.679
Cp(16)	-0.047	-0.151	-0.250	-0.361	-0.521	-1.045	-1.617	-0.767	-0.707
Cp(17)	-0.071	-0.175	-0.286	-0.391	-0.542	-0.807	-1.557	-0.779	-0.687
Cp(18)	-0.058	-0.158	-0.260	-0.372	-0.483	-0.616	-1.302	-0.779	-0.693
Cp(19)	-0.045	-0.137	-0.238	-0.359	-0.445	-0.561	-1.102	-0.764	-0.707
Cp(20)	-0.042	-0.132	-0.229	-0.340	-0.400	-0.535	-0.910	-0.792	-0.689
Cp(21)	-0.553	0.113	0.248	0.312	0.361	0.385	0.396	0.427	0.466
Cp(22)	0.135	-0.109	-1.396	-1.323	-1.223	-1.110	-1.145	-0.716	-0.700
Cp(23)	0.068	-0.151	-0.464	-1.449	-1.273	-1.135	-1.211	-0.728	-0.691
Cp(24)	0.010	-0.186	-0.331	-1.498	-1.348	-1.140	-1.203	-0.746	-0.703
Cp(25)	-0.107	-0.337	-0.519	-1.400	-1.565	-1.189	-1.236	-0.747	-0.699
Cp(26)	-0.114	-0.279	-0.483	-0.936	-1.488	-1.292	-1.331	-0.750	-0.711
Cp(27)	-0.090	-0.226	-0.352	-0.511	-1.256	-1.291	-1.316	-0.737	-0.698
Cp(28)	-0.073	-0.180	-0.287	-0.289	-0.958	-1.298	-1.343	-0.738	-0.689
Cp(29)	-0.080	-0.176	-0.271	-0.275	-0.641	-1.242	-1.331	-0.736	-0.700
Cp(30)	-0.059	-0.151	-0.233	-0.246	-0.462	-1.181	-1.296	-0.725	-0.697
Cp(31)	-0.068	-0.149	-0.227	-0.253	-0.400	-1.048	-1.242	-0.756	-0.697
Cp(32)	-0.057	-0.135	-0.208	-0.238	-0.363	-0.918	-1.212	-0.732	-0.700
Cp(33)	-0.072	-0.141	-0.206	-0.251	-0.374	-0.752	-1.144	-0.747	-0.706
Cp(34)	-0.060	-0.126	-0.192	-0.243	-0.356	-0.630	-1.028	-0.742	-0.708
Cp(35)	-0.395	0.073	0.201	0.247	0.262	0.267	0.275	0.286	0.314
Cp(36)	0.119	-0.099	-1.572	-0.683	-0.649	-0.706	-0.812	-0.663	-0.629
Cp(37)	0.036	-0.161	-0.201	-0.694	-0.696	-0.737	-0.830	-0.670	-0.634
Cp(38)	-0.040	-0.227	-0.369	-0.727	-0.713	-0.738	-0.843	-0.671	-0.648
Cp(39)	-0.157	-0.359	-0.492	-0.763	-0.739	-0.748	-0.862	-0.679	-0.642
Cp(40)	-0.138	-0.270	-0.472	-0.879	-0.780	-0.797	-0.893	-0.688	-0.642
Cp(41)	-0.111	-0.211	-0.354	-0.932	-0.823	-0.813	-0.923	-0.678	-0.647
Cp(42)	-0.119	-0.195	-0.275	-0.896	-0.834	-0.859	-0.949	-0.696	-0.660
Cp(43)	-0.100	-0.171	-0.218	-0.707	-0.780	-0.862	-0.967	-0.693	-0.650
Cp(44)	-0.111	-0.167	-0.219	-0.461	-0.773	-0.862	-1.001	-0.695	-0.651
Cp(45)	-0.115	-0.163	-0.222	-0.232	-0.705	-0.842	-0.994	-0.699	-0.662
Cp(46)	-0.131	-0.170	-0.230	-0.146	-0.671	-0.857	-1.005	-0.696	-0.655
Cp(47)	-0.139	-0.172	-0.231	-0.148	-0.584	-0.835	-1.010	-0.694	-0.676

Table 3 Continued.

$\alpha(\text{deg})$	0.0	5.0	10.0	15.0	20.0	25.0	30.0	35.0	40.0
$\delta(\text{deg})$	30.0	30.0	30.0	30.0	30.0	30.0	30.0	30.0	30.0
Re(+6)	2.21	2.24	2.23	2.24	2.23	2.22	2.22	2.22	2.21
Cp(1)	0.068	0.190	0.389	0.423	0.532	0.683	0.727	0.736
Cp(2)	0.163	0.056	-0.247	-1.377	-1.884	-2.115	-2.266	-0.786	-0.688
Cp(3)	0.076	-0.040	-0.276	-0.789	-1.935	-2.351	-2.225	-0.784	-0.696
Cp(4)	0.071	-0.084	-0.292	-0.554	-1.700	-2.499	-2.095	-0.839	-0.676
Cp(5)	-0.048	-0.204	-0.423	-0.499	-1.241	-2.376	-2.292	-0.810	-0.682
Cp(6)	-0.083	-0.218	-0.381	-0.524	-0.830	-1.226	-2.460	-0.789	-0.701
Cp(7)	-0.036	-0.156	-0.321	-0.465	-0.473	-0.430	-1.440	-0.803	-0.675
Cp(8)	-0.046	-0.118	-0.290	-0.342	-0.357	-0.408	-0.774	-0.786	-0.676
Cp(9)	-0.340	0.083	0.250	0.323	0.355	0.474	0.513	0.601	0.561
Cp(10)	0.180	-0.012	-0.932	-1.419	-2.117	-1.765	-1.588	-0.768	-0.716
Cp(11)	0.078	-0.067	-0.354	-2.131	-3.108	-1.738	-1.654	-0.793	-0.692
Cp(12)	0.013	-0.170	-0.311	-0.655	-2.420	-1.902	-1.630	-0.821	-0.690
Cp(13)	-0.063	-0.239	-0.449	-0.342	-0.889	-2.024	-1.689	-0.804	-0.701
Cp(14)	-0.166	-0.348	-0.582	-0.601	-0.525	-1.634	-1.768	-0.817	-0.696
Cp(15)	-0.084	-0.148	-0.304	-0.380	-0.471	-1.300	-1.777	-0.796	-0.672
Cp(16)	-0.076	-0.125	-0.262	-0.319	-0.477	-0.967	-1.620	-0.779	-0.717
Cp(17)	-0.128	-0.182	-0.335	-0.373	-0.514	-0.824	-1.518	-0.786	-0.689
Cp(18)	-0.061	-0.133	-0.262	-0.347	-0.524	-0.639	-1.232	-0.782	-0.674
Cp(19)	-0.048	-0.113	-0.235	-0.328	-0.467	-0.548	-1.022	-0.746	-0.688
Cp(20)	-0.044	-0.125	-0.226	-0.317	-0.435	-0.505	-0.786	-0.747	-0.701
Cp(21)	-0.261	0.070	0.231	0.333	0.362	0.392	0.358	0.415	0.433
Cp(22)	0.124	-0.023	-0.863	-1.253	-1.286	-1.074	-1.179	-0.727	-0.674
Cp(23)	0.095	-0.095	-0.740	-1.314	-1.292	-1.169	-1.262	-0.738	-0.675
Cp(24)	0.033	-0.145	-0.287	-1.347	-1.396	-1.142	-1.199	-0.748	-0.703
Cp(25)	-0.120	-0.296	-0.527	-1.270	-1.469	-1.133	-1.209	-0.761	-0.705
Cp(26)	-0.139	-0.378	-0.464	-0.754	-1.427	-1.213	-1.294	-0.758	-0.695
Cp(27)	-0.097	-0.200	-0.366	-0.440	-1.125	-1.226	-1.311	-0.740	-0.697
Cp(28)	-0.100	-0.173	-0.311	-0.302	-0.771	-1.172	-1.356	-0.750	-0.714
Cp(29)	-0.107	-0.164	-0.308	-0.287	-0.489	-1.121	-1.362	-0.761	-0.688
Cp(30)	-0.087	-0.120	-0.264	-0.258	-0.373	-1.068	-1.316	-0.750	-0.701
Cp(31)	-0.115	-0.140	-0.290	-0.247	-0.356	-1.009	-1.269	-0.739	-0.715
Cp(32)	-0.059	-0.105	-0.230	-0.233	-0.366	-0.914	-1.140	-0.737	-0.684
Cp(33)	-0.073	-0.116	-0.222	-0.252	-0.346	-0.777	-1.109	-0.725	-0.689
Cp(34)	-0.059	-0.117	-0.185	-0.233	-0.341	-0.659	-1.003	-0.735	-0.710
Cp(35)	-0.286	0.026	0.182	0.263	0.260	0.274	0.244	0.277	0.285
Cp(36)	0.108	-0.019	-1.082	-0.732	-0.676	-0.692	-0.779	-0.673	-0.608
Cp(37)	0.061	-0.107	-0.186	-0.732	-0.674	-0.742	-0.816	-0.664	-0.629
Cp(38)	-0.025	-0.189	-0.368	-0.724	-0.700	-0.682	-0.810	-0.678	-0.653
Cp(39)	-0.182	-0.338	-0.527	-0.775	-0.711	-0.721	-0.831	-0.662	-0.654
Cp(40)	-0.176	-0.303	-0.441	-0.857	-0.749	-0.768	-0.848	-0.679	-0.661
Cp(41)	-0.123	-0.193	-0.374	-0.911	-0.781	-0.815	-0.915	-0.660	-0.658
Cp(42)	-0.149	-0.179	-0.320	-0.860	-0.813	-0.787	-0.945	-0.690	-0.654
Cp(43)	-0.134	-0.154	-0.274	-0.655	-0.762	-0.798	-0.966	-0.696	-0.636
Cp(44)	-0.136	-0.134	-0.266	-0.411	-0.733	-0.802	-0.998	-0.674	-0.657
Cp(45)	-0.174	-0.149	-0.262	-0.185	-0.668	-0.815	-0.958	-0.689	-0.629
Cp(46)	-0.135	-0.142	-0.226	-0.136	-0.669	-0.828	-0.951	-0.693	-0.651
Cp(47)	-0.144	-0.145	-0.221	-0.154	-0.563	-0.790	-0.907	-0.679	-0.650

Table 3 Continued.

$\alpha(\text{deg})$	0.0	5.0	10.0	15.0	20.0	25.0	30.0	35.0	40.0
$\delta(\text{deg})$	35.0	35.0	35.0	35.0	35.0	35.0	35.0	35.0	35.0
Re(+6)	2.25	2.24	2.23	2.23	2.24	2.24	2.22	2.23	2.23
Cp(1)	-0.549	-0.028	0.200	0.293	0.437	0.545	0.623	0.759	0.825
Cp(2)	0.162	0.020	-0.166	-0.473	-1.900	-2.375	-2.123	-1.135	-0.728
Cp(3)	0.161	-0.010	-0.182	-0.443	-1.742	-2.642	-2.257	-1.099	-0.718
Cp(4)	0.058	-0.086	-0.265	-0.428	-1.340	-2.327	-2.340	-1.093	-0.696
Cp(5)	-0.038	-0.243	-0.419	-0.529	-0.910	-1.780	-2.568	-1.173	-0.673
Cp(6)	-0.085	-0.205	-0.366	-0.561	-0.778	-1.087	-2.253	-1.035	-0.667
Cp(7)	-0.064	-0.189	-0.309	-0.518	-0.614	-0.573	-1.065	-1.070	-0.696
Cp(8)	-0.047	-0.143	-0.267	-0.413	-0.382	-0.414	-0.626	-1.011	-0.697
Cp(9)	-0.356	0.052	0.269	0.317	0.444	0.479	0.468	0.591	0.606
Cp(10)	0.164	0.011	-0.562	-1.291	-2.061	-2.075	-1.755	-0.917	-0.699
Cp(11)	0.105	-0.059	-0.232	-1.694	-3.179	-2.421	-1.648	-0.921	-0.701
Cp(12)	-0.032	-0.119	-0.310	-0.556	-2.101	-2.359	-1.649	-0.986	-0.680
Cp(13)	-0.096	-0.270	-0.432	-0.436	-0.480	-2.256	-1.735	-1.017	-0.737
Cp(14)	-0.201	-0.550	-0.792	-0.898	-0.674	-0.980	-1.889	-1.018	-0.726
Cp(15)	-0.061	-0.193	-0.272	-0.397	-0.484	-0.832	-1.794	-0.992	-0.721
Cp(16)	-0.055	-0.218	-0.254	-0.349	-0.437	-0.777	-1.569	-1.054	-0.729
Cp(17)	-0.092	-0.186	-0.265	-0.436	-0.476	-0.770	-1.498	-0.942	-0.728
Cp(18)	-0.089	-0.155	-0.252	-0.367	-0.453	-0.689	-1.173	-0.926	-0.690
Cp(19)	-0.050	-0.147	-0.228	-0.340	-0.445	-0.640	-0.936	-0.950	-0.669
Cp(20)	-0.046	-0.138	-0.217	-0.333	-0.424	-0.544	-0.786	-0.954	-0.675
Cp(21)	-0.270	0.014	0.170	0.298	0.334	0.351	0.432	0.393	0.445
Cp(22)	0.136	-0.008	-1.059	-1.531	-1.396	-1.188	-1.250	-0.882	-0.690
Cp(23)	0.107	-0.068	-0.167	-1.555	-1.441	-1.255	-1.206	-0.902	-0.725
Cp(24)	0.017	-0.160	-0.316	-0.739	-1.489	-1.199	-1.167	-0.871	-0.699
Cp(25)	-0.122	-0.319	-0.526	-0.675	-1.589	-1.261	-1.206	-0.866	-0.701
Cp(26)	-0.164	-0.342	-0.516	-0.714	-1.394	-1.315	-1.300	-0.872	-0.692
Cp(27)	-0.146	-0.236	-0.411	-0.586	-1.015	-1.303	-1.326	-0.879	-0.731
Cp(28)	-0.088	-0.225	-0.342	-0.452	-0.589	-1.234	-1.379	-0.941	-0.701
Cp(29)	-0.088	-0.247	-0.429	-0.396	-0.392	-1.198	-1.292	-0.906	-0.714
Cp(30)	-0.067	-0.210	-0.258	-0.355	-0.305	-1.057	-1.275	-0.963	-0.725
Cp(31)	-0.071	-0.149	-0.203	-0.355	-0.302	-0.897	-1.235	-0.909	-0.707
Cp(32)	-0.085	-0.135	-0.199	-0.317	-0.302	-0.720	-1.175	-0.897	-0.701
Cp(33)	-0.076	-0.150	-0.204	-0.289	-0.312	-0.600	-1.115	-0.872	-0.682
Cp(34)	-0.056	-0.124	-0.169	-0.235	-0.299	-0.540	-0.935	-0.857	-0.678
Cp(35)	-0.249	-0.038	0.124	0.227	0.212	0.234	0.298	0.251	0.290
Cp(36)	0.132	0.012	-0.716	-0.743	-0.655	-0.693	-0.800	-0.734	-0.612
Cp(37)	0.085	-0.068	-0.265	-0.730	-0.675	-0.749	-0.809	-0.708	-0.605
Cp(38)	-0.033	-0.186	-0.348	-0.754	-0.711	-0.739	-0.781	-0.745	-0.633
Cp(39)	-0.177	-0.353	-0.534	-0.812	-0.730	-0.726	-0.783	-0.757	-0.641
Cp(40)	-0.177	-0.413	-0.444	-0.774	-0.747	-0.788	-0.861	-0.752	-0.634
Cp(41)	-0.166	-0.264	-0.344	-0.705	-0.730	-0.826	-0.887	-0.783	-0.664
Cp(42)	-0.149	-0.224	-0.312	-0.538	-0.714	-0.826	-0.940	-0.808	-0.670
Cp(43)	-0.113	-0.198	-0.289	-0.372	-0.720	-0.815	-0.924	-0.784	-0.671
Cp(44)	-0.164	-0.210	-0.249	-0.302	-0.697	-0.844	-0.928	-0.815	-0.673
Cp(45)	-0.117	-0.162	-0.182	-0.313	-0.646	-0.779	-0.925	-0.799	-0.675
Cp(46)	-0.157	-0.172	-0.201	-0.290	-0.591	-0.773	-0.955	-0.780	-0.654
Cp(47)	-0.139	-0.177	-0.207	-0.283	-0.493	-0.745	-0.962	-0.749	-0.633

Table 3 Continued.

$\alpha(\text{deg})$	0.0	5.0	10.0	15.0	20.0	25.0	30.0	35.0	40.0
$\delta(\text{deg})$	40.0	40.0	40.0	40.0	40.0	40.0	40.0	40.0	40.0
Re(+6)	2.17	2.17	2.16	2.17	2.17	2.18	2.17	2.16	2.18
Cp(1)	-0.831	-0.075	0.186	0.329	0.452	0.568	0.682	0.758	0.817
Cp(2)	0.272	0.119	-0.089	-0.351	-2.439	-2.521	-2.380	-1.650	-0.734
Cp(3)	0.209	0.037	-0.160	-0.337	-1.166	-2.696	-2.595	-1.687	-0.721
Cp(4)	0.138	-0.047	-0.242	-0.397	-0.766	-2.085	-2.545	-1.687	-0.743
Cp(5)	0.013	-0.199	-0.412	-0.571	-0.693	-1.358	-2.166	-1.876	-0.728
Cp(6)	-0.038	-0.349	-0.486	-0.607	-0.814	-1.082	-2.119	-1.737	-0.725
Cp(7)	-0.026	-0.163	-0.322	-0.537	-0.796	-0.836	-1.149	-1.689	-0.747
Cp(8)	-0.015	-0.153	-0.306	-0.483	-0.539	-0.535	-0.619	-1.478	-0.752
Cp(9)	-0.426	-0.128	0.218	0.330	0.411	0.480	0.547	0.592	0.652
Cp(10)	0.237	0.094	-0.169	-1.182	-1.866	-2.296	-1.623	-1.368	-0.733
Cp(11)	0.177	0.008	-0.210	-1.229	-2.996	-2.896	-1.587	-1.297	-0.733
Cp(12)	0.099	-0.085	-0.304	-0.436	-1.370	-2.763	-1.700	-1.314	-0.730
Cp(13)	-0.021	-0.233	-0.463	-0.480	-0.394	-2.161	-1.803	-1.358	-0.721
Cp(14)	-0.304	-0.660	-0.989	-1.128	-0.986	-0.870	-1.738	-1.352	-0.722
Cp(15)	-0.048	-0.161	-0.348	-0.606	-0.769	-0.743	-1.683	-1.457	-0.725
Cp(16)	-0.055	-0.177	-0.309	-0.437	-0.557	-0.708	-1.516	-1.357	-0.732
Cp(17)	-0.103	-0.235	-0.370	-0.496	-0.572	-0.728	-1.449	-1.277	-0.724
Cp(18)	-0.062	-0.186	-0.310	-0.401	-0.549	-0.698	-1.174	-1.329	-0.709
Cp(19)	-0.046	-0.146	-0.239	-0.341	-0.518	-0.687	-0.943	-1.184	-0.719
Cp(20)	-0.043	-0.139	-0.228	-0.324	-0.490	-0.638	-0.727	-1.218	-0.736
Cp(21)	-0.266	0.036	0.202	0.293	0.360	0.407	0.438	0.469	0.517
Cp(22)	0.209	0.062	-0.523	-1.427	-1.510	-1.451	-1.173	-1.084	-0.714
Cp(23)	0.144	-0.016	-0.192	-1.286	-1.571	-1.459	-1.187	-1.085	-0.717
Cp(24)	0.083	-0.092	-0.291	-0.354	-1.663	-1.435	-1.158	-1.115	-0.716
Cp(25)	-0.067	-0.258	-0.487	-0.669	-1.598	-1.464	-1.199	-1.120	-0.713
Cp(26)	-0.210	-0.554	-0.705	-0.757	-1.381	-1.462	-1.216	-1.151	-0.715
Cp(27)	-0.122	-0.453	-0.654	-0.620	-1.090	-1.396	-1.244	-1.176	-0.695
Cp(28)	-0.132	-0.339	-0.567	-0.579	-0.715	-1.333	-1.217	-1.154	-0.718
Cp(29)	-0.083	-0.256	-0.527	-0.593	-0.500	-1.221	-1.205	-1.132	-0.718
Cp(30)	-0.060	-0.138	-0.371	-0.543	-0.417	-1.009	-1.227	-1.124	-0.712
Cp(31)	-0.067	-0.141	-0.238	-0.457	-0.396	-0.784	-1.192	-1.128	-0.719
Cp(32)	-0.056	-0.127	-0.181	-0.322	-0.375	-0.652	-1.134	-1.123	-0.740
Cp(33)	-0.075	-0.144	-0.197	-0.261	-0.362	-0.568	-1.071	-1.060	-0.724
Cp(34)	-0.057	-0.127	-0.188	-0.243	-0.338	-0.527	-0.974	-1.057	-0.712
Cp(35)	-0.205	-0.033	0.135	0.224	0.263	0.282	0.297	0.314	0.350
Cp(36)	0.190	0.075	-0.347	-1.218	-0.826	-0.743	-0.822	-0.822	-0.635
Cp(37)	0.105	-0.016	-0.192	-1.143	-0.877	-0.752	-0.835	-0.827	-0.647
Cp(38)	0.013	-0.110	-0.287	-0.319	-0.951	-0.773	-0.845	-0.846	-0.651
Cp(39)	-0.154	-0.266	-0.444	-0.580	-0.897	-0.793	-0.868	-0.846	-0.666
Cp(40)	-0.200	-0.456	-0.489	-0.580	-0.725	-0.829	-0.869	-0.858	-0.654
Cp(41)	-0.154	-0.377	-0.557	-0.606	-0.772	-0.850	-0.888	-0.877	-0.658
Cp(42)	-0.154	-0.402	-0.529	-0.551	-0.787	-0.871	-0.904	-0.890	-0.669
Cp(43)	-0.128	-0.302	-0.491	-0.437	-0.753	-0.846	-0.906	-0.925	-0.658
Cp(44)	-0.128	-0.212	-0.445	-0.355	-0.710	-0.838	-0.921	-0.909	-0.668
Cp(45)	-0.125	-0.138	-0.320	-0.303	-0.614	-0.814	-0.928	-0.929	-0.675
Cp(46)	-0.143	-0.154	-0.254	-0.302	-0.521	-0.792	-0.928	-0.951	-0.674
Cp(47)	-0.153	-0.178	-0.241	-0.309	-0.412	-0.762	-0.922	-0.964	-0.676

Table 3 Concluded.

$\alpha(\text{deg})$	0.0	5.0	10.0	15.0	20.0	25.0	30.0	35.0	40.0
$\delta(\text{deg})$	45.0	45.0	45.0	45.0	45.0	45.0	45.0	45.0	45.0
Re(+6)	2.01	2.01	2.01	2.01	2.01	2.01	2.02	2.02	2.02
Cp(1)	-0.741	-0.279	0.125	0.295	0.421	0.532	0.641	0.744	0.783
Cp(2)	0.272	0.137	-0.047	-0.312	-0.585	-2.830	-2.750	-2.260	-0.980
Cp(3)	0.213	0.046	-0.138	-0.340	-0.481	-2.440	-3.120	-2.490	-0.992
Cp(4)	0.141	-0.049	-0.237	-0.428	-0.527	-1.610	-2.600	-2.510	-1.010
Cp(5)	-0.005	-0.254	-0.473	-0.672	-0.724	-1.020	-1.770	-2.360	-1.010
Cp(6)	-0.062	-0.244	-0.418	-0.599	-0.789	-1.120	-1.480	-2.740	-1.010
Cp(7)
Cp(8)	-0.030	-0.168	-0.324	-0.534	-0.622	-0.667	-0.742	-1.130	-1.040
Cp(9)	-0.435	-0.284	0.179	0.304	0.388	0.457	0.521	0.584	0.619
Cp(10)	0.232	0.119	-0.104	-1.150	-1.760	-2.310	-1.960	-1.850	-0.958
Cp(11)	0.177	0.030	-0.172	-0.543	-2.390	-3.360	-2.020	-1.760	-0.975
Cp(12)	0.108	-0.058	-0.264	-0.431	-1.030	-2.720	-2.040	-1.810	-0.953
Cp(13)	-0.007	-0.202	-0.429	-0.590	-0.465	-0.909	-2.180	-1.860	-0.963
Cp(14)	-0.334	-0.750	-1.140	-1.330	-1.280	-1.060	-1.950	-1.940	-0.948
Cp(15)	-0.065	-0.170	-0.346	-0.605	-0.759	-0.892	-1.600	-1.810	-0.956
Cp(16)	-0.073	-0.181	-0.336	-0.499	-0.584	-0.708	-1.320	-1.910	-0.984
Cp(17)	-0.085	-0.195	-0.318	-0.453	-0.571	-0.710	-1.150	-1.700	-0.983
Cp(18)	-0.063	-0.176	-0.286	-0.406	-0.558	-0.709	-1.080	-1.560	-0.961
Cp(19)	-0.062	-0.165	-0.259	-0.367	-0.521	-0.735	-1.020	-1.450	-0.948
Cp(20)	-0.053	-0.155	-0.248	-0.348	-0.500	-0.672	-0.876	-1.160	-0.920
Cp(21)	-0.203	-0.132	0.171	0.269	0.326	0.381	0.426	0.448	0.466
Cp(22)	0.320	0.242	0.107	-1.170	-1.560	-1.350	-0.990	-1.050	-0.803
Cp(23)	0.147	0.006	-0.212	-0.617	-1.910	-1.560	-1.160	-1.360	-0.896
Cp(24)	0.087	-0.078	-0.274	-0.363	-1.670	-1.560	-1.180	-1.380	-0.959
Cp(25)	-0.058	-0.254	-0.468	-0.656	-0.993	-1.600	-1.240	-1.370	-0.919
Cp(26)	-0.268	-0.544	-0.713	-0.794	-0.957	-1.570	-1.230	-1.450	-0.959
Cp(27)	-0.227	-0.544	-0.769	-0.806	-0.954	-1.510	-1.210	-1.450	-0.913
Cp(28)	-0.165	-0.396	-0.780	-0.859	-0.830	-1.410	-1.270	-1.570	-0.929
Cp(29)	-0.091	-0.258	-0.627	-0.843	-0.682	-1.090	-1.230	-1.470	-0.890
Cp(30)	-0.087	-0.183	-0.411	-0.727	-0.610	-0.853	-1.180	-1.430	-0.909
Cp(31)	-0.096	-0.179	-0.231	-0.465	-0.579	-0.669	-1.190	-1.460	-0.937
Cp(32)
Cp(33)	-0.057	-0.116	-0.162	-0.218	-0.371	-0.498	-0.942	-1.250	-0.938
Cp(34)	-0.056	-0.117	-0.170	-0.225	-0.340	-0.477	-0.911	-1.270	-0.936
Cp(35)	-0.218	-0.162	0.087	0.183	0.226	0.248	0.260	0.293	0.288
Cp(36)	0.189	0.087	-0.111	-1.240	-0.924	-0.733	-0.799	-0.948	-0.778
Cp(37)	0.107	-0.005	-0.174	-0.345	-0.925	-0.755	-0.828	-0.986	-0.810
Cp(38)	0.019	-0.105	-0.256	-0.372	-0.909	-0.773	-0.809	-0.976	-0.834
Cp(39)	-0.128	-0.272	-0.392	-0.581	-0.884	-0.792	-0.833	-0.957	-0.814
Cp(40)
Cp(41)	-0.297	-0.371	-0.502	-0.589	-0.963	-0.855	-0.841	-0.997	-0.811
Cp(42)	-0.194	-0.443	-0.517	-0.580	-0.921	-0.856	-0.831	-1.070	-0.850
Cp(43)	-0.146	-0.396	-0.585	-0.570	-0.820	-0.842	-0.853	-1.100	-0.822
Cp(44)	-0.120	-0.172	-0.533	-0.477	-0.670	-0.841	-0.849	-1.090	-0.821
Cp(45)	-0.145	-0.167	-0.433	-0.446	-0.567	-0.816	-0.864	-1.110	-0.837
Cp(46)	-0.169	-0.196	-0.356	-0.453	-0.514	-0.835	-0.868	-1.170	-0.827
Cp(47)	-0.169	-0.197	-0.287	-0.421	-0.451	-0.763	-0.876	-1.150	-0.841

Table 4 Effect of various parameters in computation.

The baseline parameters are, NW=7, NF=3, AFACT=1.25, $\Delta t_c=0.07$, FEDG=0.03, FVEND=1.2, and at $\alpha=10^\circ$ with $\delta=0^\circ$

TESTED PARAMETER	ITERATION STEPS	CPU TIME* (sec)	C_L	C_D	C_M
NW=6, NF=2	12	28.44	0.644	0.114	-0.017
NW=7, NF=3	10	41.84	0.659	0.116	-0.015
NW=9, NF=4	12	100.60	0.679	0.120	-0.013
NF=2	12	42.02	0.642	0.113	-0.019
NW=3	10	41.84	0.659	0.116	-0.015
NW=4	12	59.74	0.662	0.117	-0.016
NW=5	11	63.94	0.664	0.117	-0.018
AFACT=0.50	11	46.22	0.658	0.116	-0.016
AFACT=1.00	10	41.83	0.659	0.116	-0.015
AFACT=1.25	10	41.84	0.659	0.116	-0.015
AFACT=1.50	11	46.24	0.659	0.116	-0.015
$\Delta t = 0.05$	15	92.01	0.676	0.119	-0.009
$\Delta t = 0.07$	10	41.84	0.659	0.116	-0.015
$\Delta t = 0.09$	10	33.83	0.668	0.118	-0.015
FEDG=0.02	28	117.91	0.603	0.106	-0.025
FEDG=0.03	10	41.84	0.659	0.116	-0.015
FEDG=0.04	10	42.20	0.703	0.124	-0.018
FVEND=1.20	10	41.84	0.659	0.116	-0.015
FVEND=1.60	14	129.57	0.660	0.116	-0.015
FVEND=2.00	17	268.60	0.660	0.116	-0.015

* : IBM 3084, compiled with optimization level 3

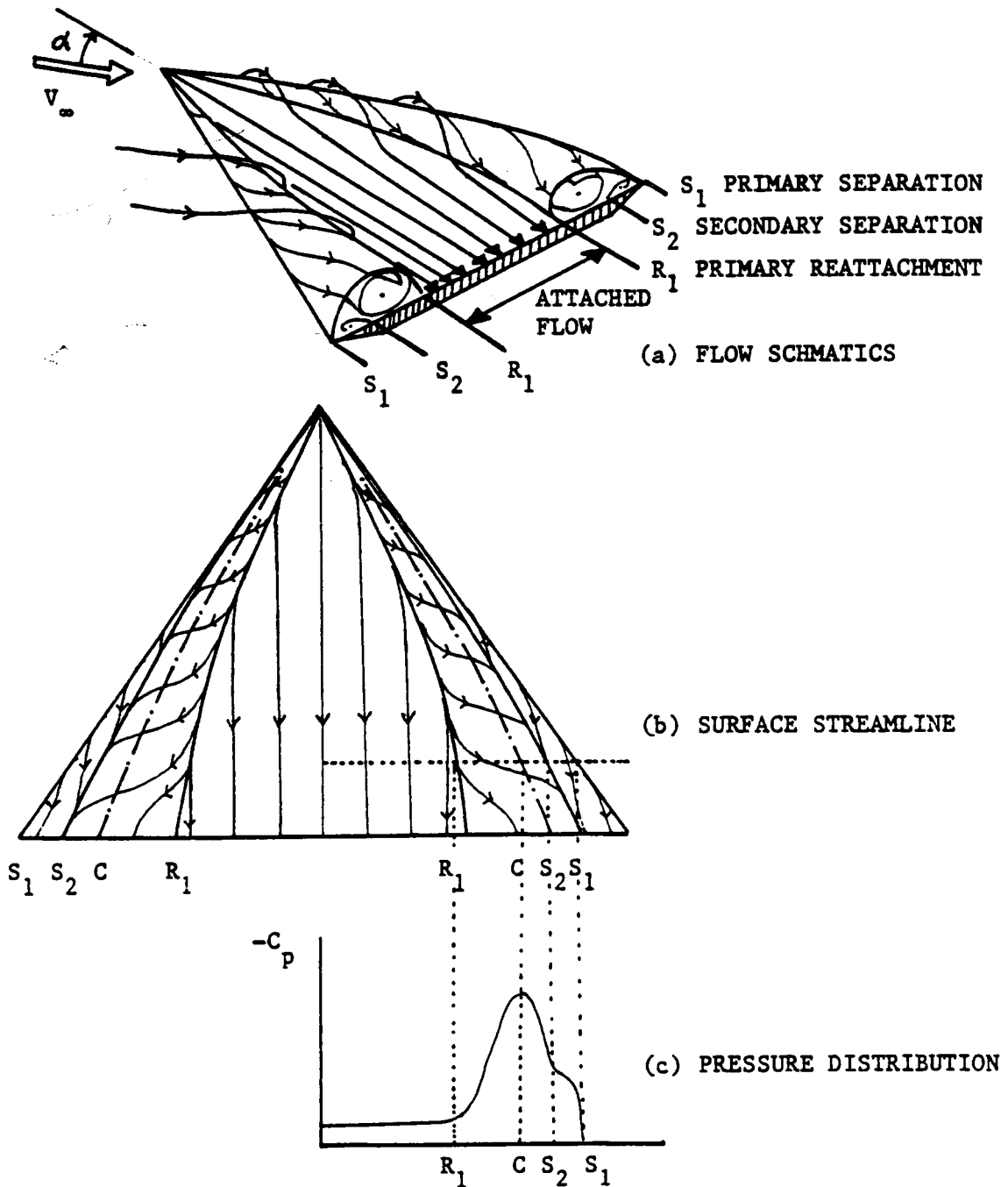


Fig. 1. Sketch of flow field over a delta wing

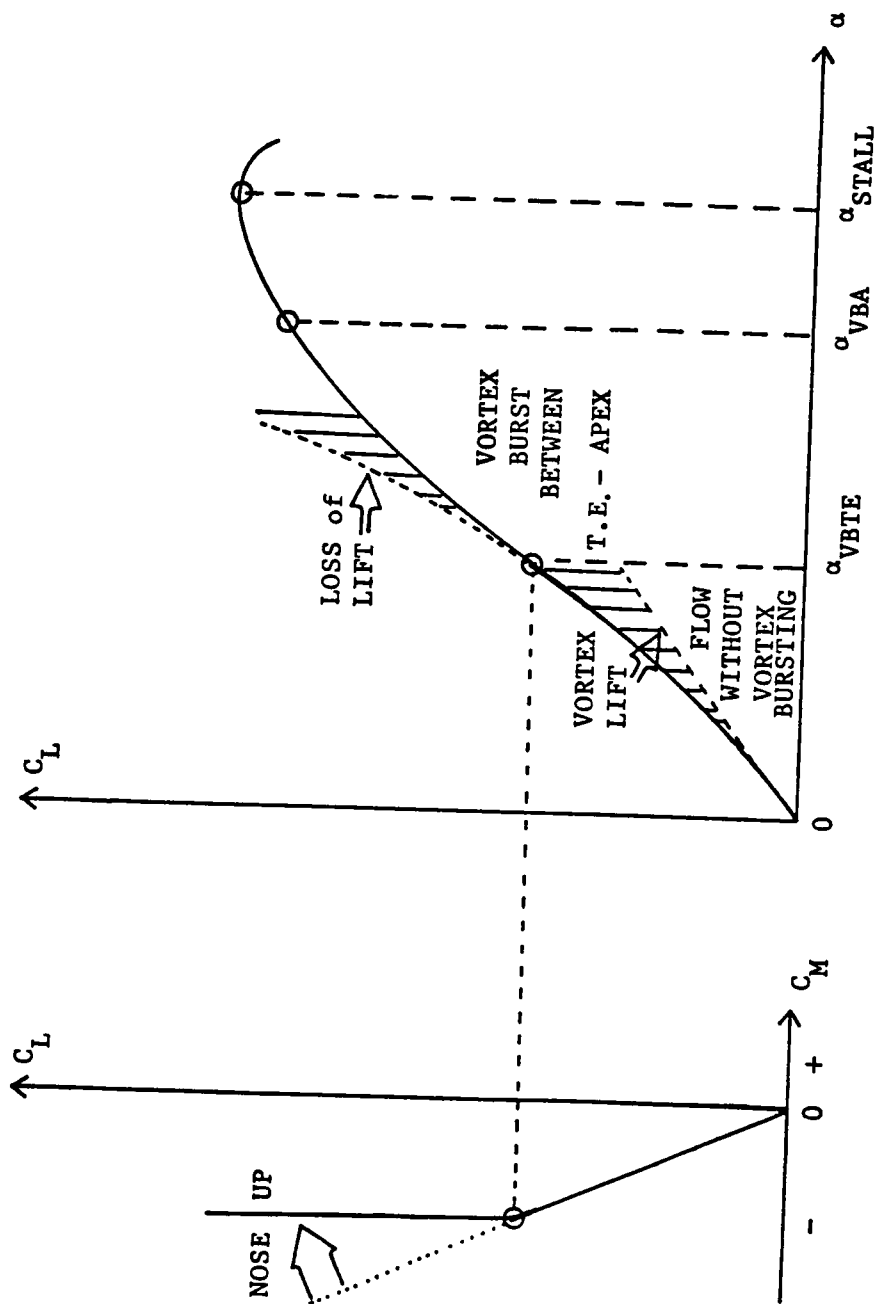
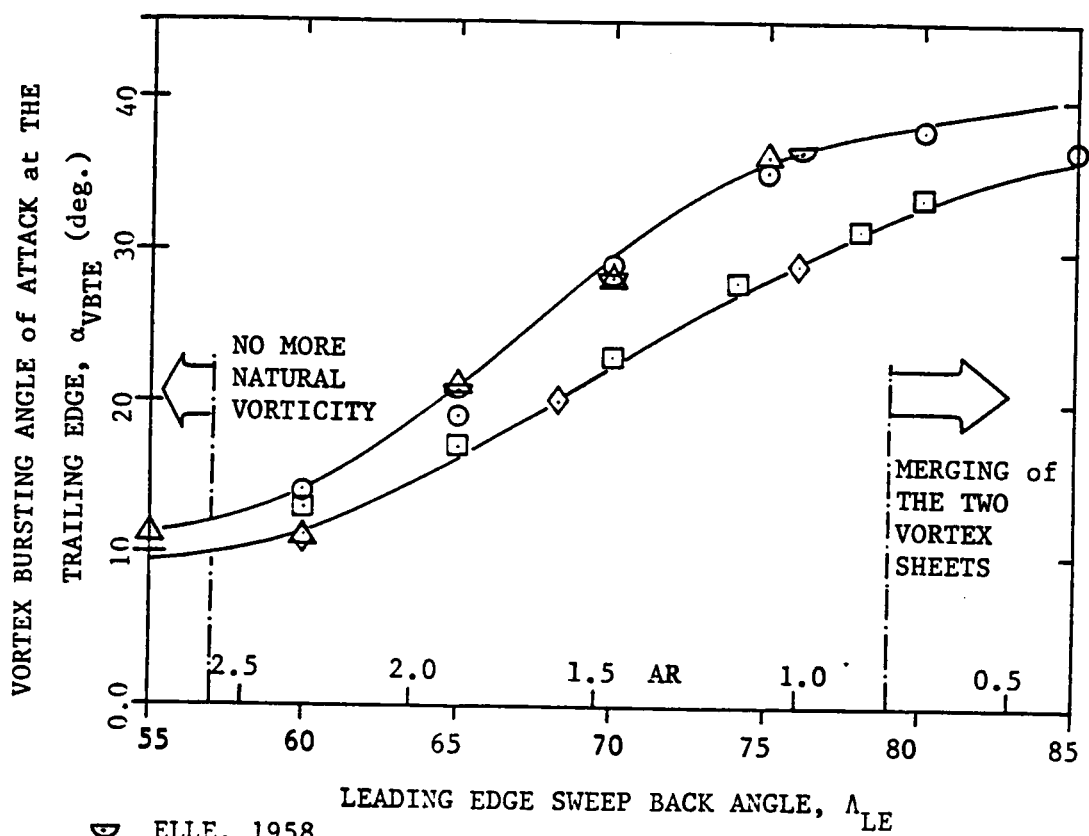


Fig. 2. Effect of vortex on aerodynamic loads



● ELLE, 1958

△ EARNSHAW and LAWFORD, 1964

○ WENTZ and KOHLMAN, 1968

◇ HUMMEL and SRINIVASAN, 1967

□ ERICKSON, 1982

Fig. 3. Effect of leading edge sweep angle on vortex bursting angle of attack, α_{VBTE}

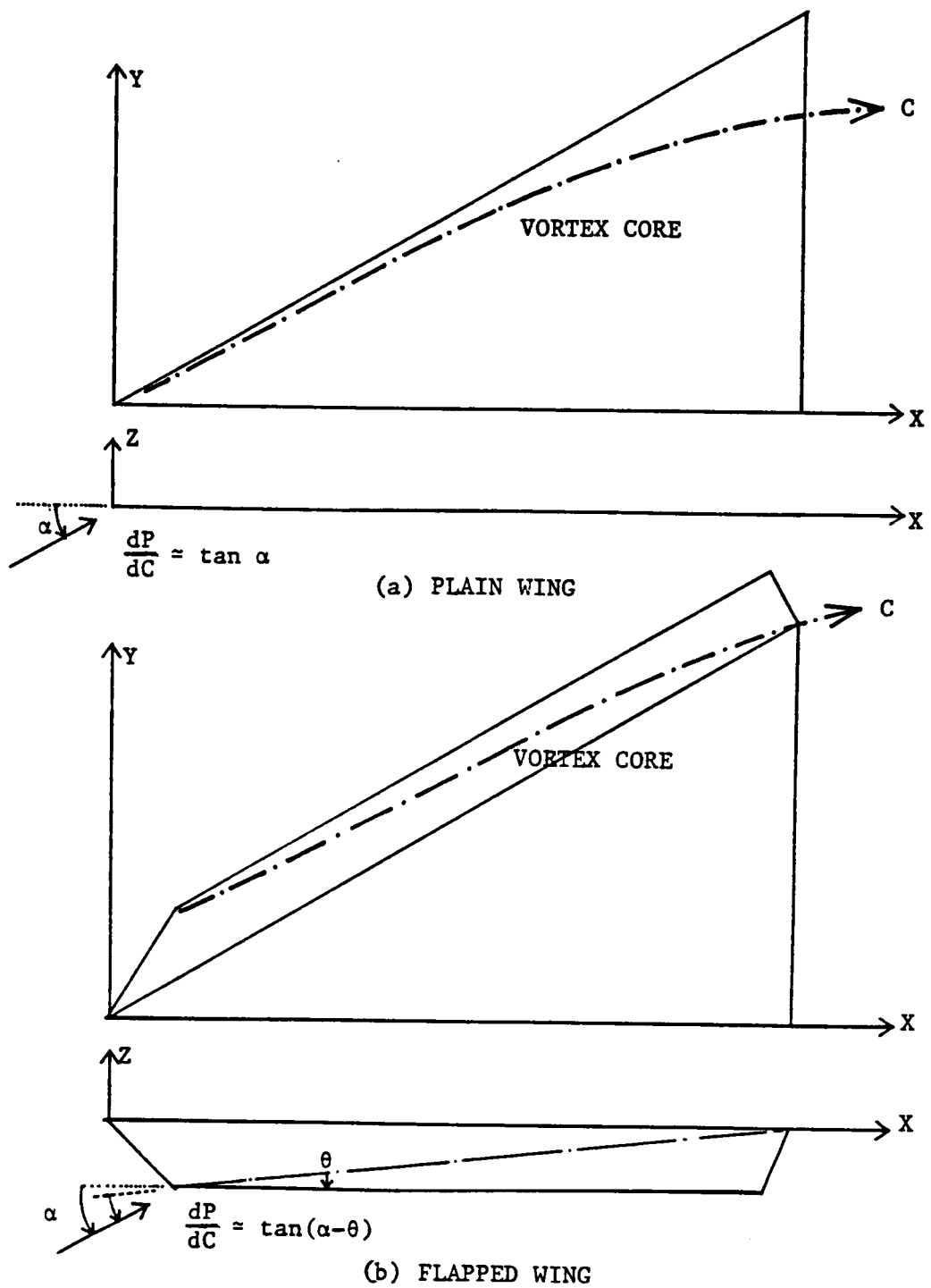


Fig. 4. Reduction of pressure gradient along the vortex core by leading edge vortex flap

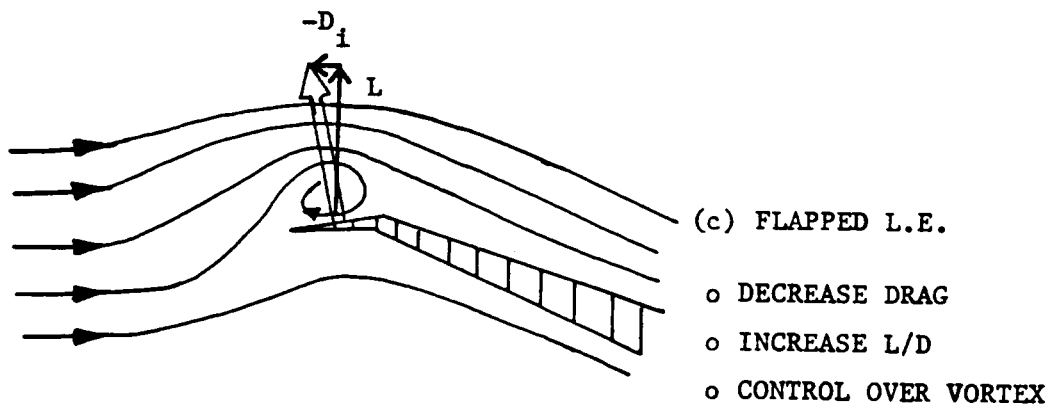
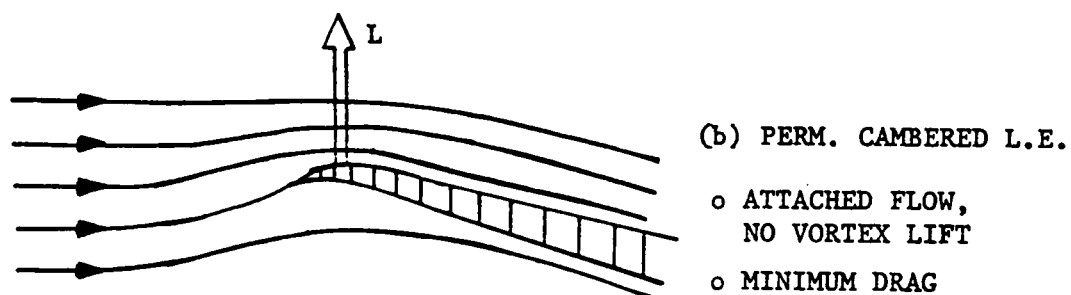
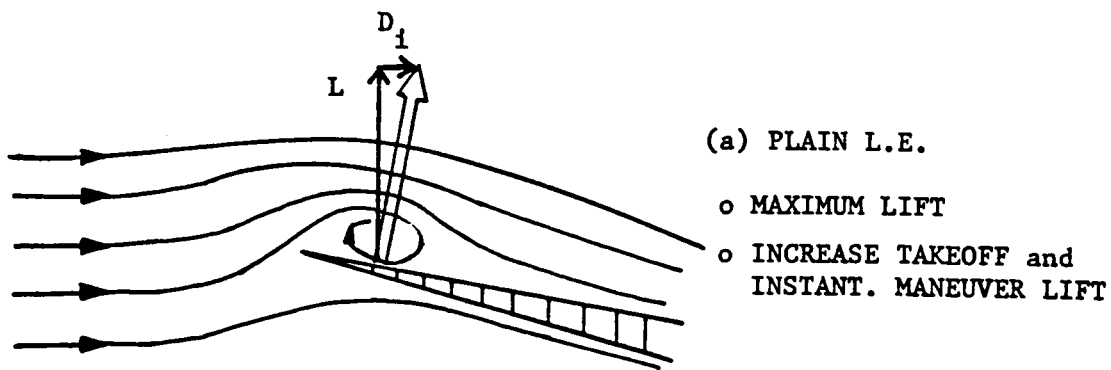


Fig. 5. Leading edge camber effect

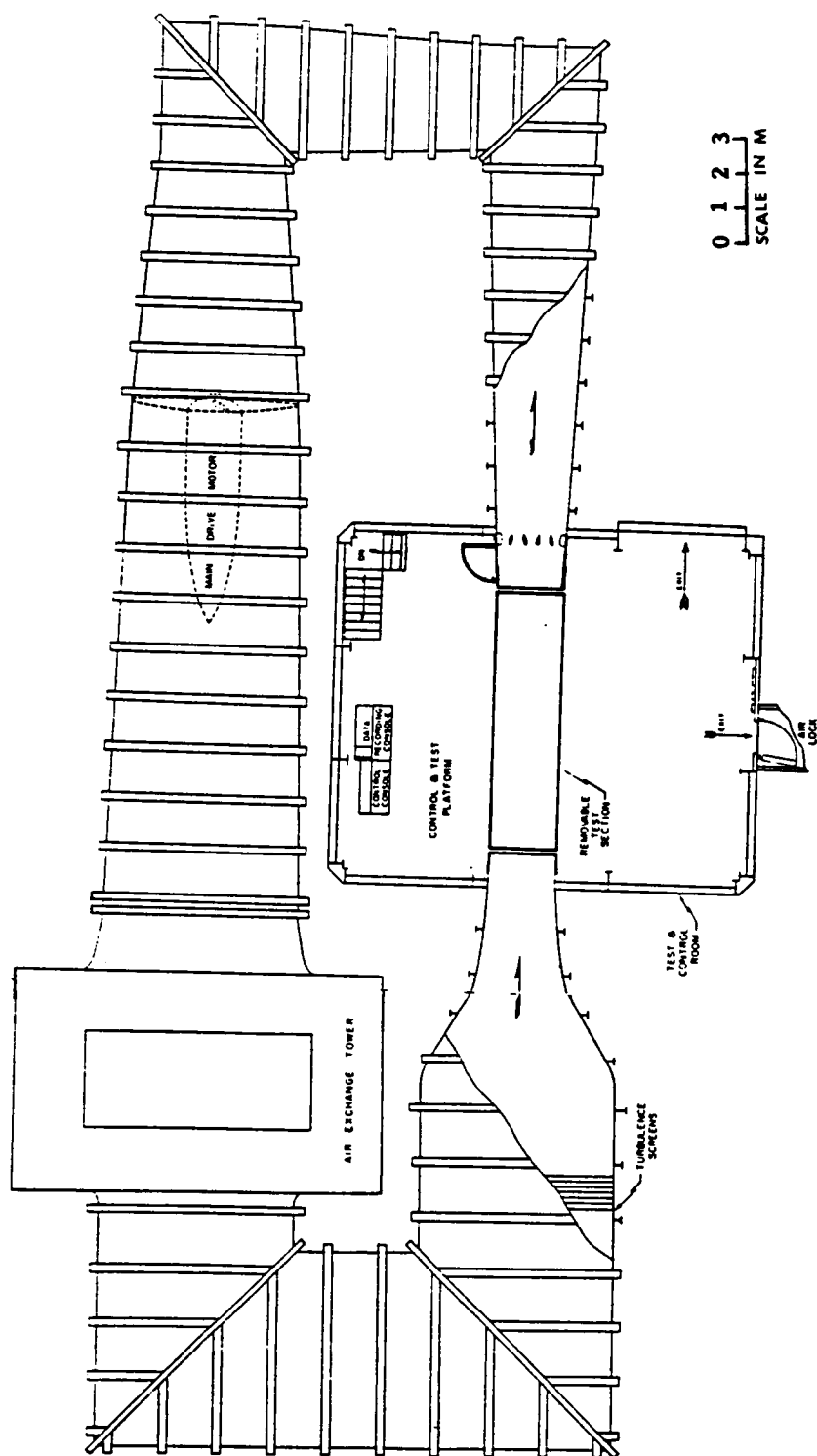
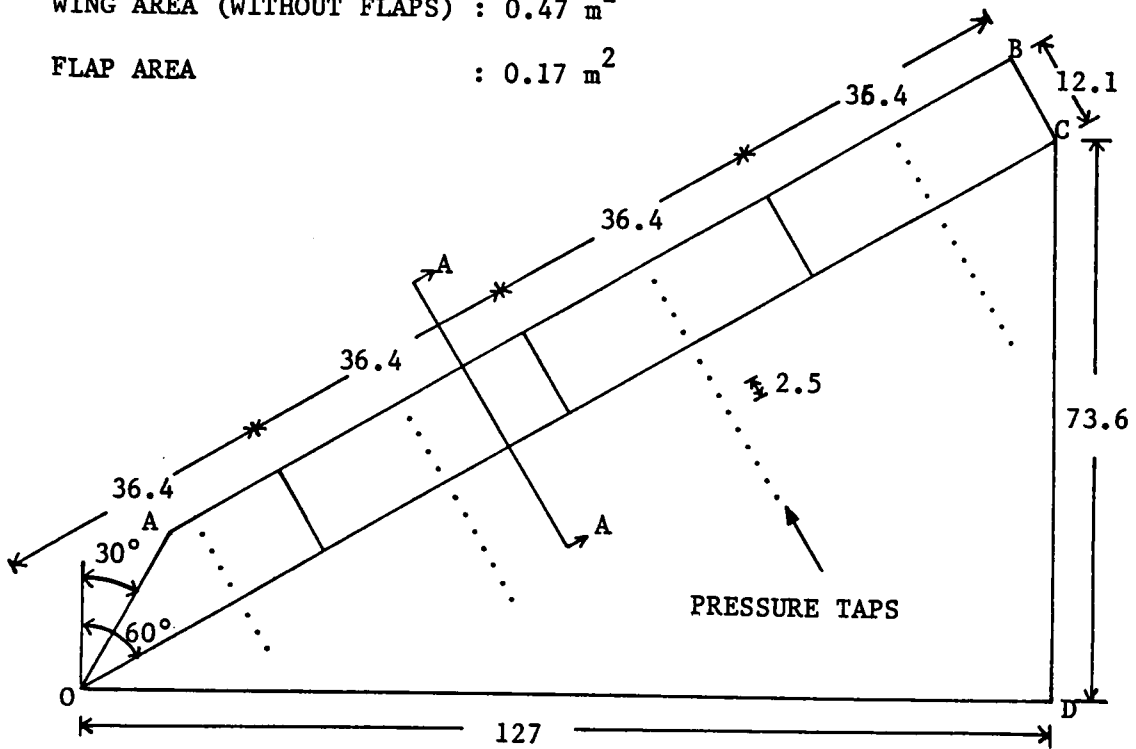


Fig. 6. Schematic of Virginia Tech Stability Wind Tunnel

WING AREA (WITHOUT FLAPS) : 0.47 m^2

FLAP AREA : 0.17 m^2



SECTION A-A

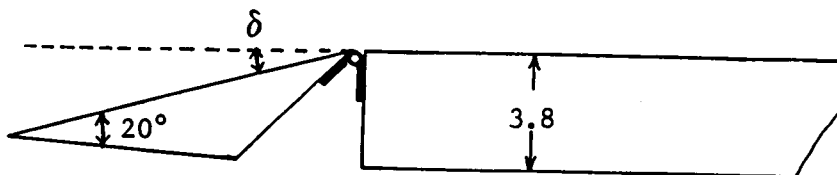


Fig. 7. Geometry of the 60° delta wing model with leading edge vortex flap. Dimensions in centimeters.

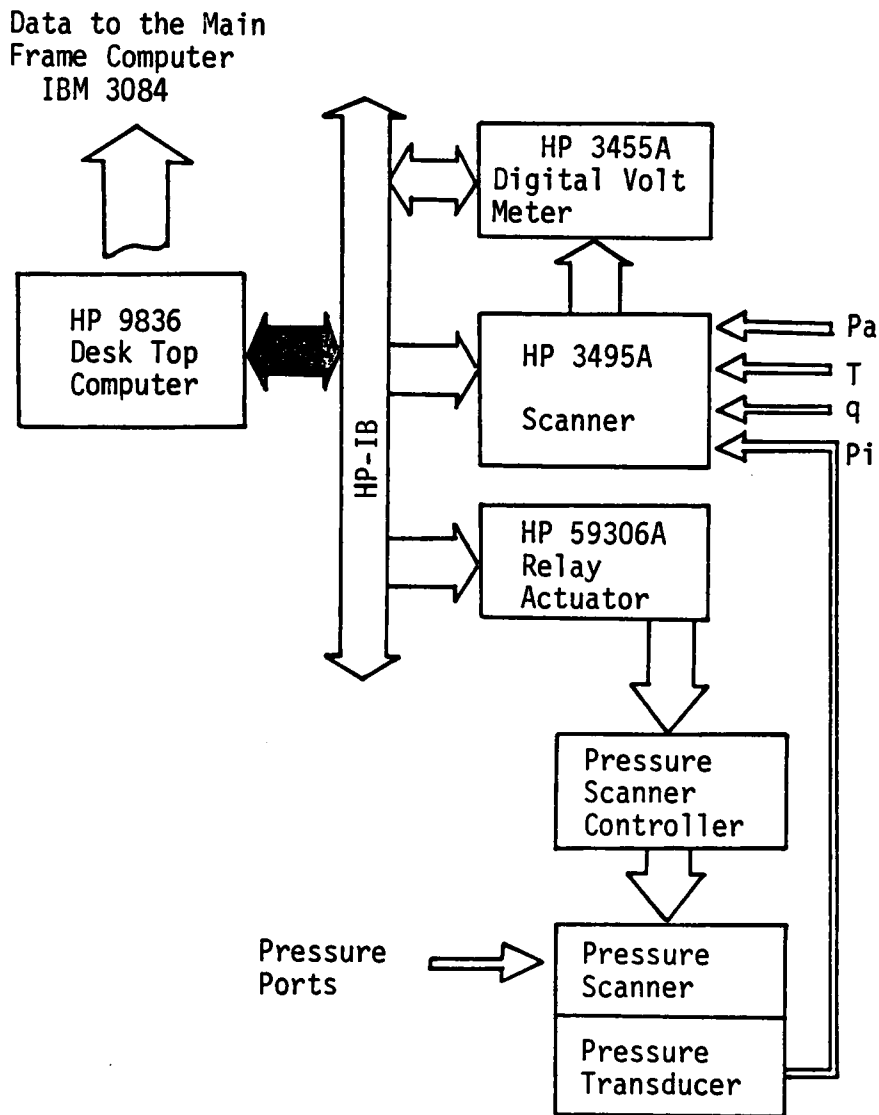


Fig. 8. Schematic diagram of Instrumentation

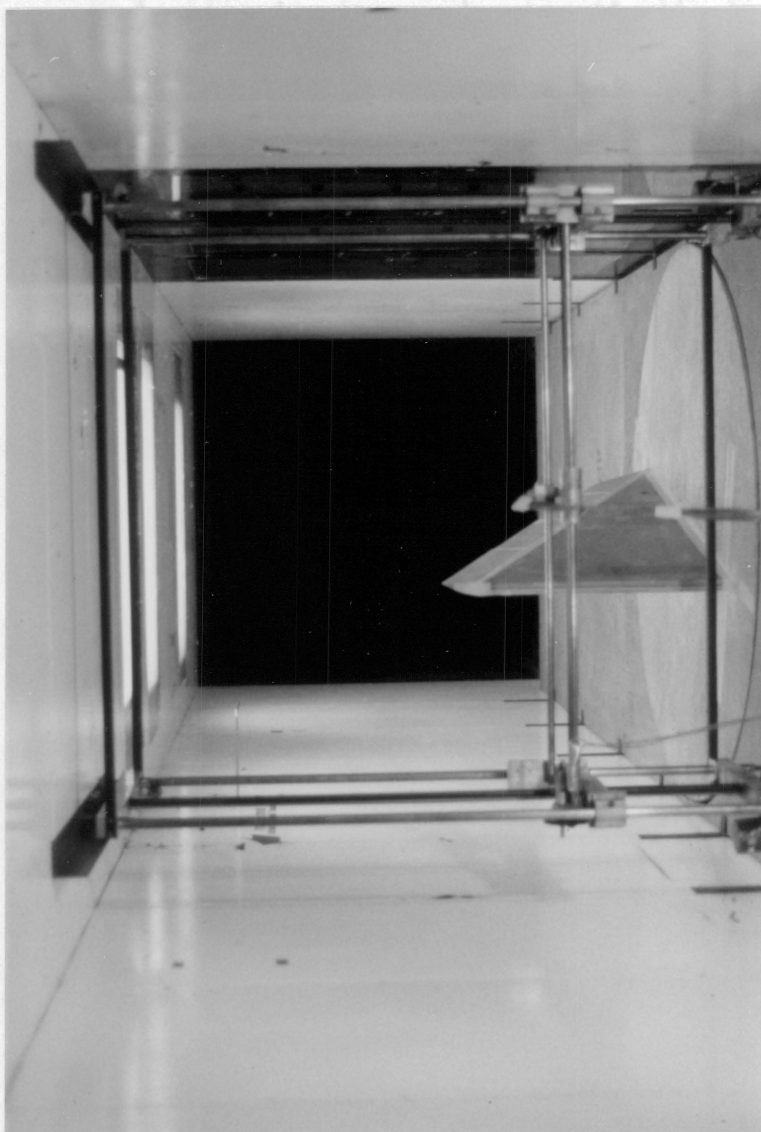


Fig. 9. Test set-up for mean flow field measurement.

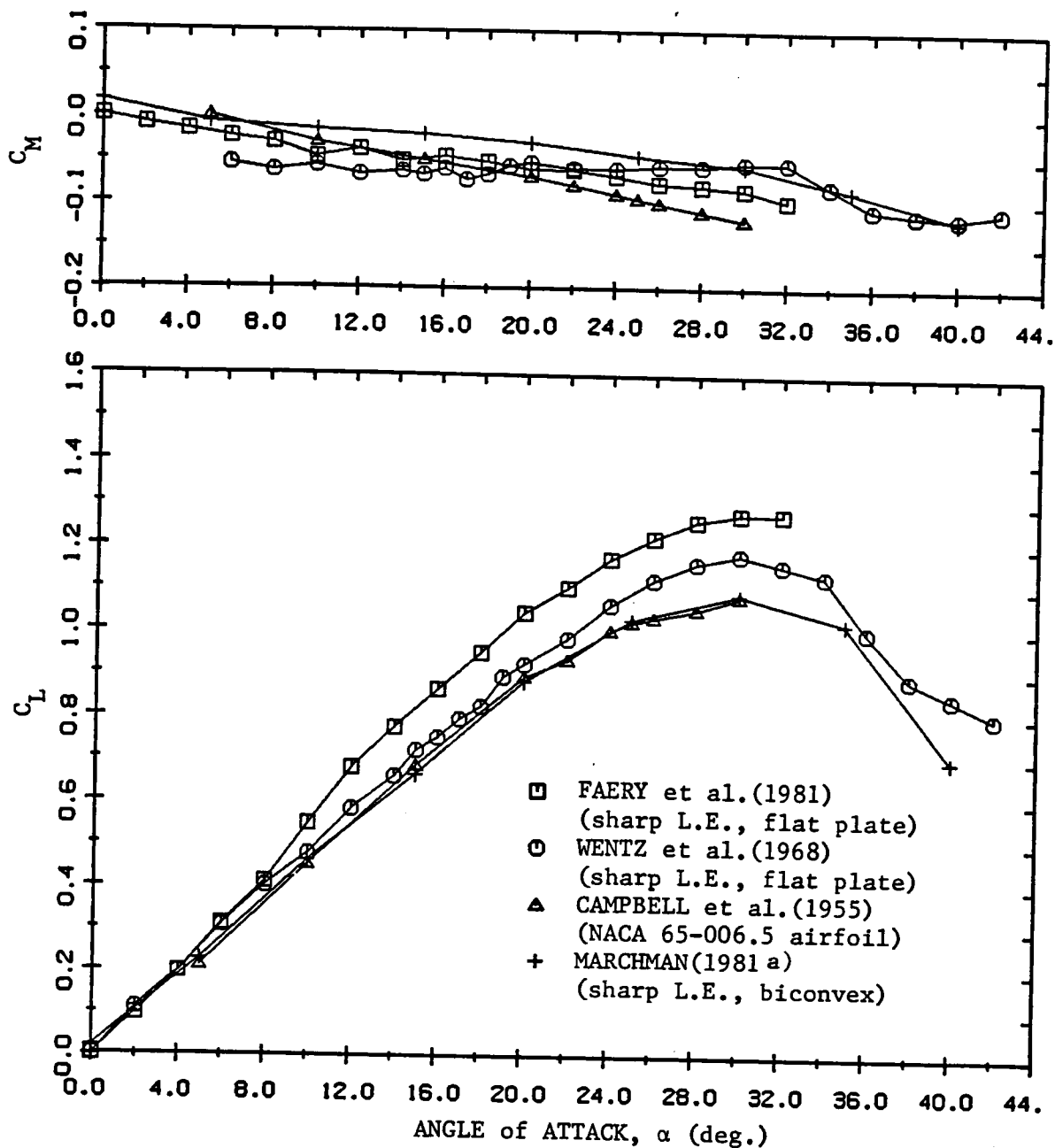


Fig. 10.a Effect of profile shape and leading edge on the aerodynamic characteristics of a 60° delta wing.

Faery : Flat plate wing, 15° beveled L.E., $t/C=0.014$
 Wentz : Flat plate wing, 15° beveled L.E., $t/C=0.012$
 Campbell : NACA 65-006.5 profile, $t/C=0.060$
 Marchman : Biconvex profile, sharp L.E., $t/C=0.032$

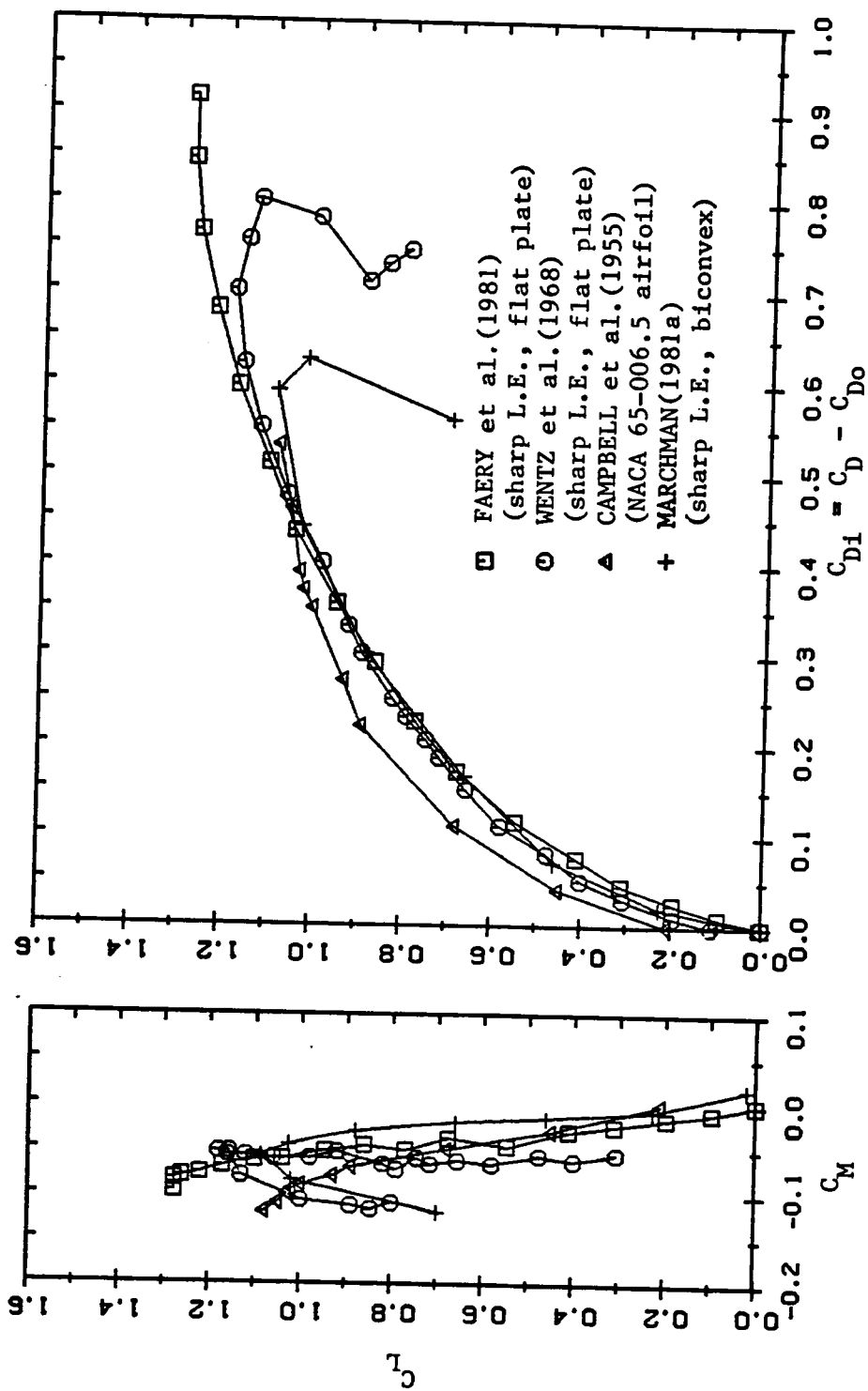


Fig. 10.b Concluded

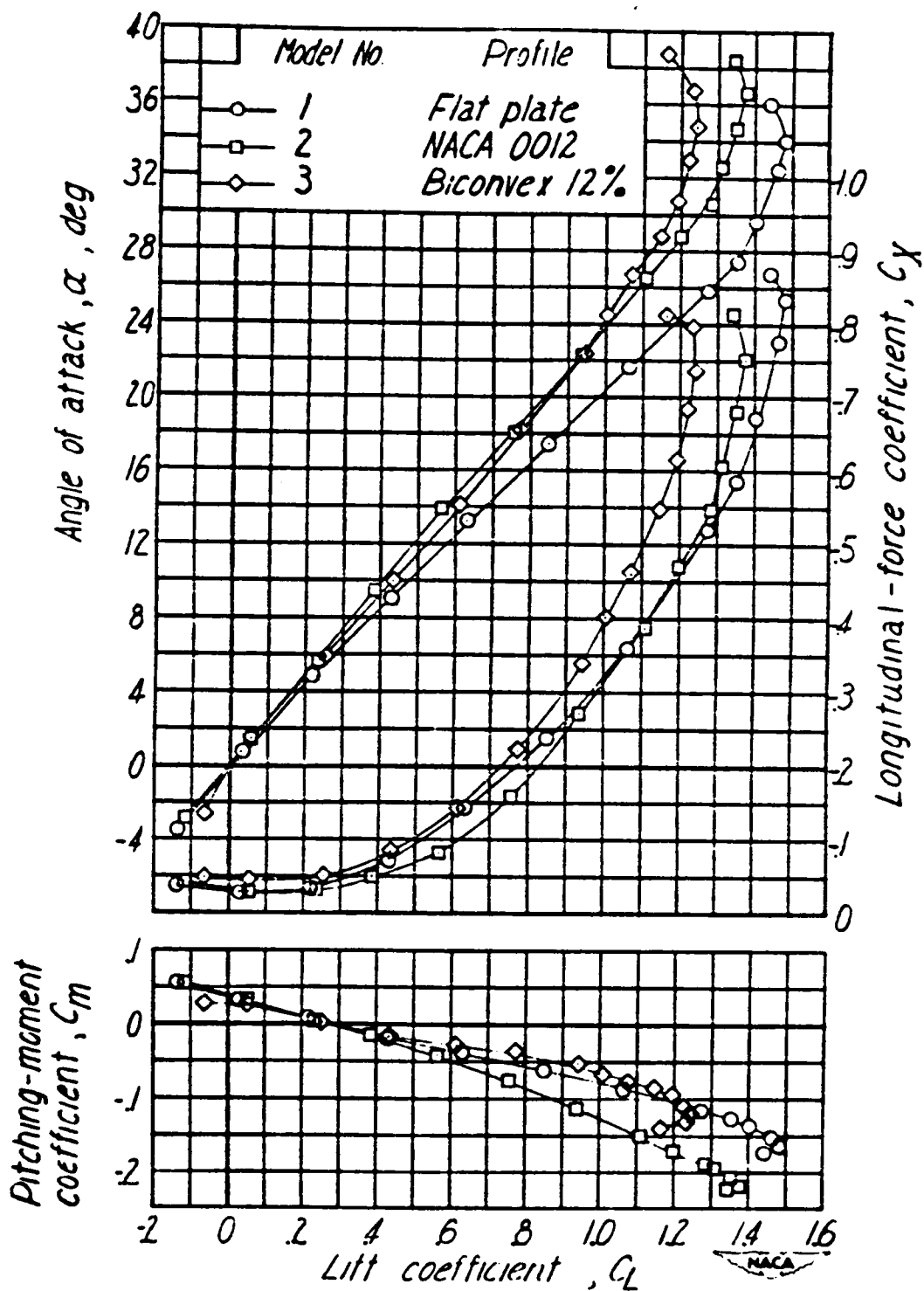


Fig. 11. Effect of profile on aerodynamic performance of a delta wing with Aspect Ratio 2.31 (From NACA RM L8L29).

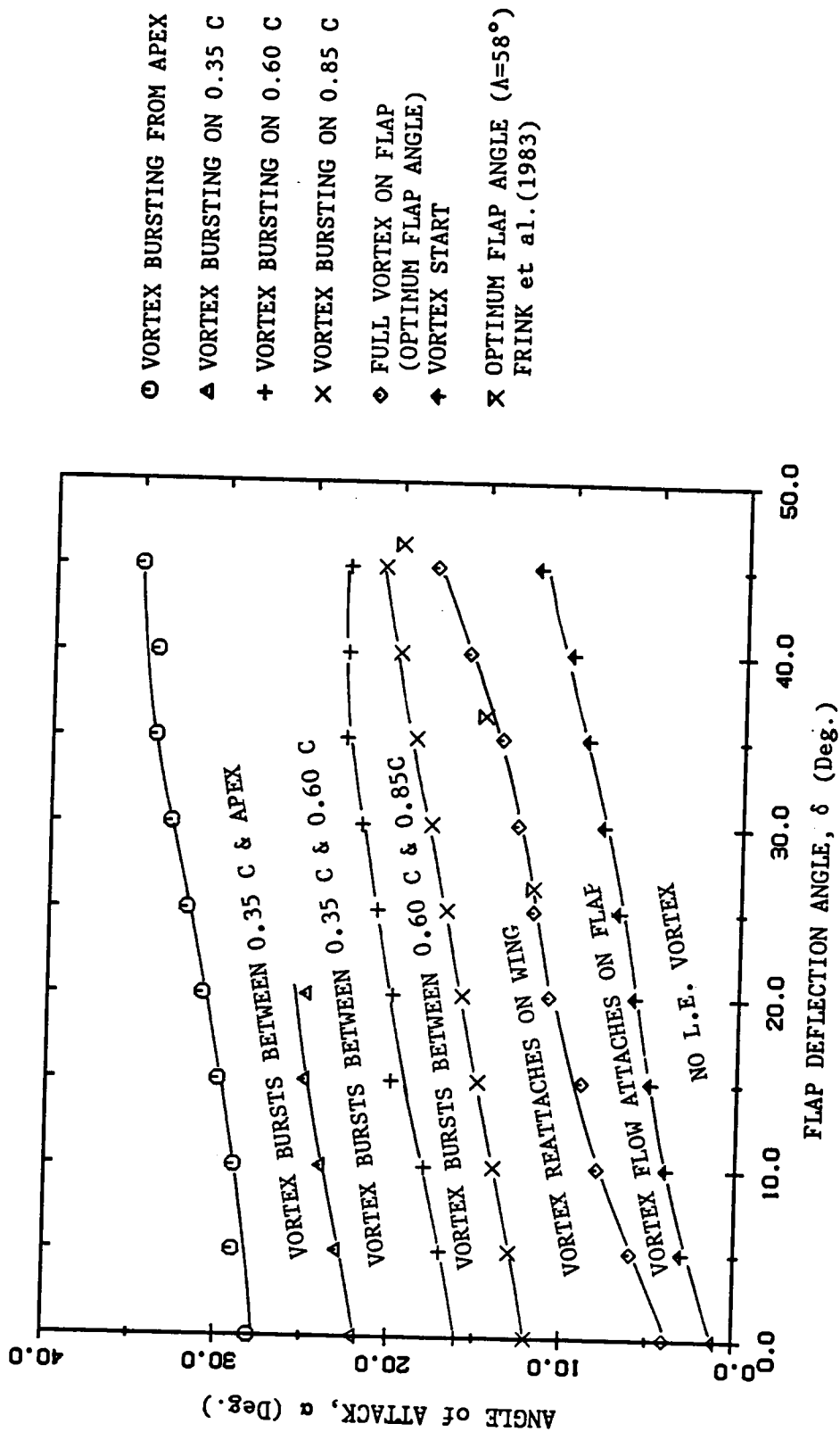


Fig. 12. Flow regime over a 60° delta wing with leading edge vortex flap.

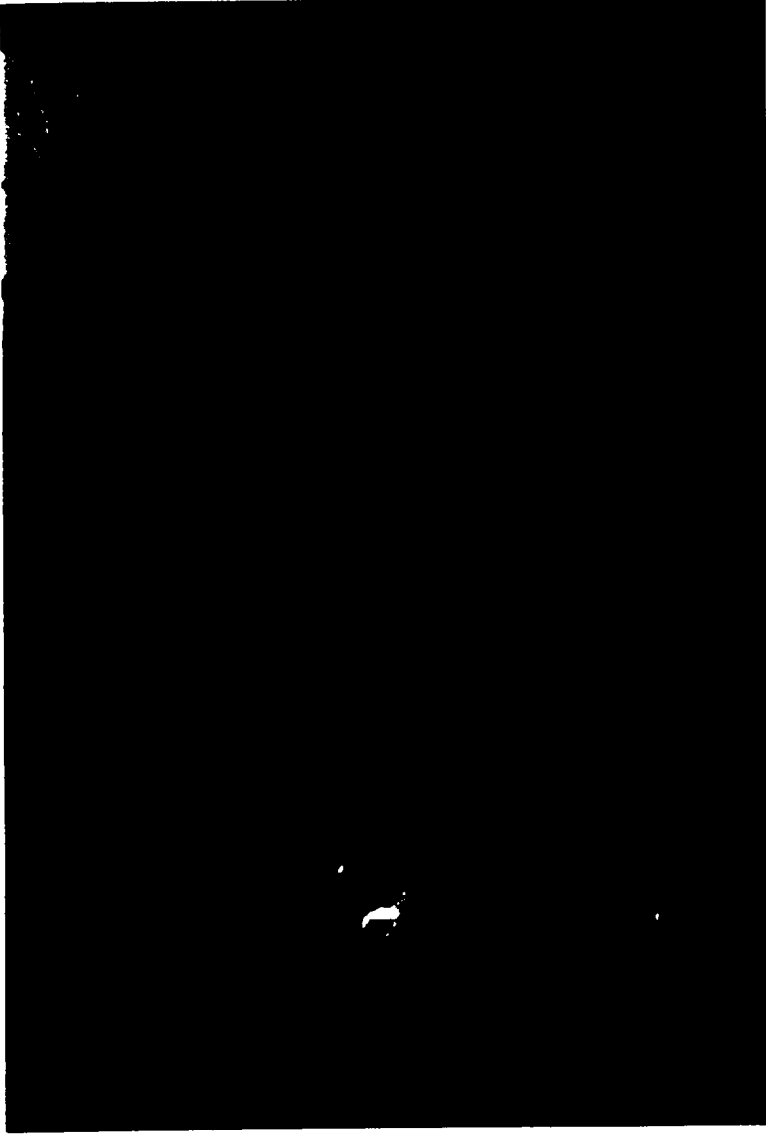
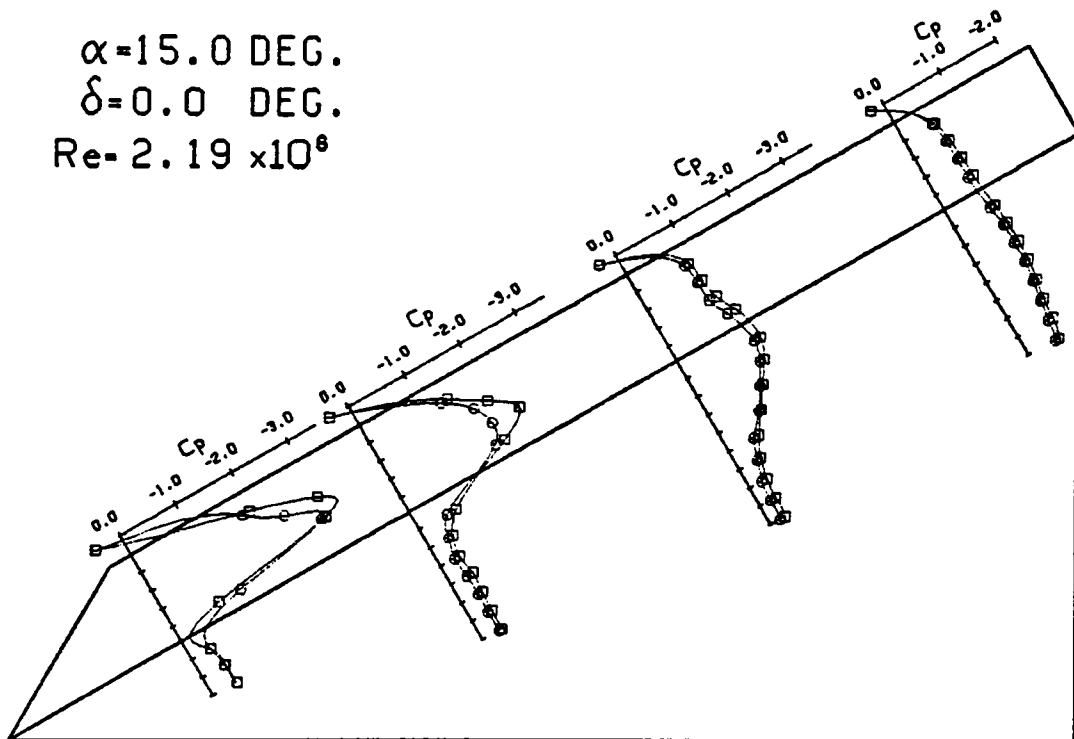
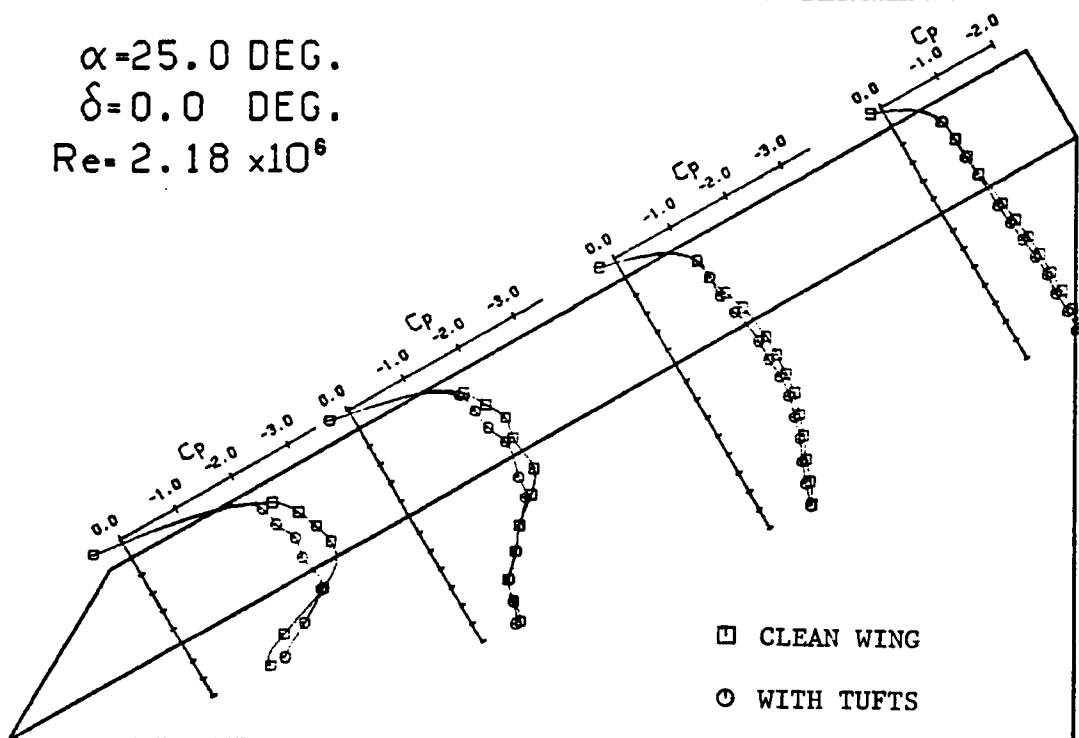


Fig. 13. Representative photograph of woolen tufts flow visualization experiment ($\alpha=10^\circ$, $\delta=10^\circ$).

$\alpha = 15.0 \text{ DEG.}$
 $\delta = 0.0 \text{ DEG.}$
 $Re = 2.19 \times 10^6$



$\alpha = 25.0 \text{ DEG.}$
 $\delta = 0.0 \text{ DEG.}$
 $Re = 2.18 \times 10^6$

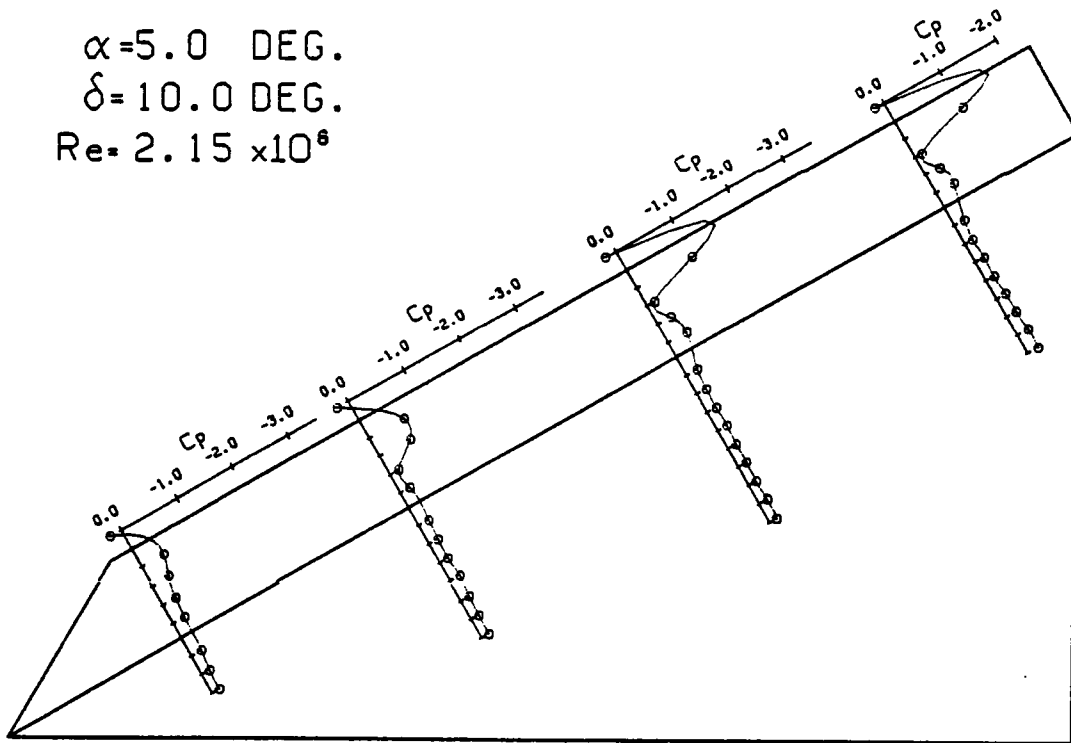


□ CLEAN WING

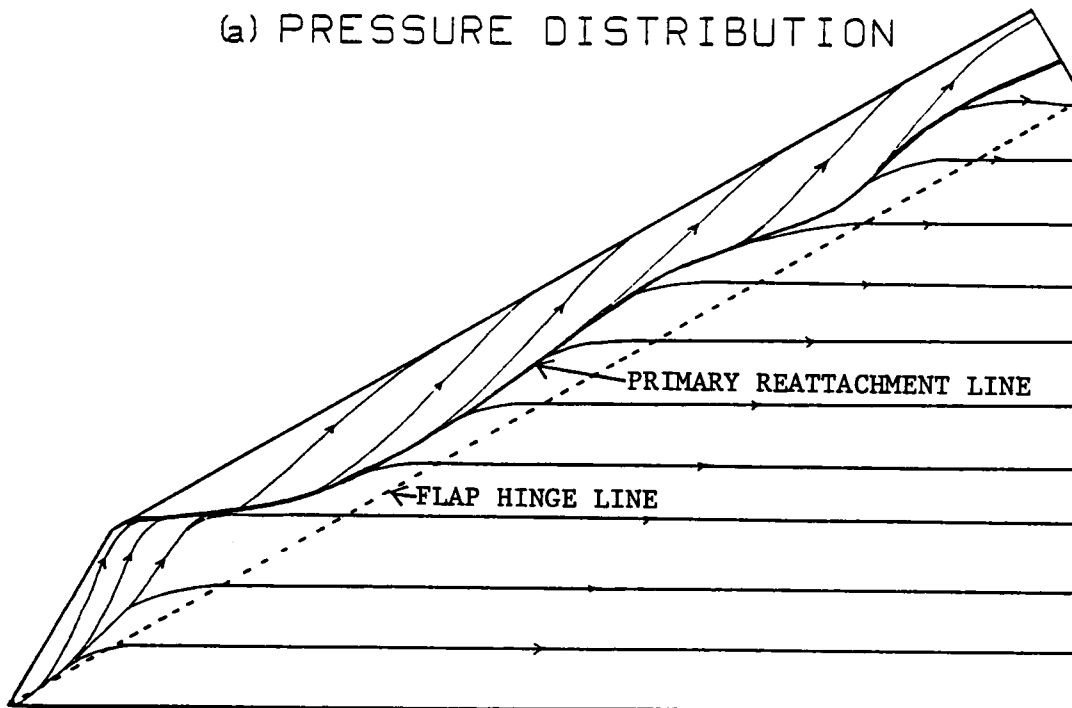
○ WITH TUFTS

Fig. 14. Effect of tufts on pressure distribution.

$\alpha = 5.0 \text{ DEG.}$
 $\delta = 10.0 \text{ DEG.}$
 $Re = 2.15 \times 10^6$



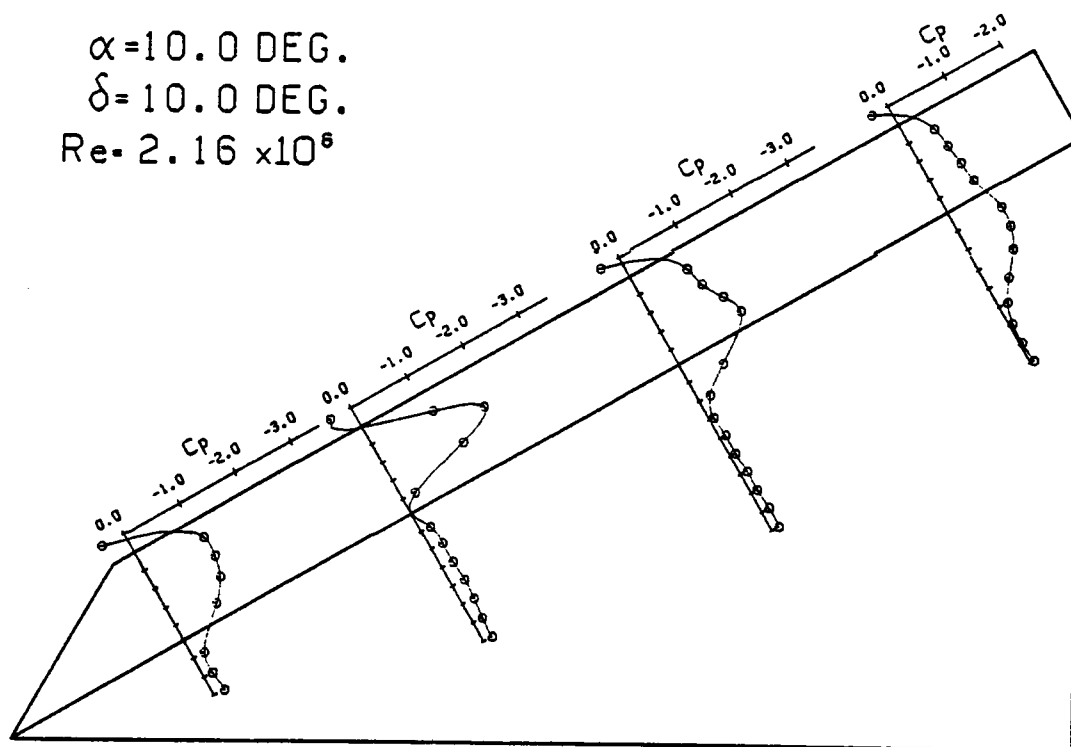
(a) PRESSURE DISTRIBUTION



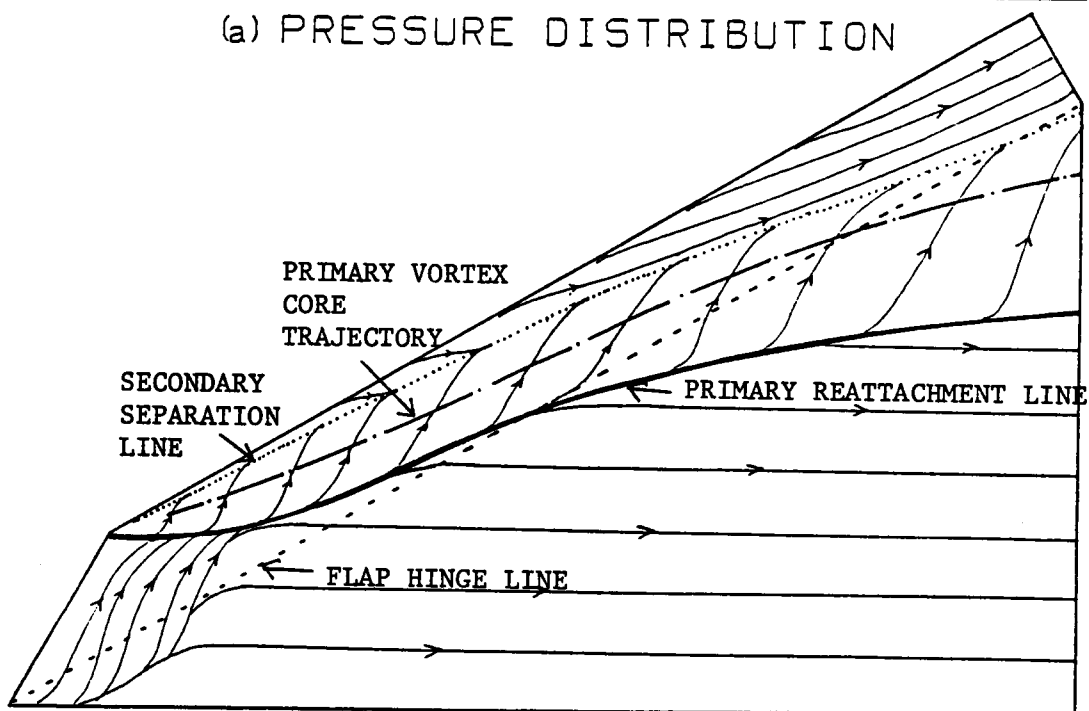
(b) SURFACE STREAMLINES

Fig. 15. Pressure distribution and surface streamlines at $\alpha = 5^\circ$, $\delta = 10^\circ$.

$\alpha = 10.0 \text{ DEG.}$
 $\delta = 10.0 \text{ DEG.}$
 $Re = 2.16 \times 10^6$



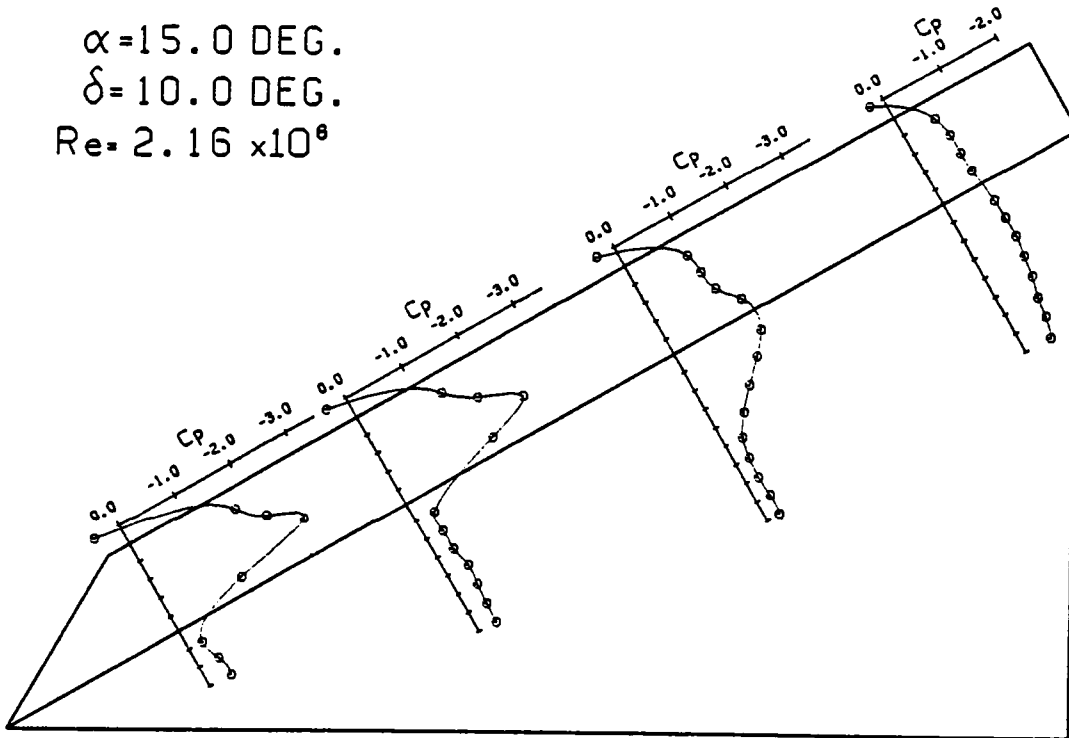
(a) PRESSURE DISTRIBUTION



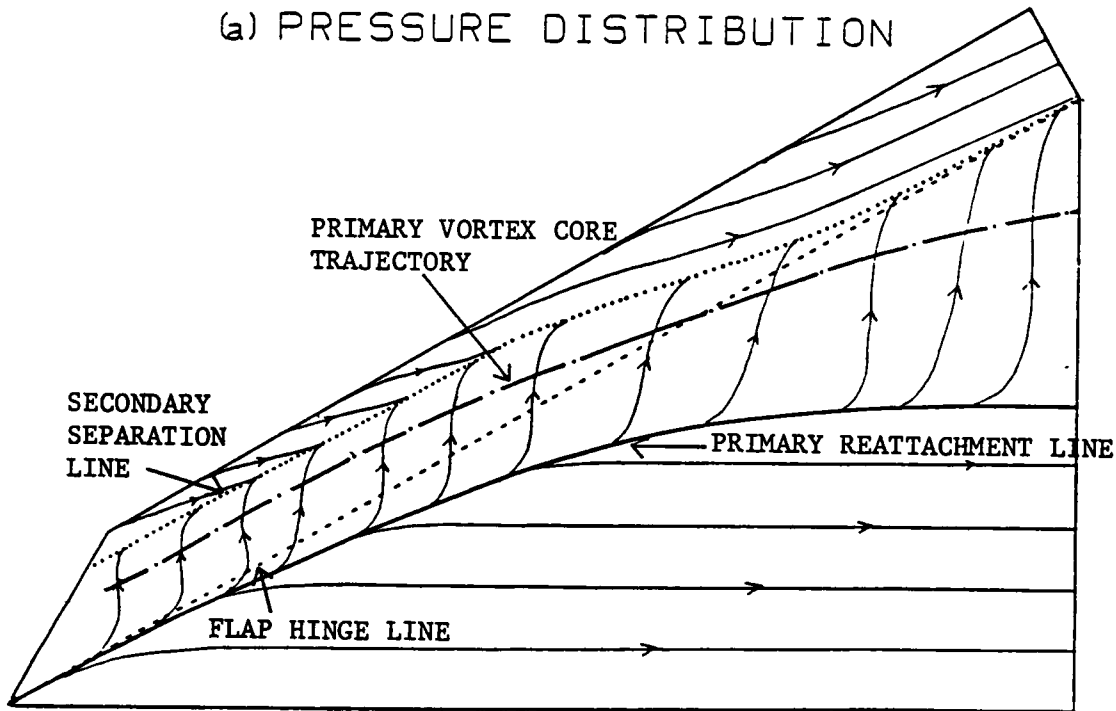
(b) SURFACE STREAMLINES

Fig. 16. Pressure distribution and surface streamlines at $\alpha = 10^\circ$, $\delta = 10^\circ$.

$\alpha = 15.0 \text{ DEG.}$
 $\delta = 10.0 \text{ DEG.}$
 $Re = 2.16 \times 10^6$



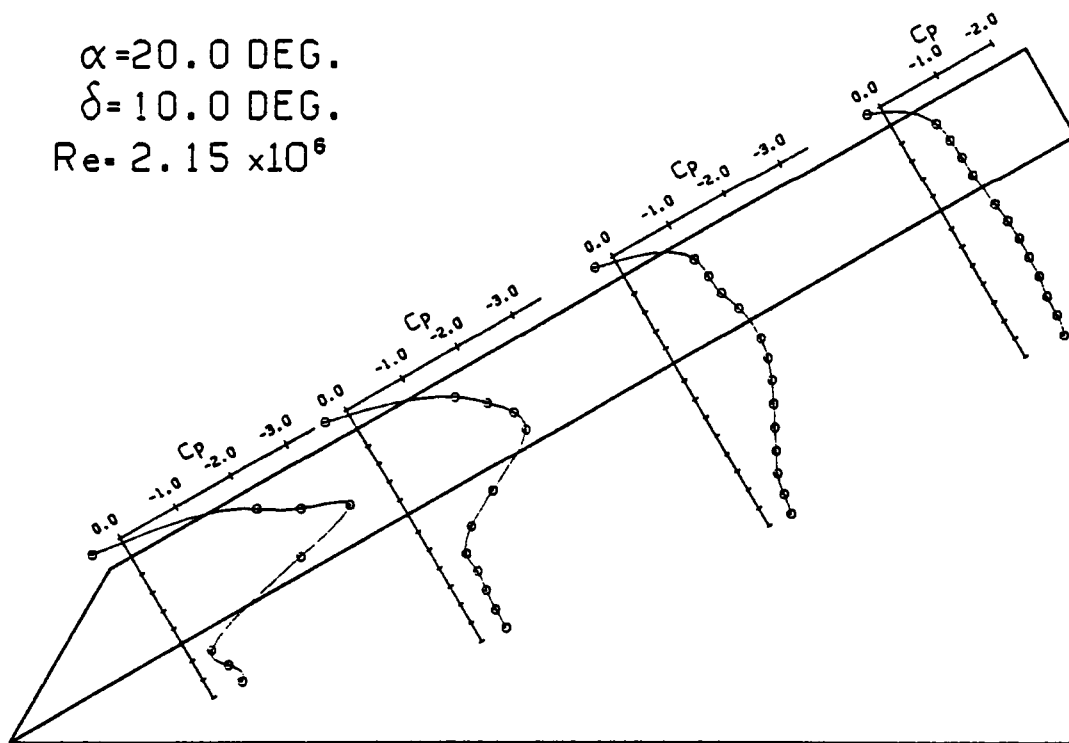
(a) PRESSURE DISTRIBUTION



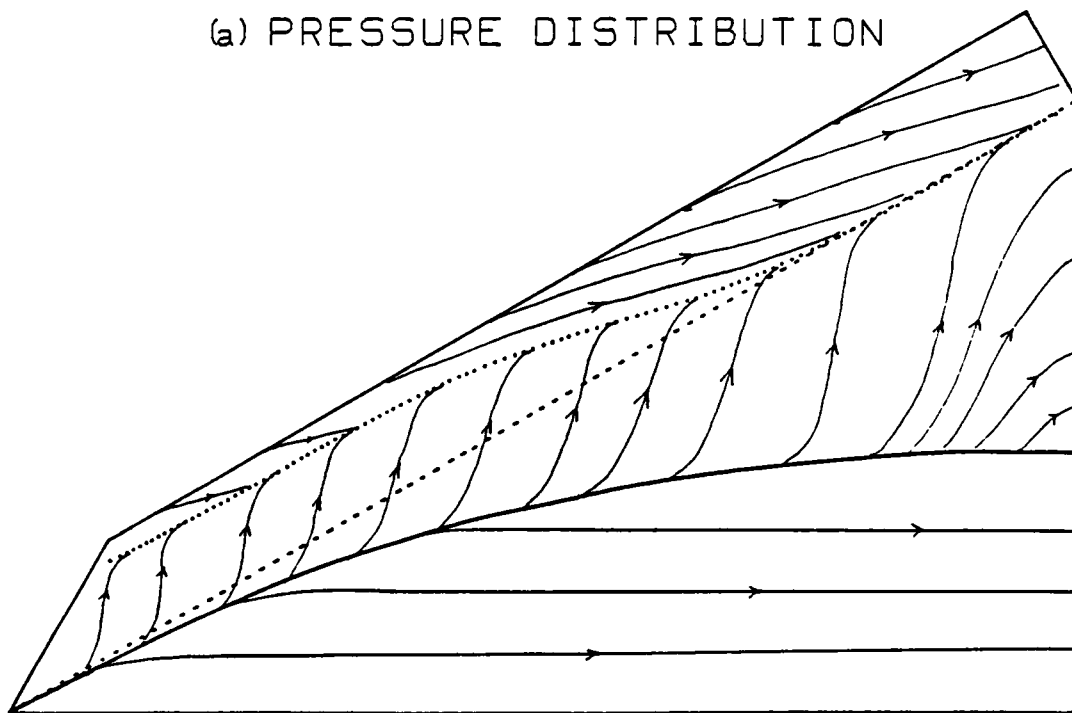
(b) SURFACE STREAMLINES

Fig. 17. Pressure distribution and surface streamlines at $\alpha = 15^\circ$, $\delta = 10^\circ$.

$\alpha = 20.0 \text{ DEG.}$
 $\delta = 10.0 \text{ DEG.}$
 $Re = 2.15 \times 10^6$



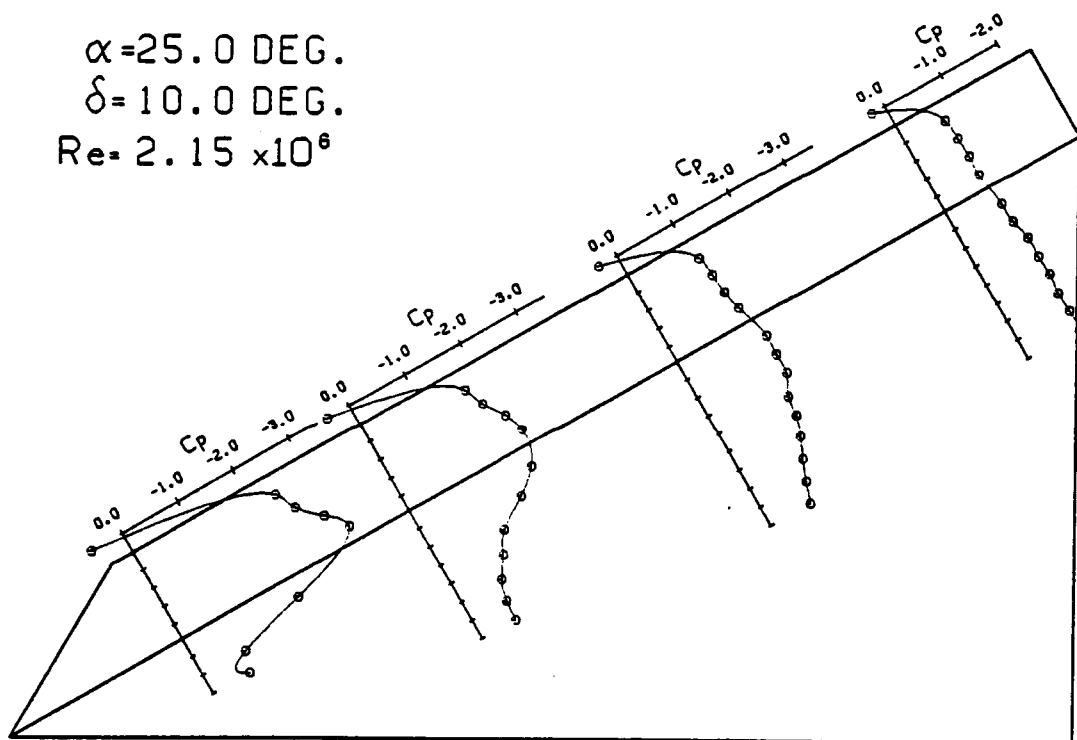
(a) PRESSURE DISTRIBUTION



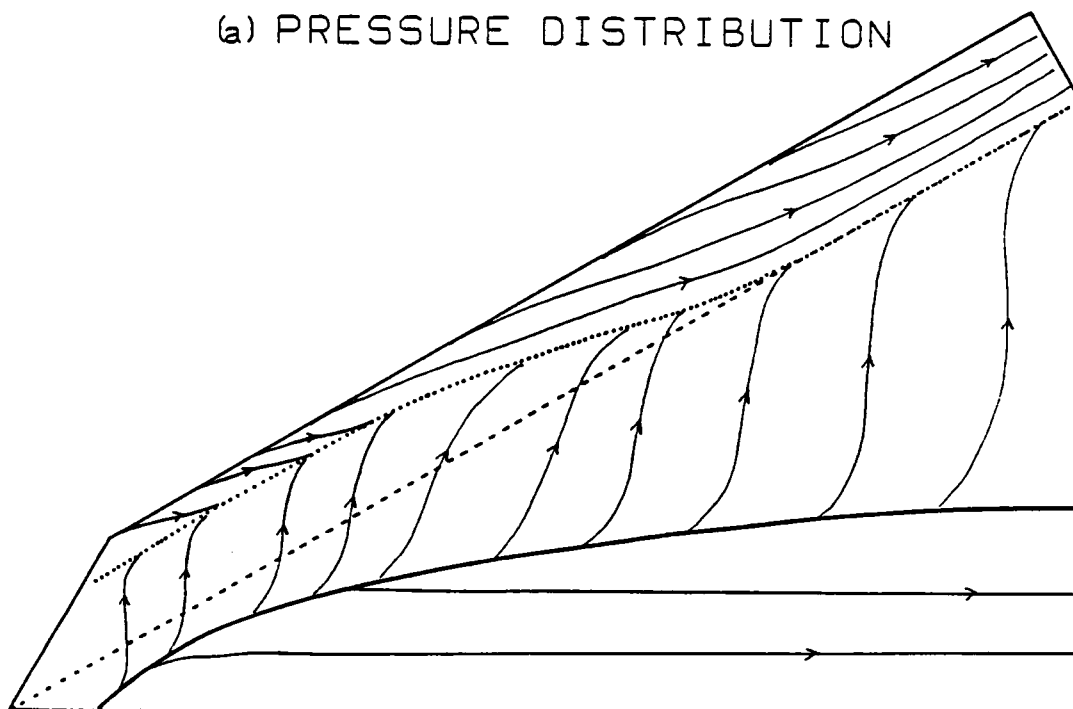
(b) SURFACE STREAMLINES

Fig. 18. Pressure distribution and surface streamlines at $\alpha = 20^\circ$, $\delta = 10^\circ$.

$\alpha = 25.0 \text{ DEG.}$
 $\delta = 10.0 \text{ DEG.}$
 $Re = 2.15 \times 10^6$



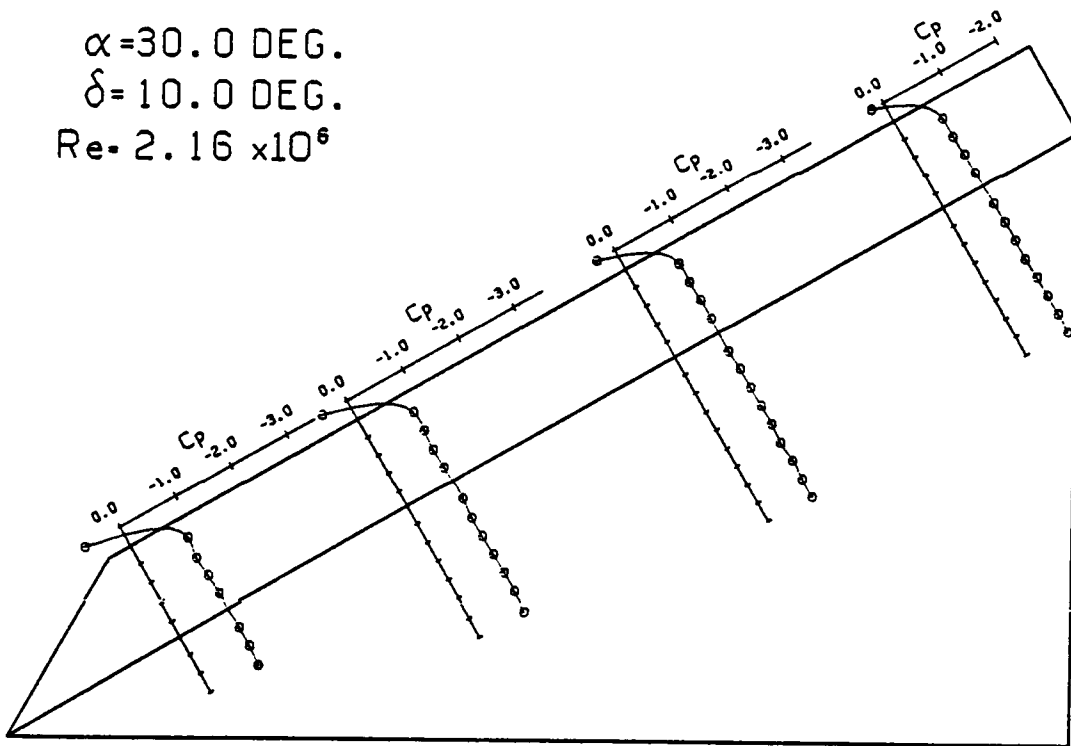
(a) PRESSURE DISTRIBUTION



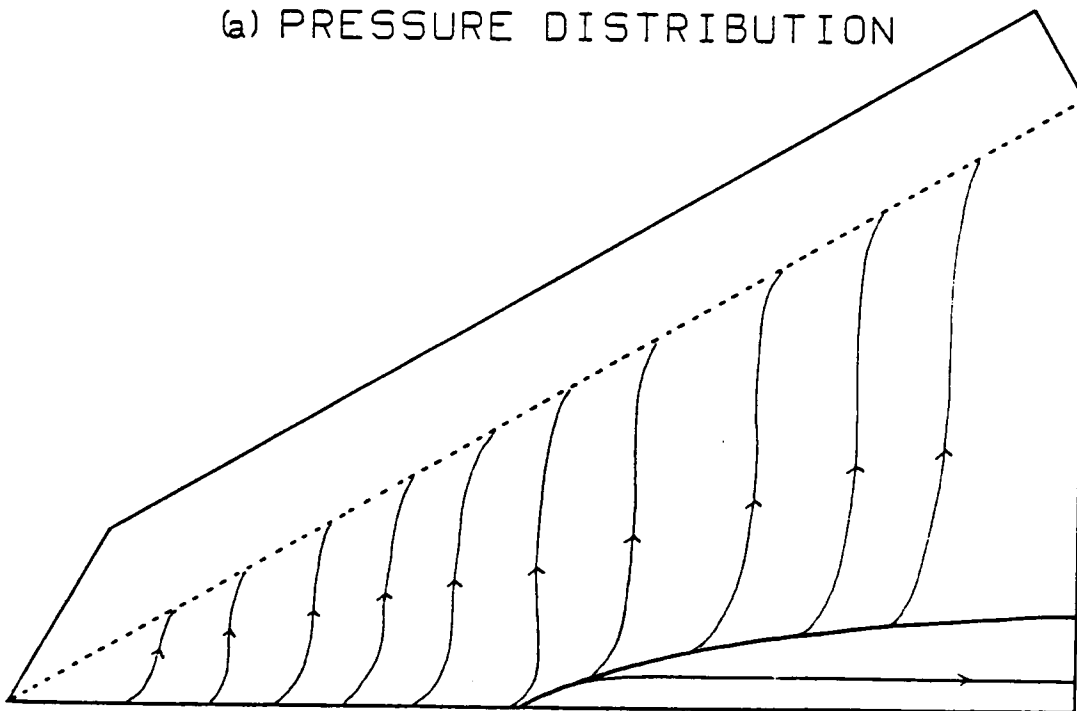
(b) SURFACE STREAMLINES

Fig. 19. Pressure distribution and surface streamlines at $\alpha = 25^\circ$, $\delta = 10^\circ$.

$\alpha = 30.0 \text{ DEG.}$
 $\delta = 10.0 \text{ DEG.}$
 $Re = 2.16 \times 10^6$



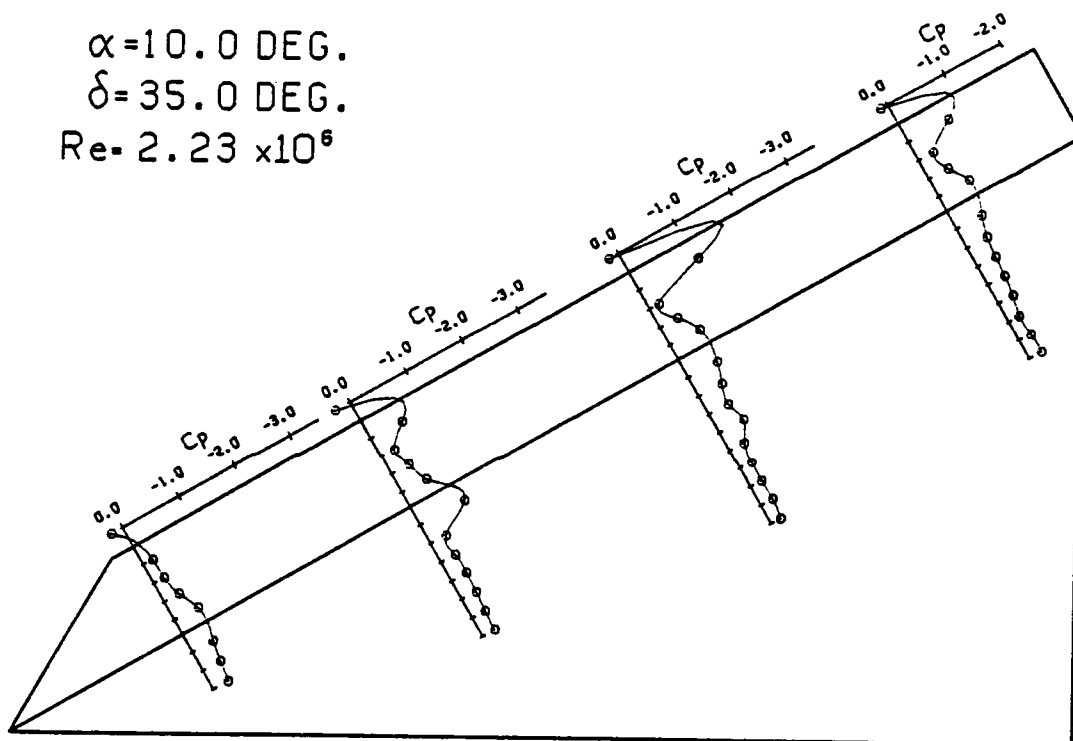
(a) PRESSURE DISTRIBUTION



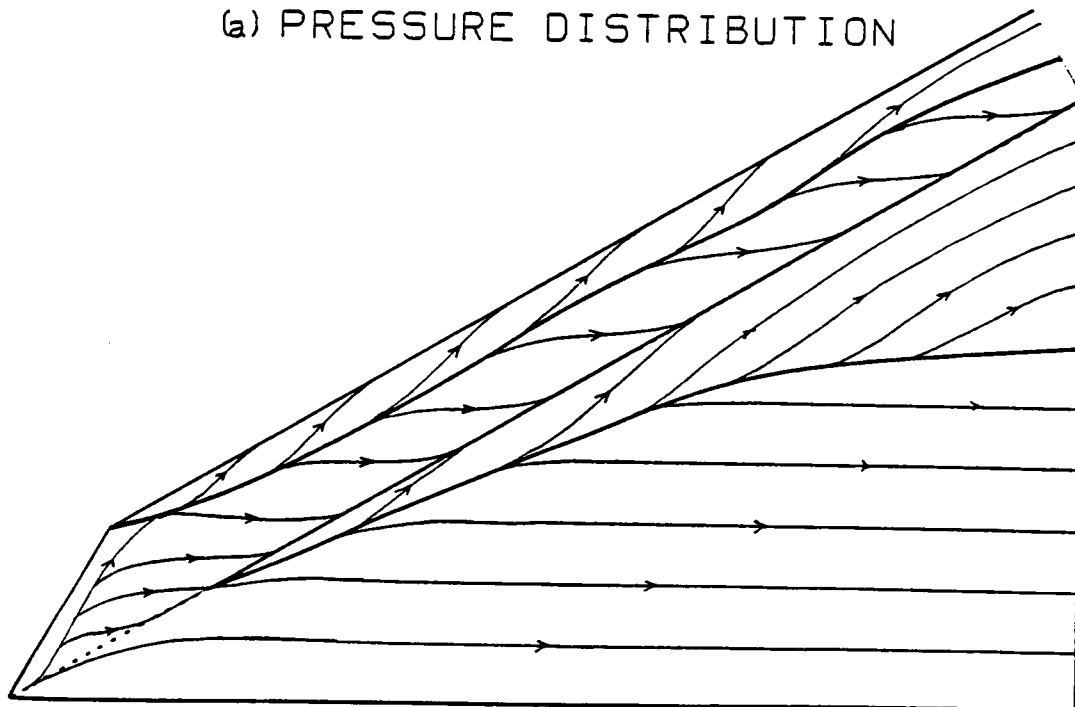
(b) SURFACE STREAMLINES

Fig. 20. Pressure distribution and surface streamlines at $\alpha = 30^\circ$, $\delta = 10^\circ$.

$\alpha = 10.0 \text{ DEG.}$
 $\delta = 35.0 \text{ DEG.}$
 $Re = 2.23 \times 10^6$



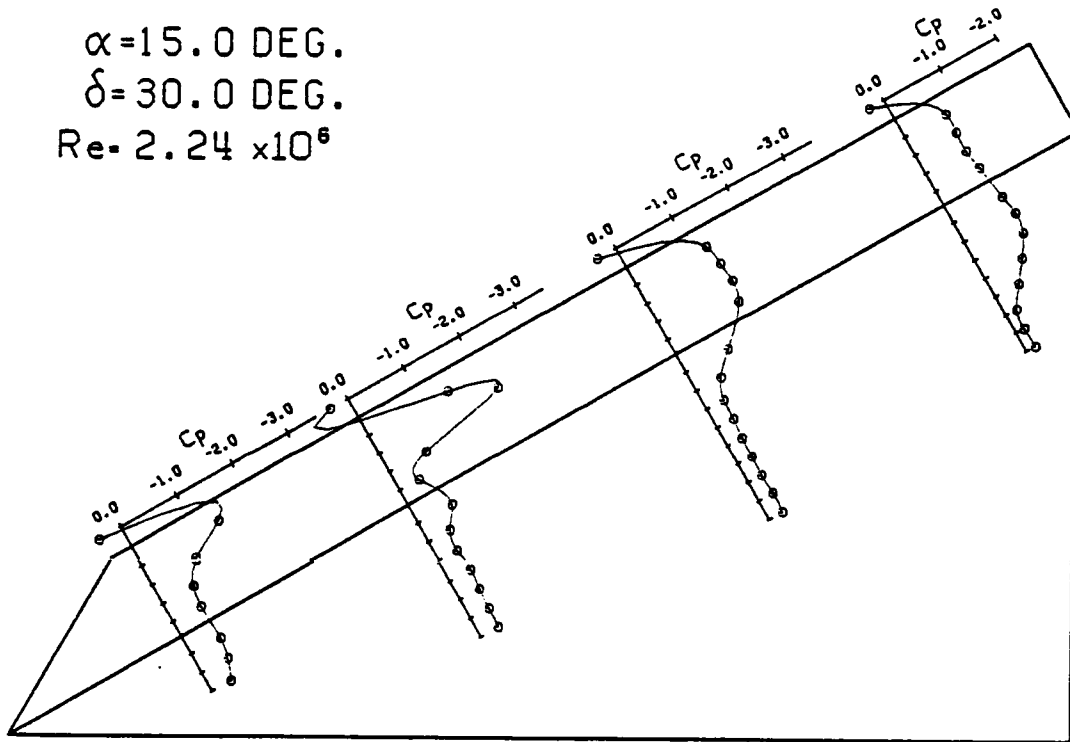
(a) PRESSURE DISTRIBUTION



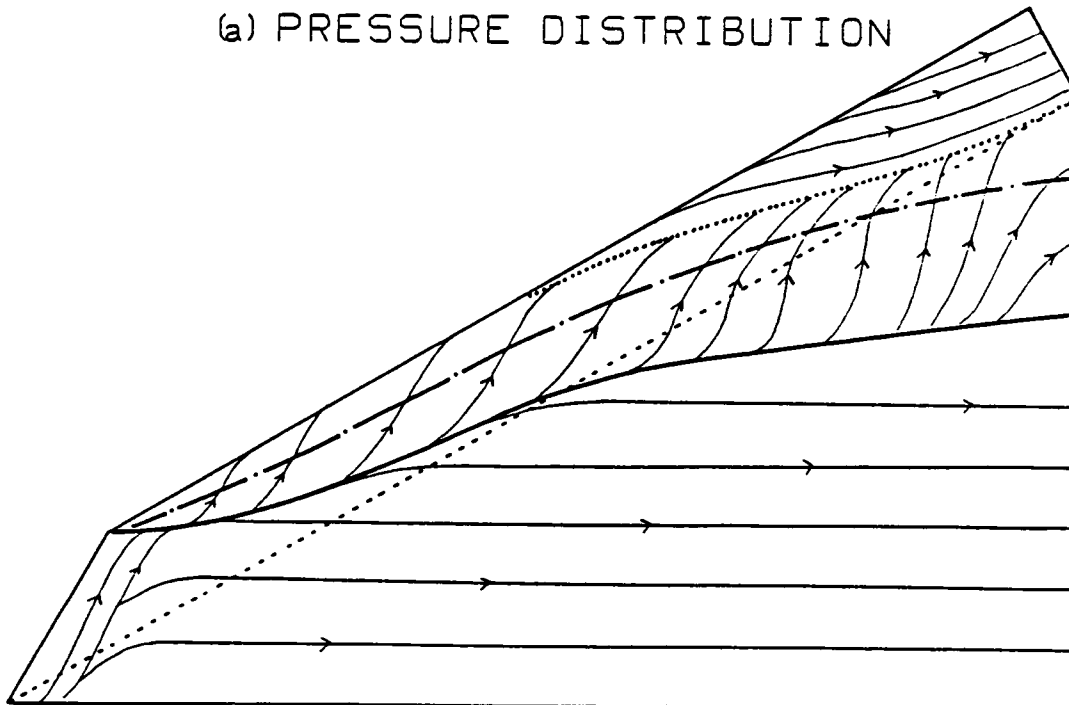
(b) SURFACE STREAMLINES

Fig. 21. Pressure distribution and surface streamlines at $\alpha = 10^\circ$, $\delta = 35^\circ$.

$\alpha = 15.0 \text{ DEG.}$
 $\delta = 30.0 \text{ DEG.}$
 $Re = 2.24 \times 10^6$



(a) PRESSURE DISTRIBUTION



(b) SURFACE STREAMLINES

Fig. 22. Pressure distribution and surface streamlines at $\alpha = 15^\circ$, $\delta = 30^\circ$.

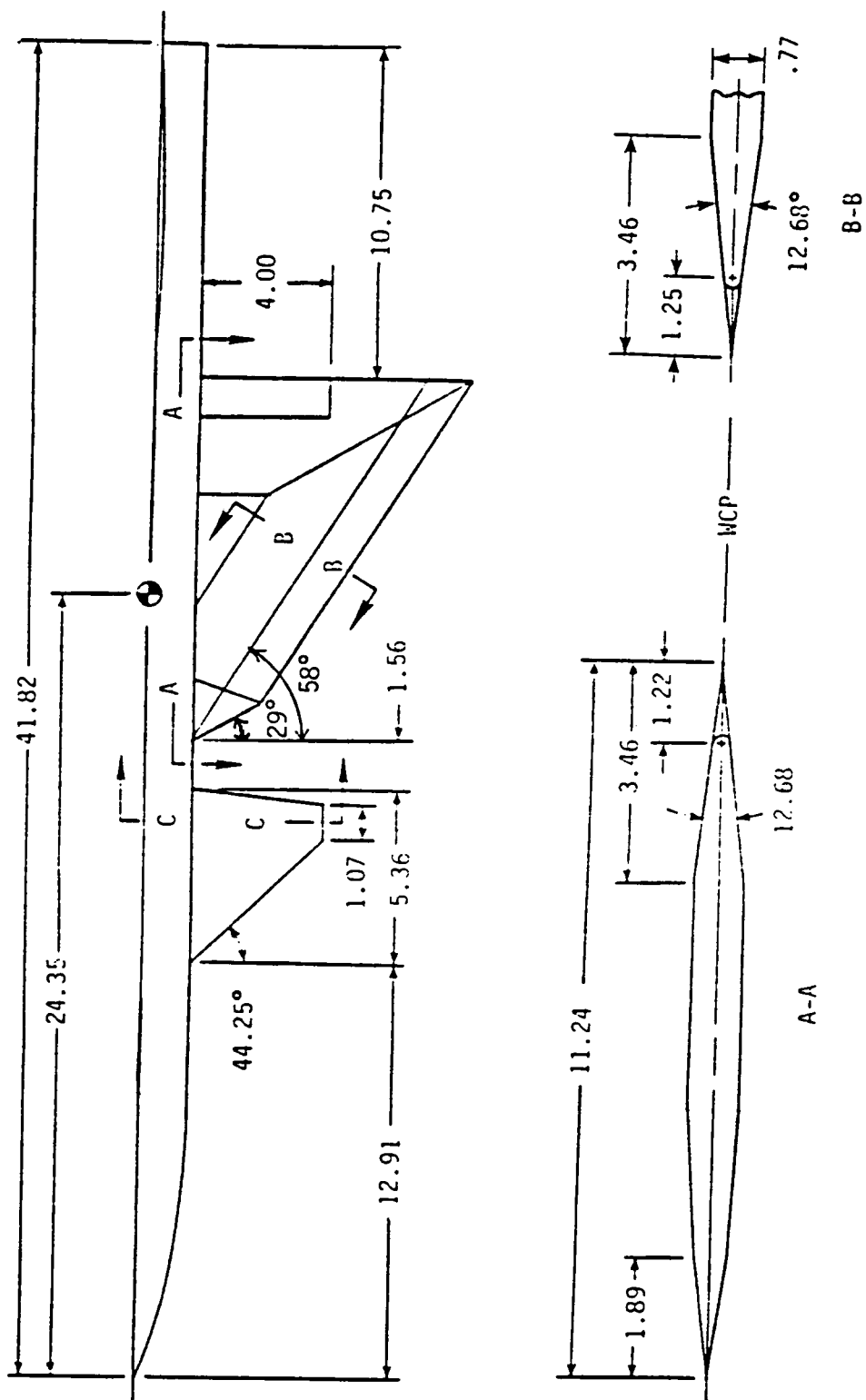


Fig. 23. 58° delta wing model of Frink et al. (1983).
Dimensions are in inches. (From NASA TM 84618)

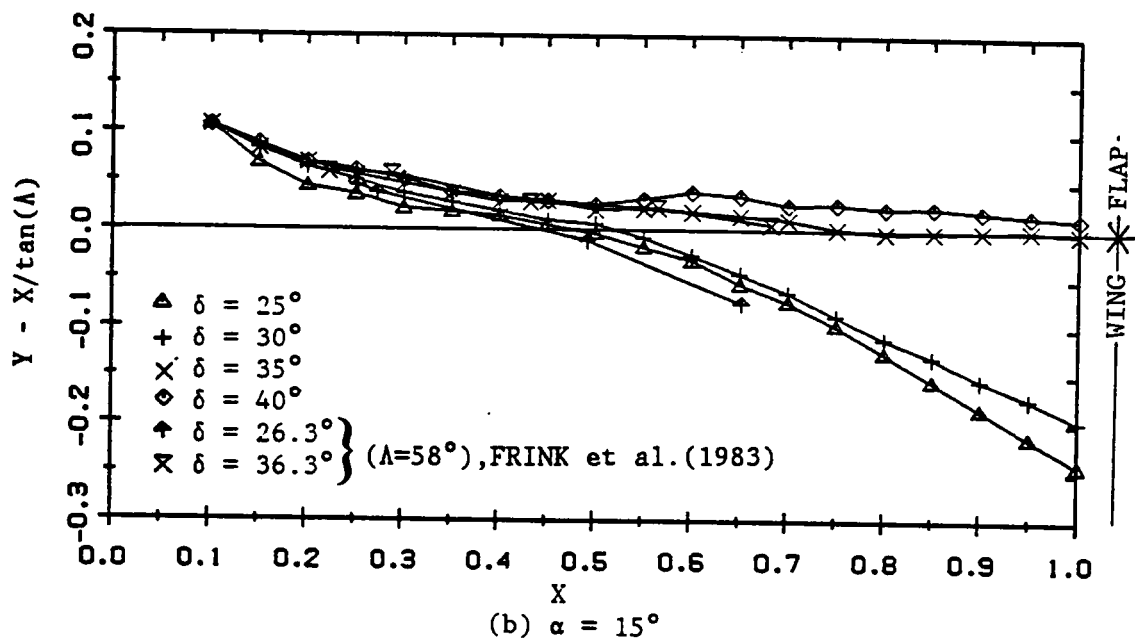
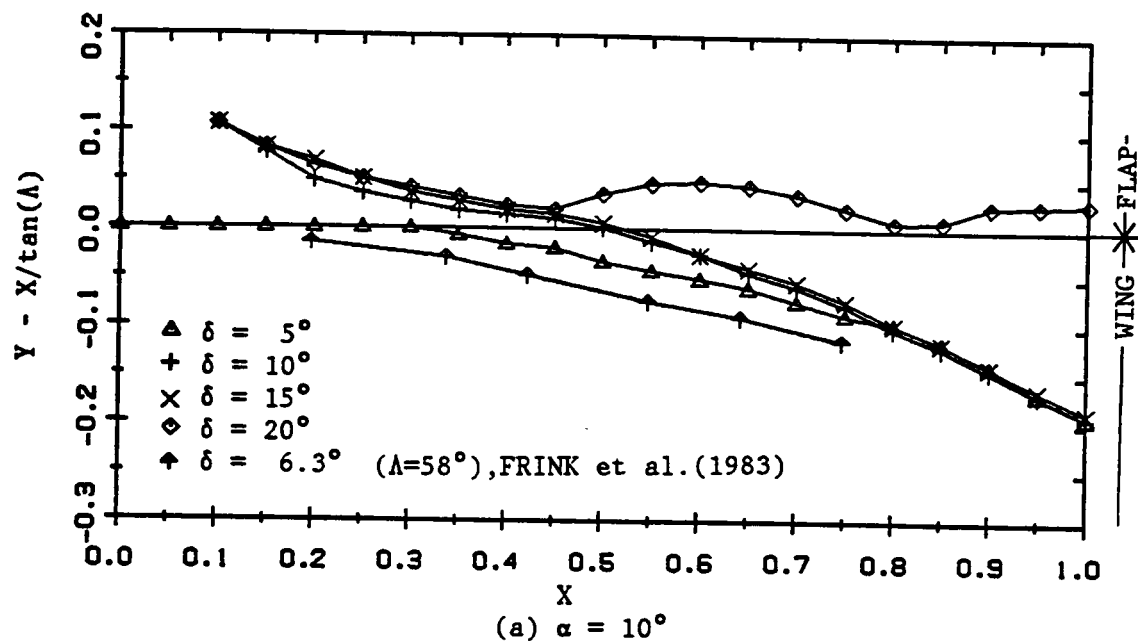


Fig. 24. Comparison of reattachment line data with the result of Frink et al. (1983).

ALPHA= 0
 RE=2,150,000

□	$\alpha=0.0$	$\delta=0.0$
○	$\alpha=0.0$	$\delta=5.0$
△	$\alpha=0.0$	$\delta=10.0$
+	$\alpha=0.0$	$\delta=15.0$
X	$\alpha=0.0$	$\delta=20.0$
◇	$\alpha=0.0$	$\delta=25.0$
⊕	$\alpha=0.0$	$\delta=30.0$
⊗	$\alpha=0.0$	$\delta=35.0$
Z	$\alpha=0.0$	$\delta=40.0$
Y	$\alpha=0.0$	$\delta=45.0$

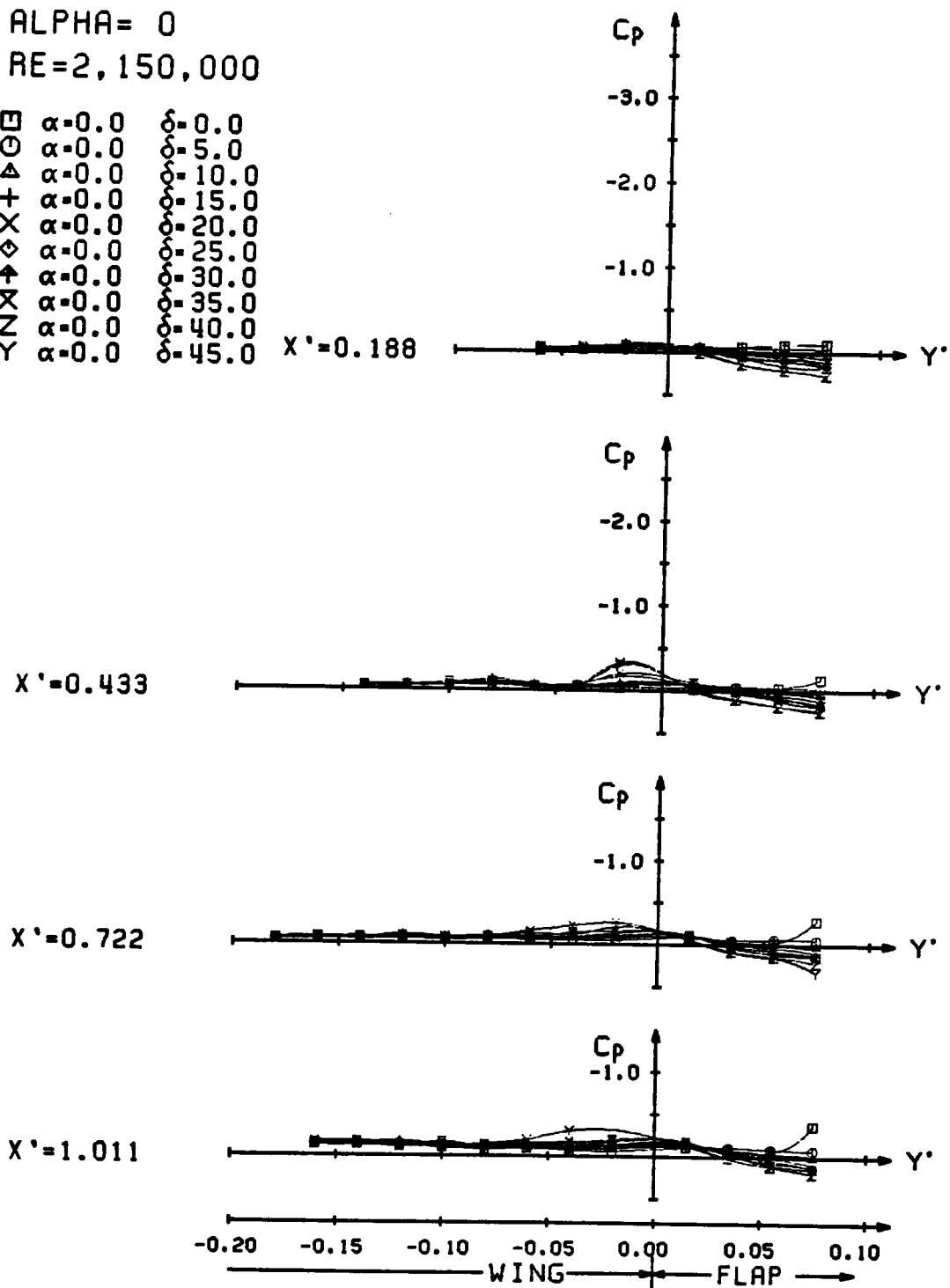
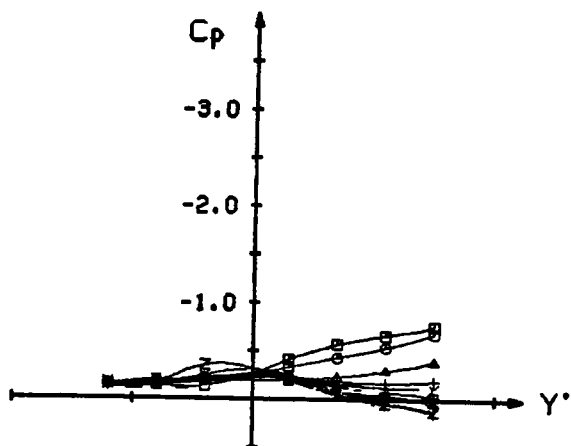


Fig. 25. Effect of flap deflection at $\alpha=0^\circ$ (experiment).

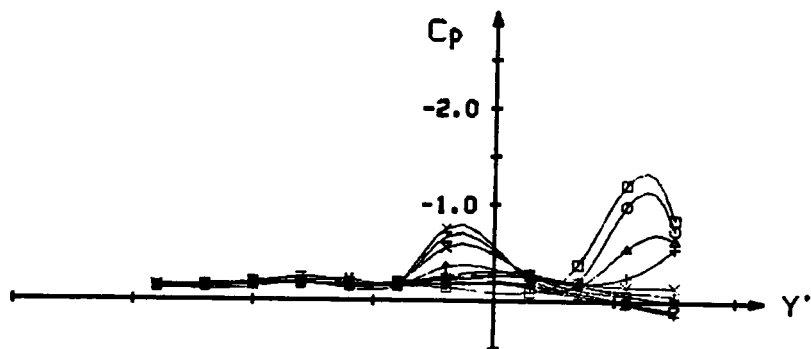
ALPHA= 5
 RE=2,150,000

□	$\alpha=5.0$	$\delta=0.0$
○	$\alpha=5.0$	$\delta=5.0$
△	$\alpha=5.0$	$\delta=10.0$
+	$\alpha=5.0$	$\delta=15.0$
x	$\alpha=5.0$	$\delta=20.0$
◇	$\alpha=5.0$	$\delta=25.0$
↑	$\alpha=5.0$	$\delta=30.0$
×	$\alpha=5.0$	$\delta=35.0$
z	$\alpha=5.0$	$\delta=40.0$
Y	$\alpha=5.0$	$\delta=45.0$

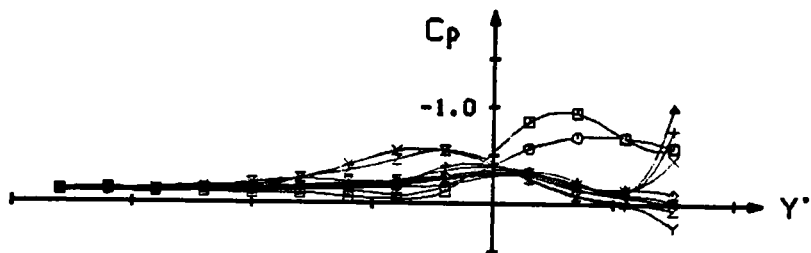
$X'=0.188$



$X'=0.433$



$X'=0.722$



$X'=1.011$

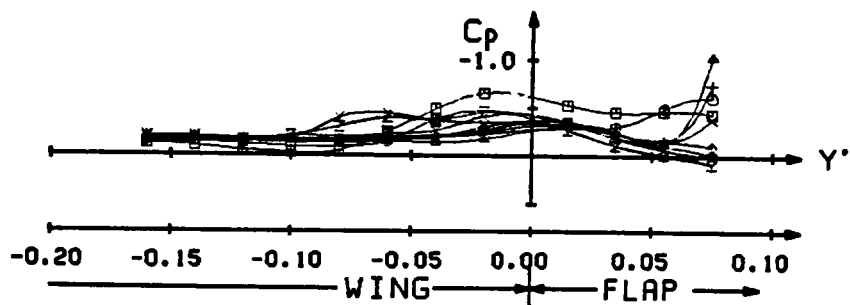
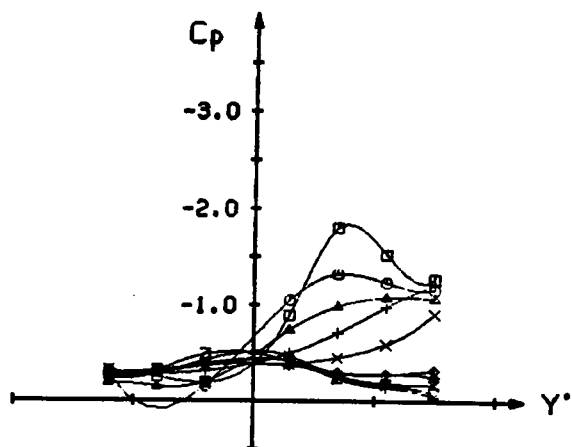


Fig. 26. Effect of flap deflection at $\alpha=5^\circ$ (experiment).

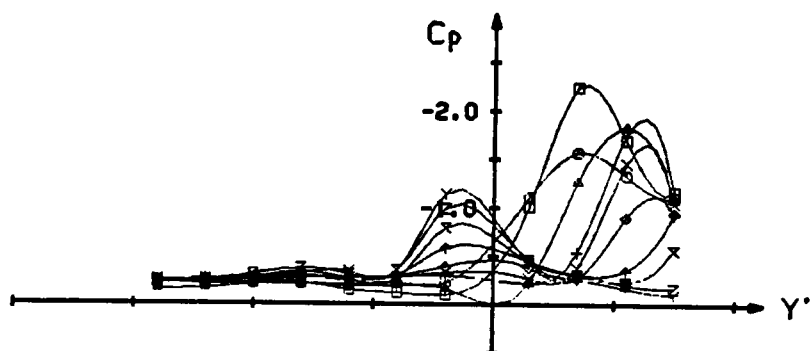
ALPHA=10
 RE=2,140,000

□	$\alpha=10.0$	$\delta=0.0$
○	$\alpha=10.0$	$\delta=5.0$
△	$\alpha=10.0$	$\delta=10.0$
+	$\alpha=10.0$	$\delta=15.0$
x	$\alpha=10.0$	$\delta=20.0$
◇	$\alpha=10.0$	$\delta=25.0$
↑	$\alpha=10.0$	$\delta=30.0$
XX	$\alpha=10.0$	$\delta=35.0$
ZZ	$\alpha=10.0$	$\delta=40.0$
Y	$\alpha=10.0$	$\delta=45.0$

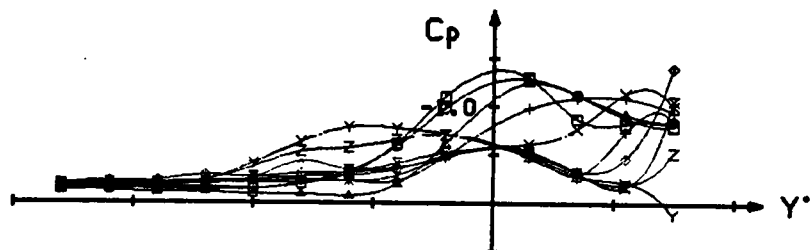
$X'=0.188$



$X'=0.433$



$X'=0.722$



$X'=1.011$

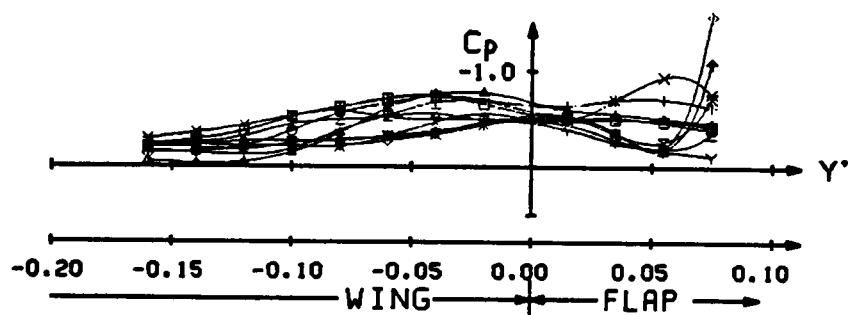
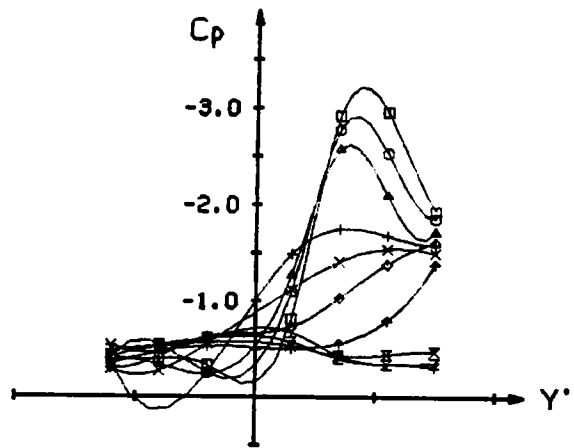


Fig. 27. Effect of flap deflection at $\alpha=10^\circ$ (experiment).

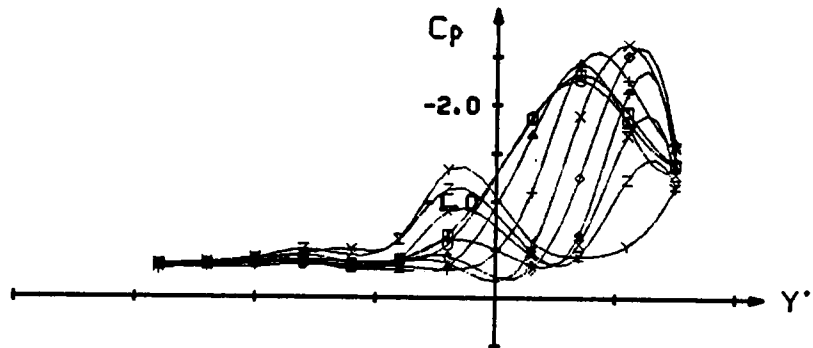
ALPHA=15
 RE=2,140,000

□	$\alpha=15.0$	$\delta=0.0$
○	$\alpha=15.0$	$\delta=5.0$
△	$\alpha=15.0$	$\delta=10.0$
+	$\alpha=15.0$	$\delta=15.0$
x	$\alpha=15.0$	$\delta=20.0$
◇	$\alpha=15.0$	$\delta=25.0$
⬆	$\alpha=15.0$	$\delta=30.0$
XX	$\alpha=15.0$	$\delta=35.0$
ZZ	$\alpha=15.0$	$\delta=40.0$
Y	$\alpha=15.0$	$\delta=45.0$

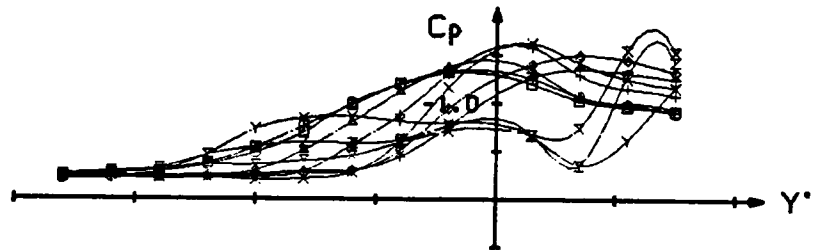
$X'=0.188$



$X'=0.433$



$X'=0.722$



$X'=1.011$

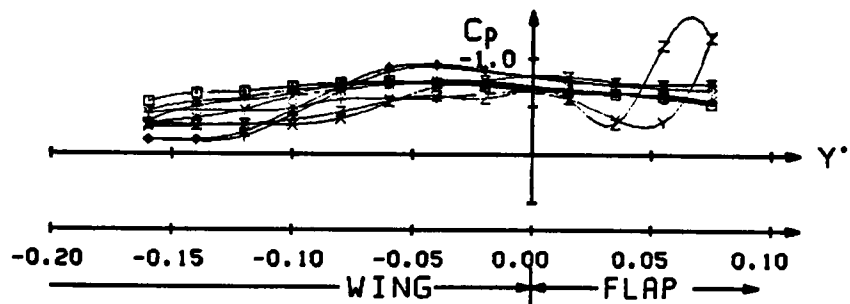
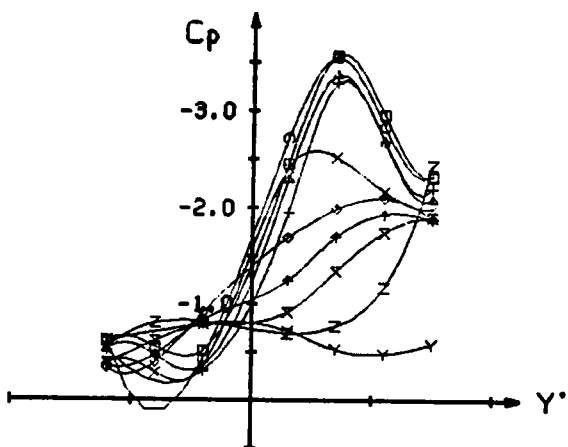


Fig. 28. Effect of flap deflection at $\alpha=15^\circ$ (experiment).

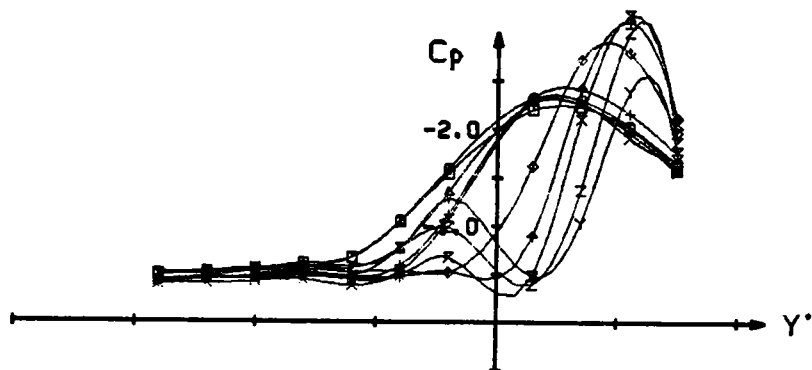
ALPHA=20
 RE=2,140,000

□	$\alpha=20.0$	$\delta=0.0$
○	$\alpha=20.0$	$\delta=5.0$
△	$\alpha=20.0$	$\delta=10.0$
+	$\alpha=20.0$	$\delta=15.0$
X	$\alpha=20.0$	$\delta=20.0$
◇	$\alpha=20.0$	$\delta=25.0$
▲	$\alpha=20.0$	$\delta=30.0$
X	$\alpha=20.0$	$\delta=35.0$
Z	$\alpha=20.0$	$\delta=40.0$
Y	$\alpha=20.0$	$\delta=45.0$

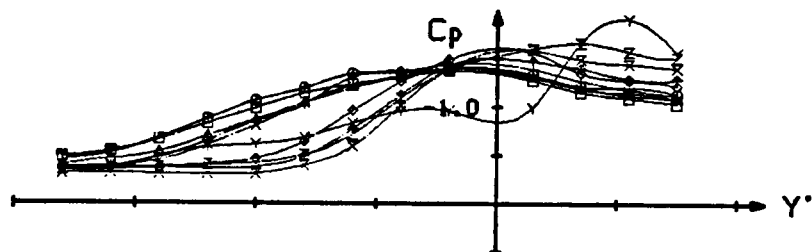
$X'=0.188$



$X'=0.433$



$X'=0.722$



$X'=1.011$

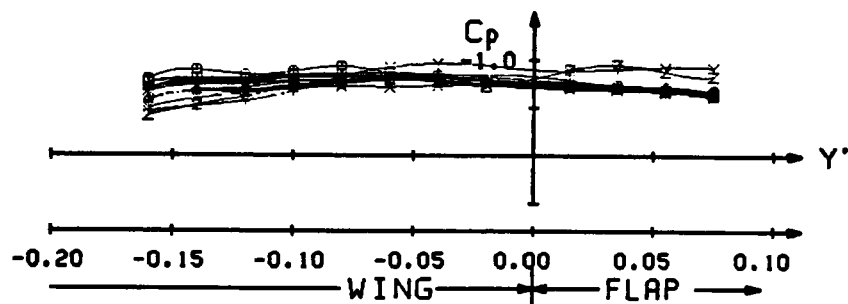


Fig. 29. Effect of flap deflection at $\alpha=20^\circ$ (experiment).

ALPHA=25
 RE=2,140,000

□	$\alpha=25.0$	$\delta=0.0$
○	$\alpha=25.0$	$\delta=5.0$
△	$\alpha=25.0$	$\delta=10.0$
+	$\alpha=25.0$	$\delta=15.0$
x	$\alpha=25.0$	$\delta=20.0$
◇	$\alpha=25.0$	$\delta=25.0$
↑	$\alpha=25.0$	$\delta=30.0$
X	$\alpha=25.0$	$\delta=35.0$
Z	$\alpha=25.0$	$\delta=40.0$
Y	$\alpha=25.0$	$\delta=45.0$

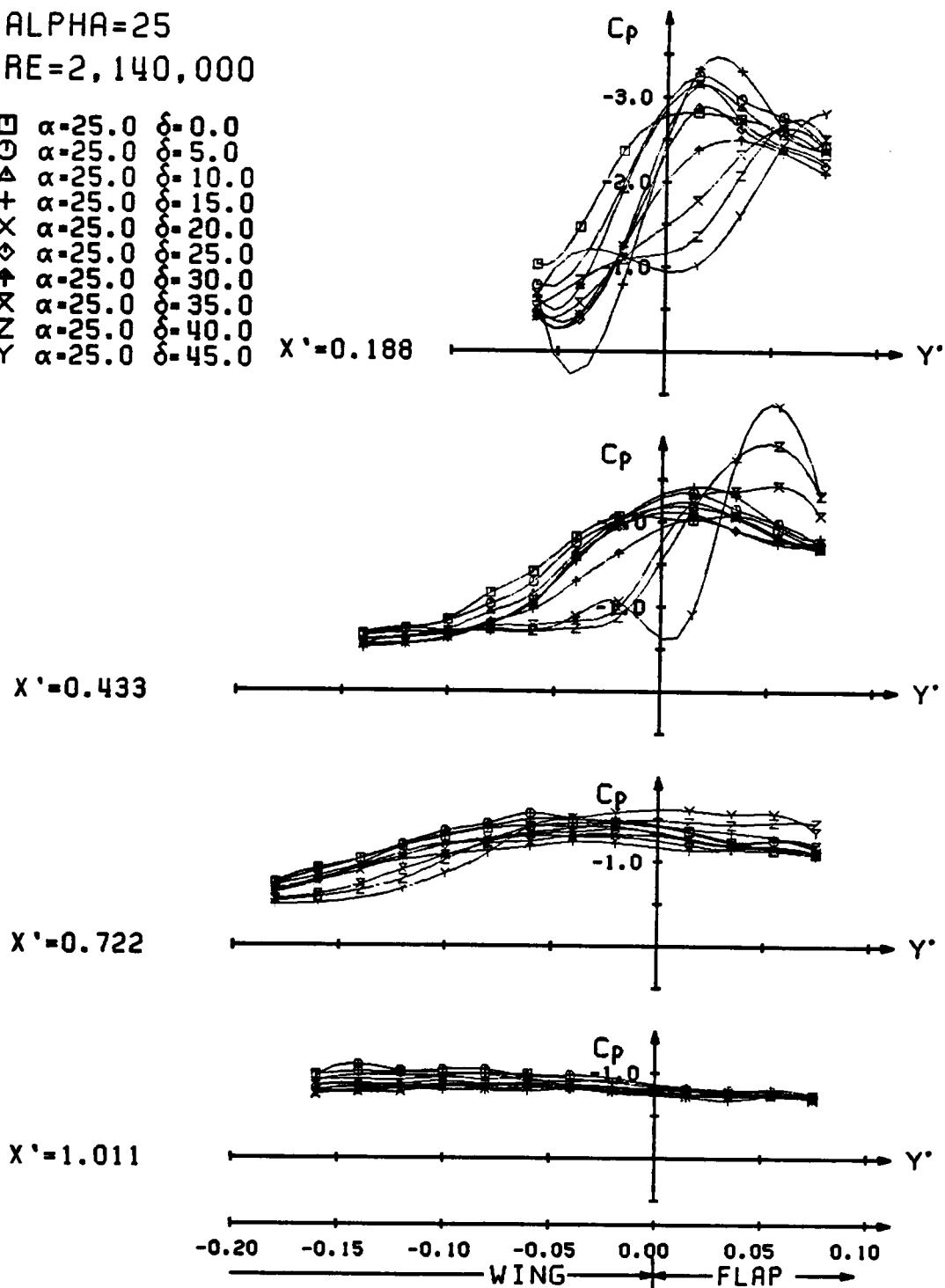


Fig. 30. Effect of flap deflection at $\alpha=25^\circ$ (experiment).

ALPHA=30
 RE=2,140,000

□	$\alpha=30.0$	$\delta=0.0$
○	$\alpha=30.0$	$\delta=5.0$
△	$\alpha=30.0$	$\delta=10.0$
+	$\alpha=30.0$	$\delta=15.0$
x	$\alpha=30.0$	$\delta=20.0$
◇	$\alpha=30.0$	$\delta=25.0$
↑	$\alpha=30.0$	$\delta=30.0$
X	$\alpha=30.0$	$\delta=35.0$
Z	$\alpha=30.0$	$\delta=40.0$
Y	$\alpha=30.0$	$\delta=45.0$

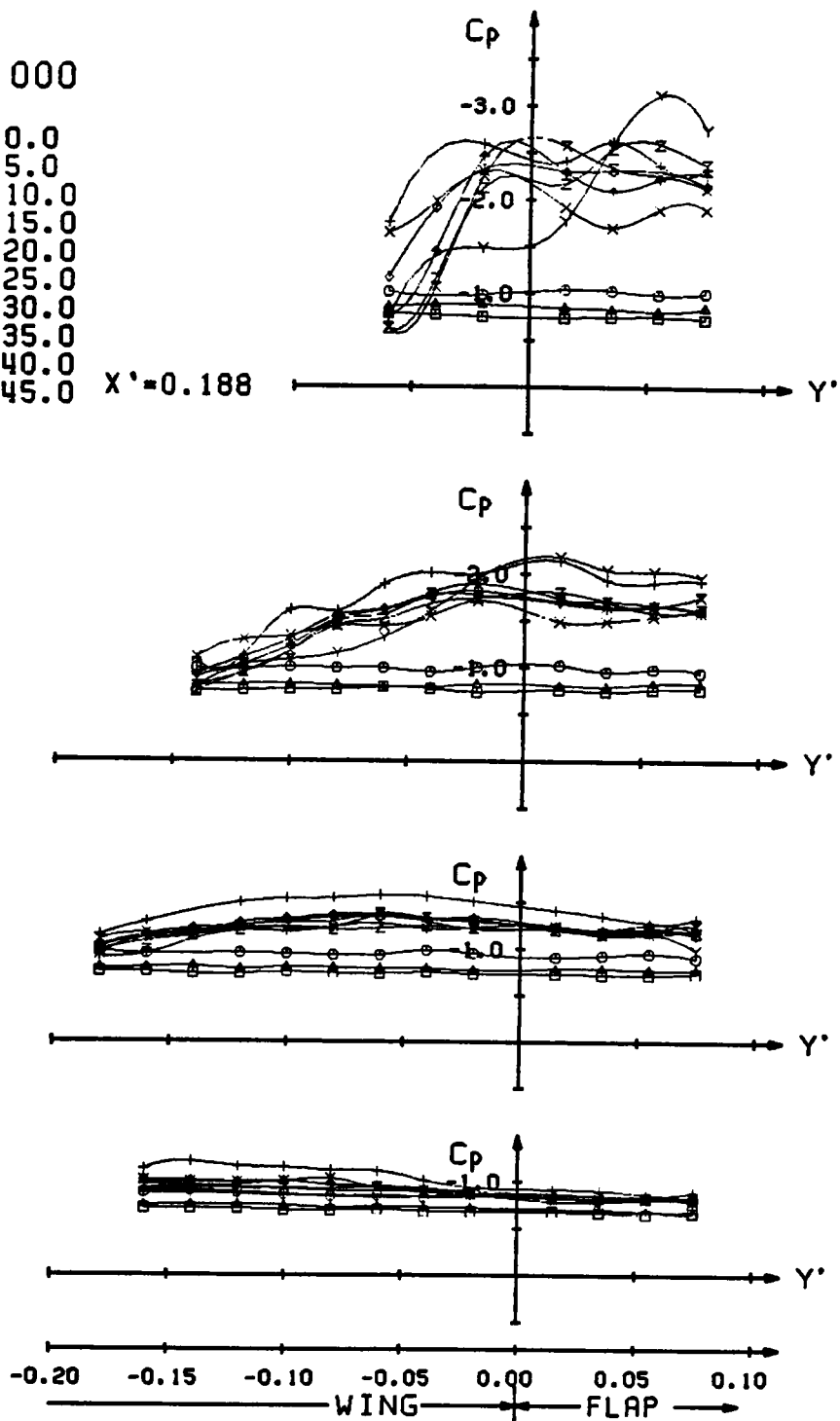
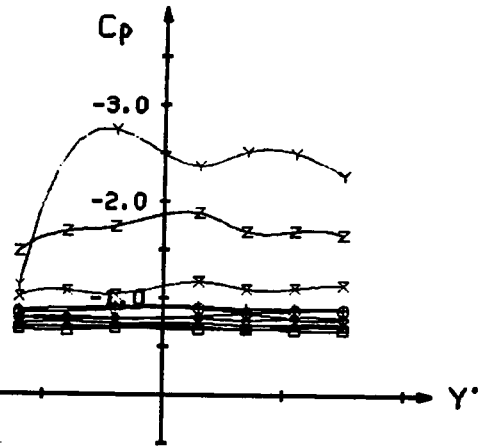


Fig. 31. Effect of flap deflection at $\alpha=30^\circ$ (experiment).

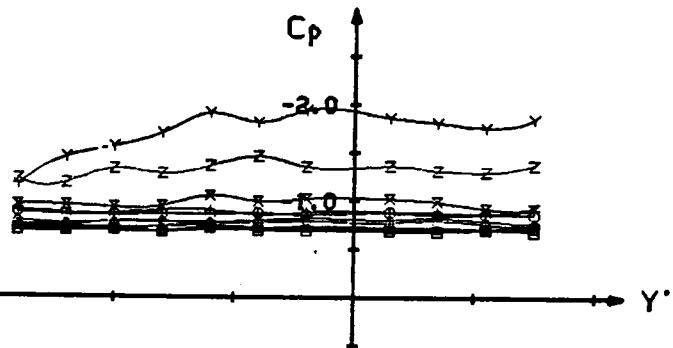
ALPHA=35
 RE=2,140,000

□	$\alpha=35.0$	$\delta=0.0$
○	$\alpha=35.0$	$\delta=5.0$
△	$\alpha=35.0$	$\delta=10.0$
+	$\alpha=35.0$	$\delta=15.0$
x	$\alpha=35.0$	$\delta=20.0$
◇	$\alpha=35.0$	$\delta=25.0$
↑	$\alpha=35.0$	$\delta=30.0$
×	$\alpha=35.0$	$\delta=35.0$
Z	$\alpha=35.0$	$\delta=40.0$
Y	$\alpha=35.0$	$\delta=45.0$

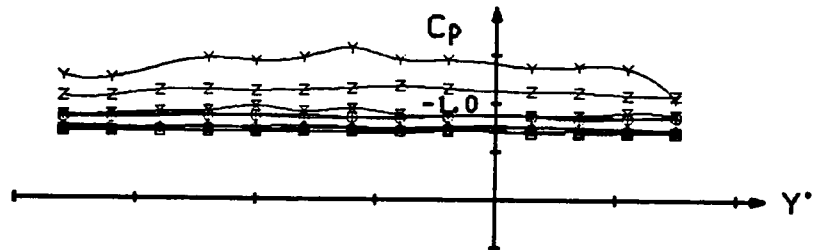
$X'=0.188$



$X'=0.433$



$X'=0.722$



$X'=1.011$

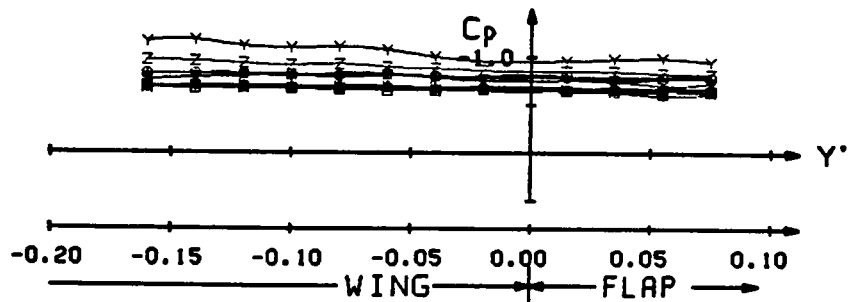
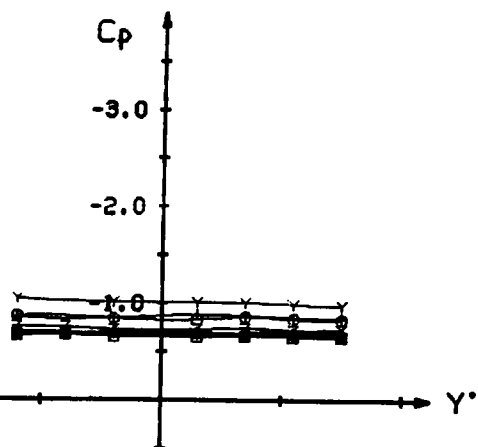


Fig. 32. Effect of flap deflection at $\alpha=35^\circ$ (experiment).

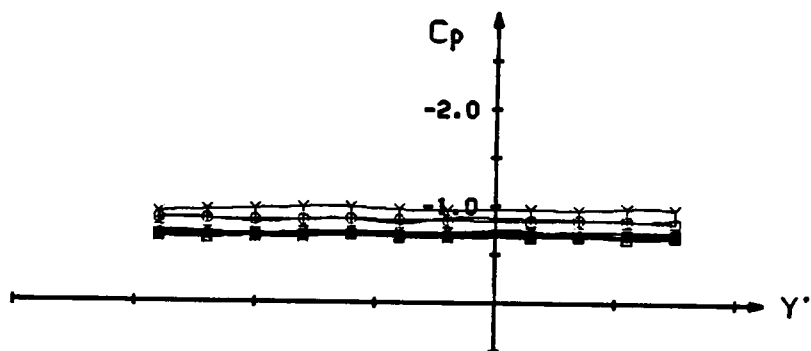
ALPHA=40
 RE=2,140,000

□ $\alpha=40.0$ $\delta=0.0$
 ○ $\alpha=40.0$ $\delta=5.0$
 △ $\alpha=40.0$ $\delta=10.0$
 + $\alpha=40.0$ $\delta=15.0$
 × $\alpha=40.0$ $\delta=20.0$
 ◇ $\alpha=40.0$ $\delta=25.0$
 ↑ $\alpha=40.0$ $\delta=30.0$
 X $\alpha=40.0$ $\delta=35.0$
 Z $\alpha=40.0$ $\delta=40.0$
 Y $\alpha=40.0$ $\delta=45.0$

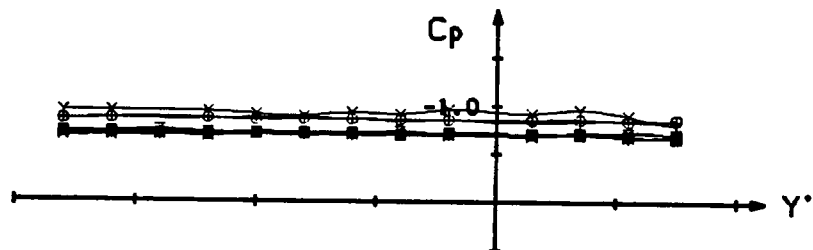
$X'=0.188$



$X'=0.433$



$X'=0.722$



$X'=1.011$

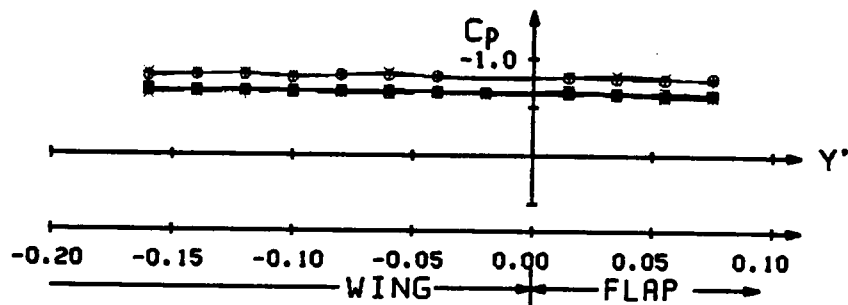


Fig. 33. Effect of flap deflection at $\alpha=40^\circ$ (experiment).

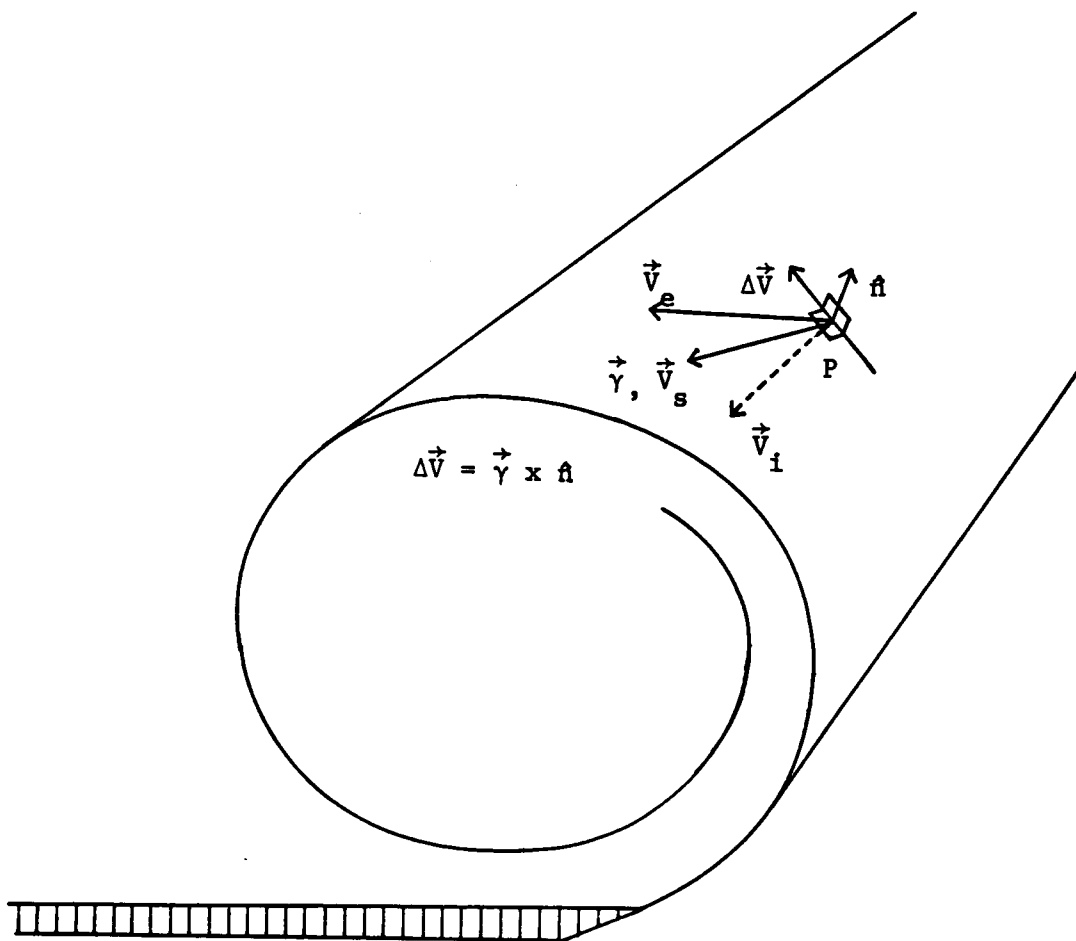


Fig. 34. Velocity jump across vortex sheet.

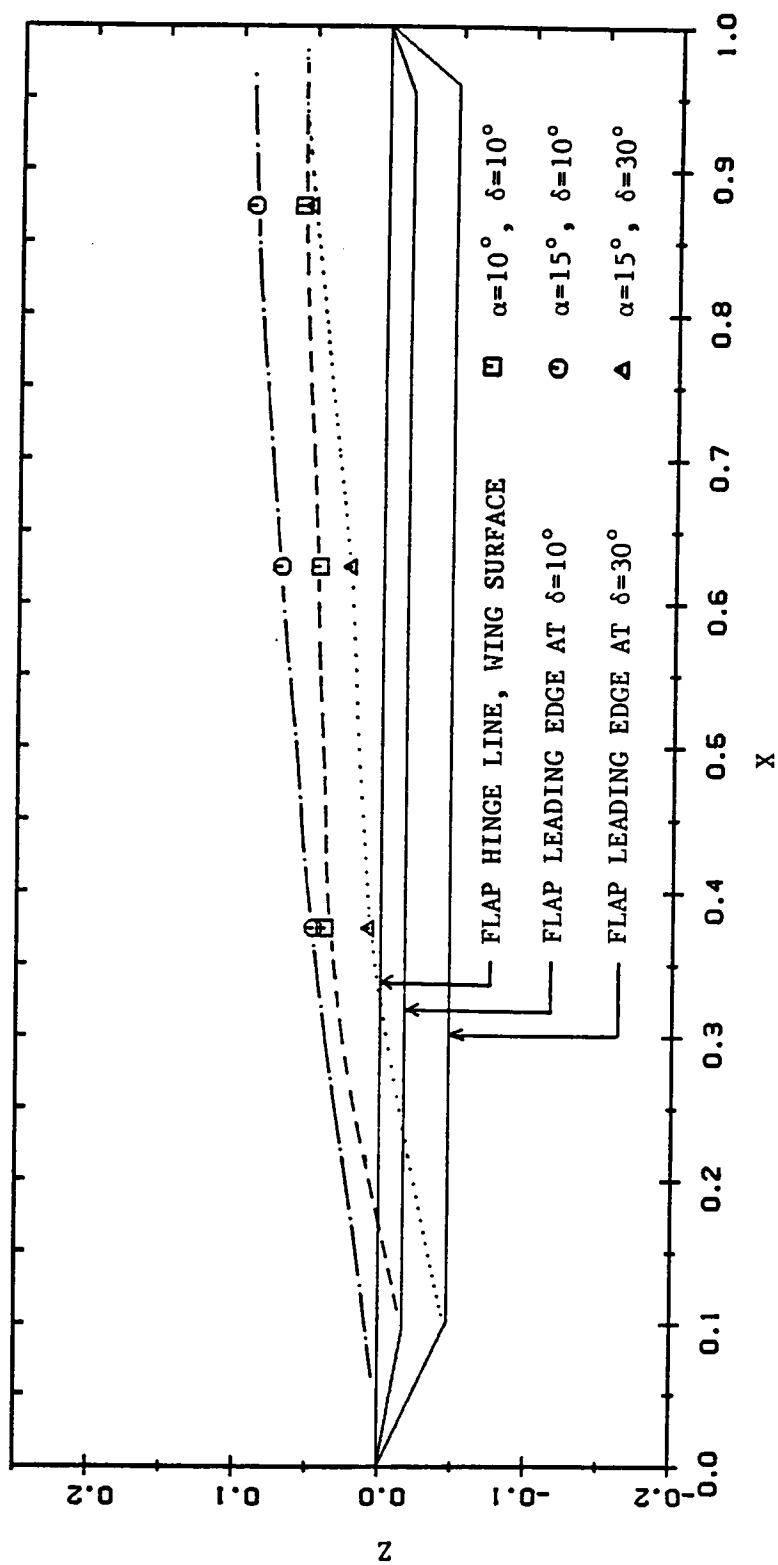


Fig. 35. Location of vortex core in the X-Z plane.

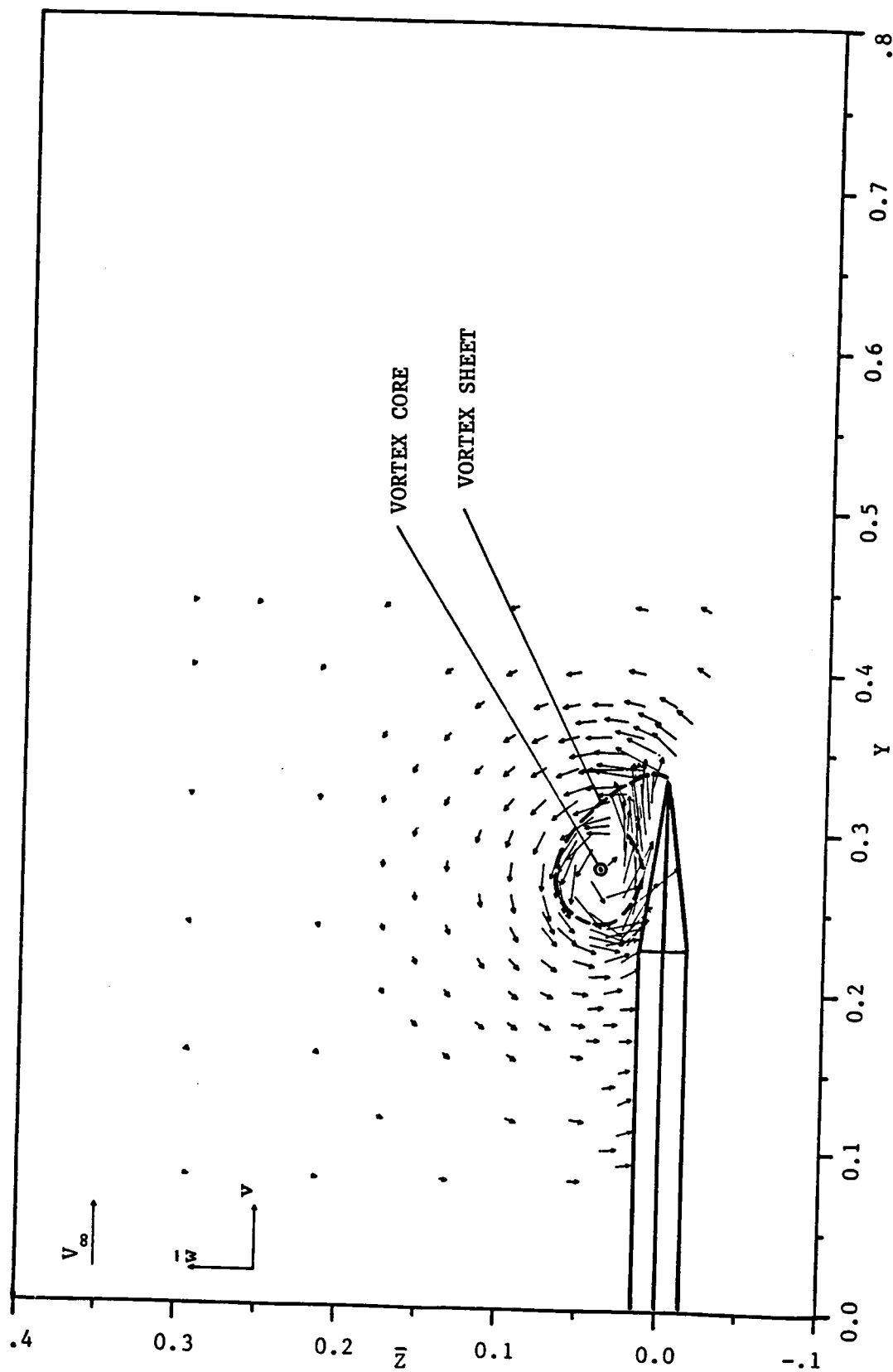


Fig. 36.a Velocity vector plot at $\alpha=10^\circ$ with $\delta=10^\circ$, $x=0.375$

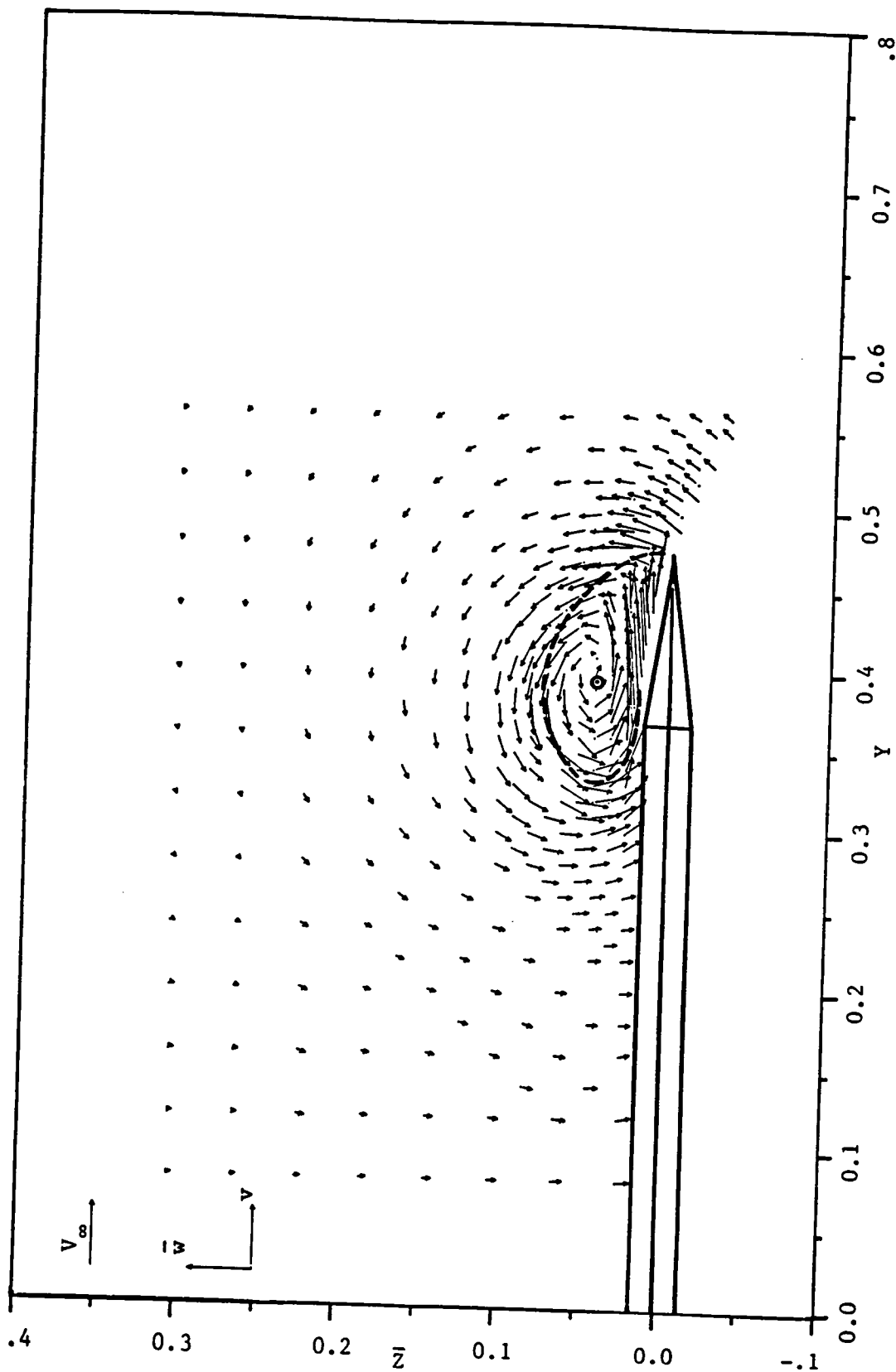


Fig. 36.b Continued. $x=0.625$

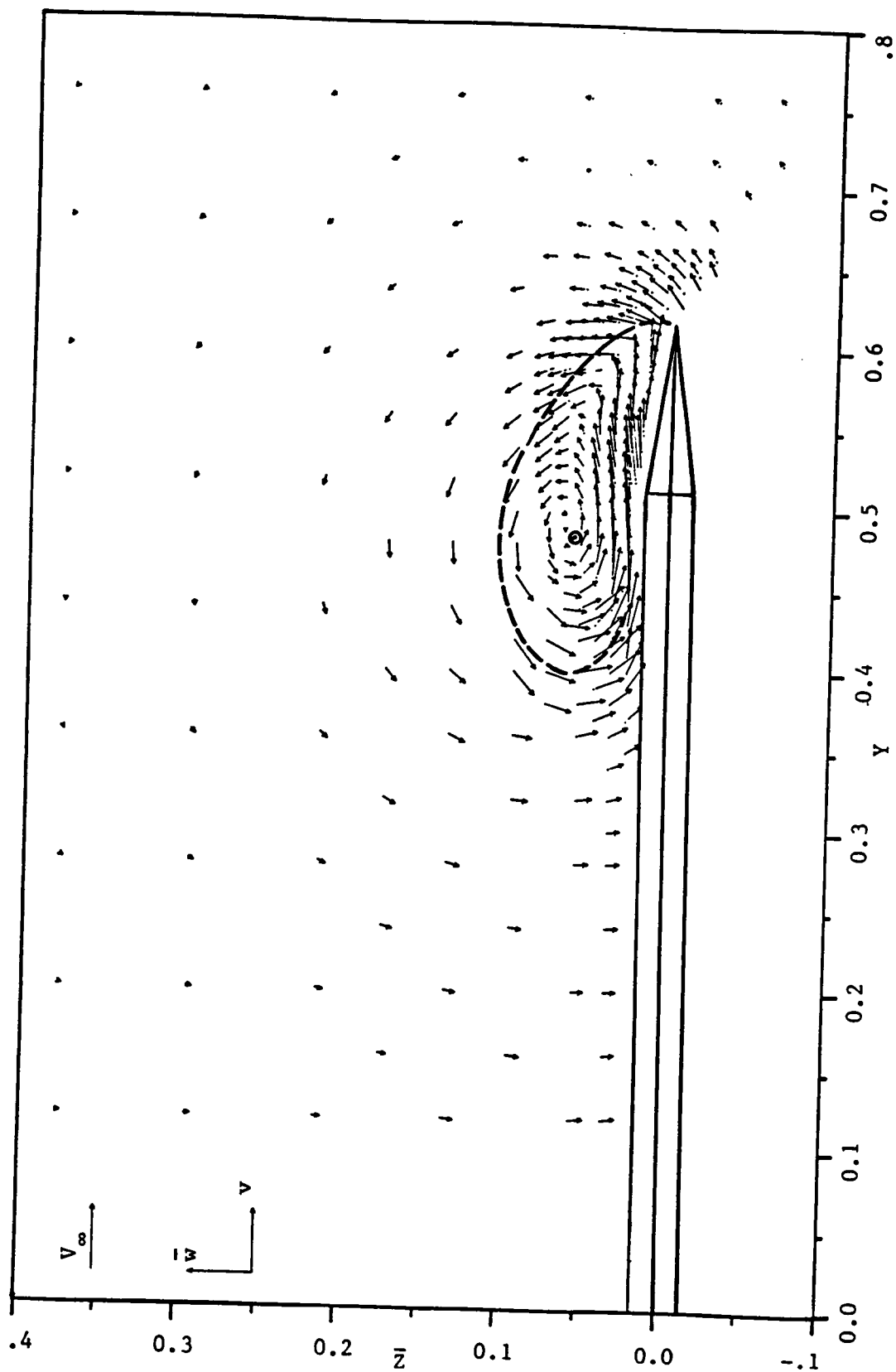


Fig. 36.c Concluded. $x=0.875$

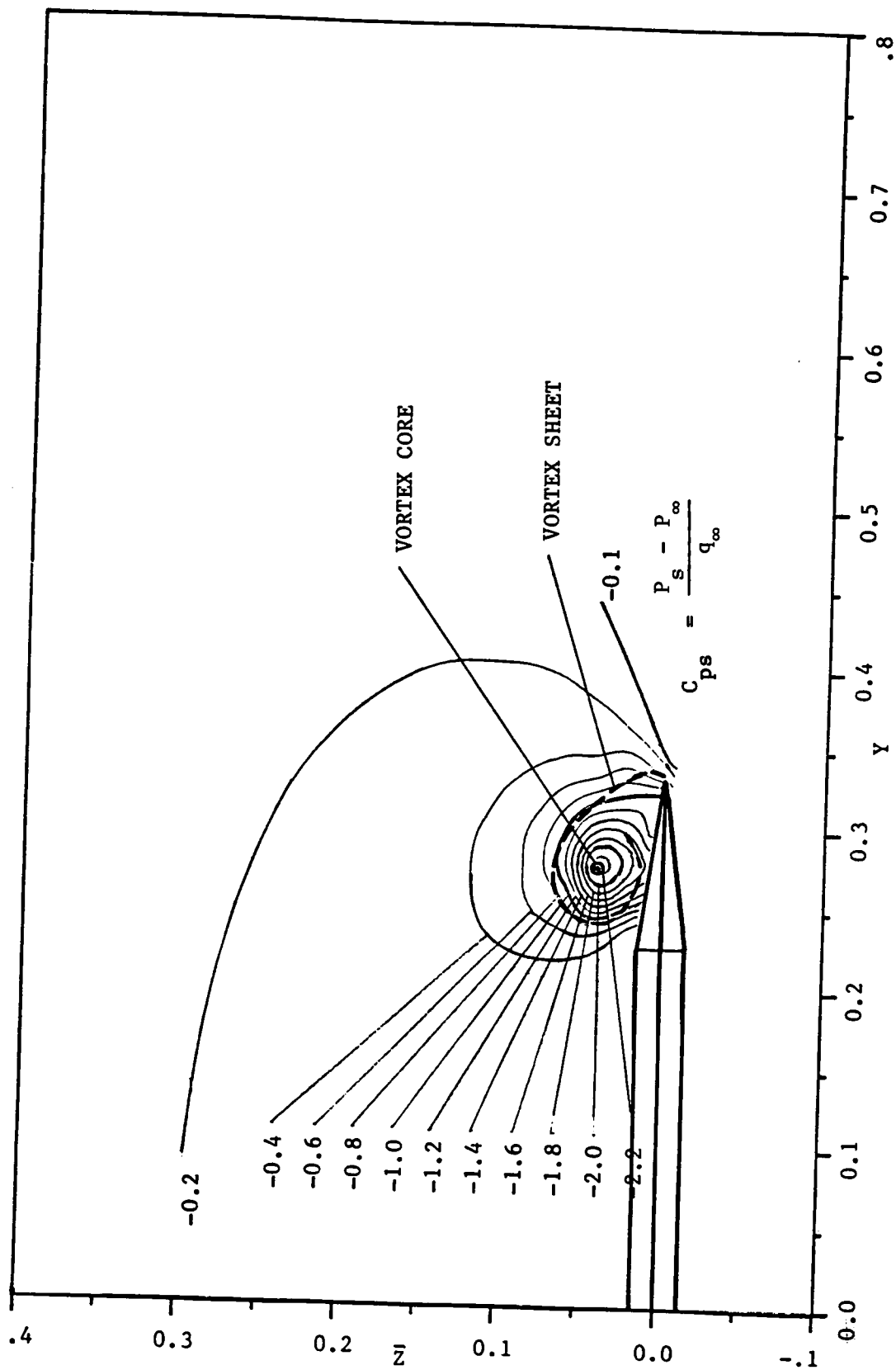


Fig. 37.a Static pressure distribution at $\alpha=10^\circ$ with $\delta=10^\circ$, $x=0.375$

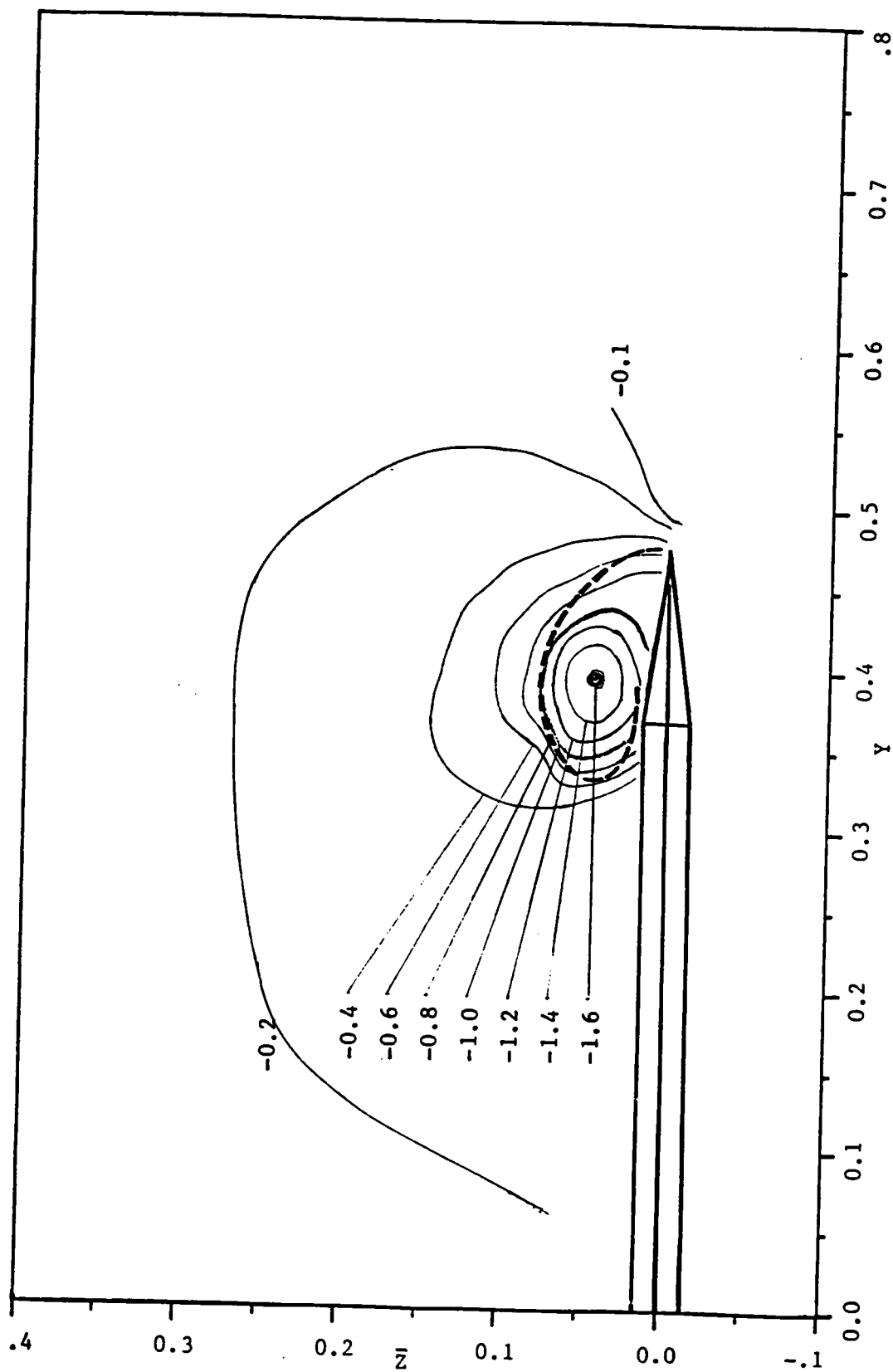


Fig. 37.b Continued, $x=0.625$

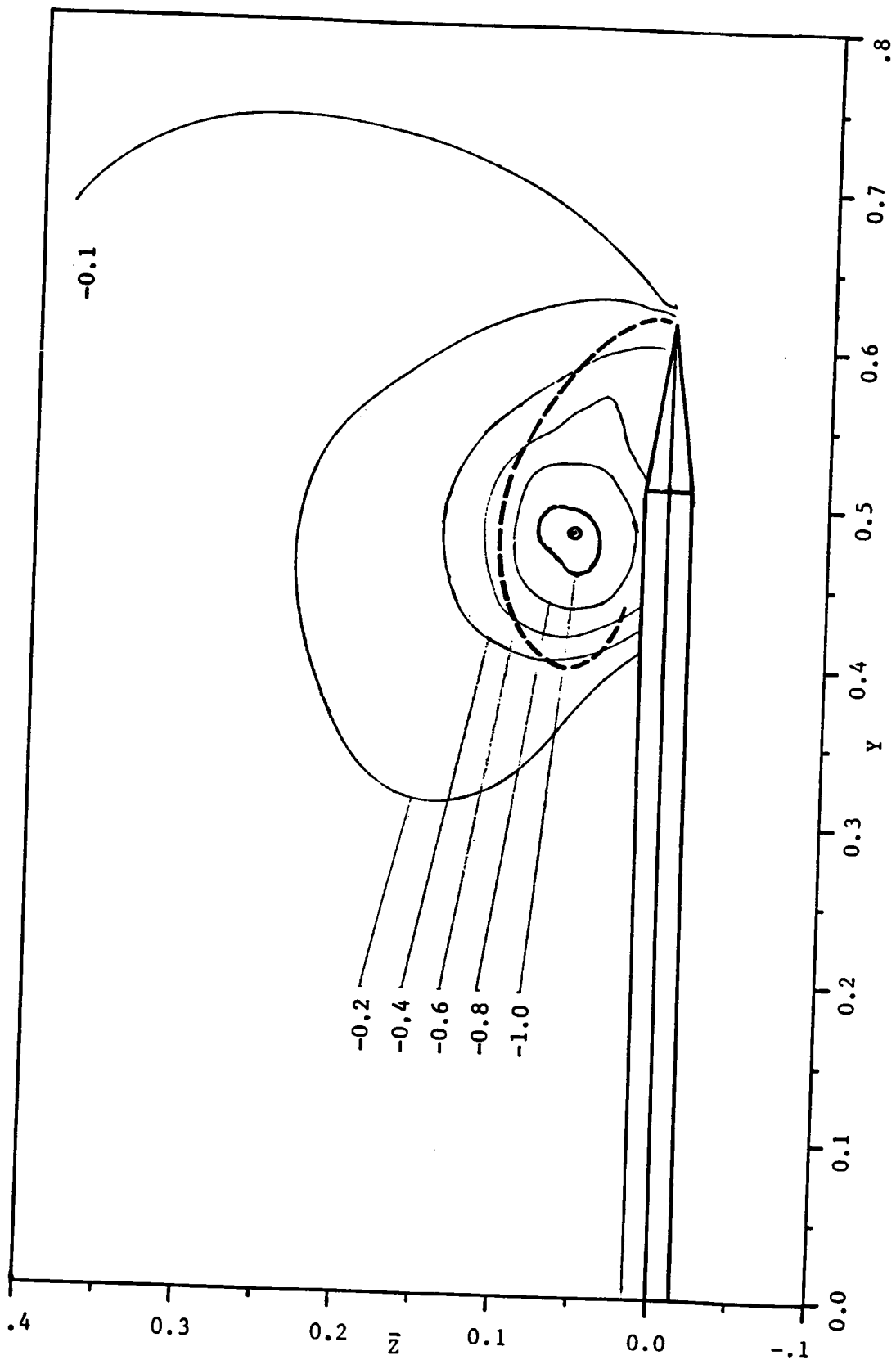


Fig. 37.c Concluded. $x=0.875$

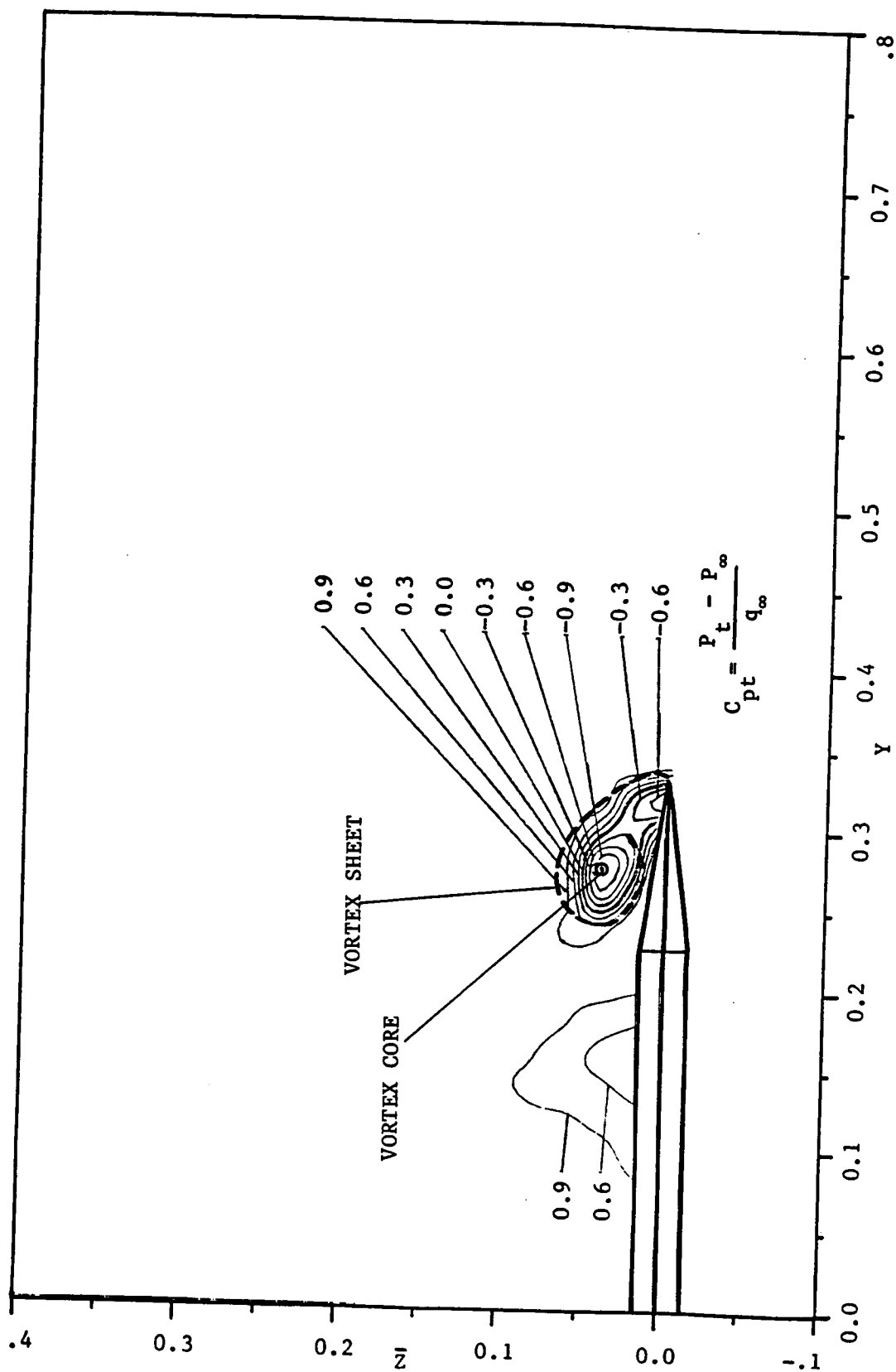


Fig. 38.a Total pressure distribution at $\alpha=10^\circ$ with $\delta=10^\circ$, $x=0.375$

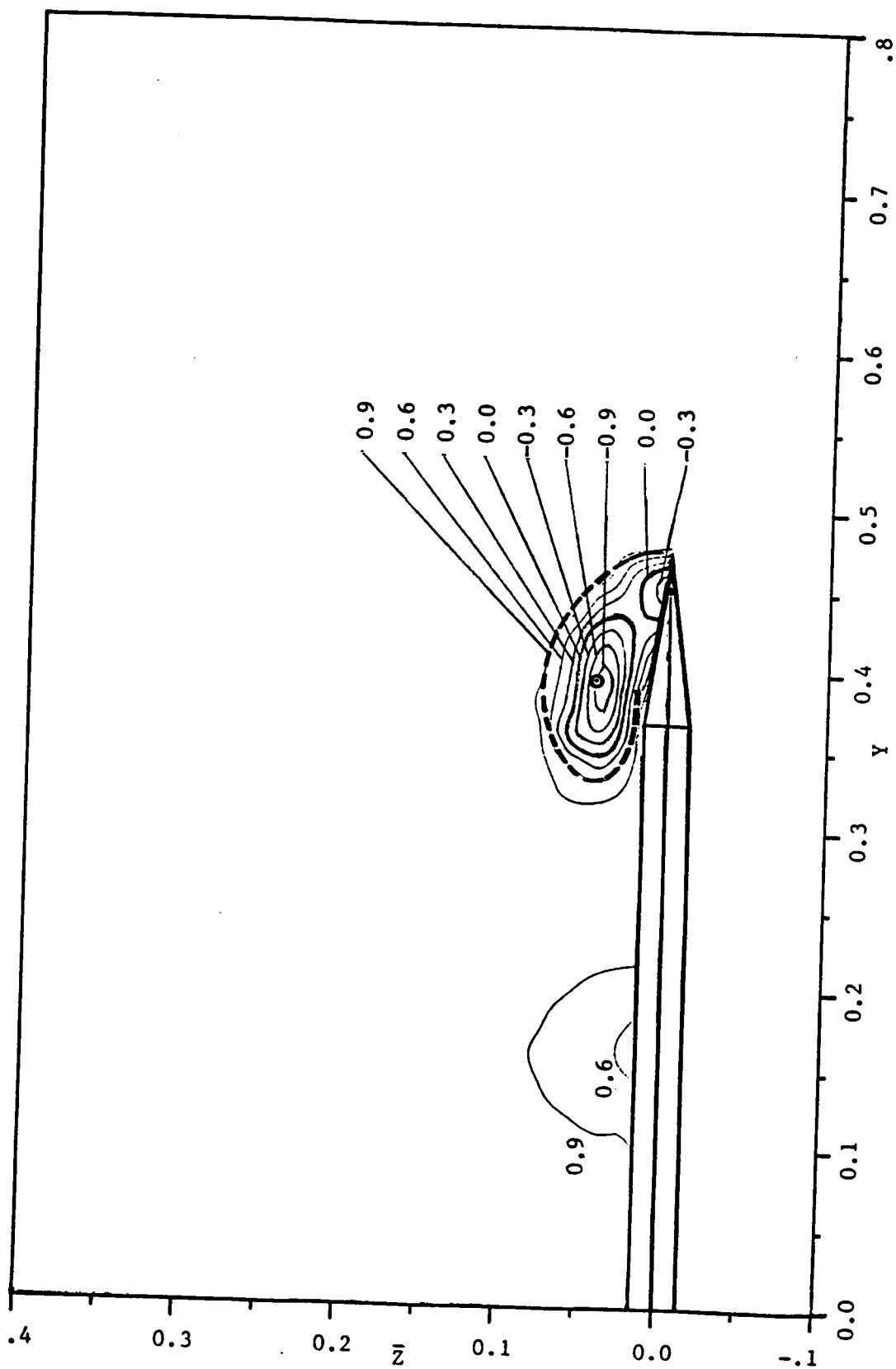


Fig. 38.b Continued. $x=0.625$

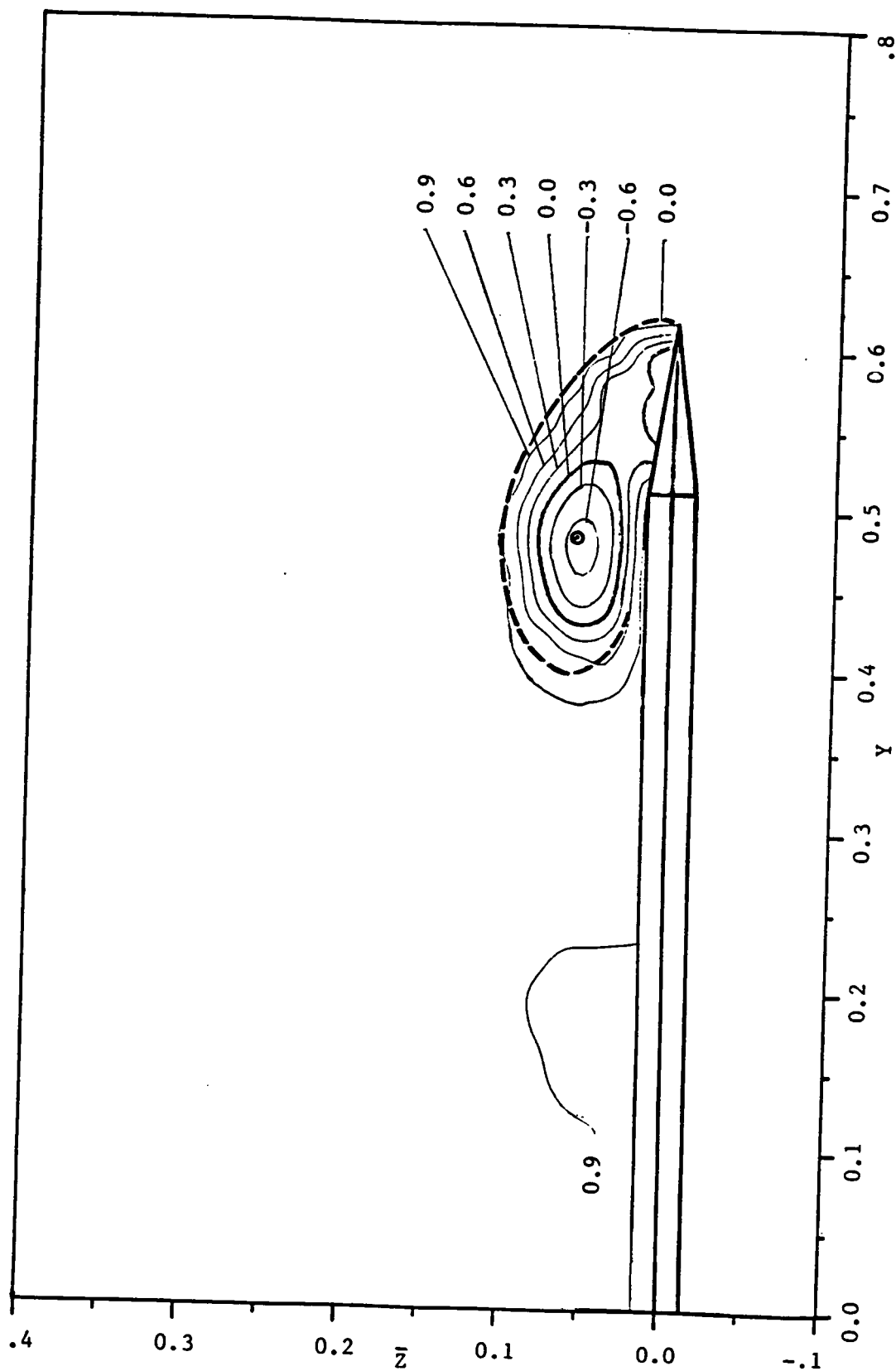


Fig. 38.c Concluded. $x=0.875$

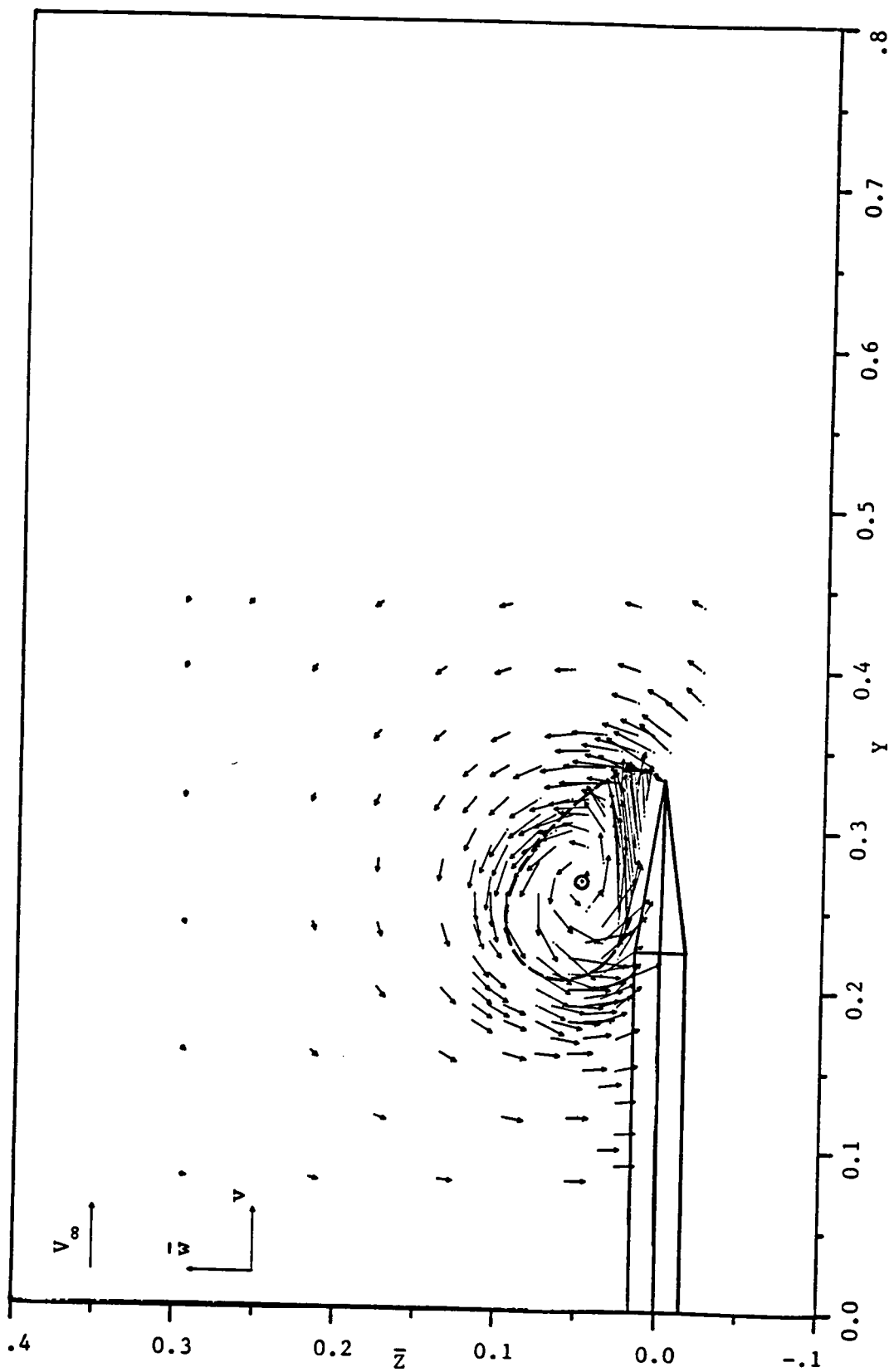


Fig. 39.a Velocity vector plot at $\alpha=15^\circ$ with $\delta=10^\circ$, $x=0.375$

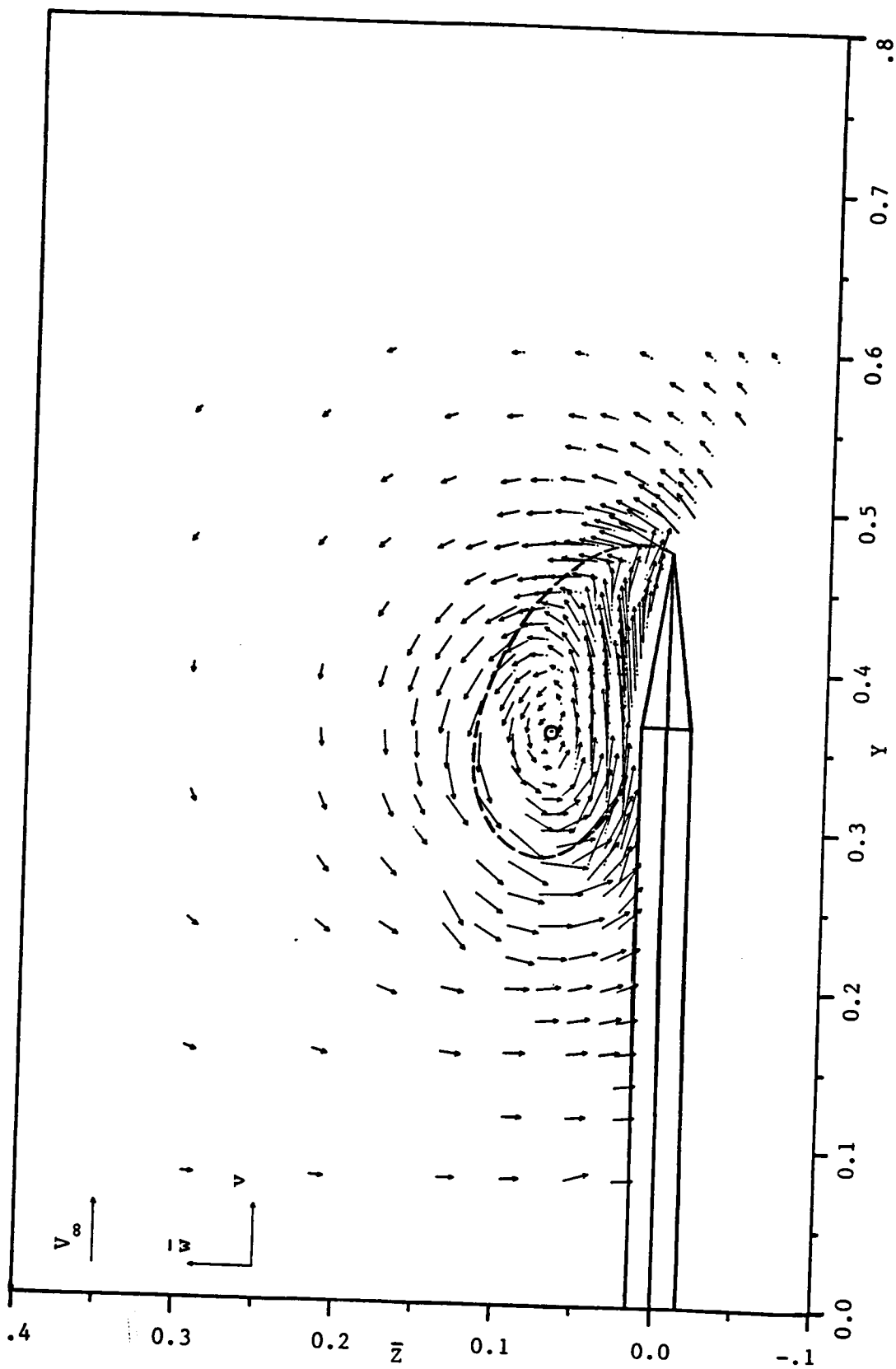


Fig. 39.b Continued. $x=0.625$

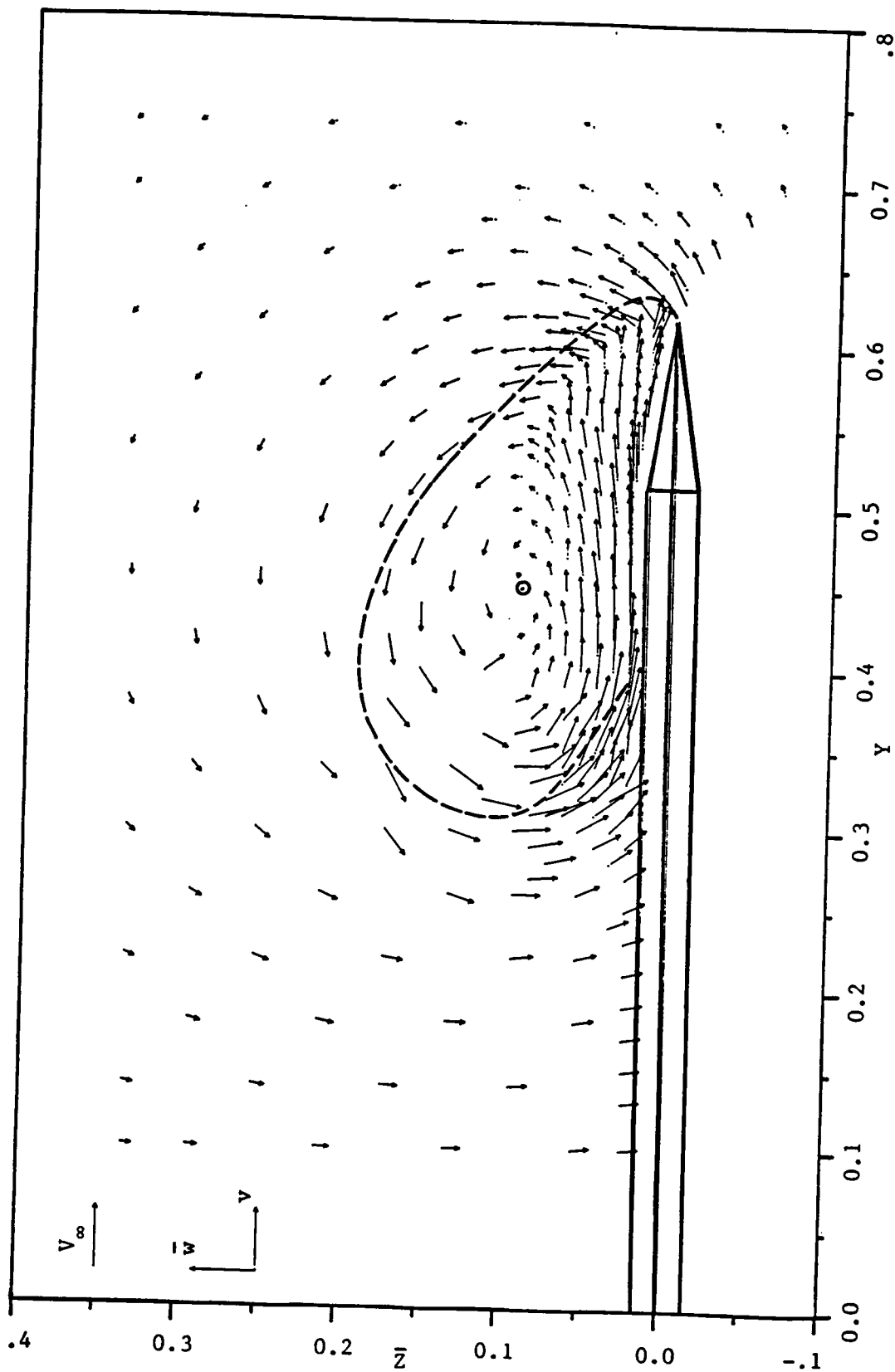


Fig. 39.c Concluded. $x=0.875$

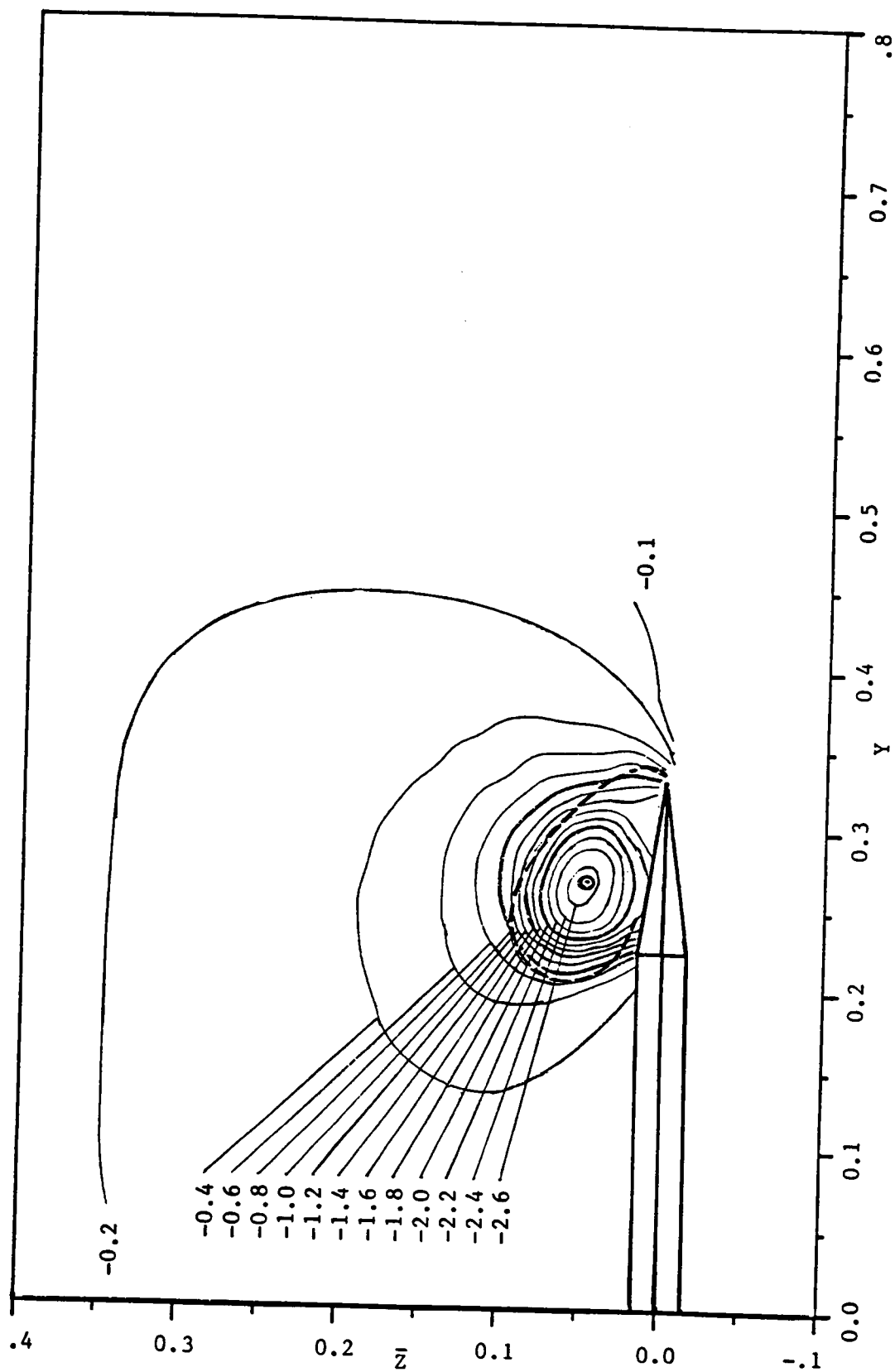


Fig. 40.a Static pressure distribution at $\alpha=15^\circ$ with $\delta=10^\circ$, $x=0.375$

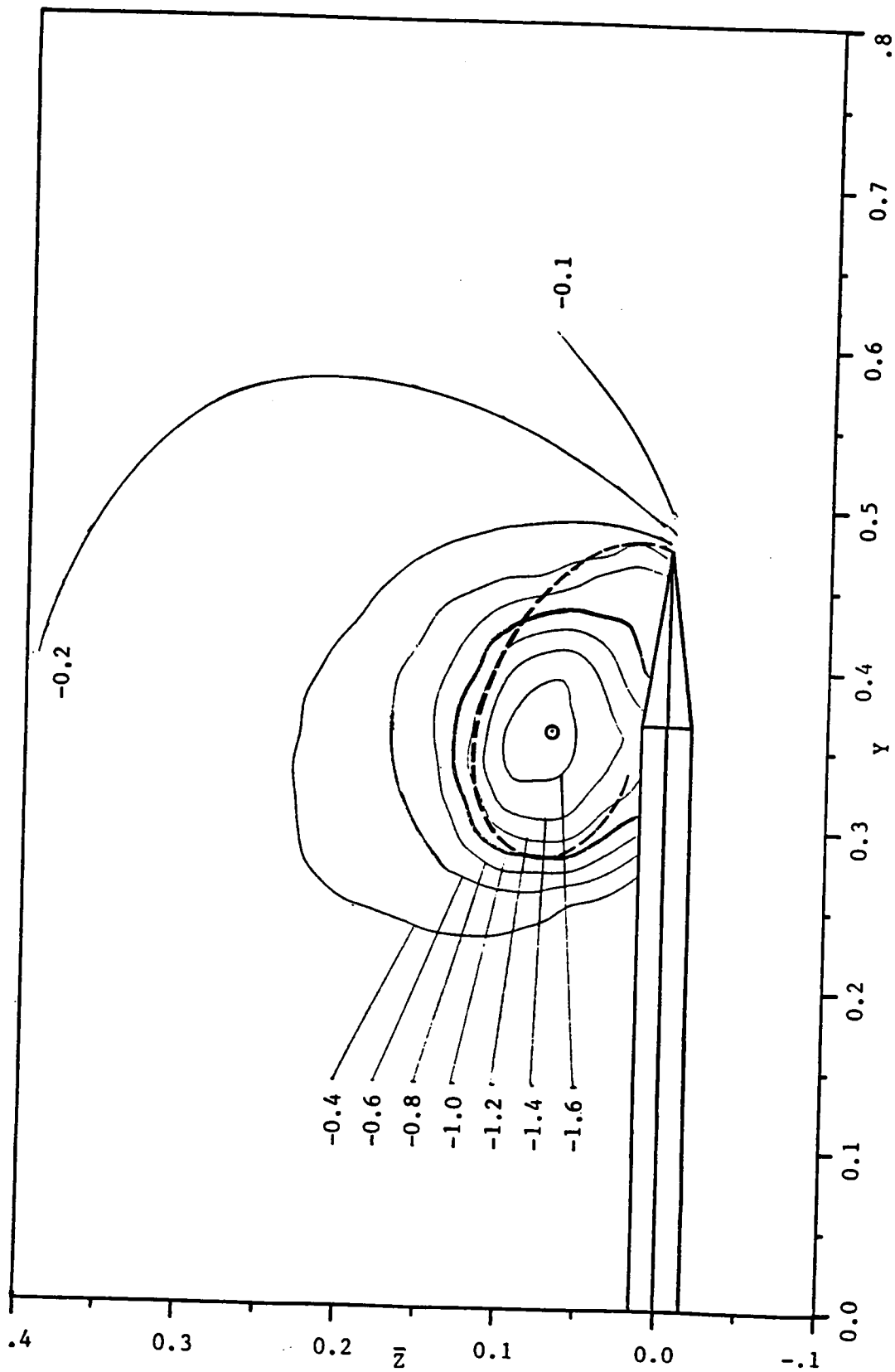


Fig. 40.b Continued. $x=0.625$

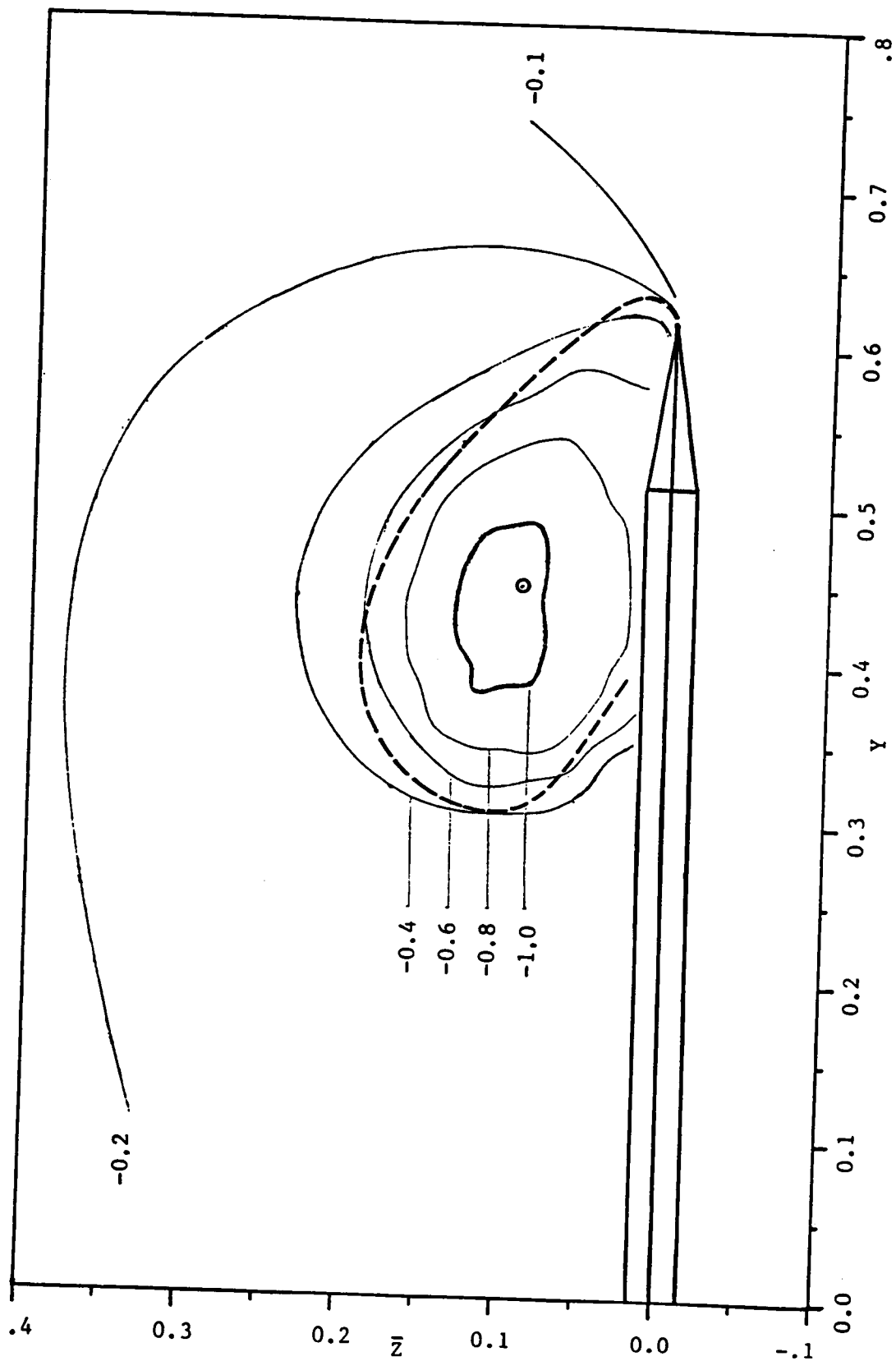


Fig. 40.c Concluded. $x=0.875$

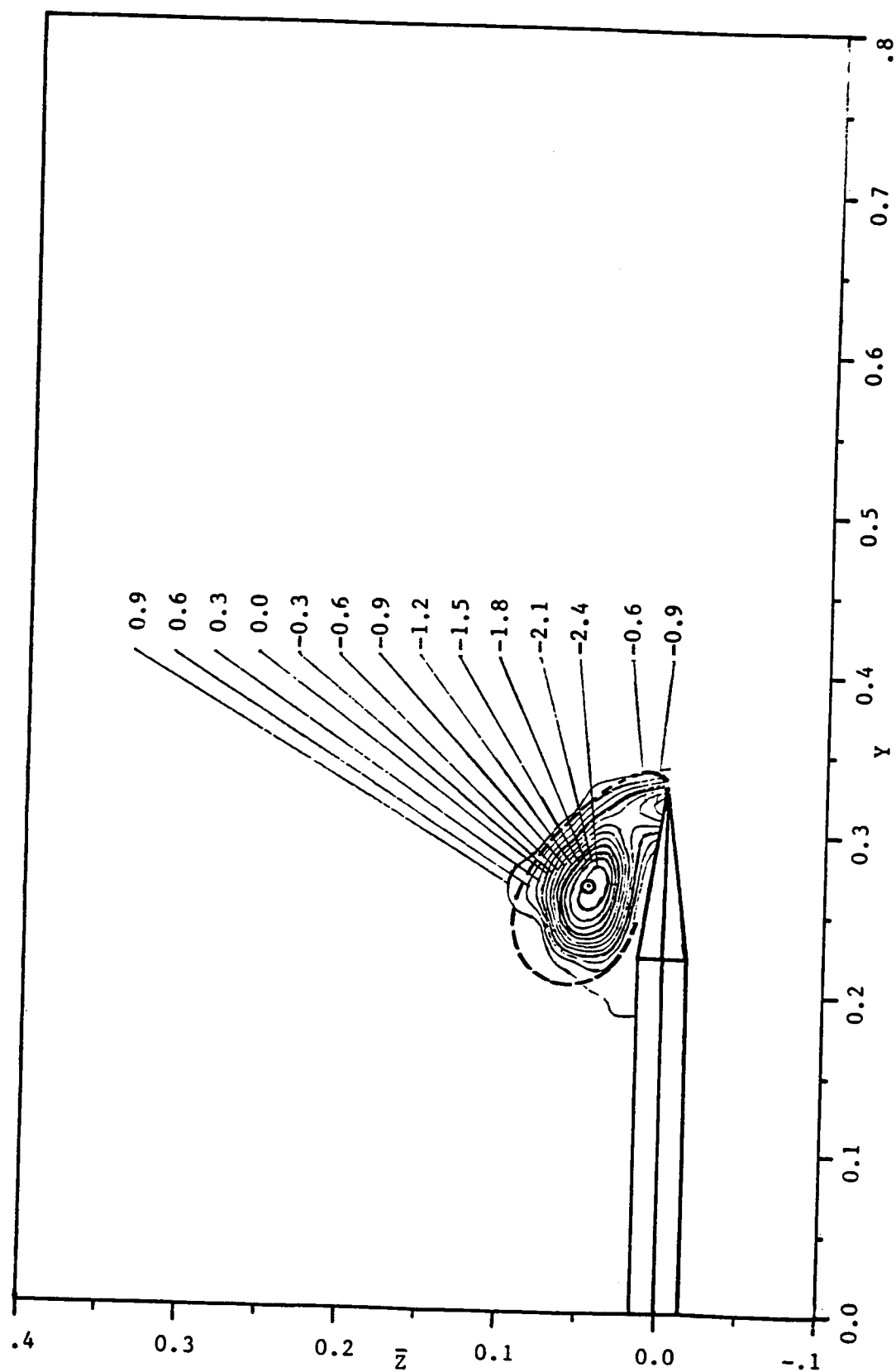


Fig. 41.a Total pressure distribution at $\alpha=15^\circ$ with $\delta=10^\circ$, $x=0.375$

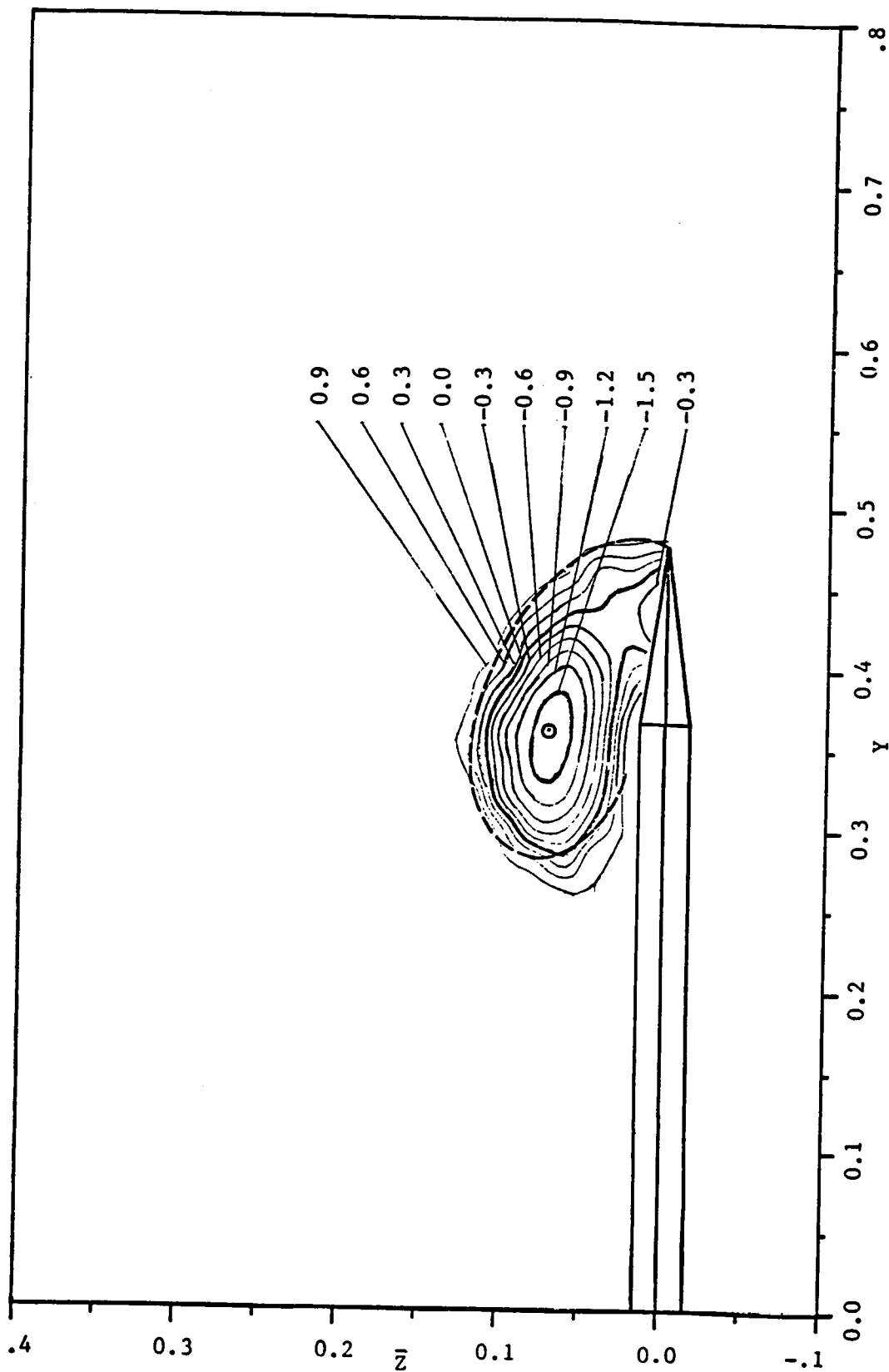


Fig. 41.b Continued. $x=0.625$

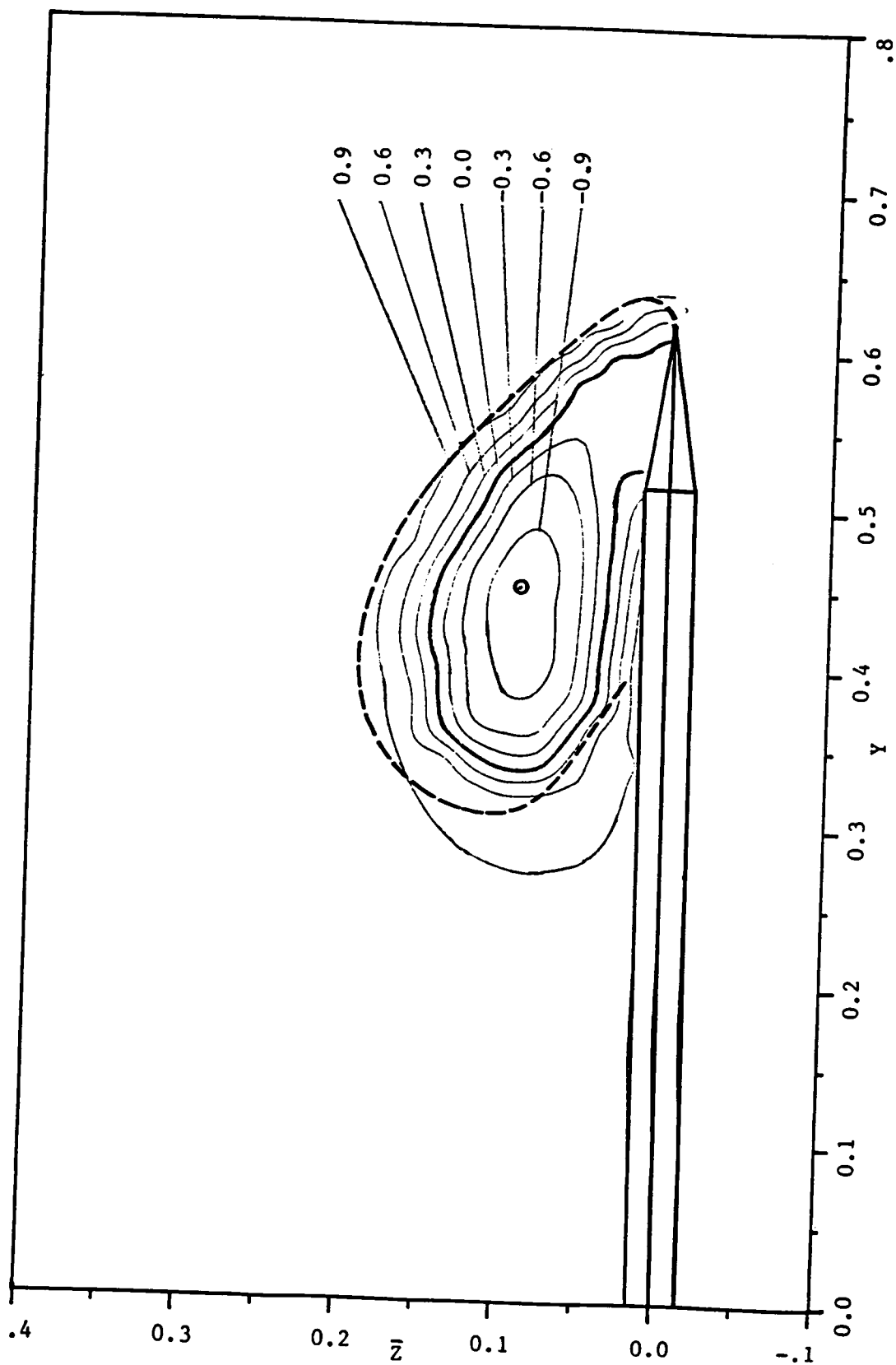


Fig. 41.c Concluded. $x=0.875$

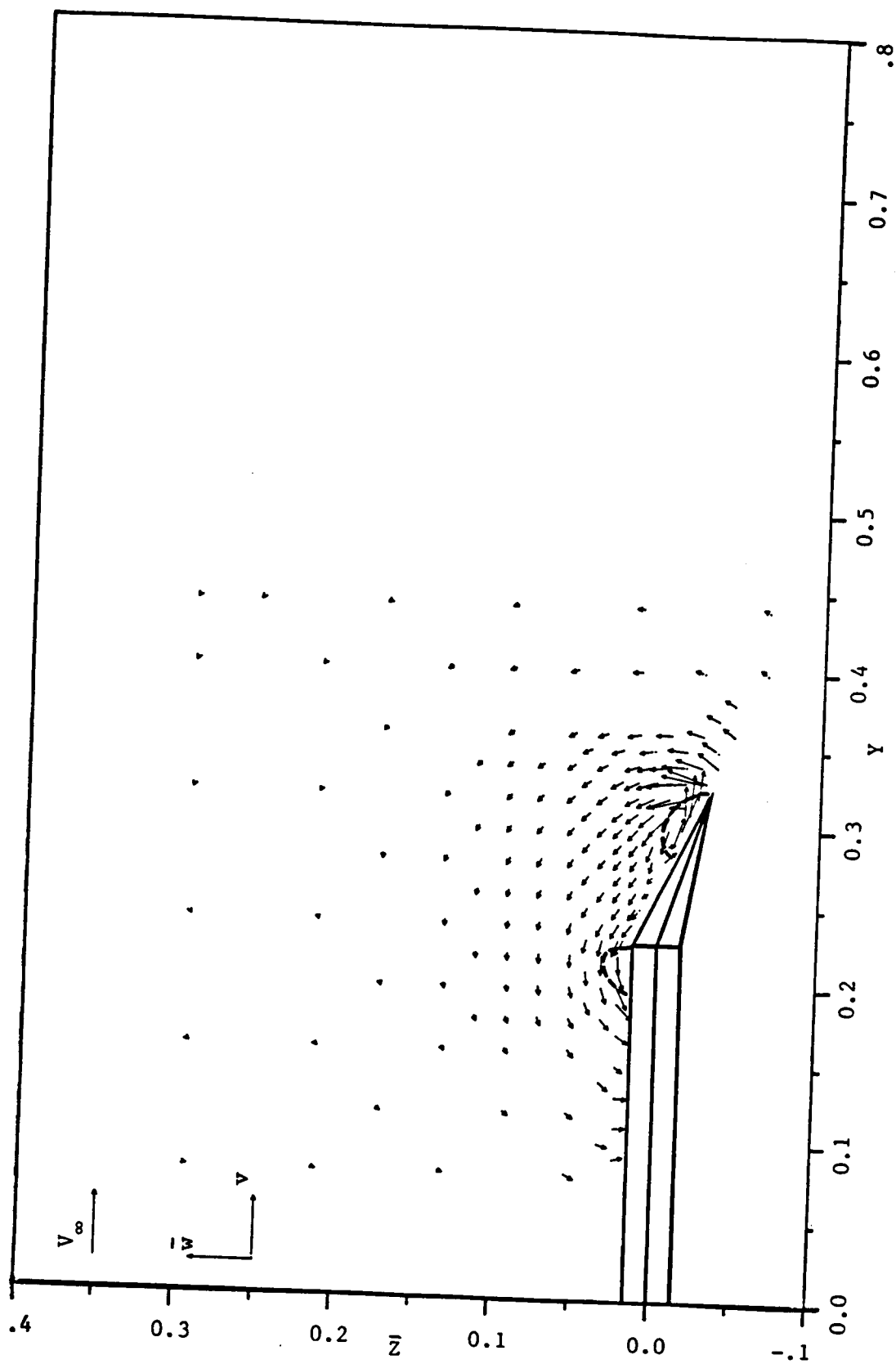


Fig. 42.a Velocity vector plot at $\alpha=10^\circ$ with $\delta=30^\circ$, $x=0.375$

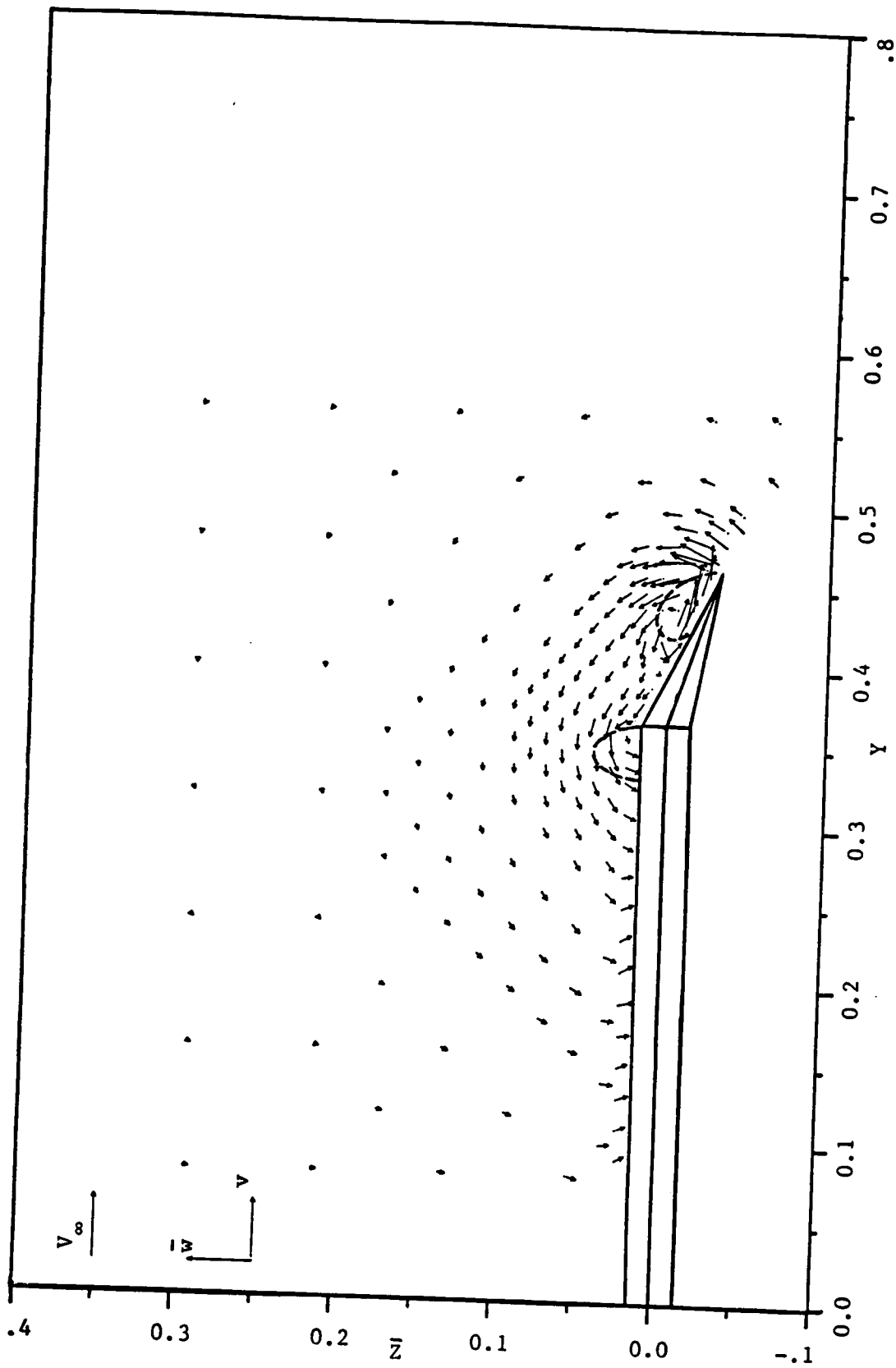


Fig. 42.b Continued. $x=0.625$

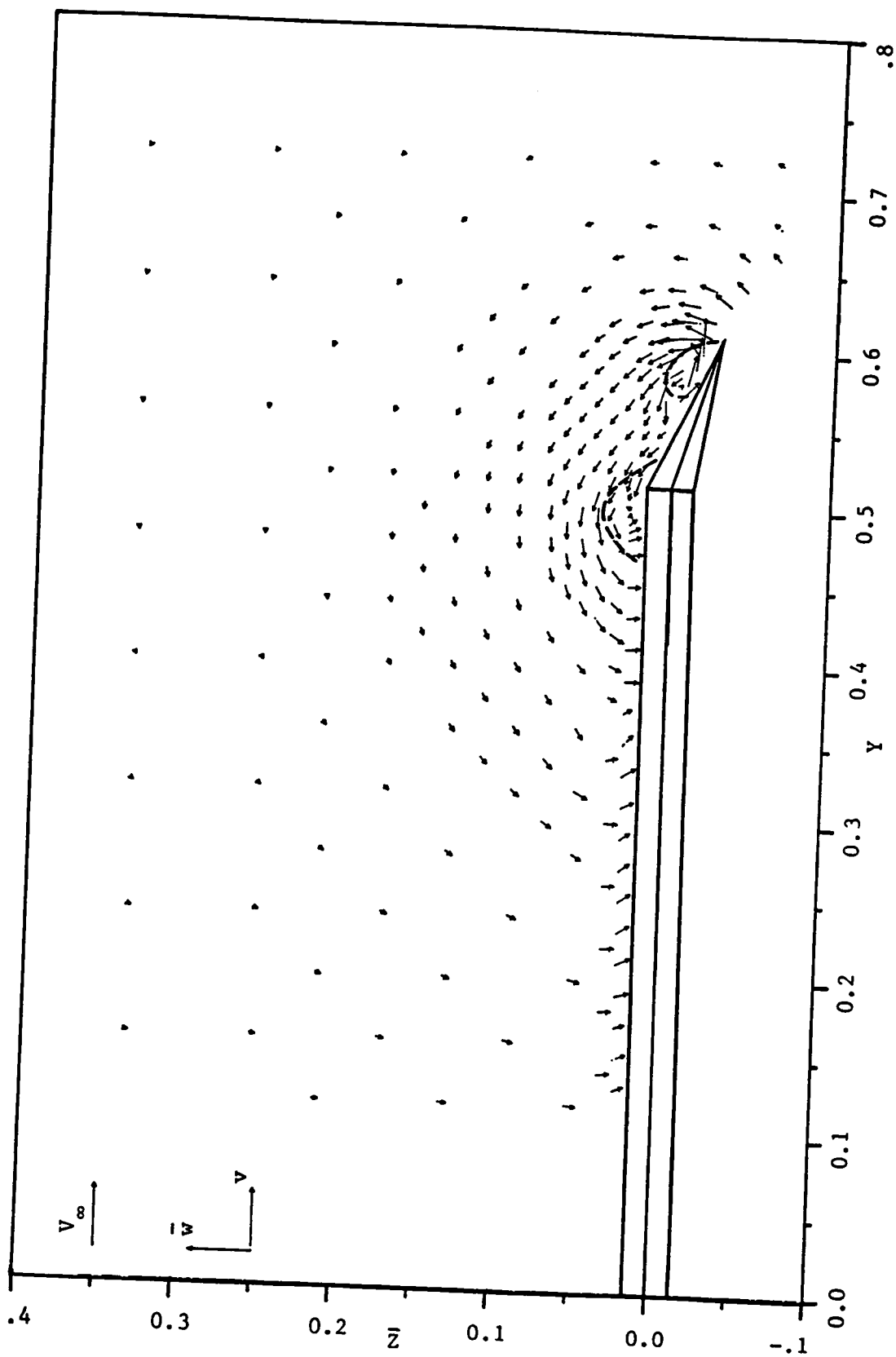


Fig. 42.c Concluded. $x=0.875$

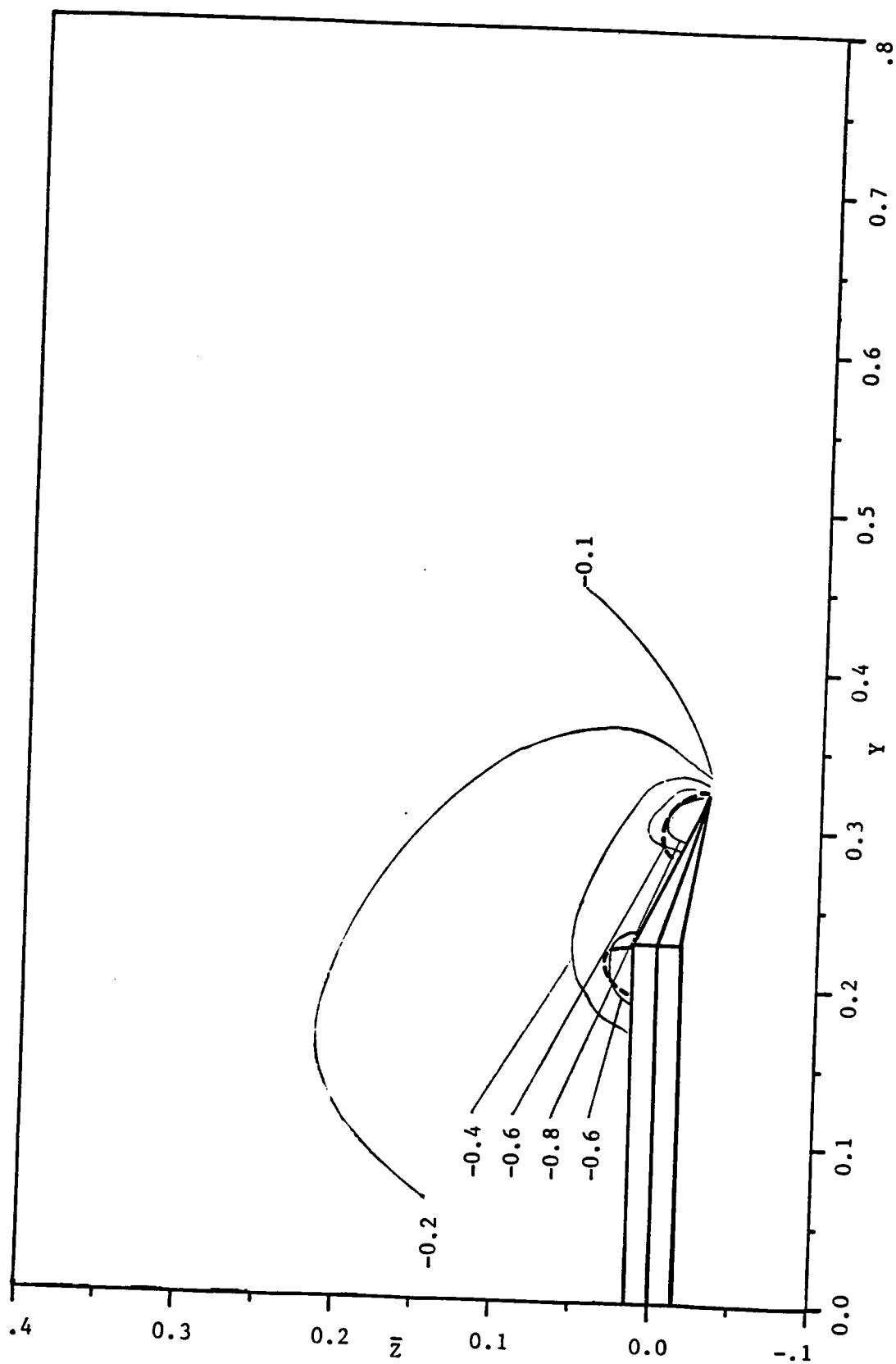


Fig. 43.a Static pressure distribution at $\alpha=10^\circ$ with $\delta=30^\circ$, $x=0.375$

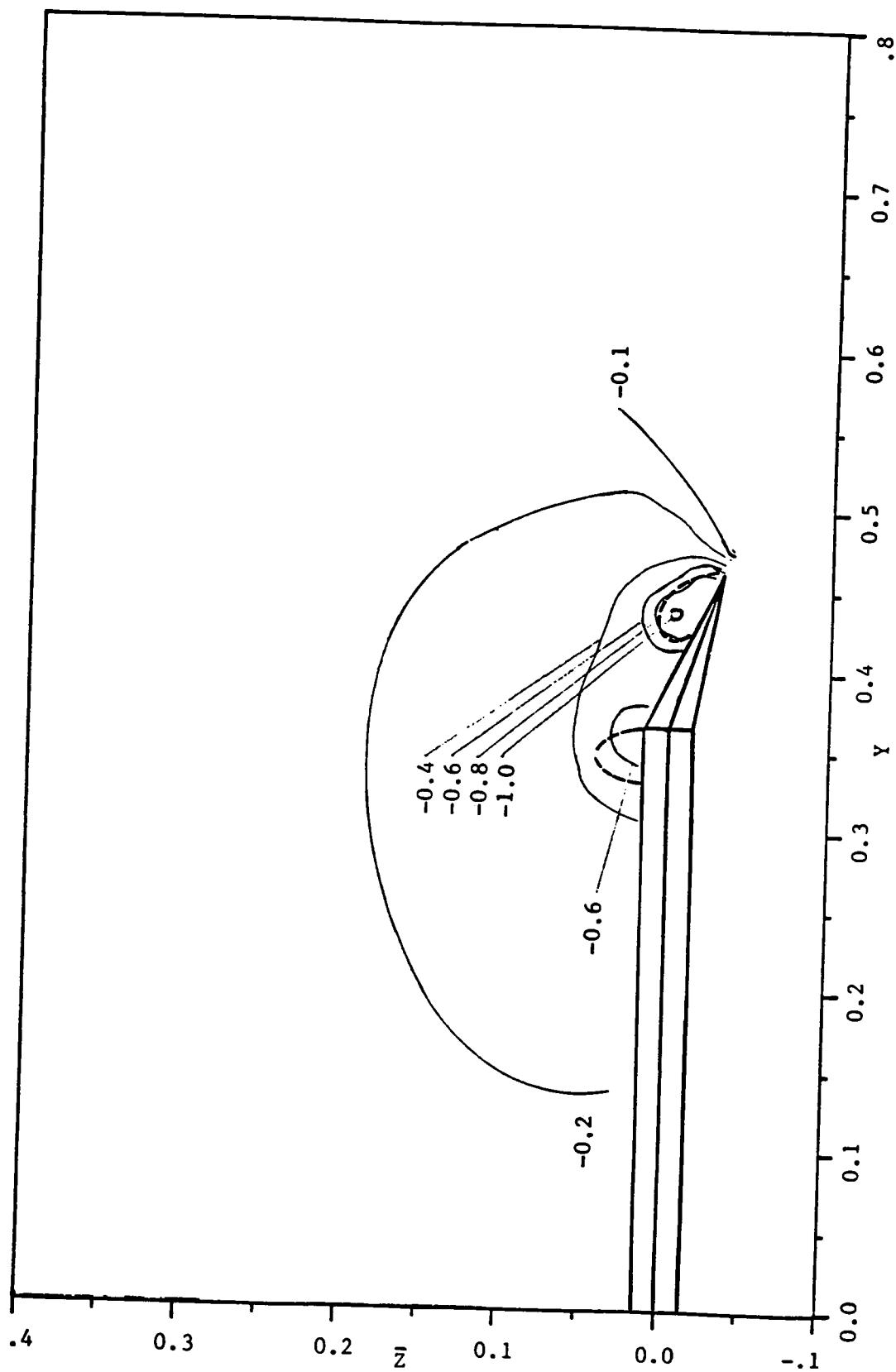


Fig. 43.b Continued. $x=0.625$

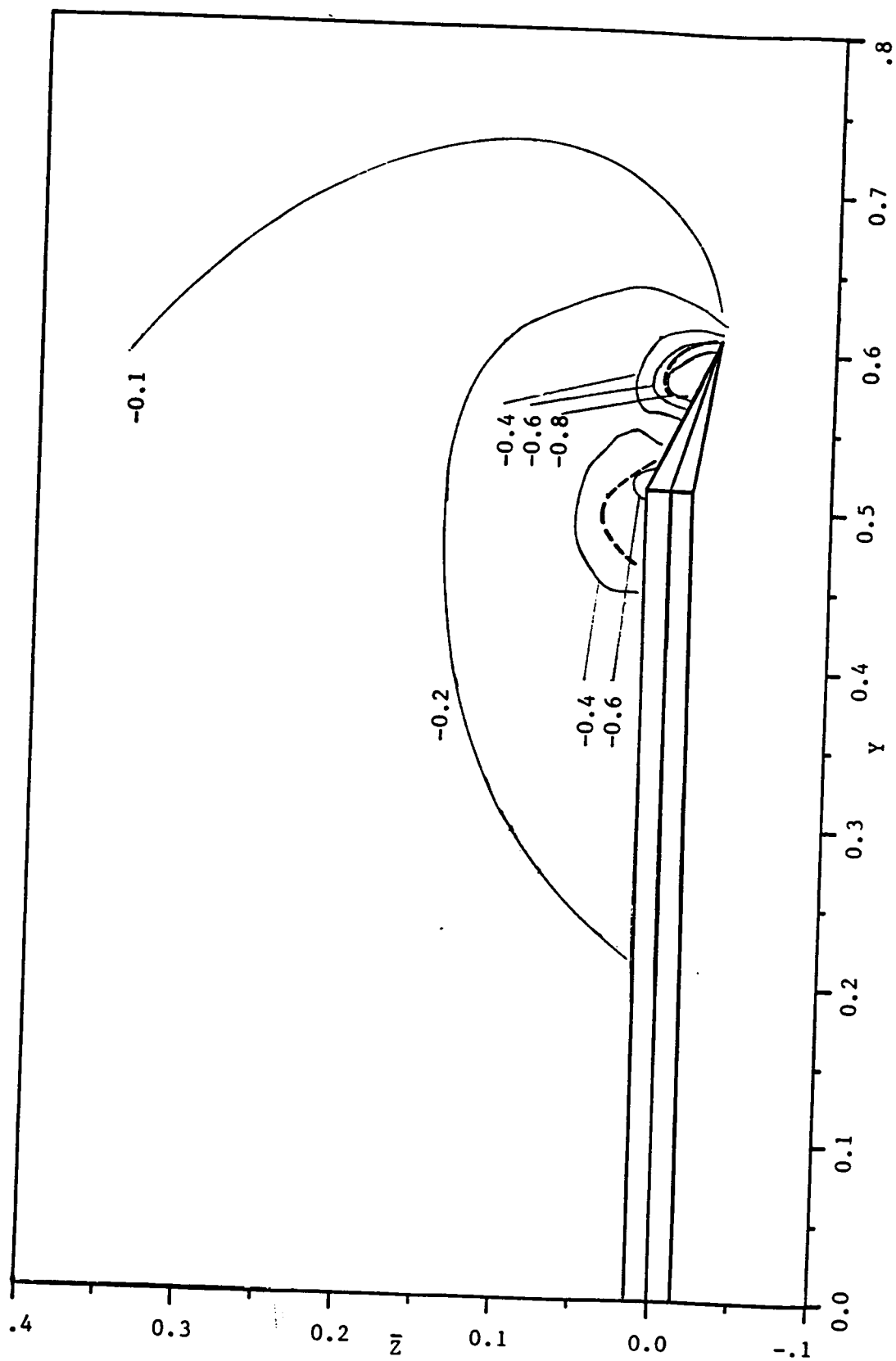


Fig. 43.c Concluded. $x=0.875$

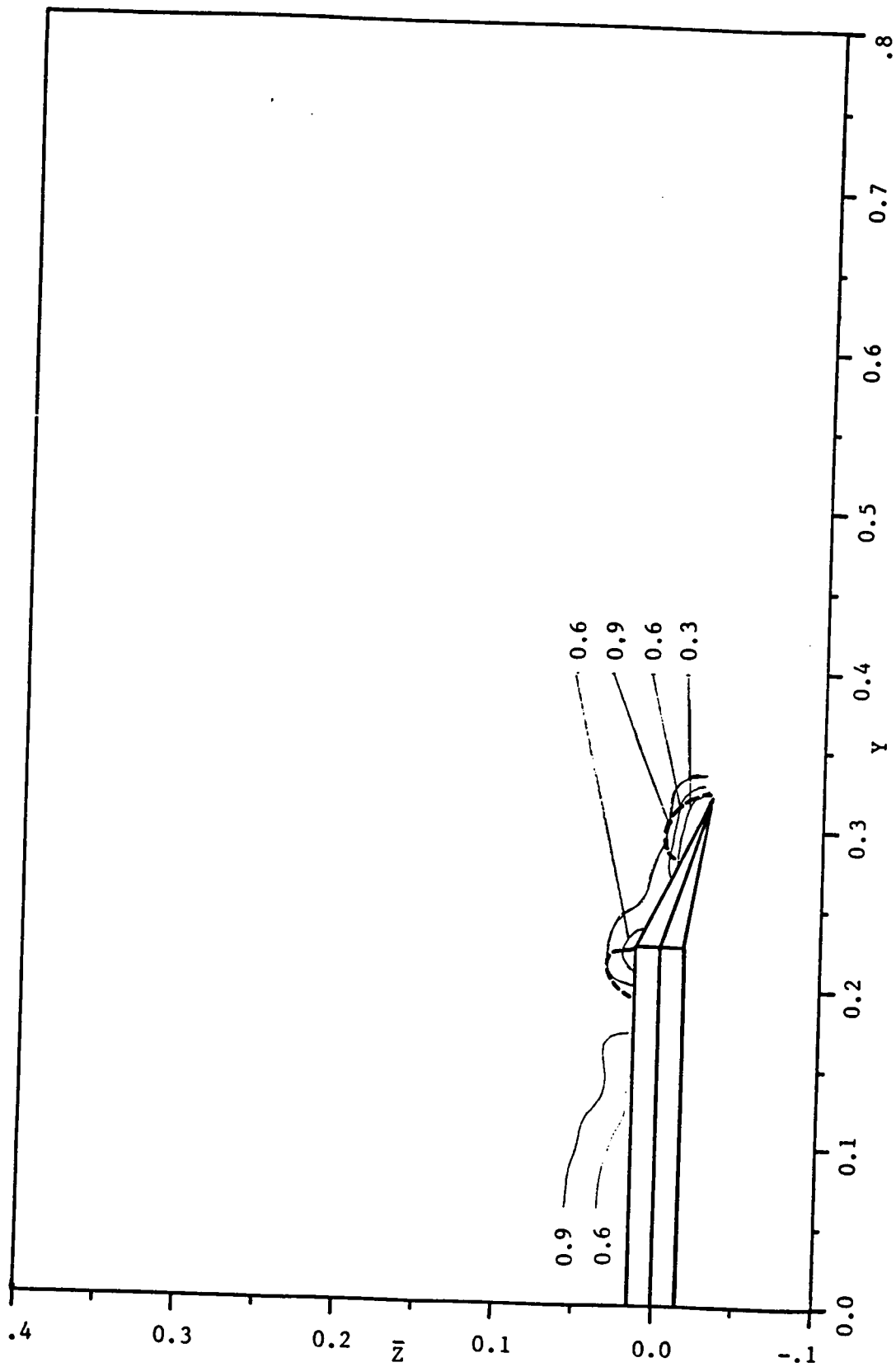


Fig. 44.a Total pressure distribution at $\alpha=10^\circ$ with $\delta=30^\circ$, $x=0.375$

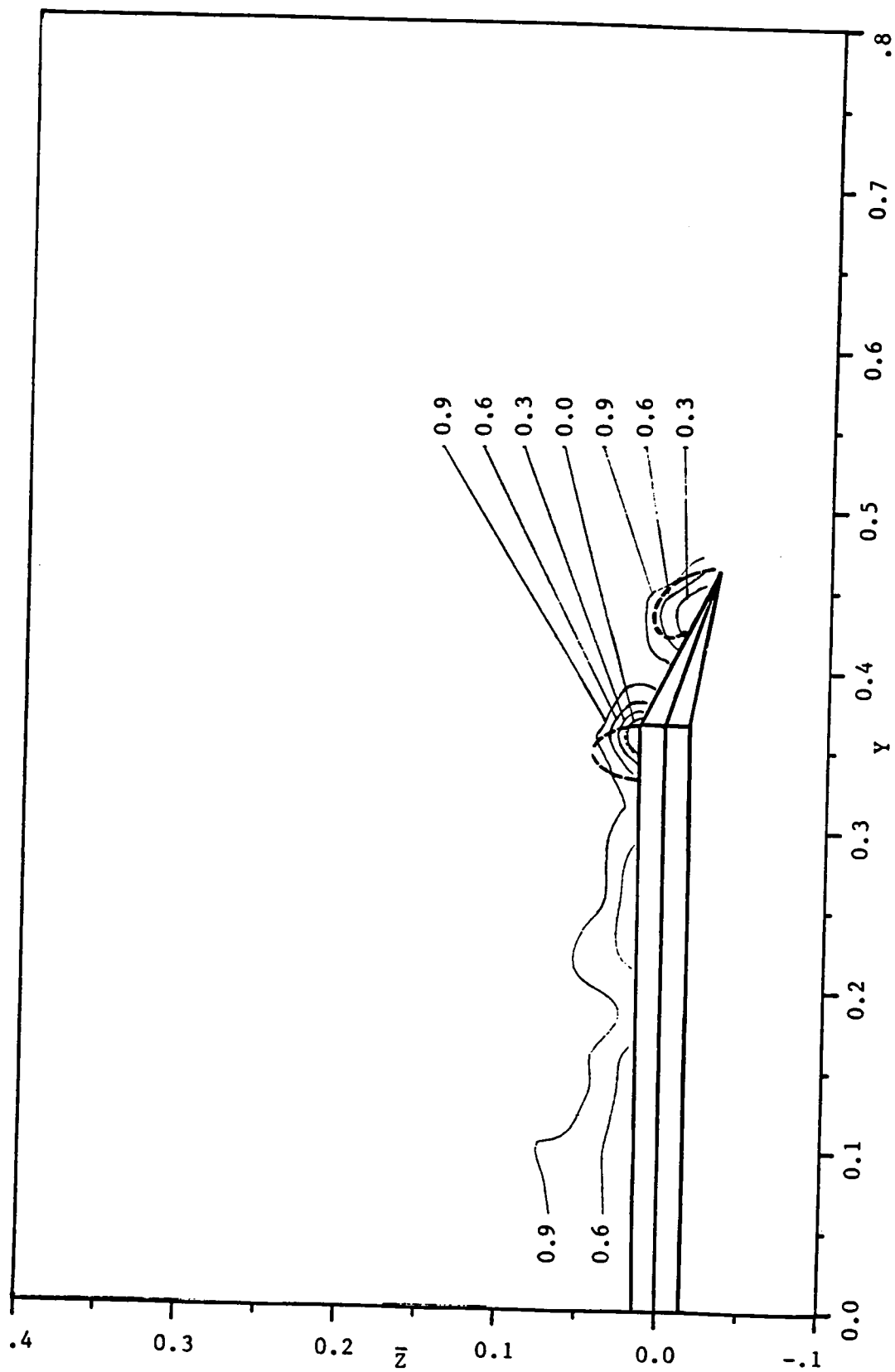


Fig. 44.b Continued. $x=0.625$

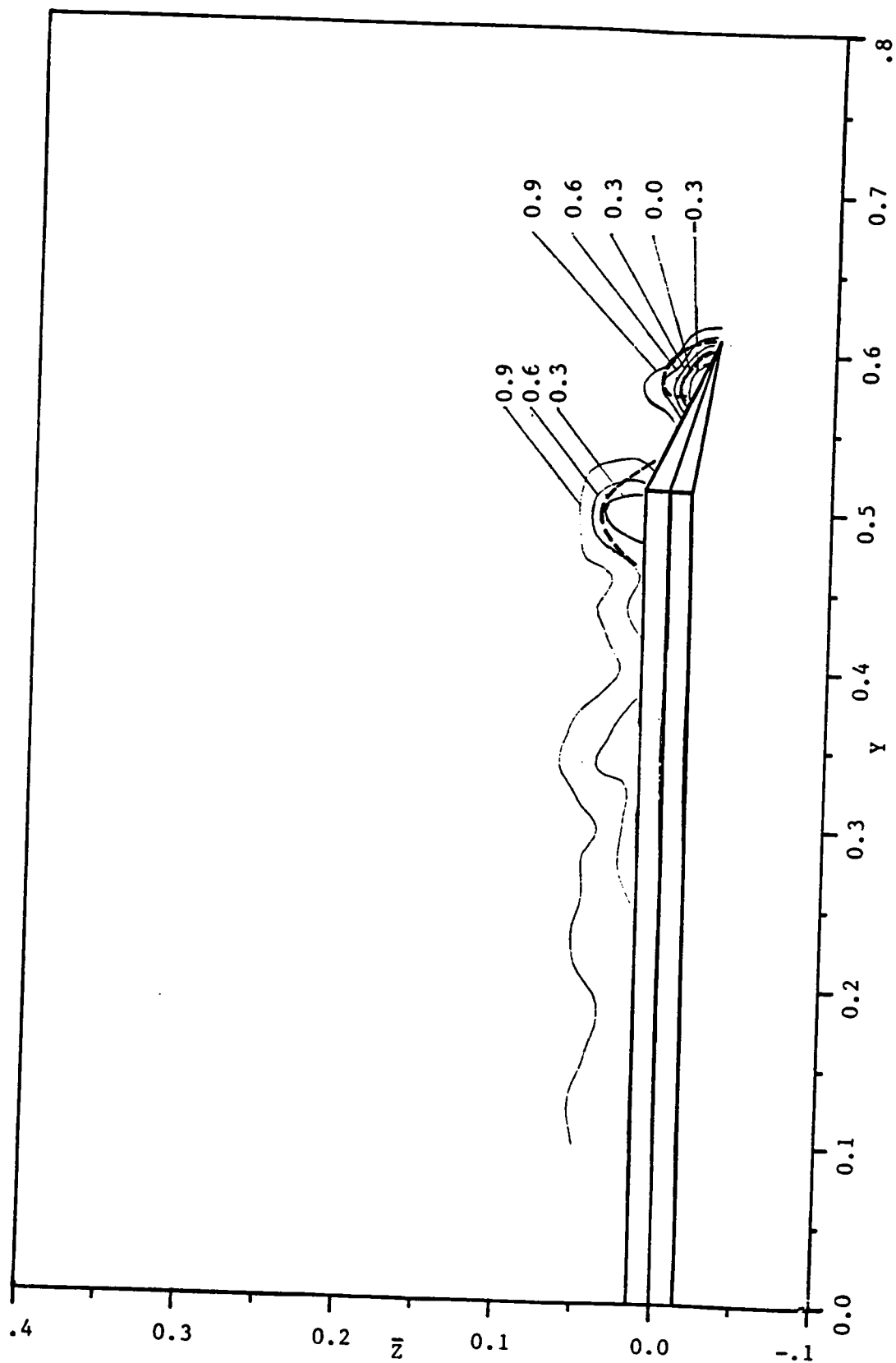


Fig. 44.c Concluded. $x=0.875$

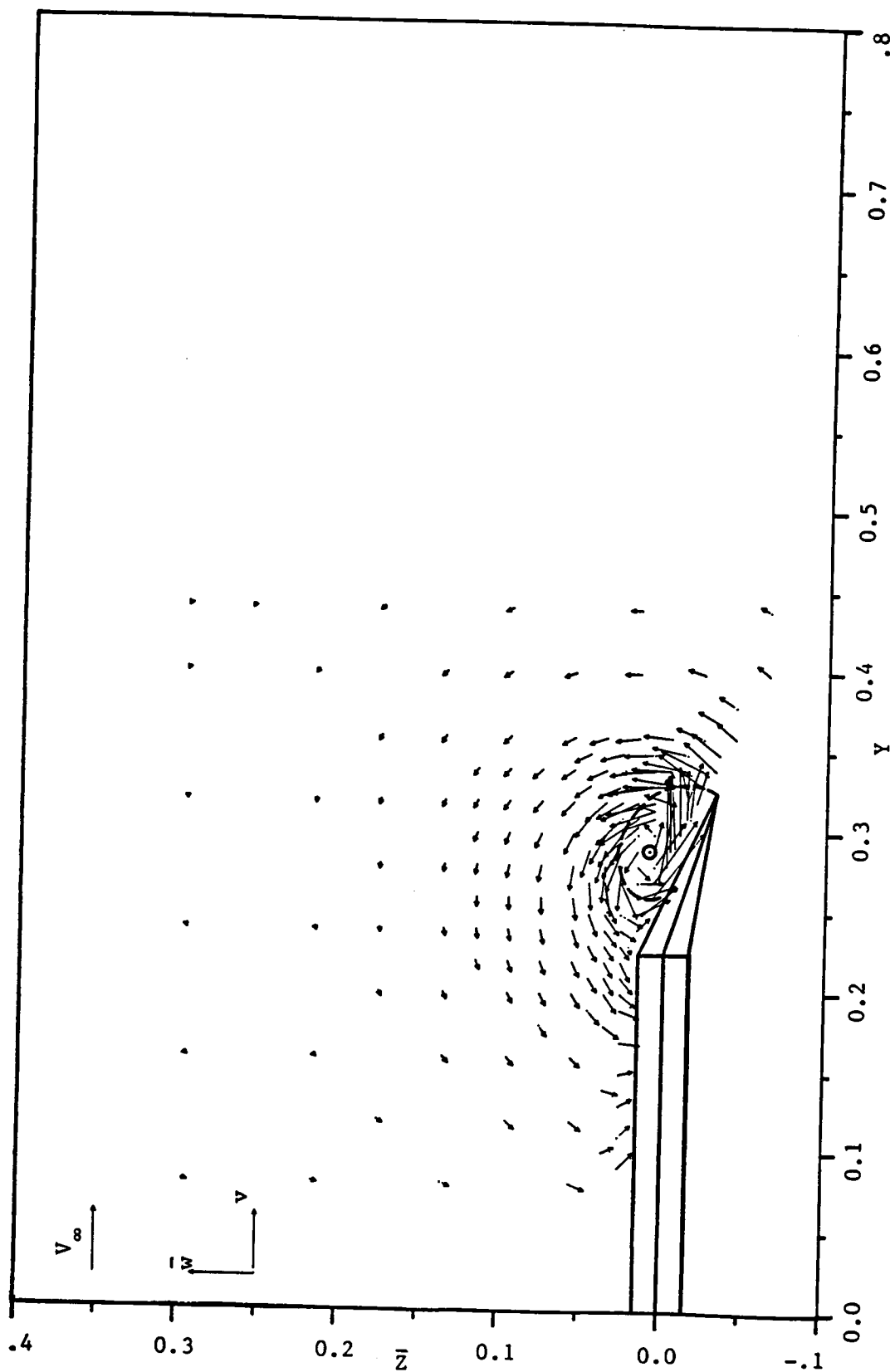


Fig. 45.a Velocity vector plot at $\alpha=15^\circ$ with $\delta=30^\circ$, $x=0.375$

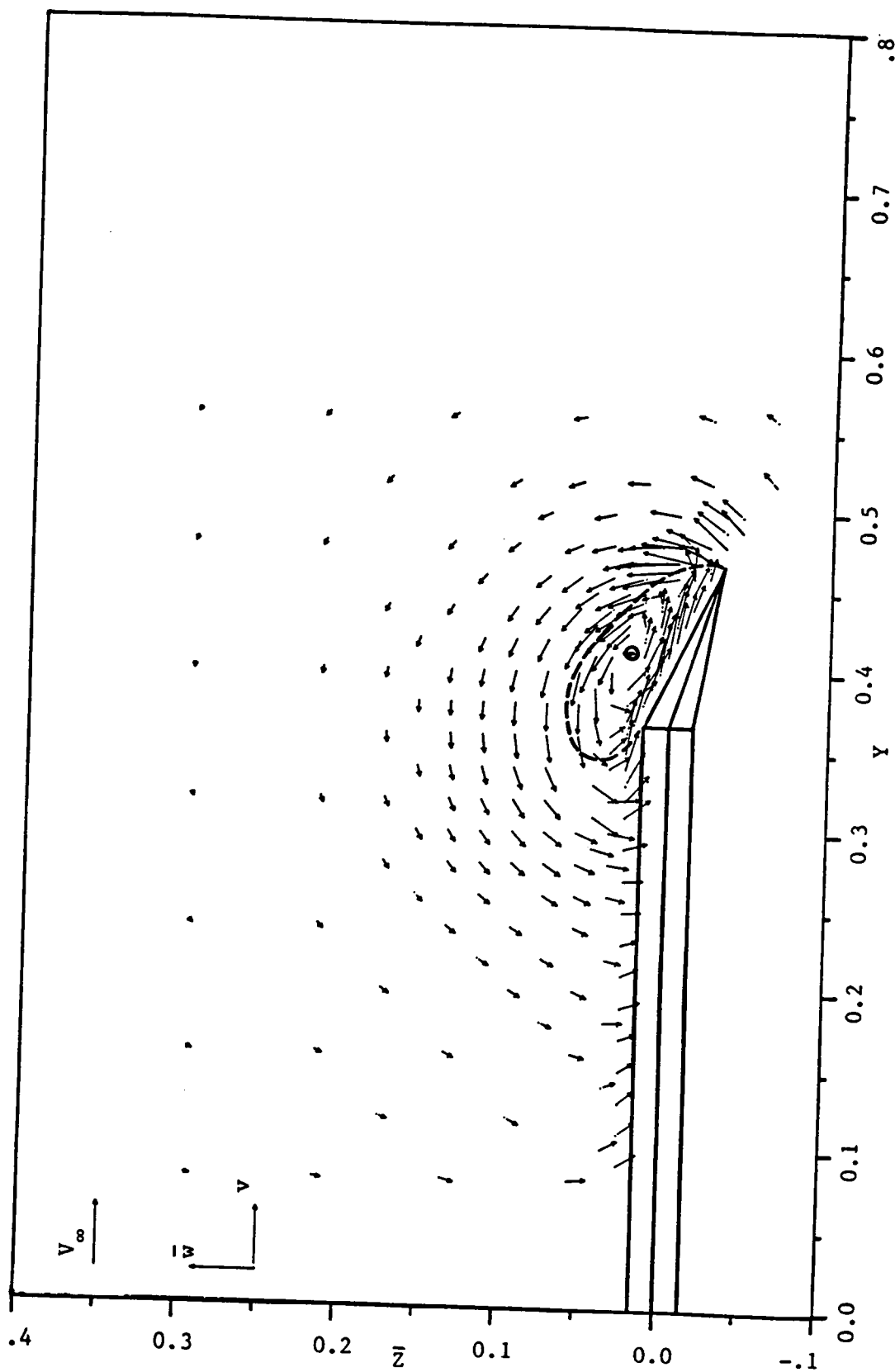


Fig. 45.b Continued. $x=0.625$

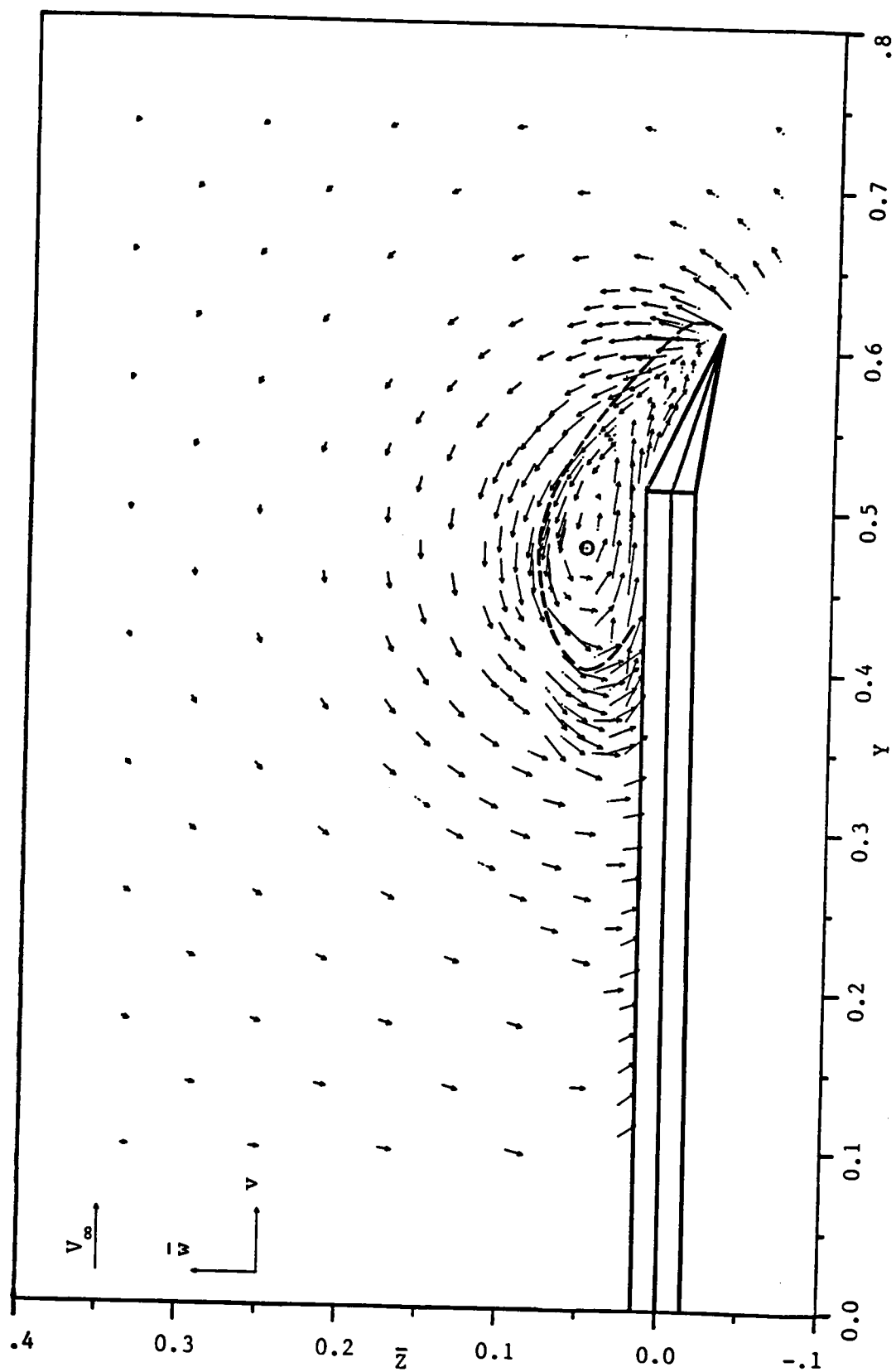


Fig. 45.c Concluded. $x=0.875$

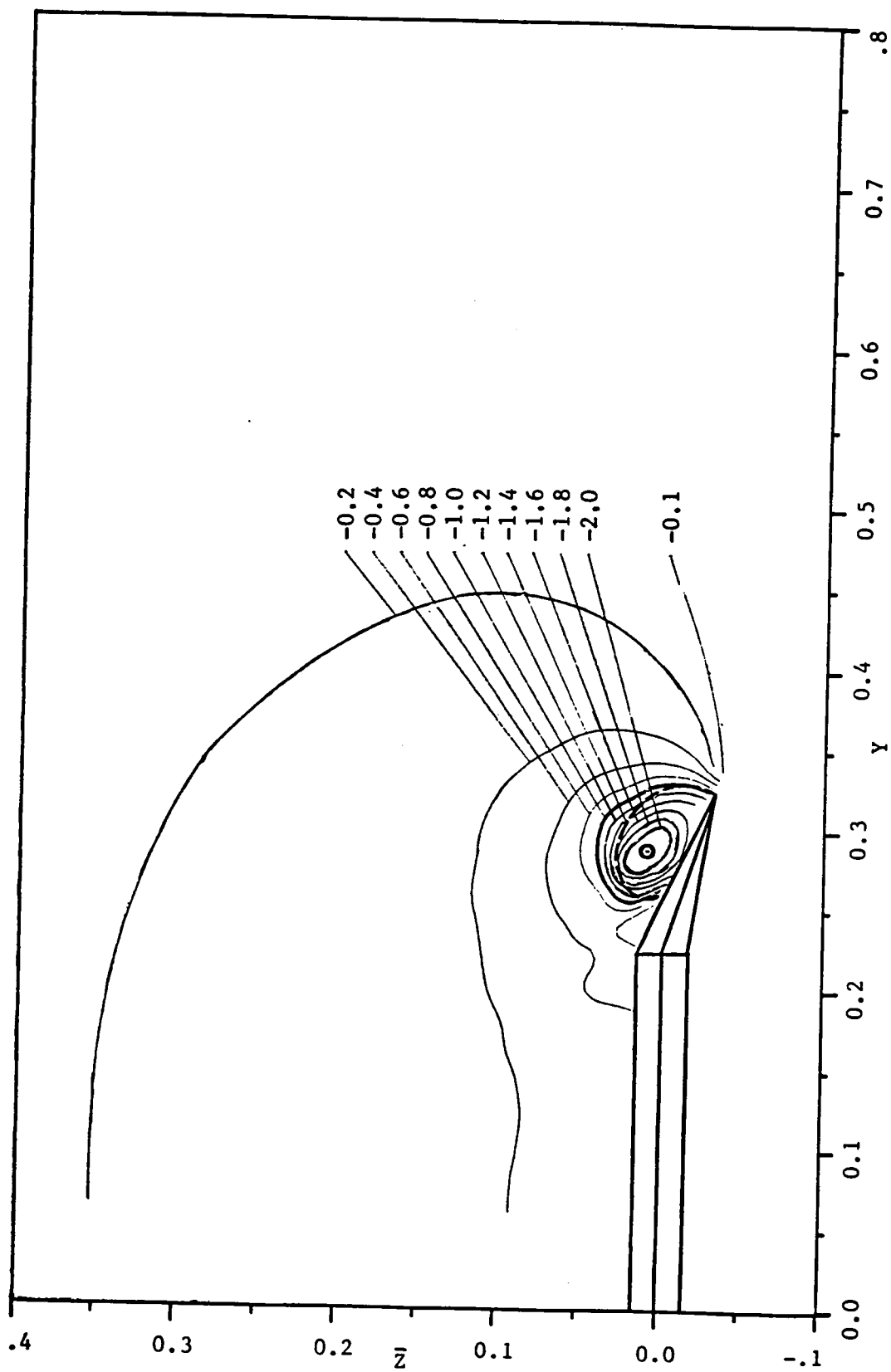


Fig. 46.a Static pressure distribution at $\alpha=15^\circ$ with $\delta=30^\circ$, $x=0.375$

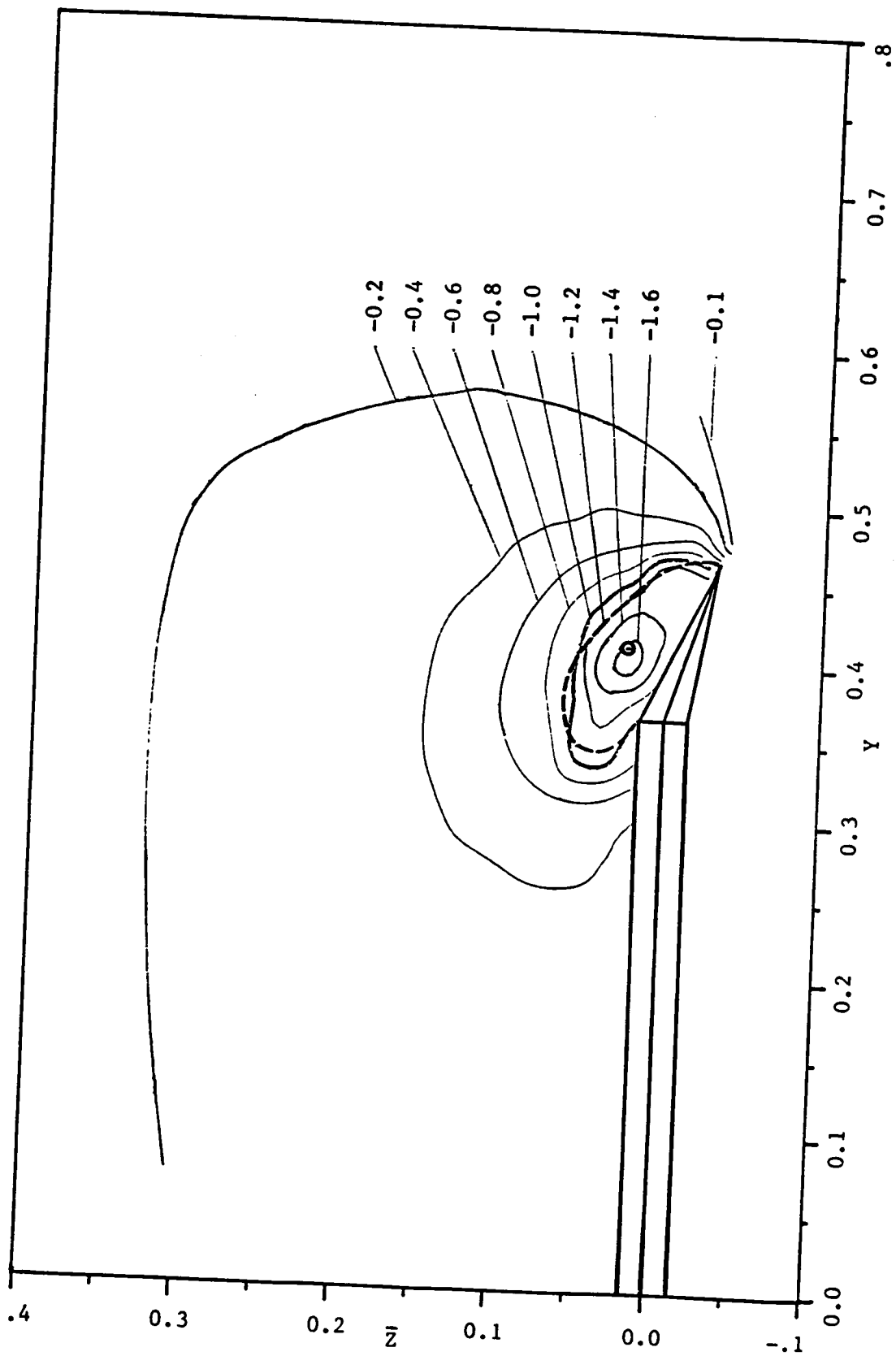


Fig. 46.b Continued. $x=0.625$

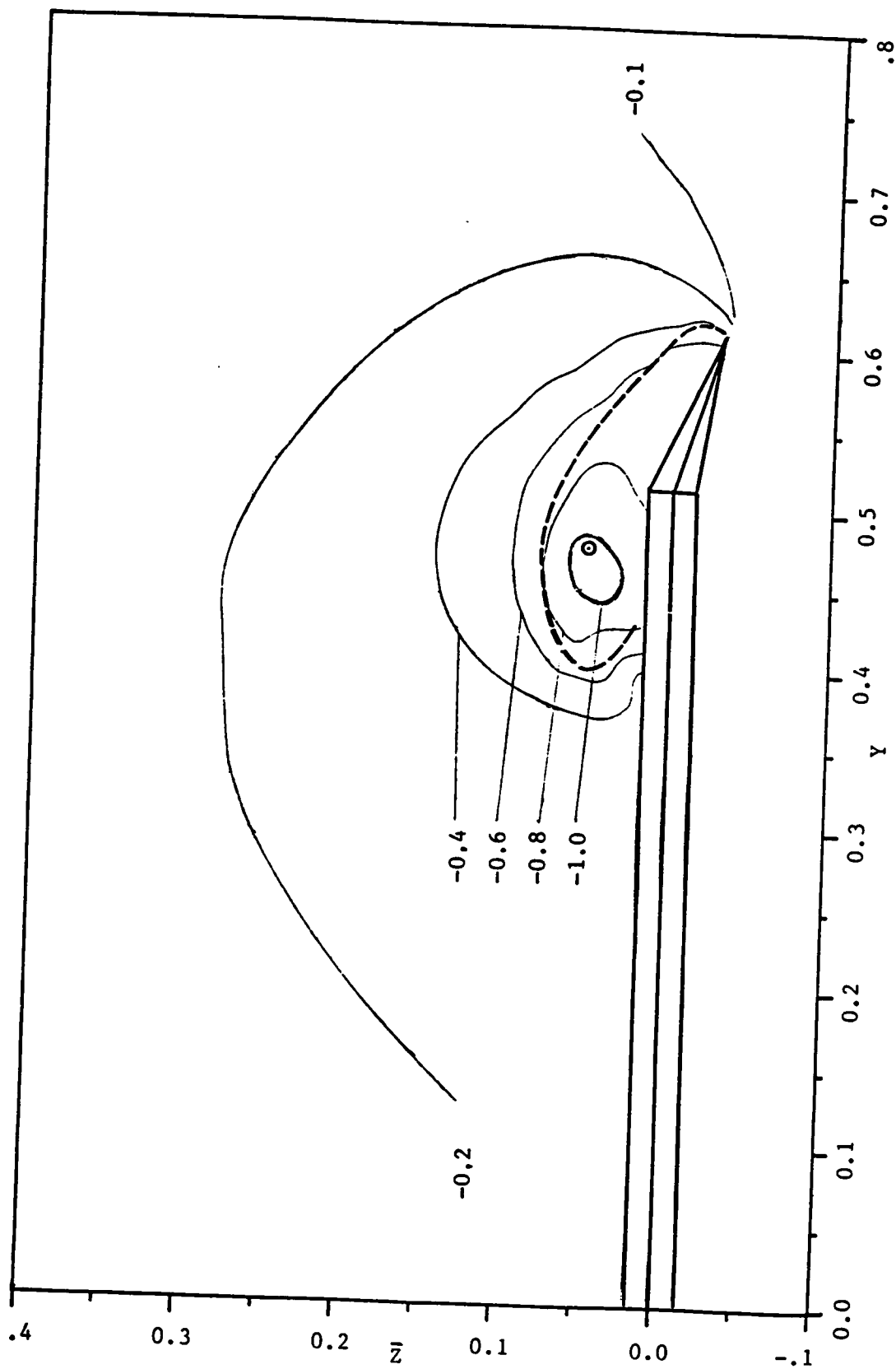


Fig. 46.c Concluded. $x=0.875$

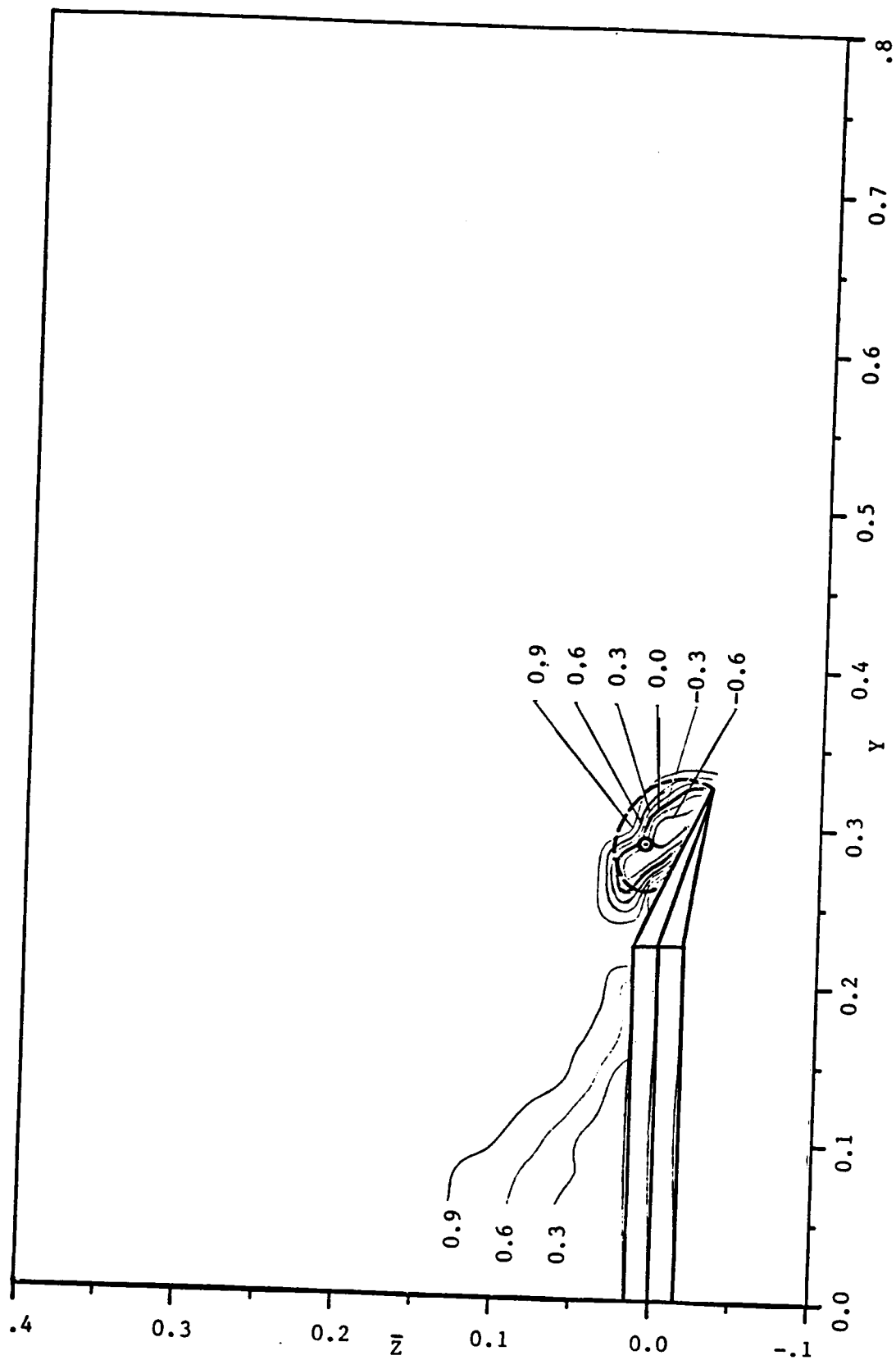


Fig. 47.a Total pressure distribution at $\alpha=15^\circ$ with $\delta=30^\circ$, $x=0.375$

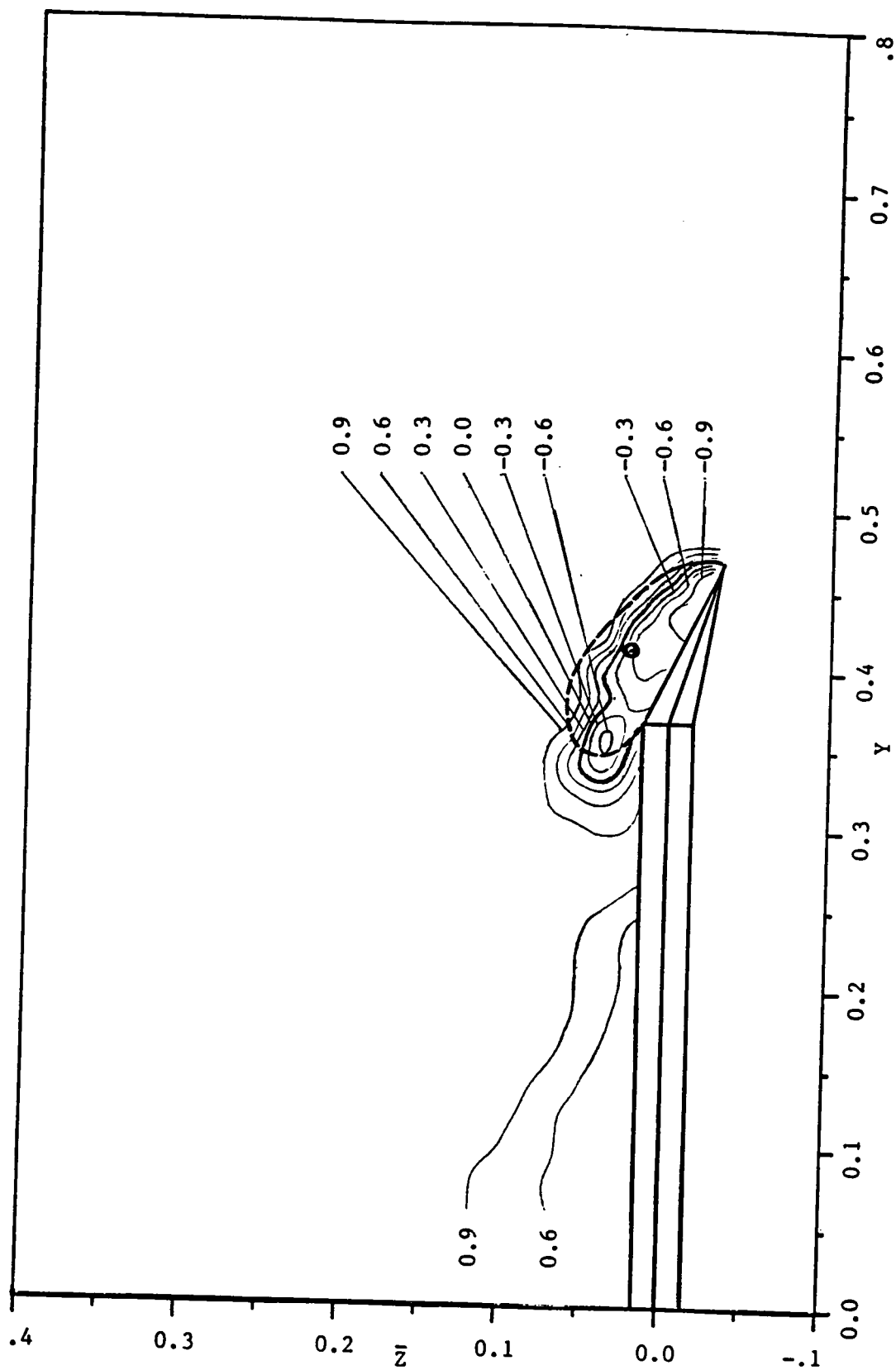


Fig. 47.b Continued. $x=0.625$

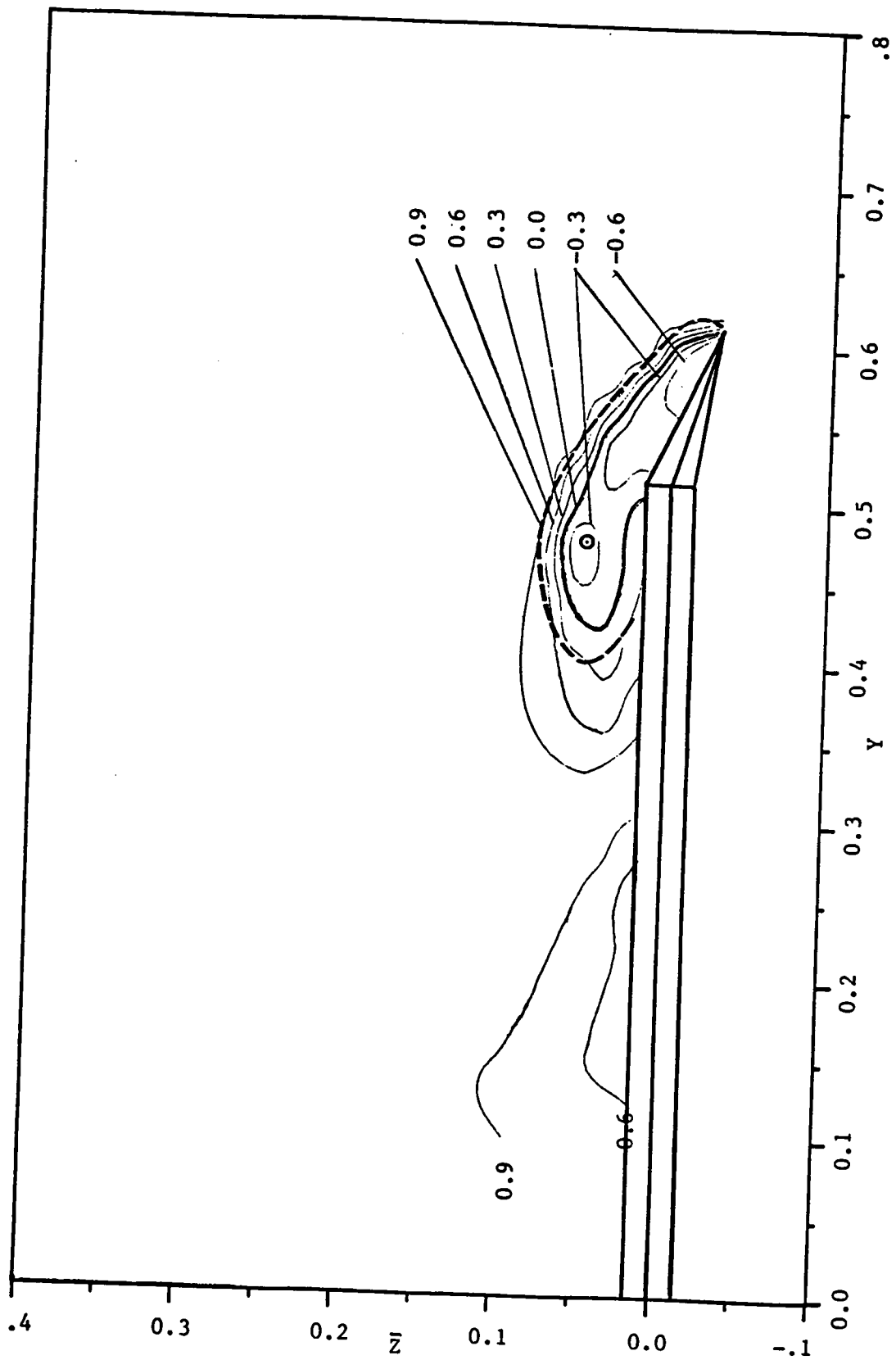


Fig. 47.c Concluded. $x=0.875$

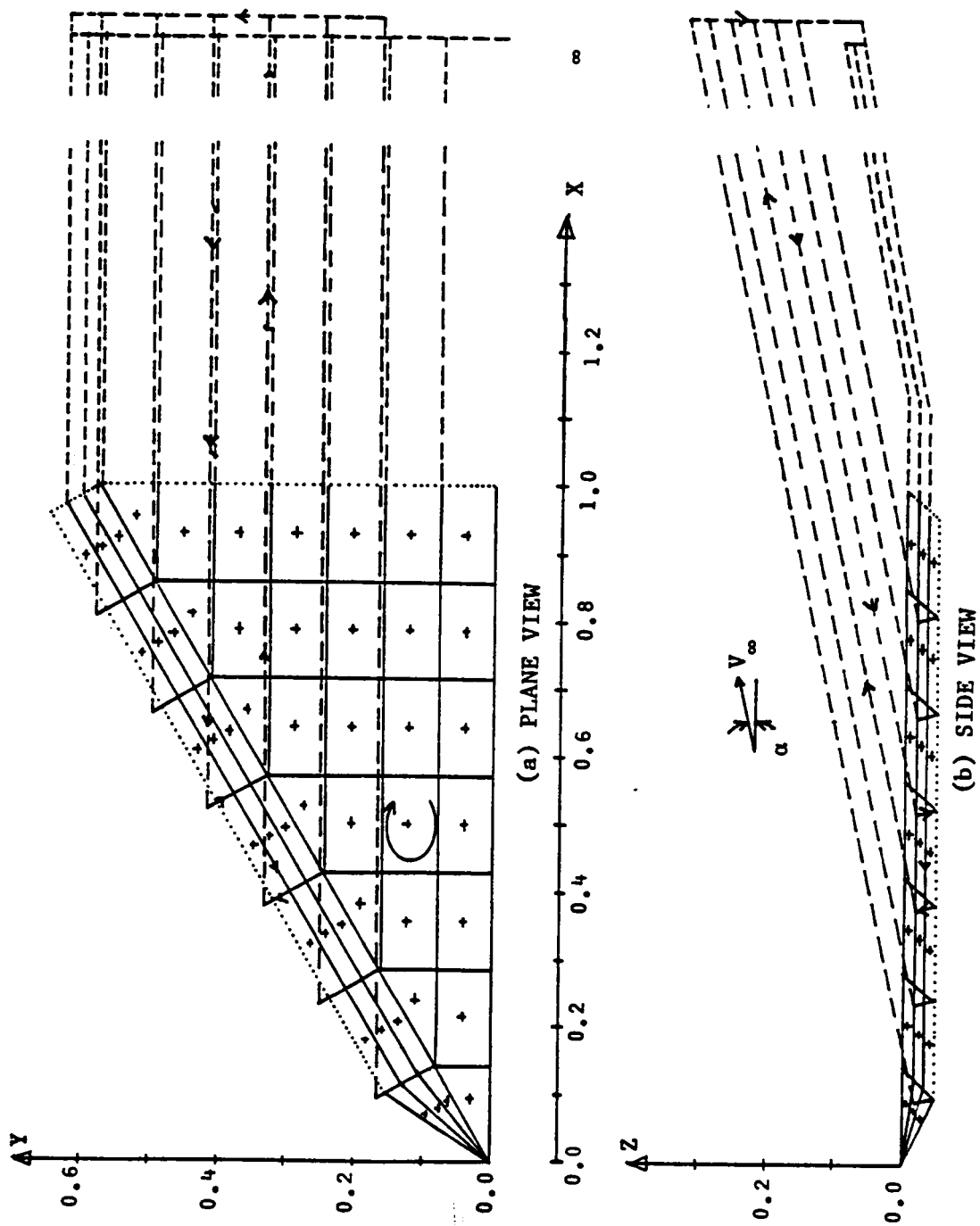
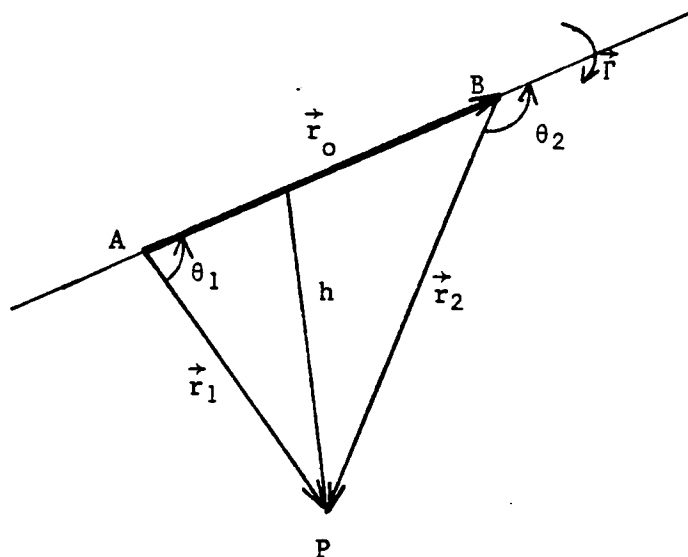


Fig. 48. Vortex loop panel arrangement and initial guess for free vortices (NW=7, NF=3).



$$\begin{aligned}\vec{r}_0 &= \overrightarrow{AB} \\ \vec{r}_1 &= \overrightarrow{AP} \\ \vec{r}_2 &= \overrightarrow{BP} \\ h &= \frac{|\vec{r}_1 \times \vec{r}_2|}{r_0}\end{aligned}$$

Fig. 49. Notation for Biot-Savart Law.

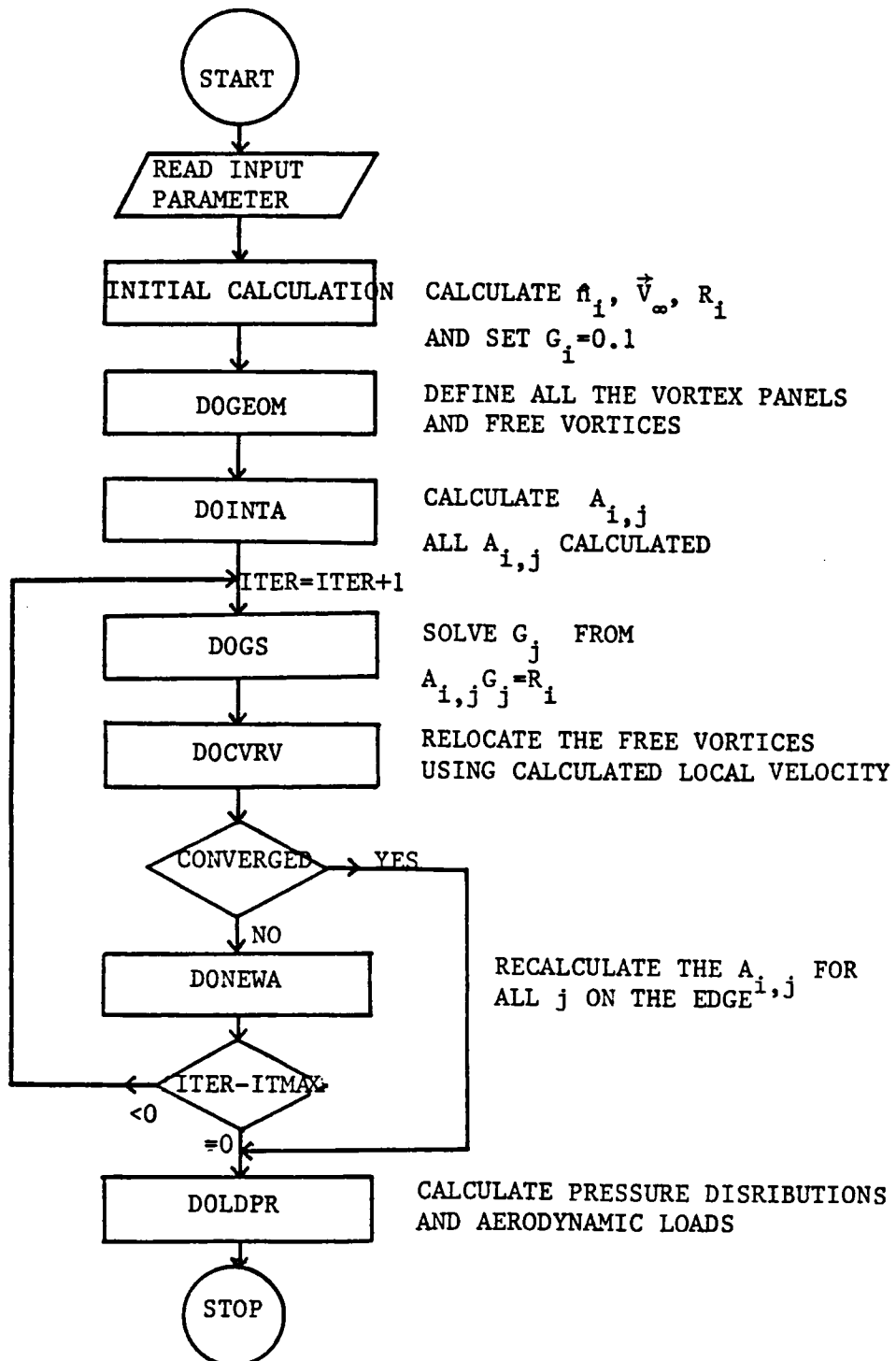
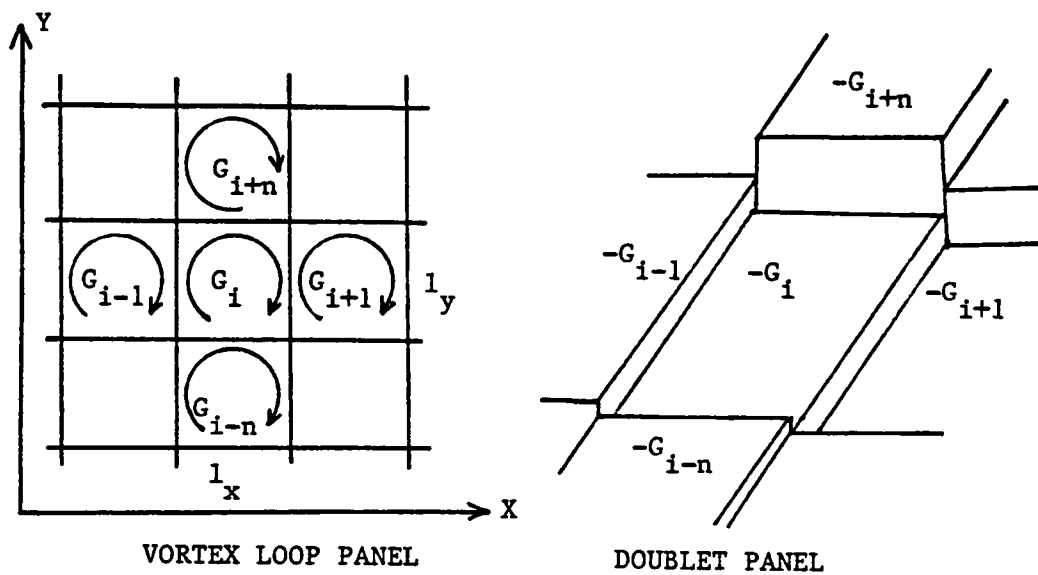
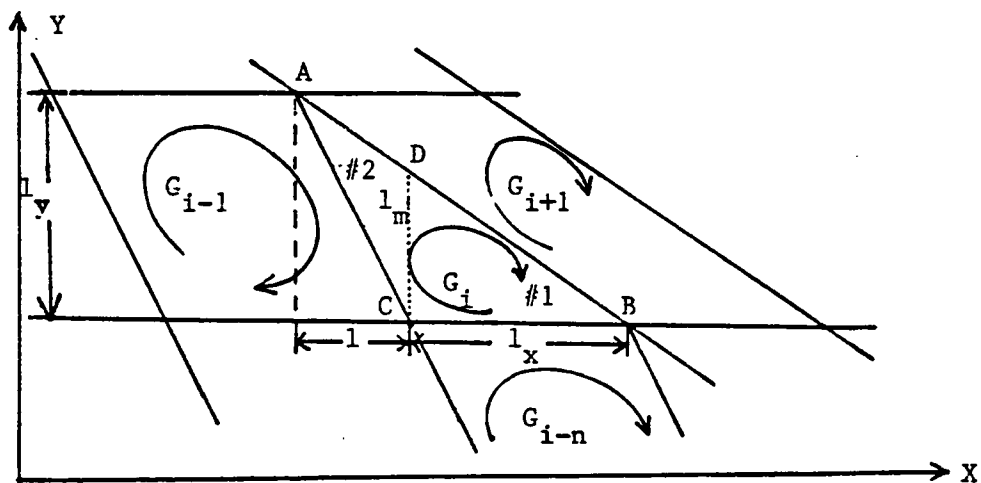


Fig. 50. Flow chart of the program.



(a) RECTANGULAR PANEL



(b) TRIANGULAR PANEL

Fig. 51. Notation for velocity jump formula.

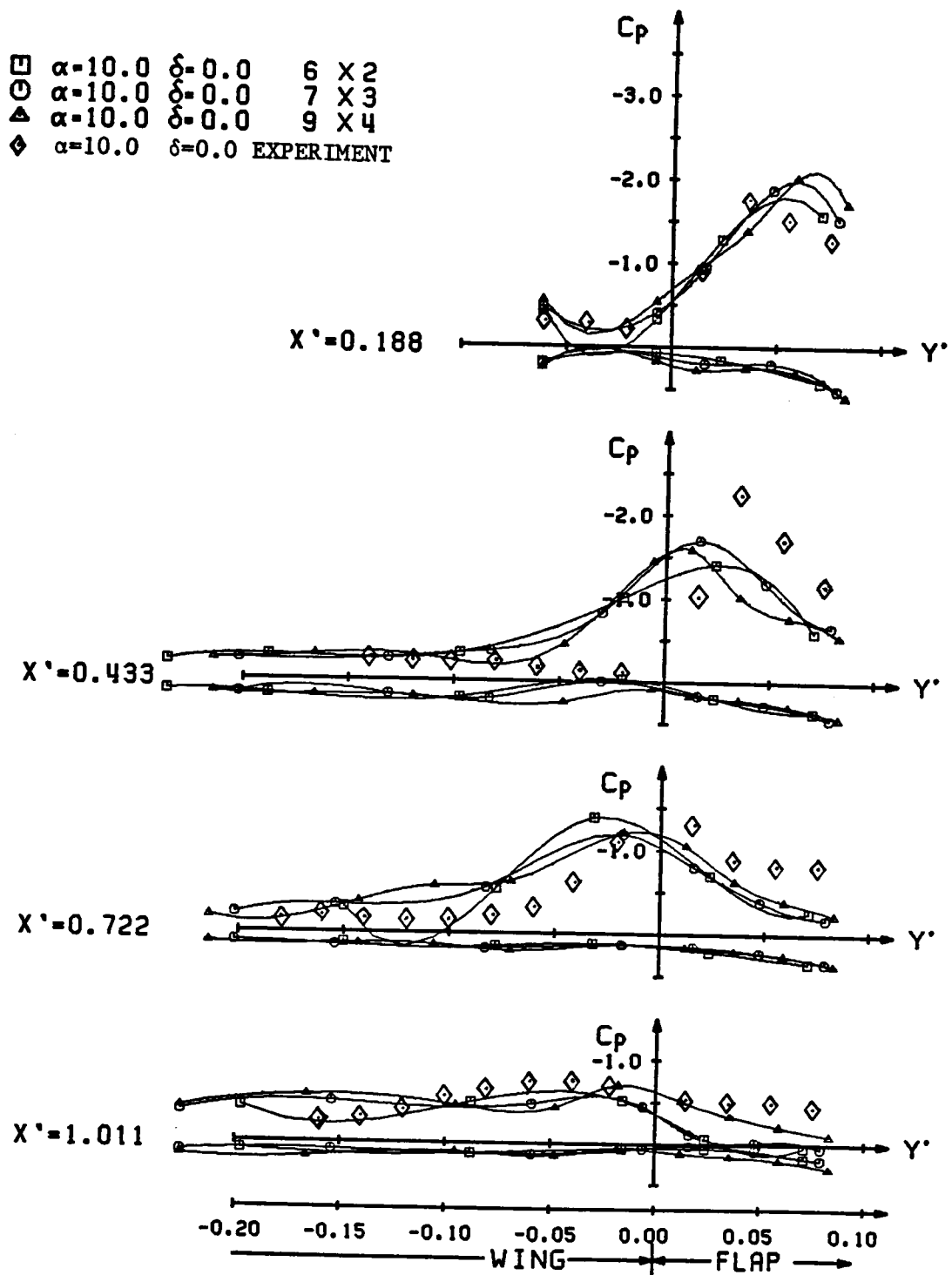


Fig. 52. Effect of number of panels.

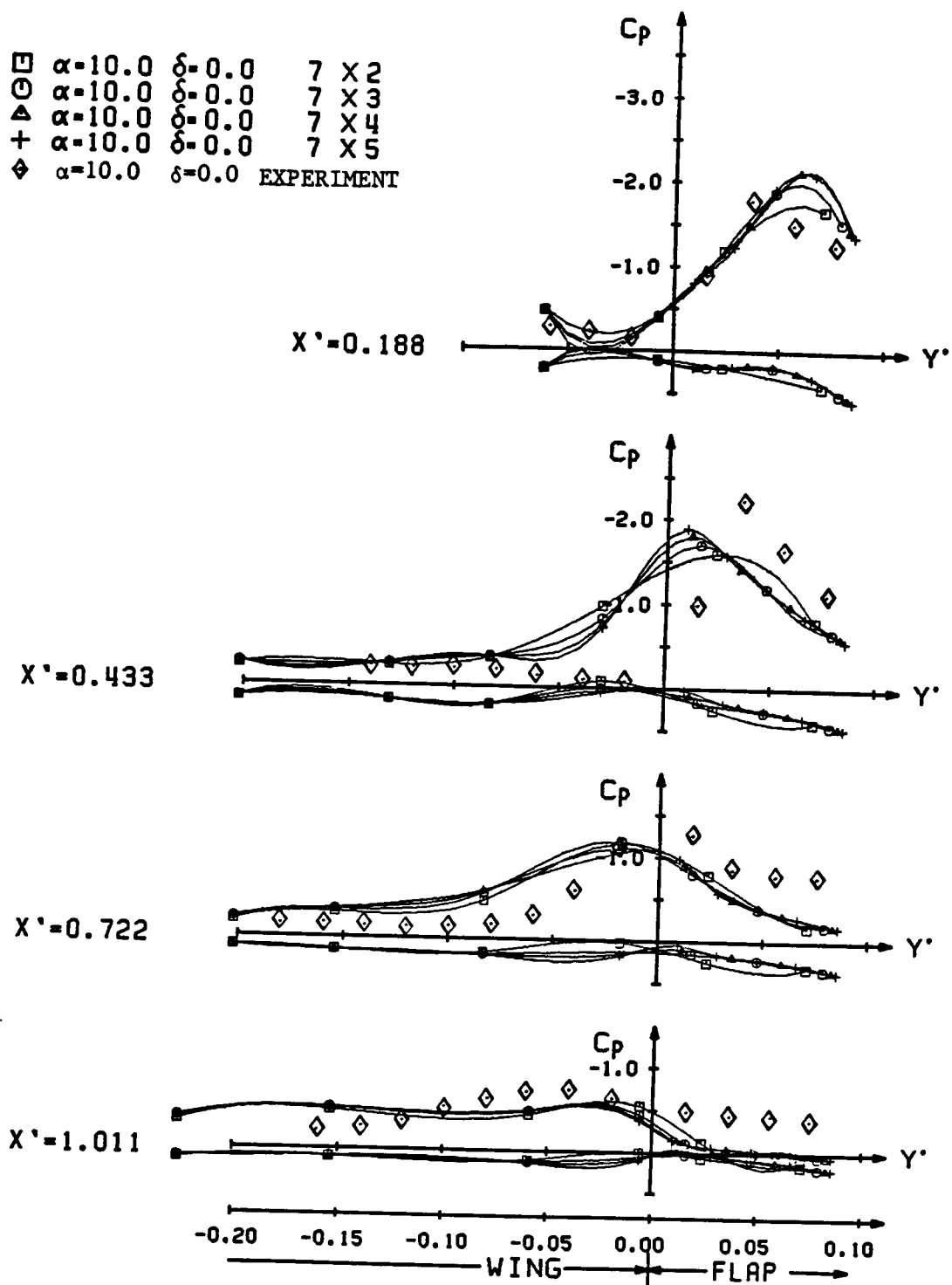


Fig. 53. Effect of number of panel columns on the flap.

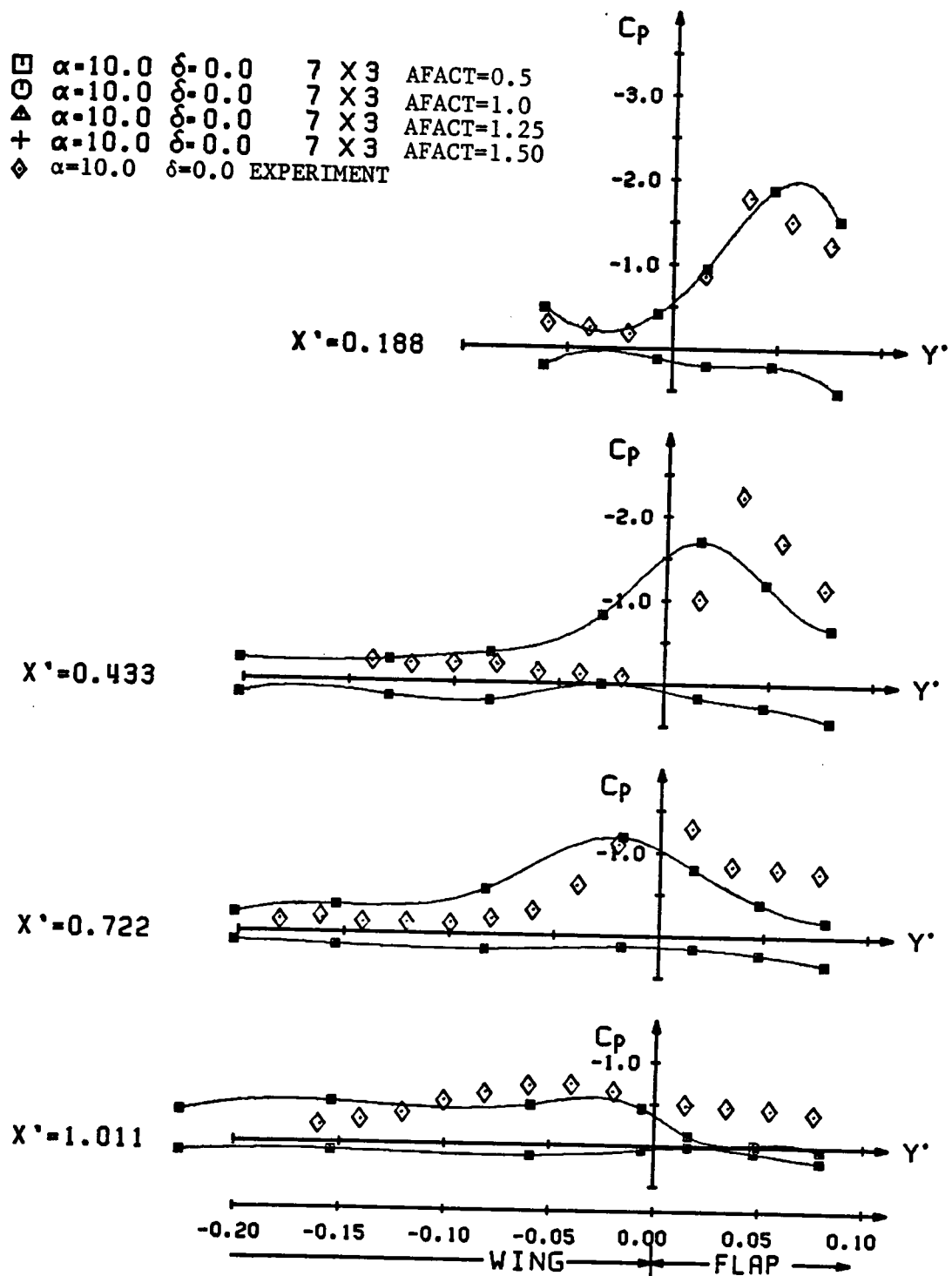


Fig. 54. Effect of initial free vortex shedding angle.

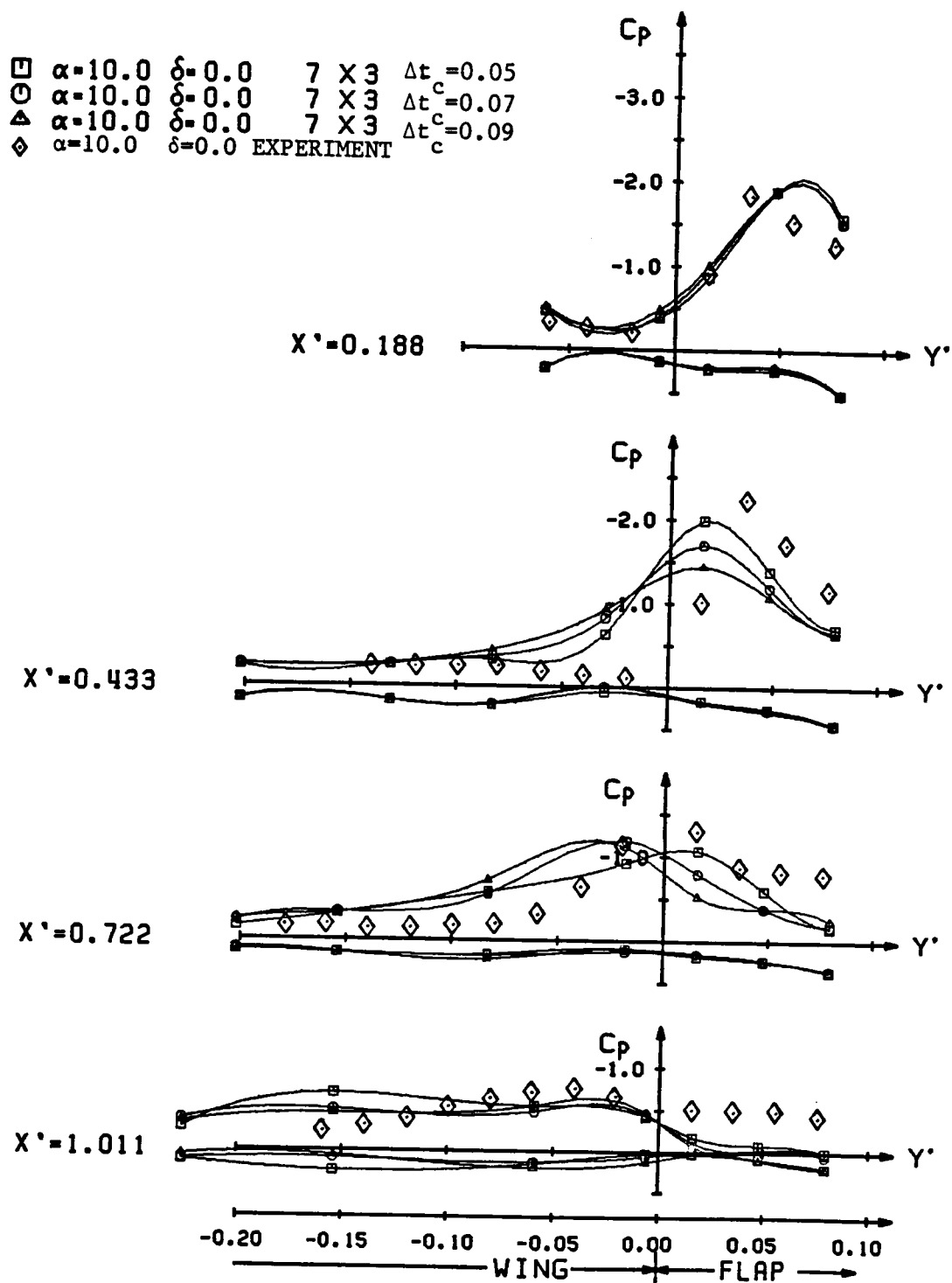


Fig. 55.a Effect of characteristic time step.

7X9, CONVERGED AT ITER=15
 FEDG=0.030, DTC=0.050, AFACT=1.250
 T= 92.01 SEC HO=0.0082 FVEND=1.20
 ALPHA= 10.0 DEG., DELTF= 0.0 DEG.
 CL=0.676, CD=0.119, CM=-0.009(AT .5 C)

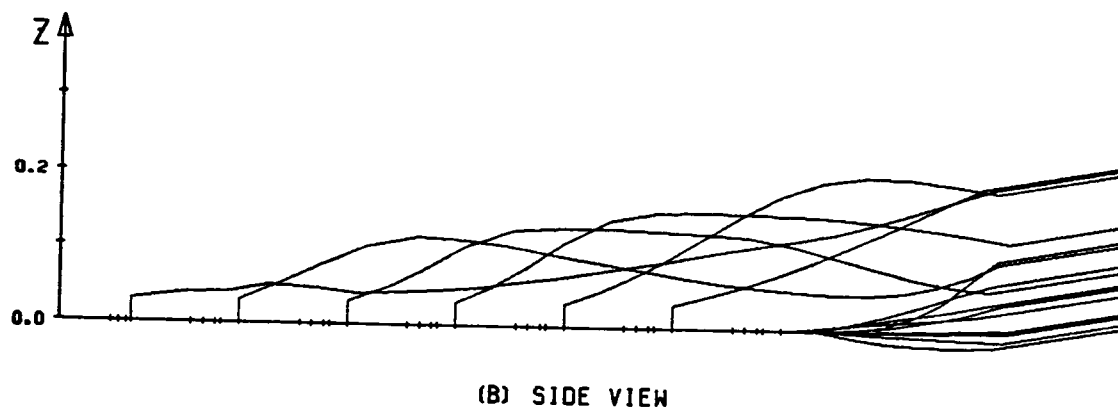
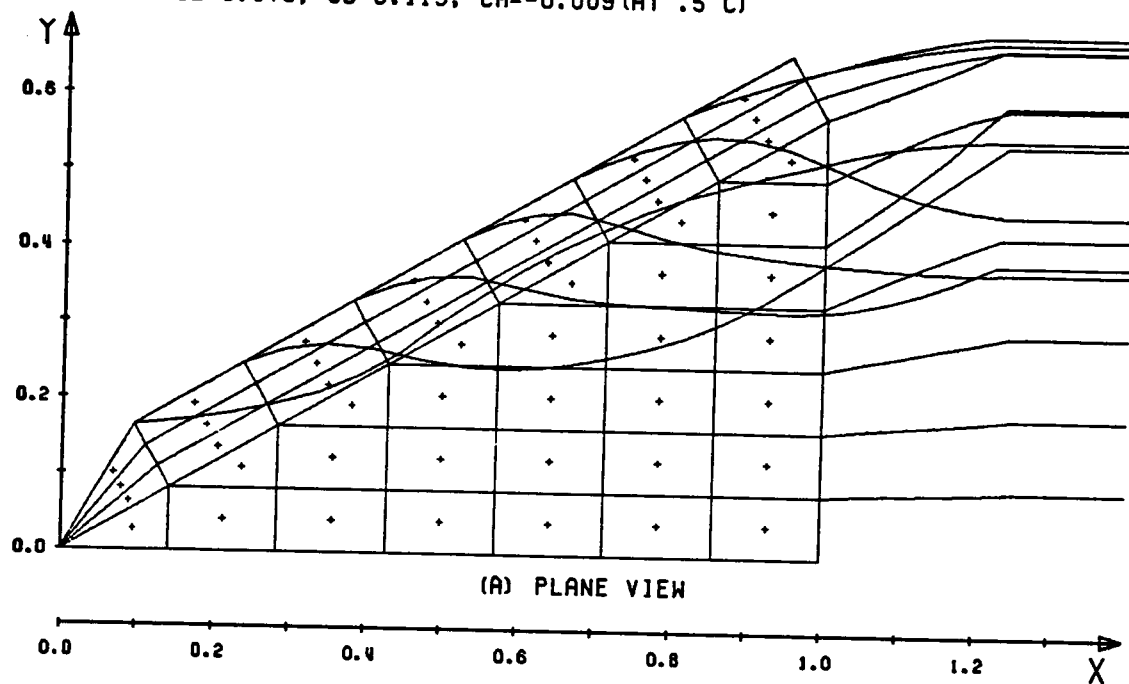
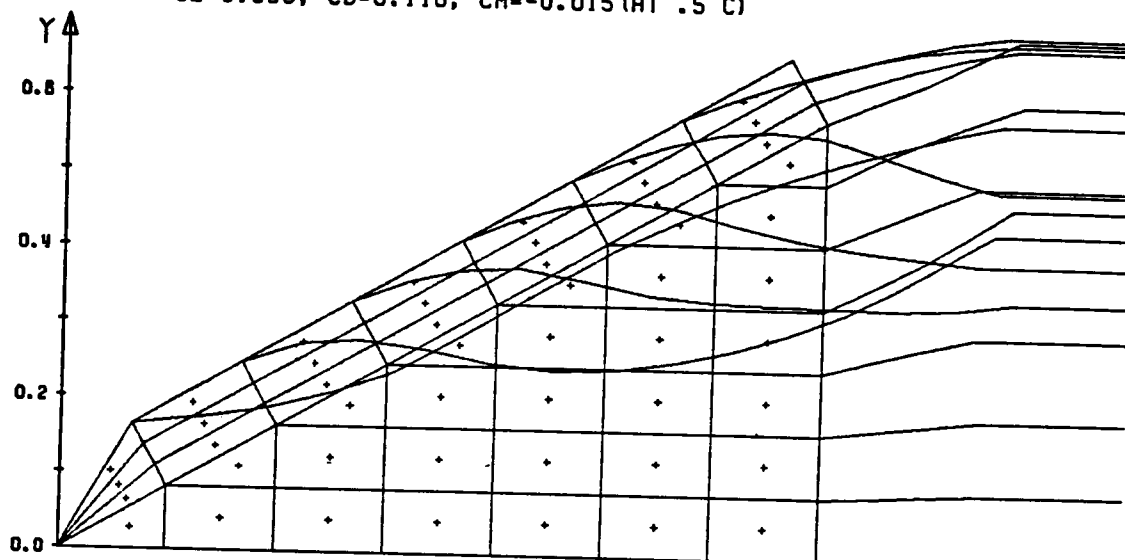
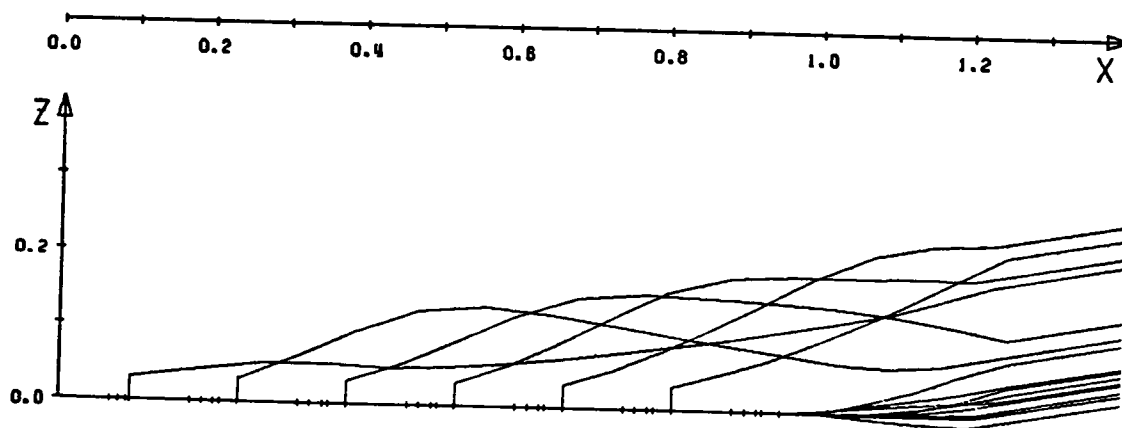


Fig. 55.b Continued.

7X3, CONVERGED AT ITER=10
 FEDG=0.030, DTC=0.070, AFACT=1.250
 T= 41.84 SEC HO=0.0082 FVEND=1.20
 ALPHA= 10.0 DEG., DELTF= 0.0 DEG.
 CL=0.659, CD=0.116, CM=-0.015 (AT .5 C)



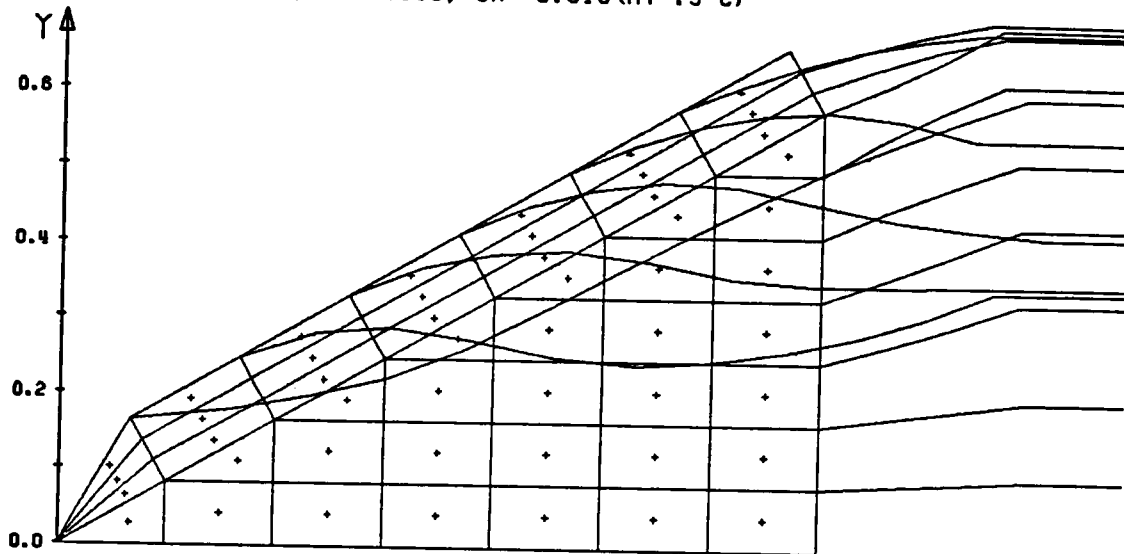
(A) PLANE VIEW



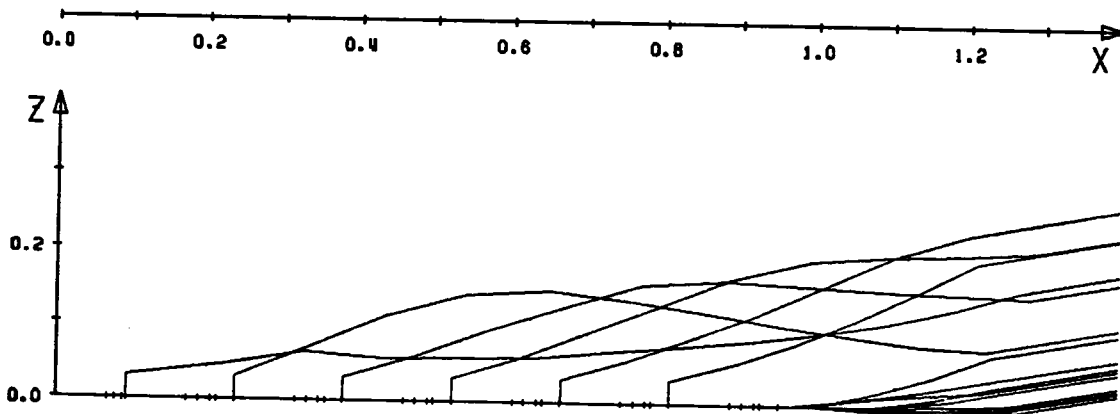
(B) SIDE VIEW

Fig. 55.c Continued.

7X3, CONVERGED AT ITER=10
 FEDG=0.030, DTC=0.090, AFACT=1.250
 T= 33.83 SEC HO=0.0082 FVEND=1.20
 ALPHA= 10.0 DEG., DELTF= 0.0 DEG.
 CL=0.668, CD=0.118, CM=-0.015 (AT .5 C)



(A) PLANE VIEW



(B) SIDE VIEW

Fig. 55.d Concluded.

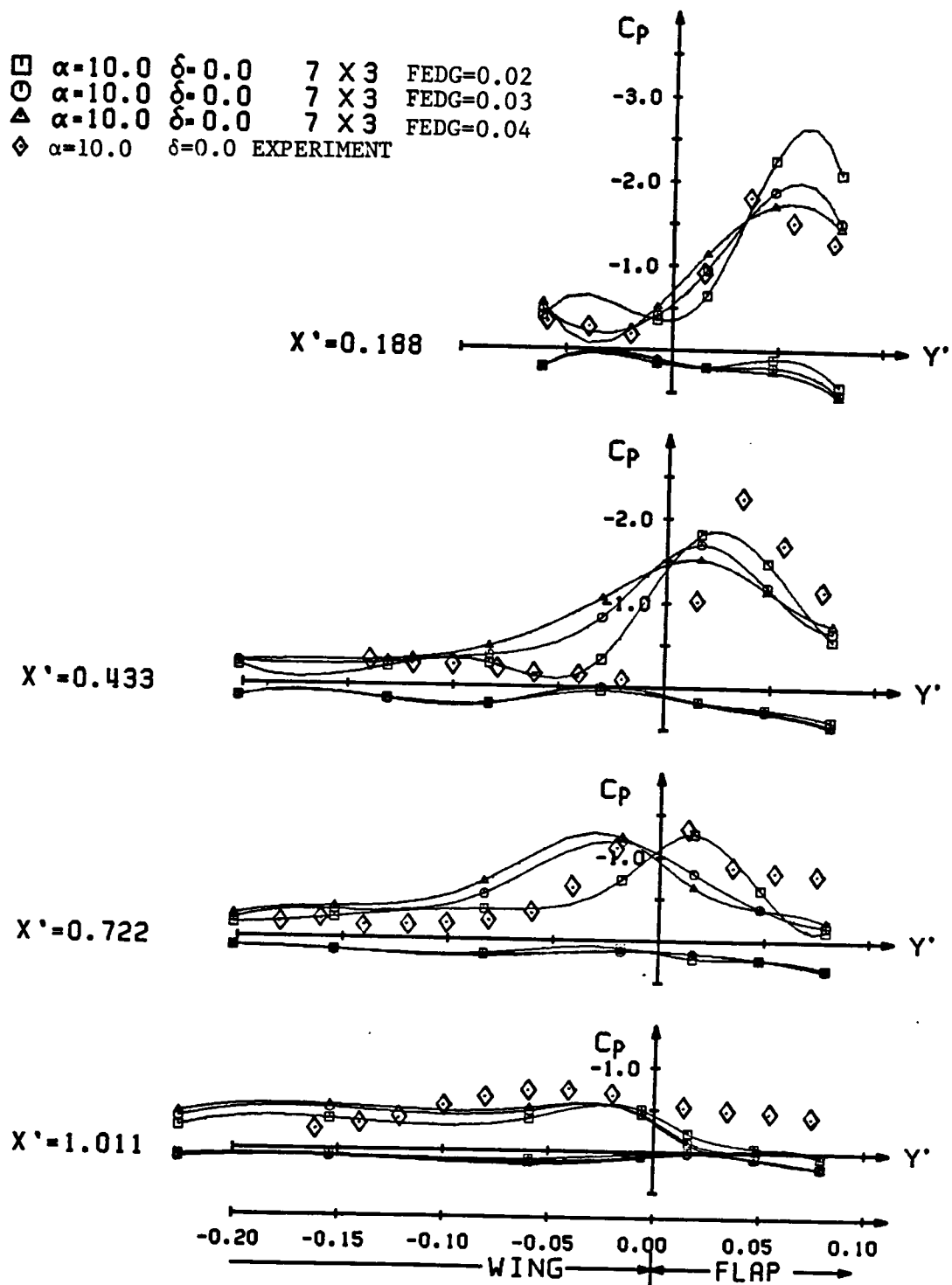
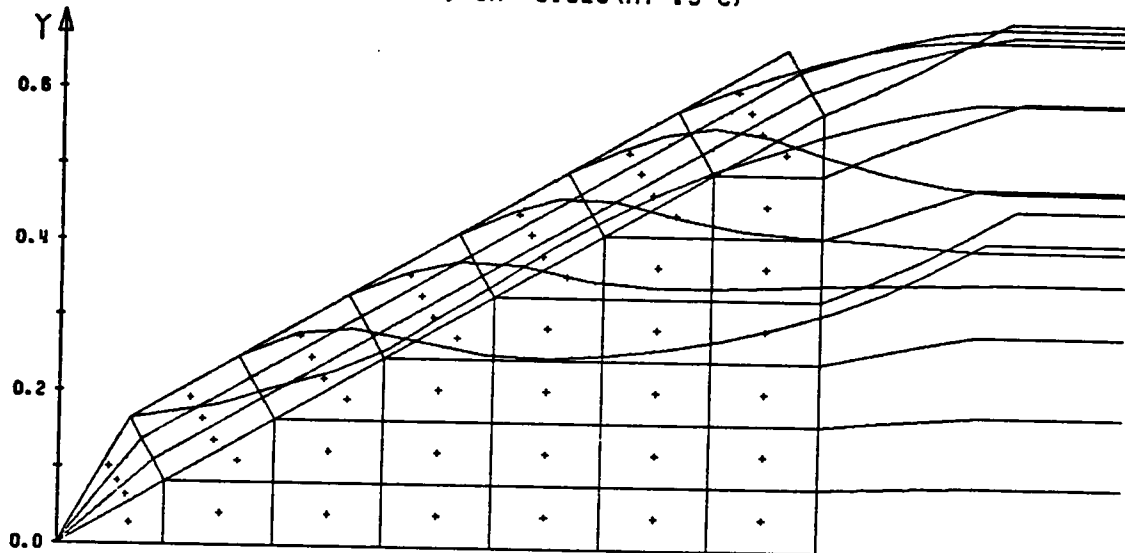
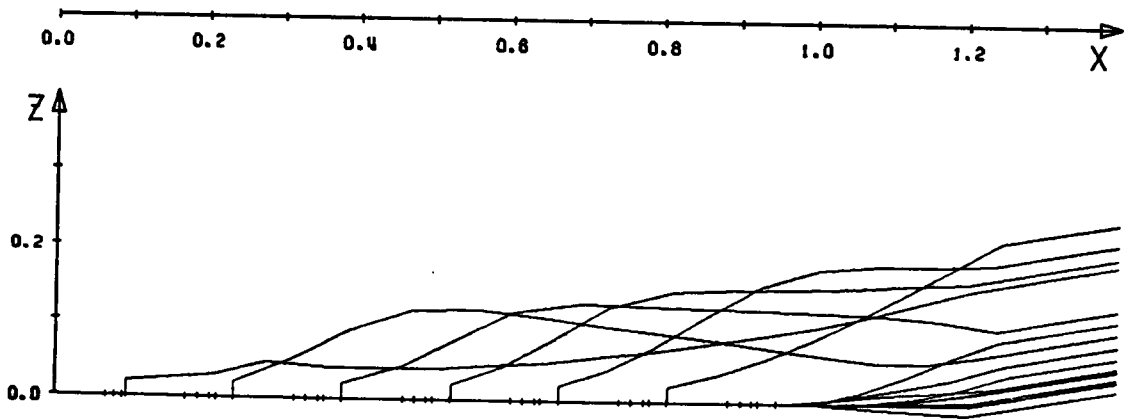


Fig. 56.a Effect of first shedding distance of free vortex from leading edge (FEDG).

7X3, CONVERGED AT ITER=28
 FEDG=0.020, DTC=0.070, AFACT=1.250
 T=117.91 SEC HO=0.0082 FVEND=1.20
 ALPHA= 10.0 DEG., DELTF= 0.0 DEG.
 CL=0.603, CD=0.106, CM=-0.025 (AT .5 C)



(A) PLANE VIEW



(B) SIDE VIEW

Fig. 56.b Continued.

7X9, CONVERGED AT ITER=10
 FEDG=0.030, DTC=0.070, AFACT=1.250
 T= 41.84 SEC HO=0.0082 FVEND=1.20
 ALPHA= 10.0 DEG., DELTF= 0.0 DEG.
 CL=0.659, CD=0.116, CM=-0.015(AT .5 C)

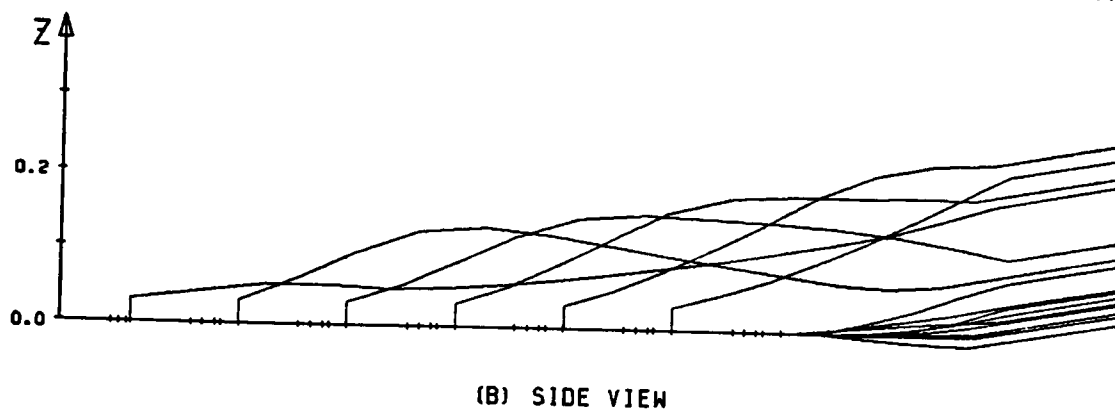
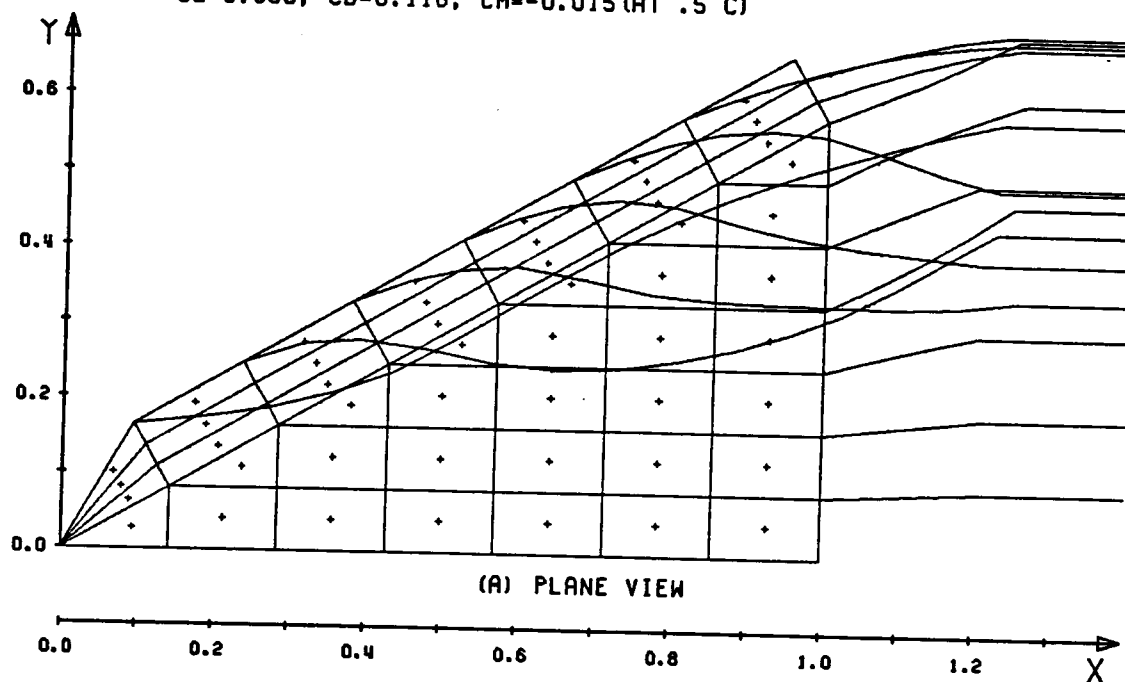
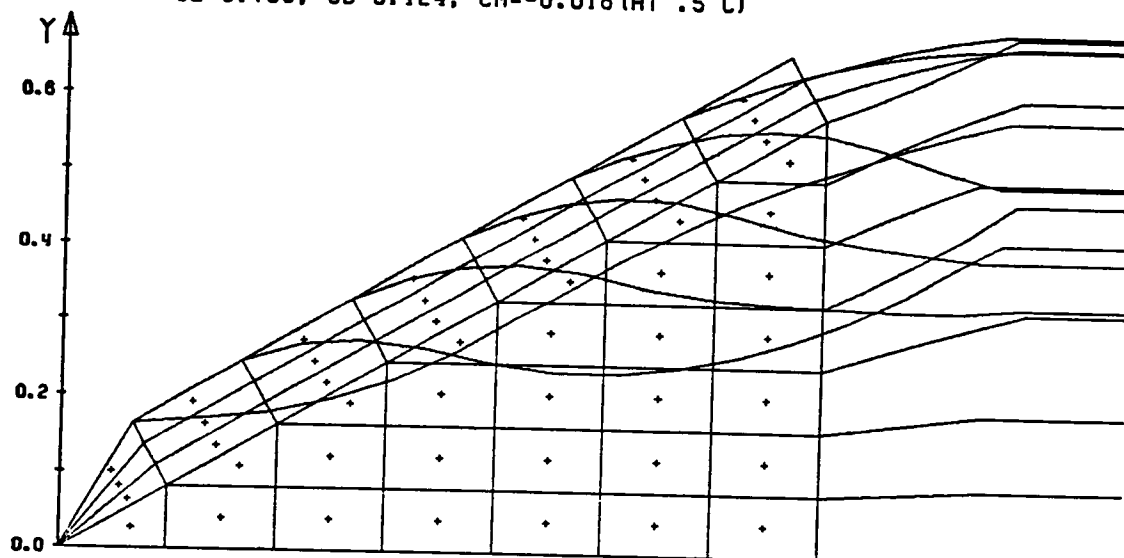
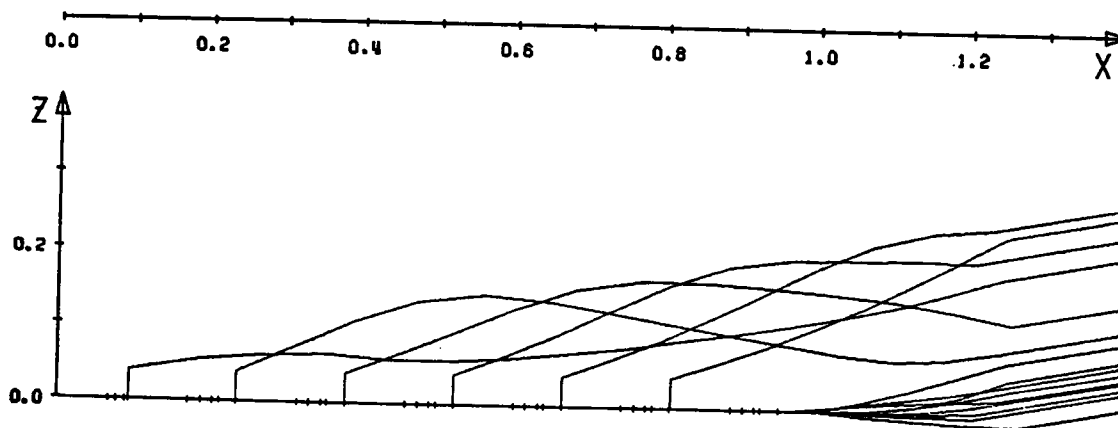


Fig. 56.c Continued.

7X3, CONVERGED AT ITER=10
 FEDG=0.040, DTC=0.070, AFACT=1.250
 T= 42.20 SEC HO=0.0082 FVEND=1.20
 ALPHA= 10.0 DEG., DELTF= 0.0 DEG.
 CL=0.703, CD=0.124, CM=-0.018(AT .5 C)



(A) PLANE VIEW



(B) SIDE VIEW

Fig. 56.d Concluded.

\square $\alpha=10.0$ $\delta=0.0$ 7 X 3 FVEND=1.2
 \circ $\alpha=10.0$ $\delta=0.0$ 7 X 3 FVEND=1.6
 \triangle $\alpha=10.0$ $\delta=0.0$ 7 X 3 FVEND=2.0
 \diamond $\alpha=10.0$ $\delta=0.0$ EXPERIMENT

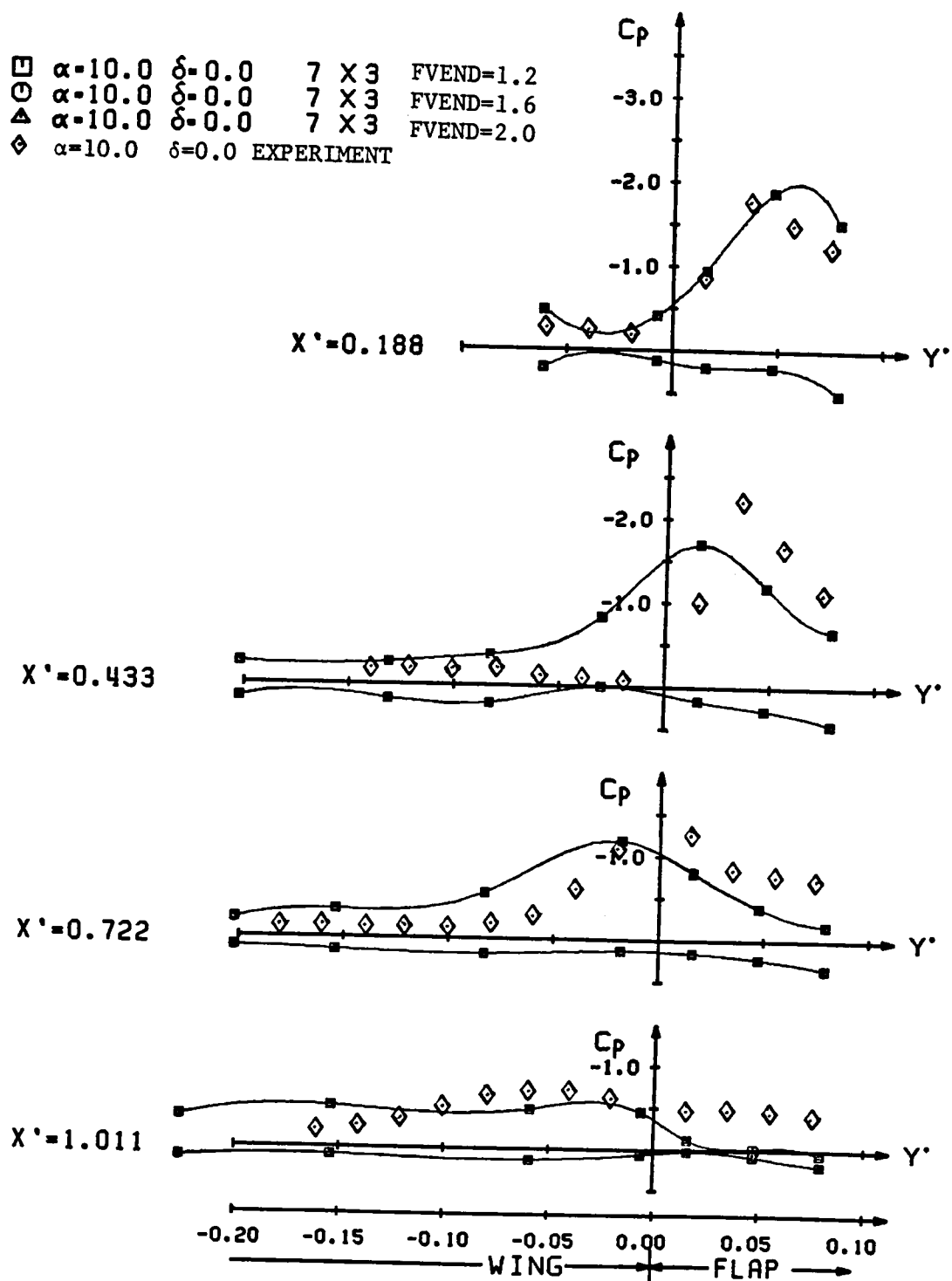


Fig. 57.a Effect of free stream matching point.

7X9, CONVERGED AT ITER=10
 FEDG=0.030, DTC=0.070, AFACT=1.250
 T= 41.84 SEC HO=0.0082 FVEND=1.20
 ALPHA= 10.0 DEG., DELTF= 0.0 DEG.
 CL=0.659, CD=0.116, CM=-0.015 (AT .5 C)

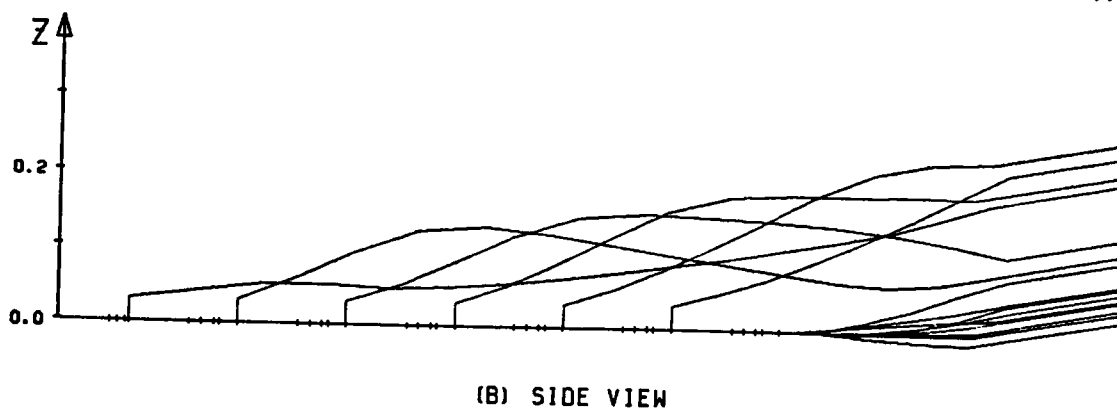
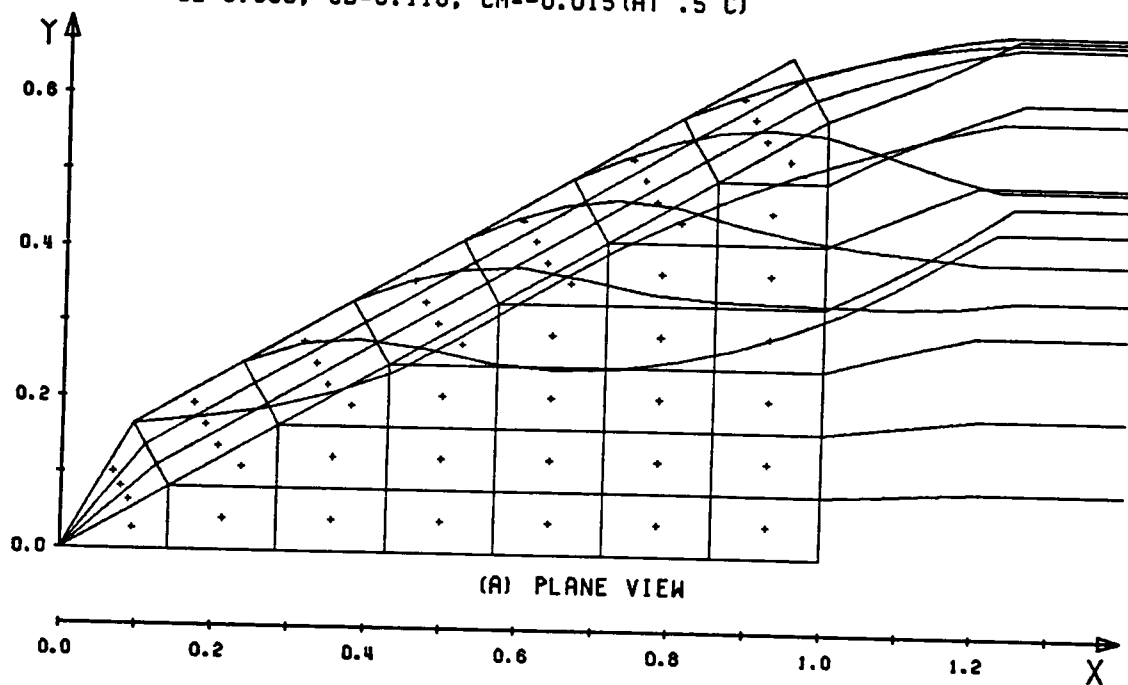


Fig. 57.b Continued.

7X3, CONVERGED AT ITER=14
 FEDG=0.030, DTC=0.070, AFACT=1.250
 T=129.57 SEC HO=0.0082 FVEND=1.60
 ALPHA= 10.0 DEG., DELTF= 0.0 DEG.
 CL=0.660, CD=0.116, CM=-0.015 (AT .5 C)

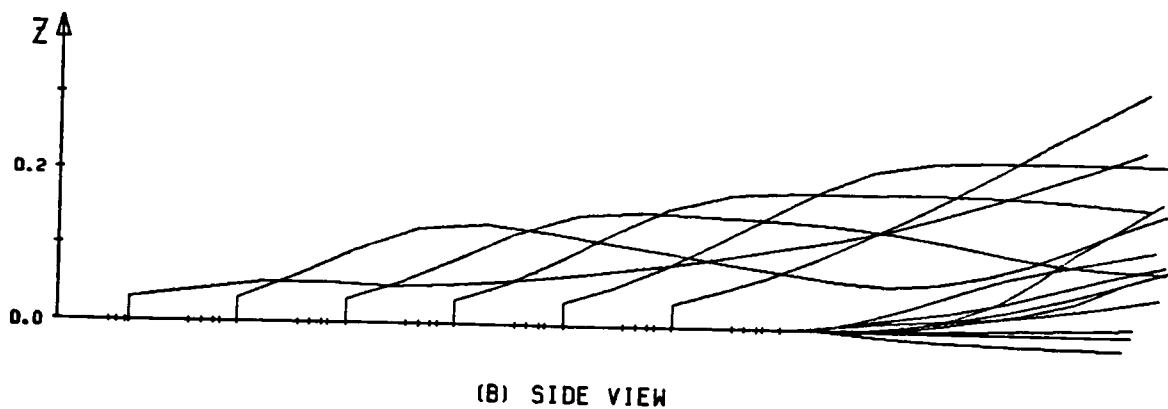
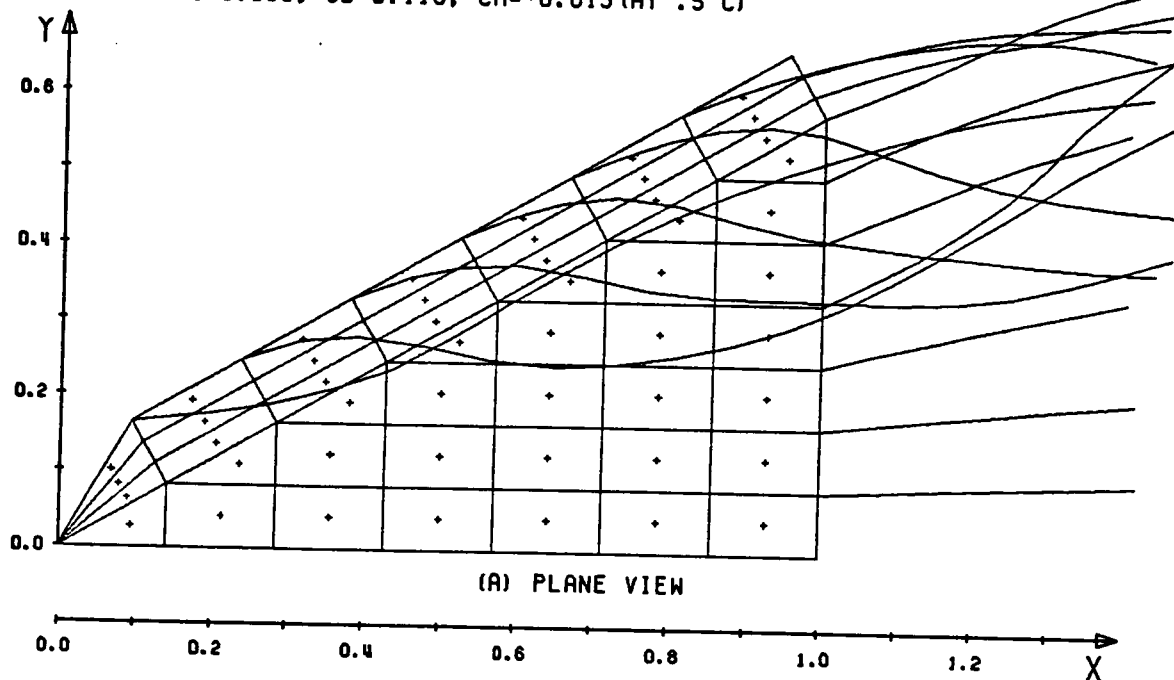
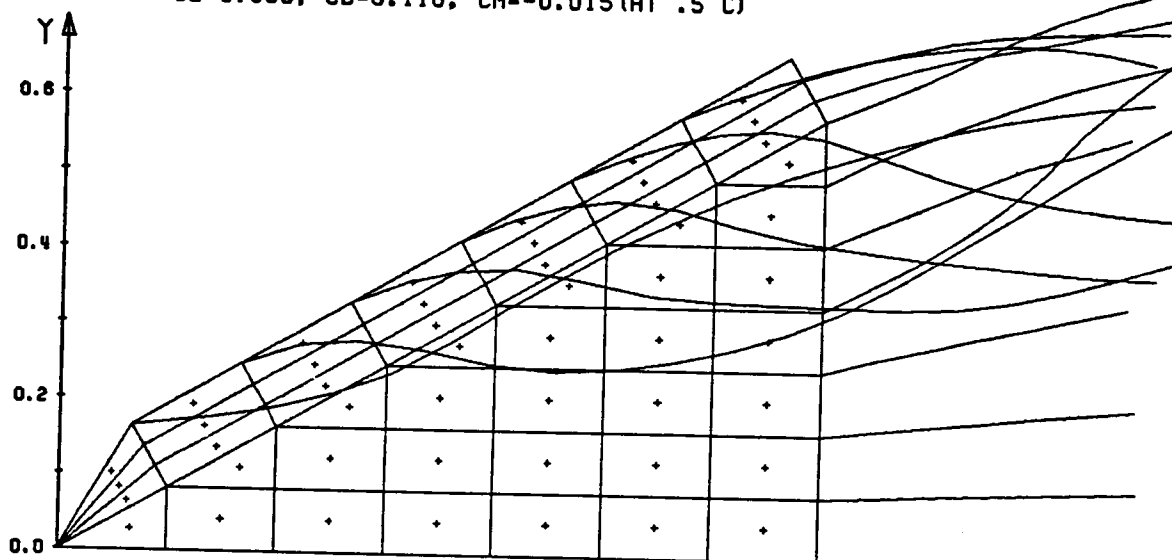
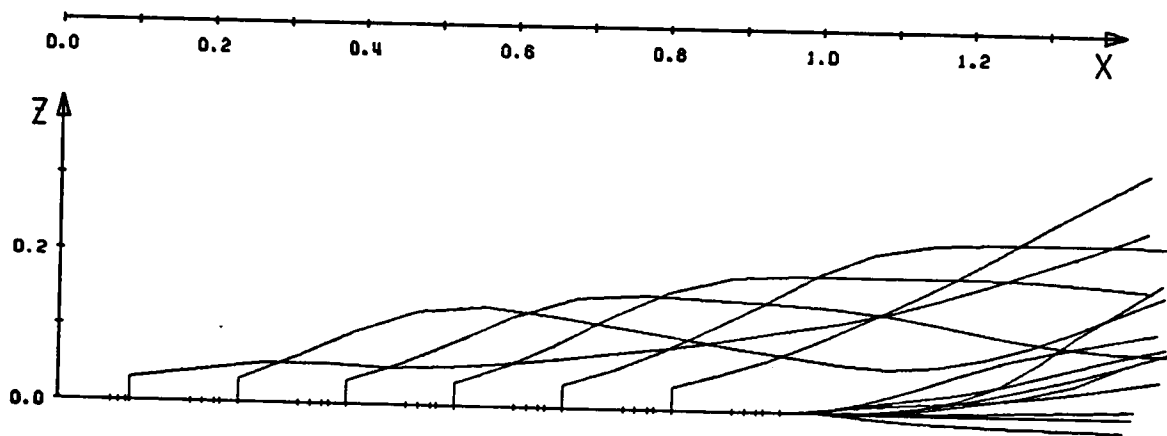


Fig. 57.c Continued.

7X3, CONVERGED AT ITER=17
 FEDG=0.030, DTC=0.070, AFACT=1.250
 T=268.60 SEC HO=0.0082 FVEND=2.00
 ALPHA= 10.0 DEG., DELTF= 0.0 DEG.
 CL=0.660, CD=0.116, CM=-0.015(AT .5 C)



(A) PLANE VIEW



(B) SIDE VIEW

Fig. 57.d Concluded.

7X2, CONVERGED AT ITER=13
 FEDG=0.020, DTC=0.070, AFACT=1.250
 T= 43.34 SEC HQ=0.0077 FVEND=1.20
 ALPHA= 20.0 DEG., DELTF= 7.5 DEG.
 CL=1.331, CD=0.454, CM=-0.087 (AT .5 C)

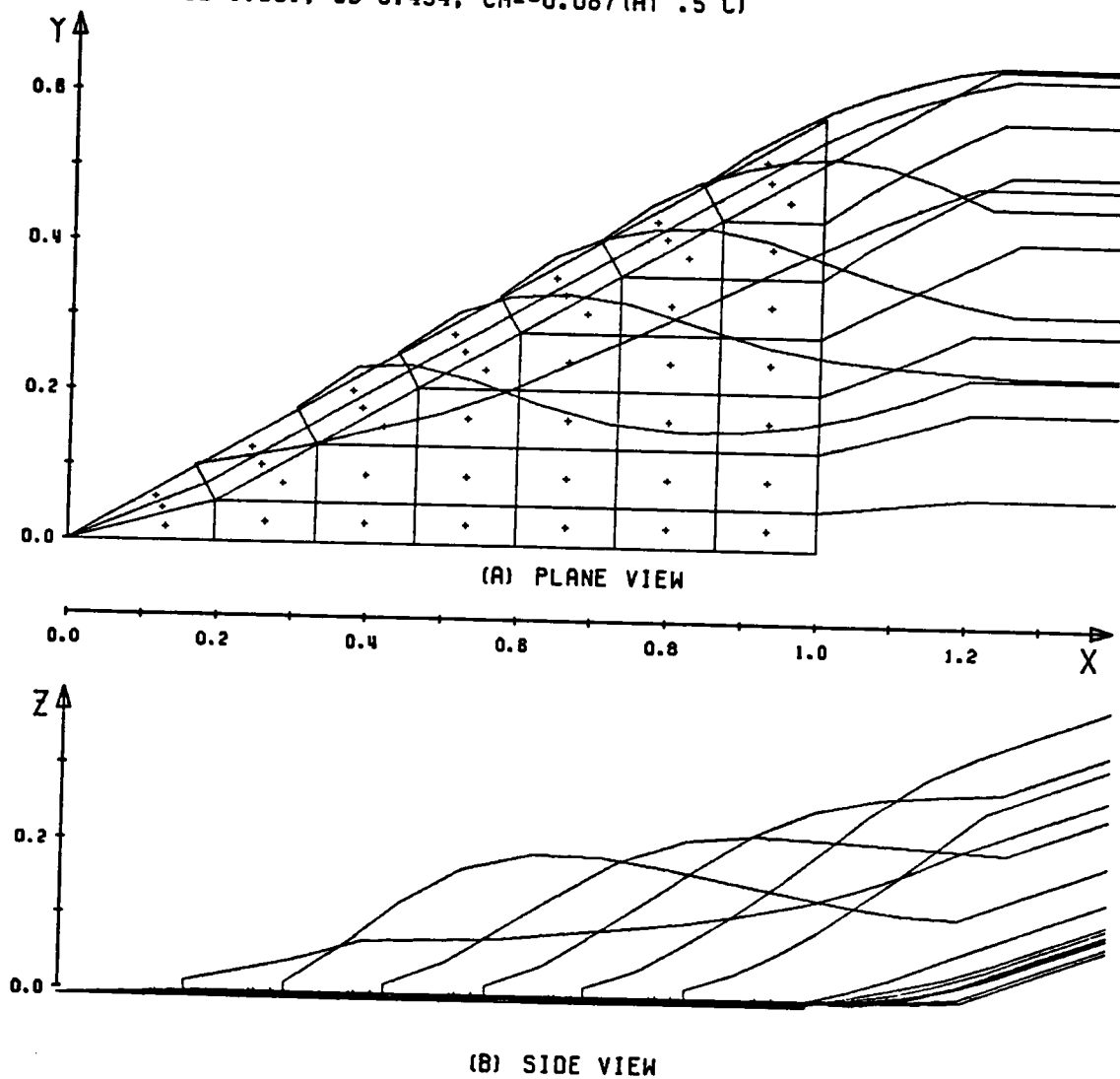


Fig. 58. Converged shape of free vortices for a plain 60° delta wing.

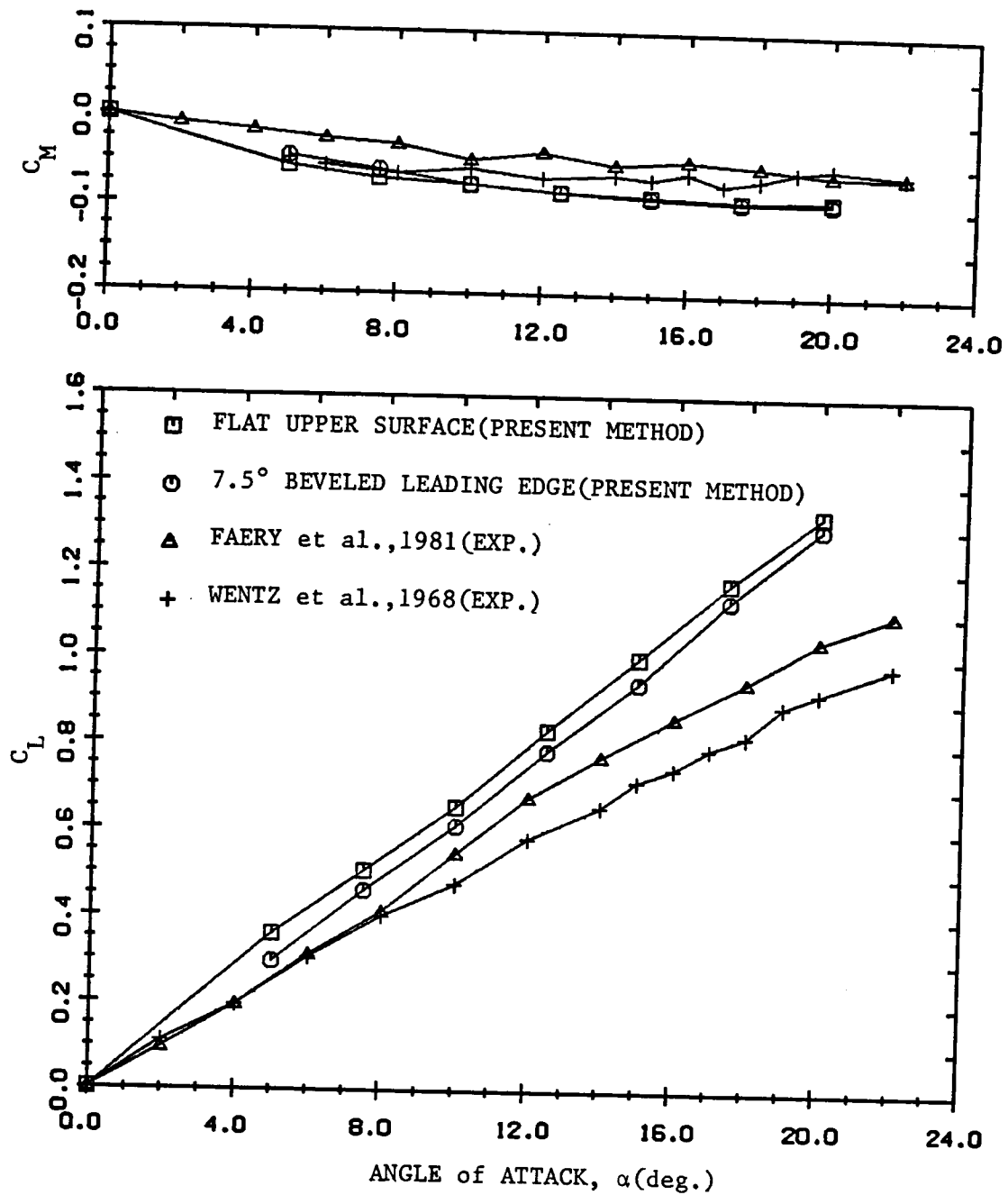


Fig. 59.a Comparison of total aerodynamic loads for a plain 60° delta wing with experimental data.

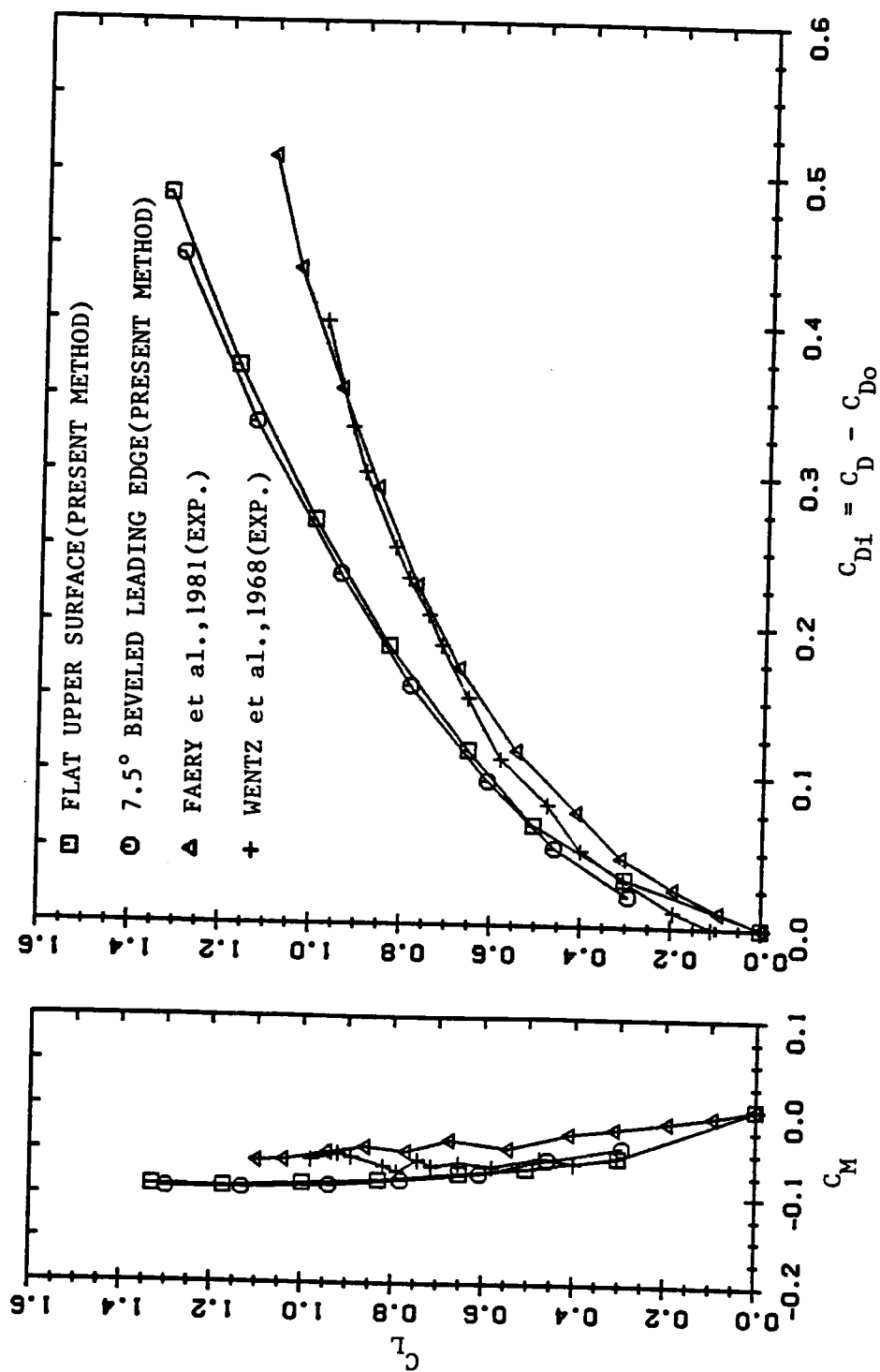
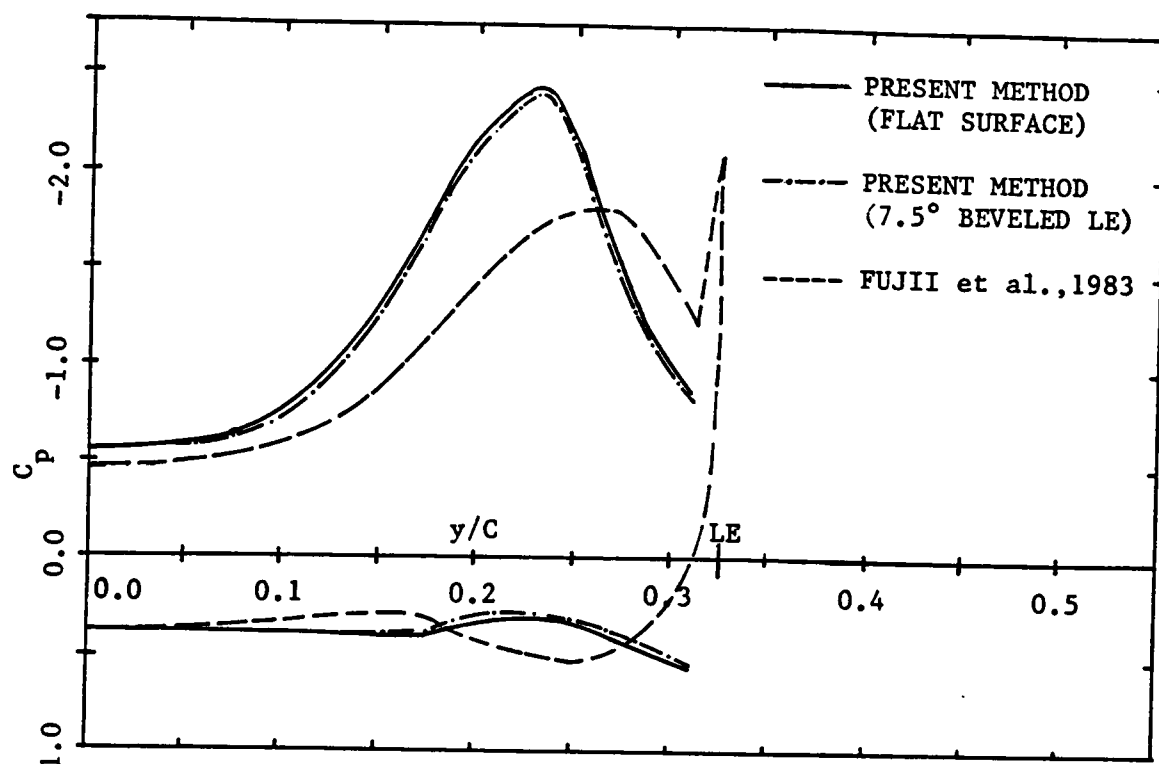
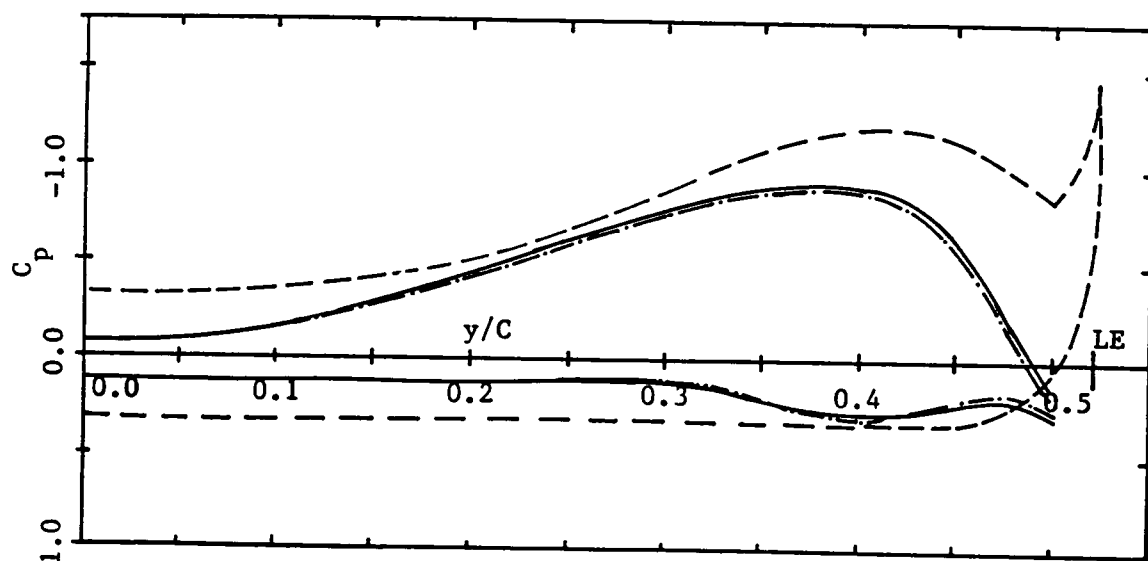


Fig. 59.b Concluded.



(a) $x/C = 0.56$



(b) $x/C = 0.90$

Fig. 60. Comparison of pressure distribution on a plain 60° delta wing at $\alpha=20^\circ$.

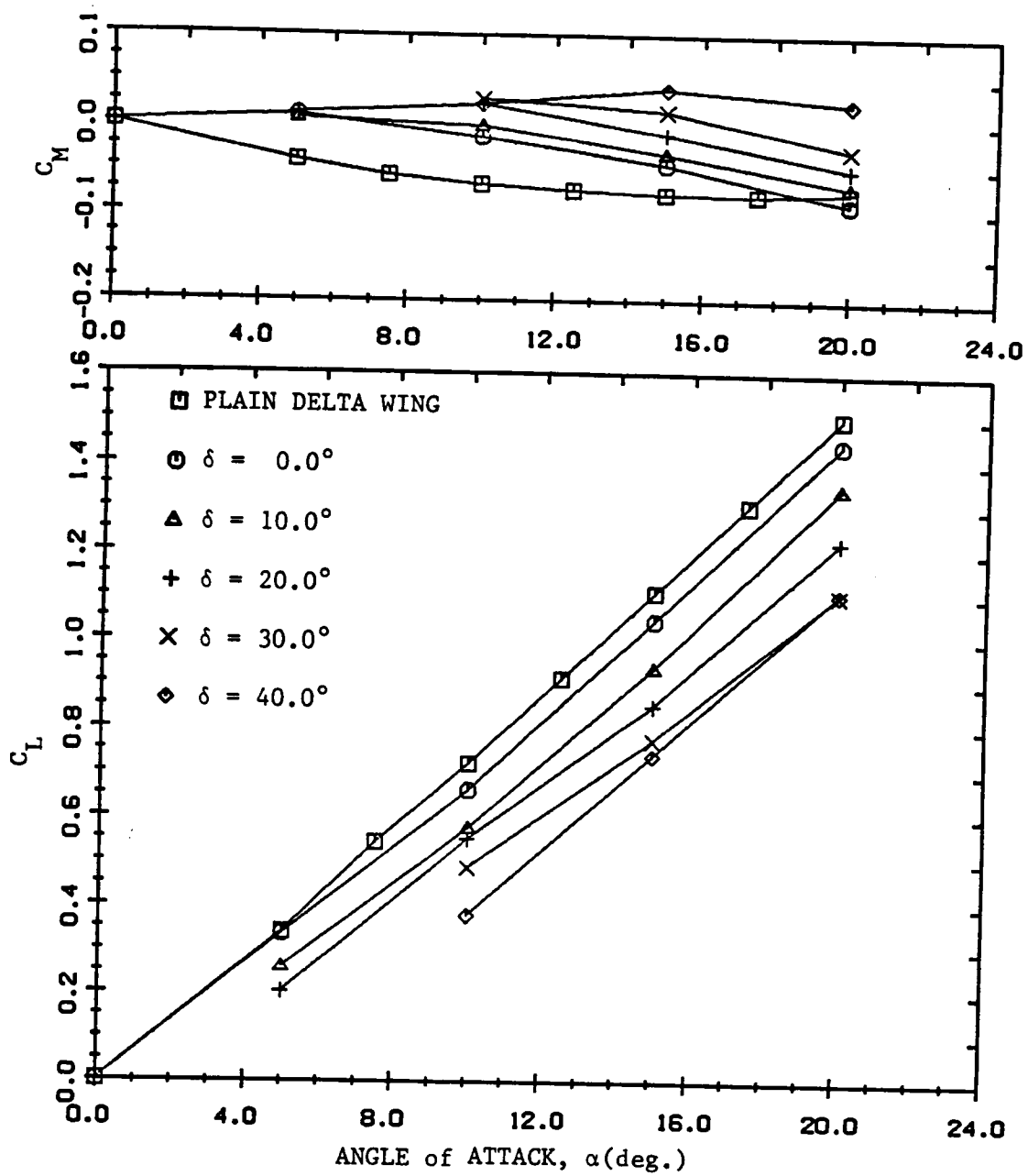


Fig. 61.a Effect of leading edge flap deflection of a 60° delta wing with leading edge flap.

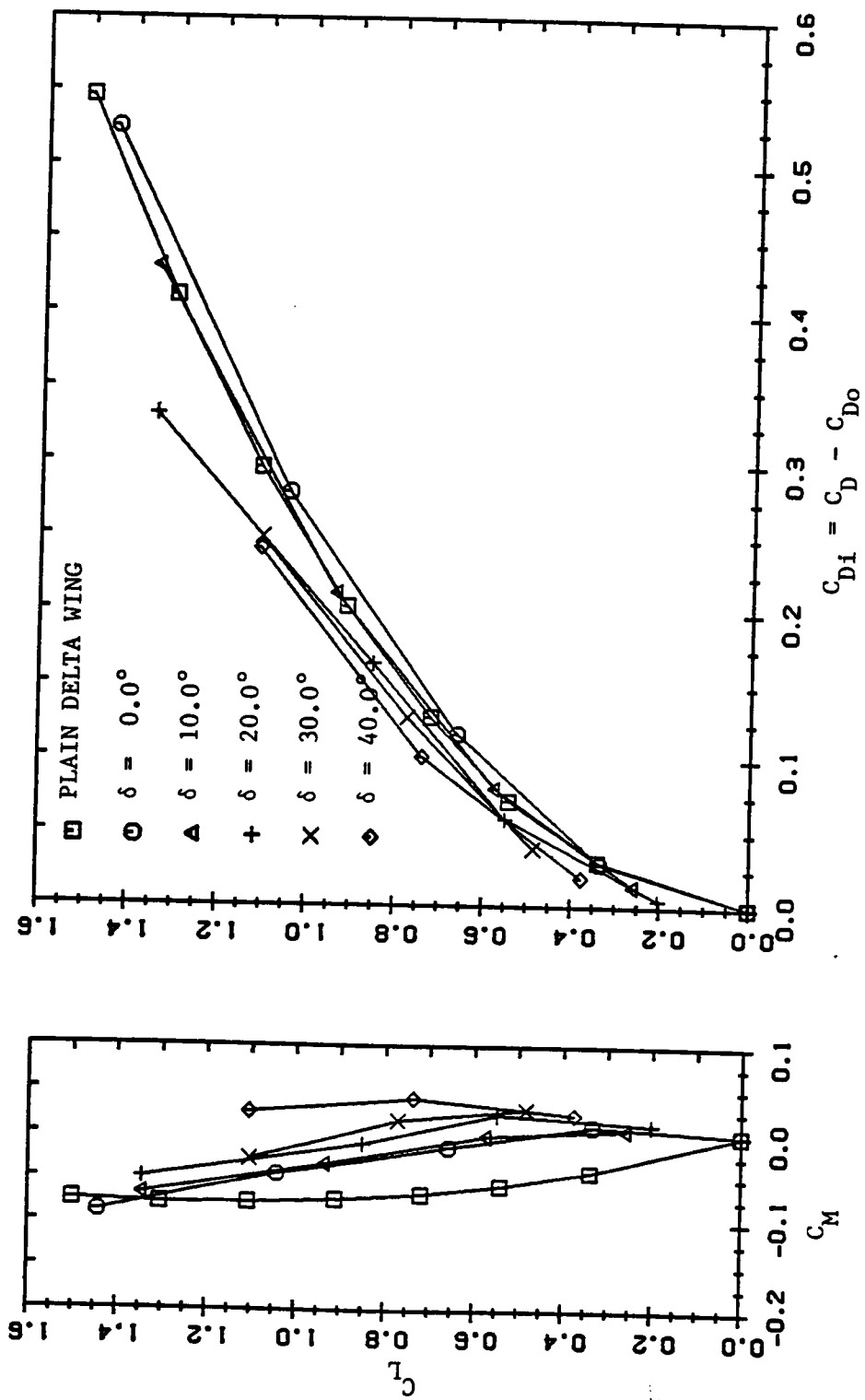


Fig. 61.b Concluded.

□	$\alpha=5.0$	$\delta=0.0$	7 X 3
○	$\alpha=5.0$	$\delta=10.0$	7 X 3
△	$\alpha=5.0$	$\delta=20.0$	7 X 3

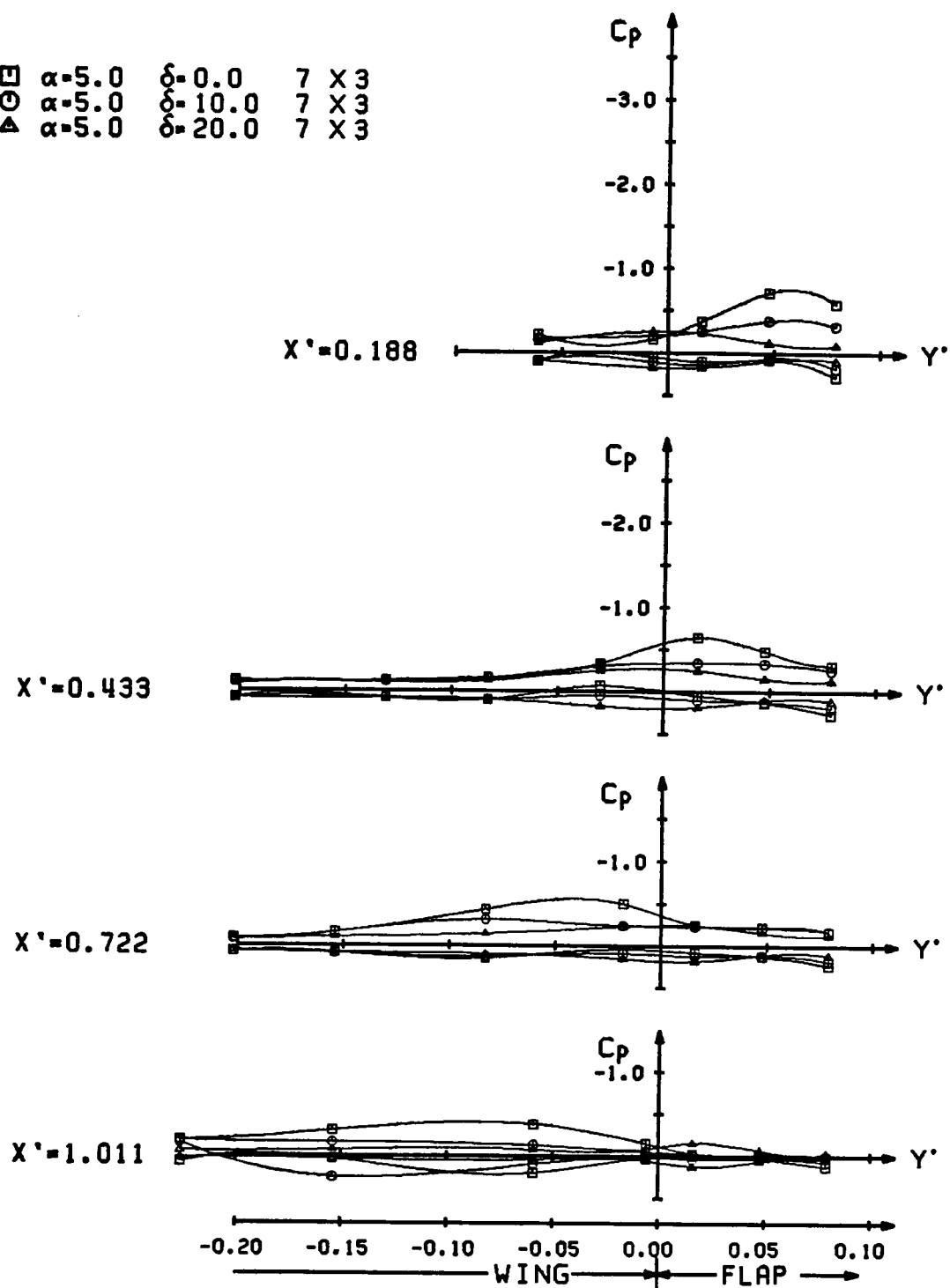


Fig. 62. Effect of flap deflection at $\alpha=5^\circ$ (computed).

□	$\alpha=10.0$	$\delta=0.0$	7 X 3
○	$\alpha=10.0$	$\delta=10.0$	7 X 3
△	$\alpha=10.0$	$\delta=20.0$	7 X 3
+	$\alpha=10.0$	$\delta=30.0$	7 X 3
X	$\alpha=10.0$	$\delta=40.0$	7 X 3

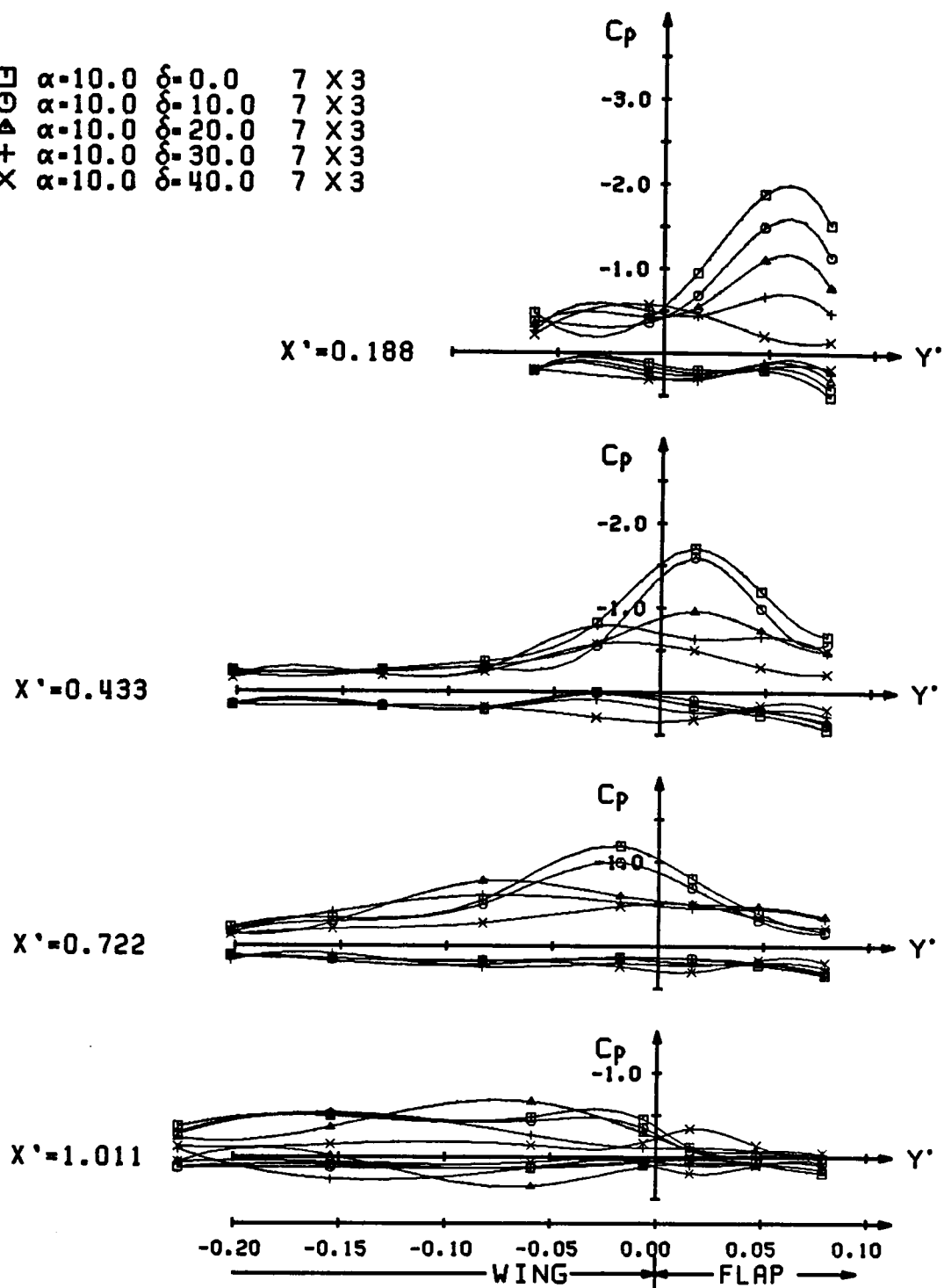


Fig. 63. Effect of flap deflection at $\alpha=10^\circ$ (computed).

□	$\alpha=15.0$	$\delta=0.0$	7 X 3
○	$\alpha=15.0$	$\delta=10.0$	7 X 3
△	$\alpha=15.0$	$\delta=20.0$	7 X 3
+	$\alpha=15.0$	$\delta=30.0$	7 X 3
X	$\alpha=15.0$	$\delta=40.0$	7 X 3

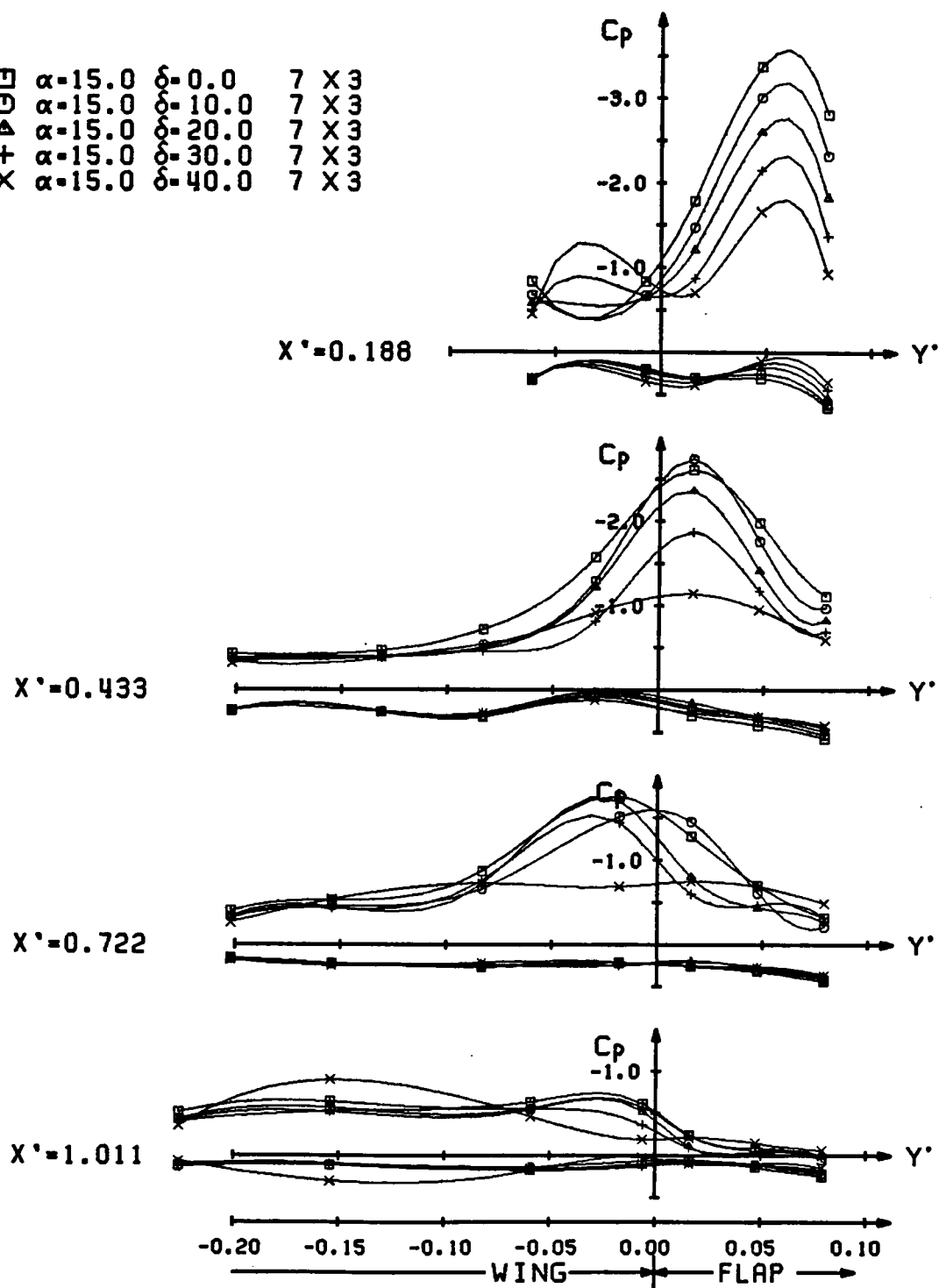


Fig. 64. Effect of flap deflection at $\alpha=15^\circ$ (computed).

□	$\alpha=20.0$	$\delta=0.0$	7 X 3
○	$\alpha=20.0$	$\delta=10.0$	7 X 3
△	$\alpha=20.0$	$\delta=20.0$	7 X 3
+	$\alpha=20.0$	$\delta=30.0$	7 X 3
X	$\alpha=20.0$	$\delta=40.0$	7 X 3

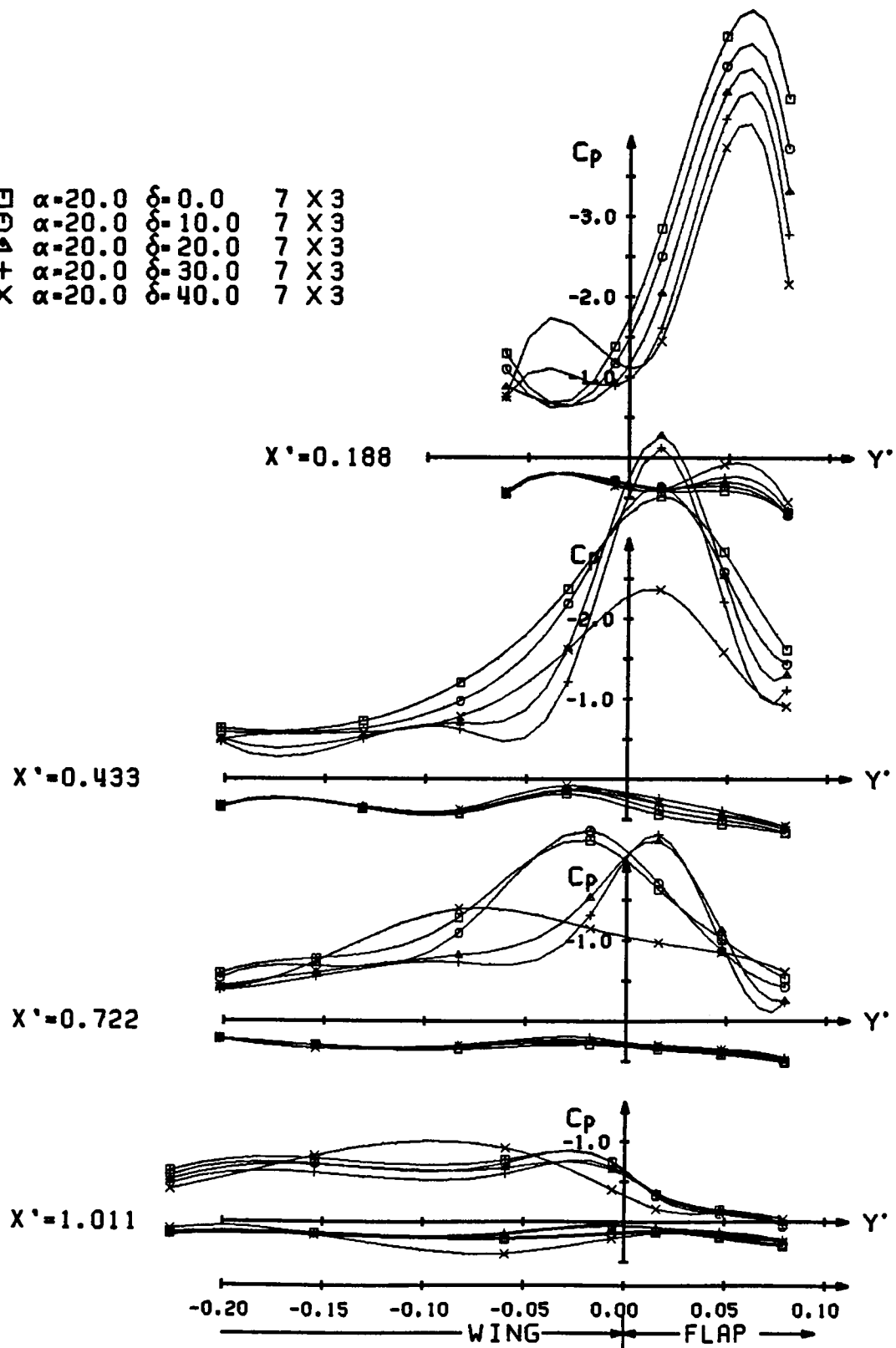


Fig. 65. Effect of flap deflection at $\alpha=20^\circ$ (computed).

7X9, CONVERGED AT ITER=10, IW=0
 FEDG=0.030, DTC=0.070, AFACT=1.250
 T= 42.22 SEC HO=0.0082 FVEND=1.20
 ALPHA= 10.0 DEG., DELTF= 0.0 DEG.
 CL=0.659, CD=0.116, CM= 0.015(AT .5 C)

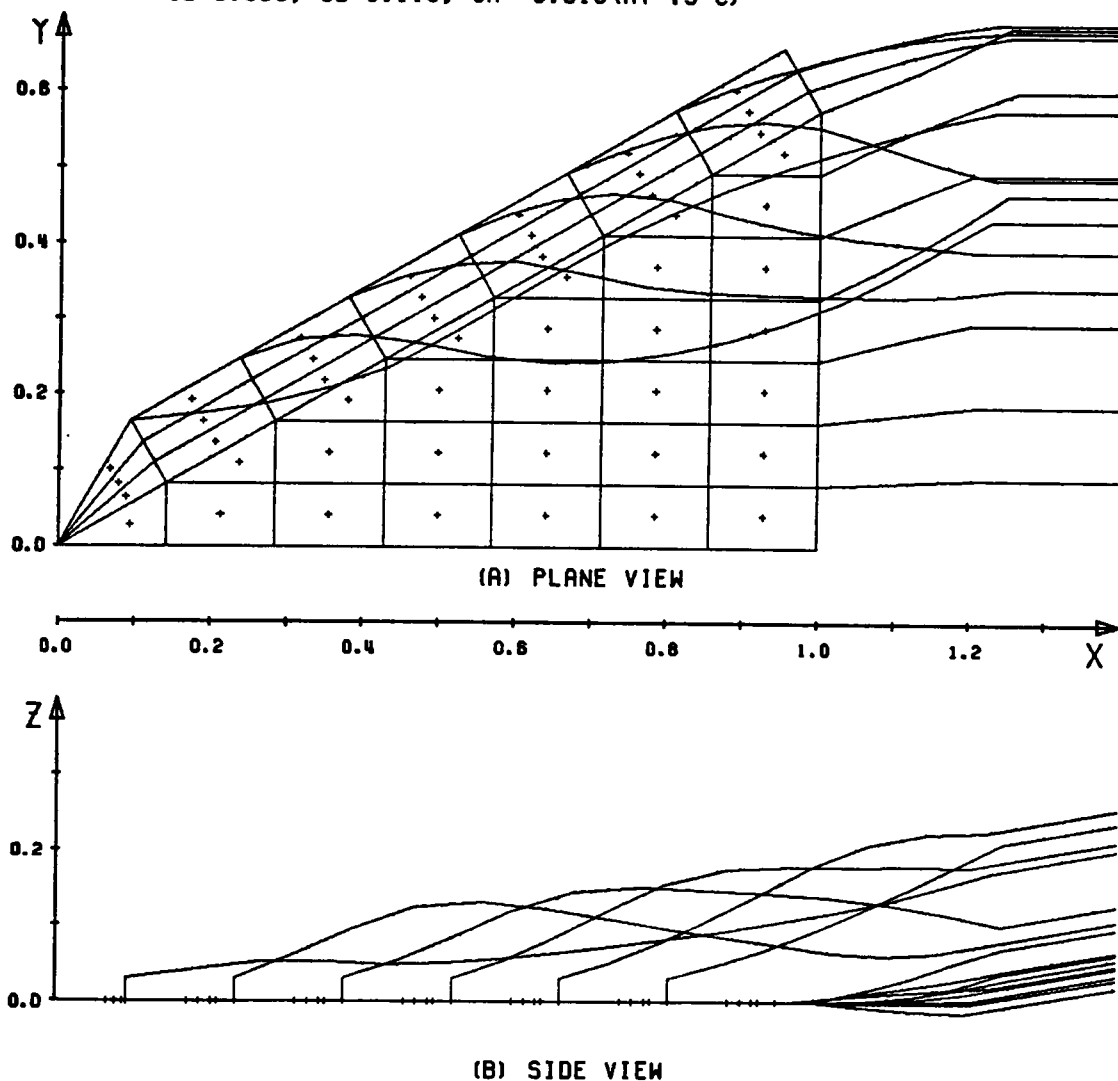
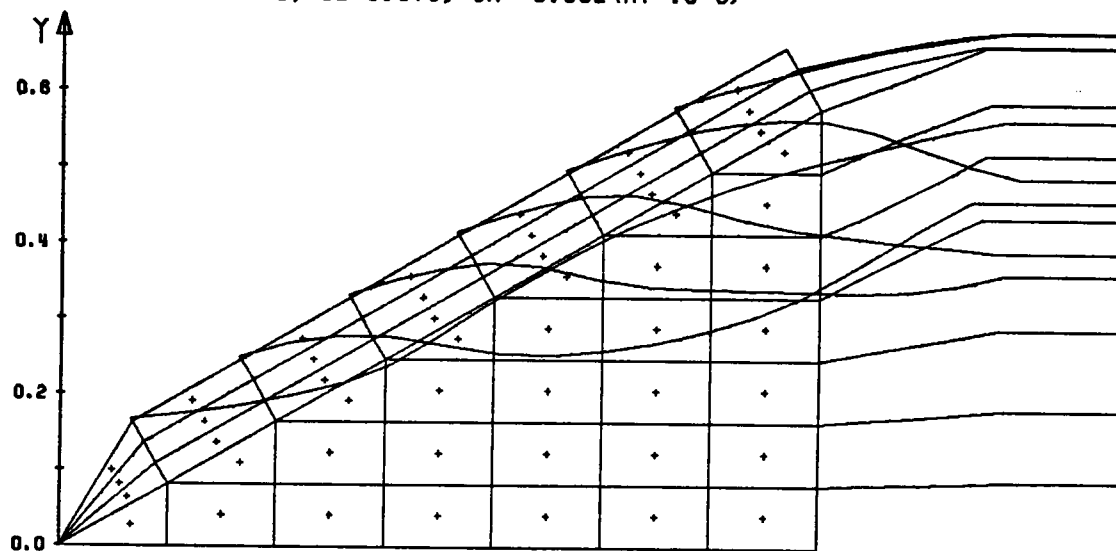
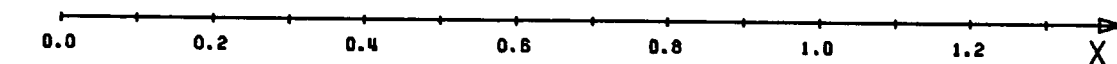


Fig. 66. Converged shape of free vortices at $\alpha=10^\circ$ with $\delta=0^\circ$

7X9, CONVERGED AT ITER=16, IW=0
 FEDG=0.030, DTC=0.060, AFACT=1.250
 T= 81.22 SEC HQ=0.0082 FVEND=1.20
 ALPHA= 10.0 DEG., DELTF= 10.0 DEG.
 CL=0.572, CD=0.079, CM= 0.002 (AT .5 C)



(A) PLANE VIEW



(B) SIDE VIEW

Fig. 67. Converged shape of free vortices at $\alpha=10^\circ$ with $\delta=10^\circ$

7X9, CONVERGED AT ITER=20, IW=0
 FEDG=0.030, DTC=0.070, AFACT=1.250
 T= 85.28 SEC HO=0.0082 FVEND=1.20
 ALPHA= 10.0 DEG., DELTF= 20.0 DEG.
 CL=0.548, CD=0.059, CM=-0.022 (AT .5 C)

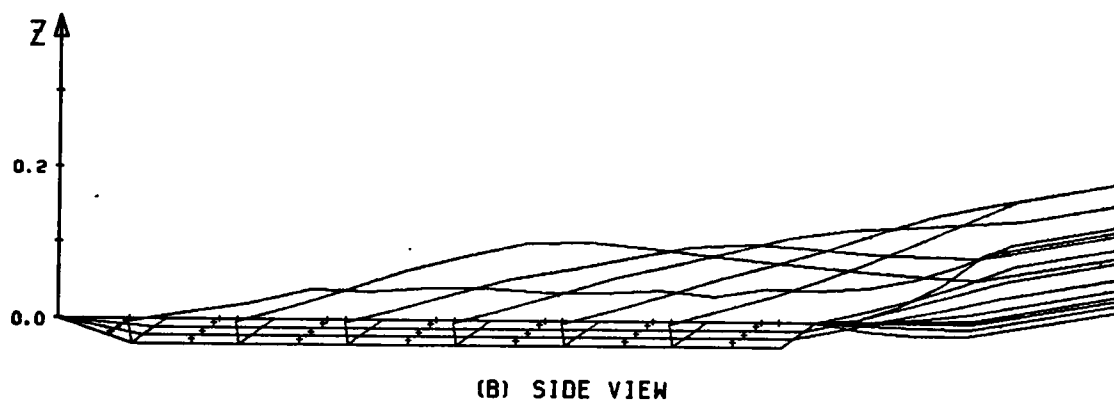
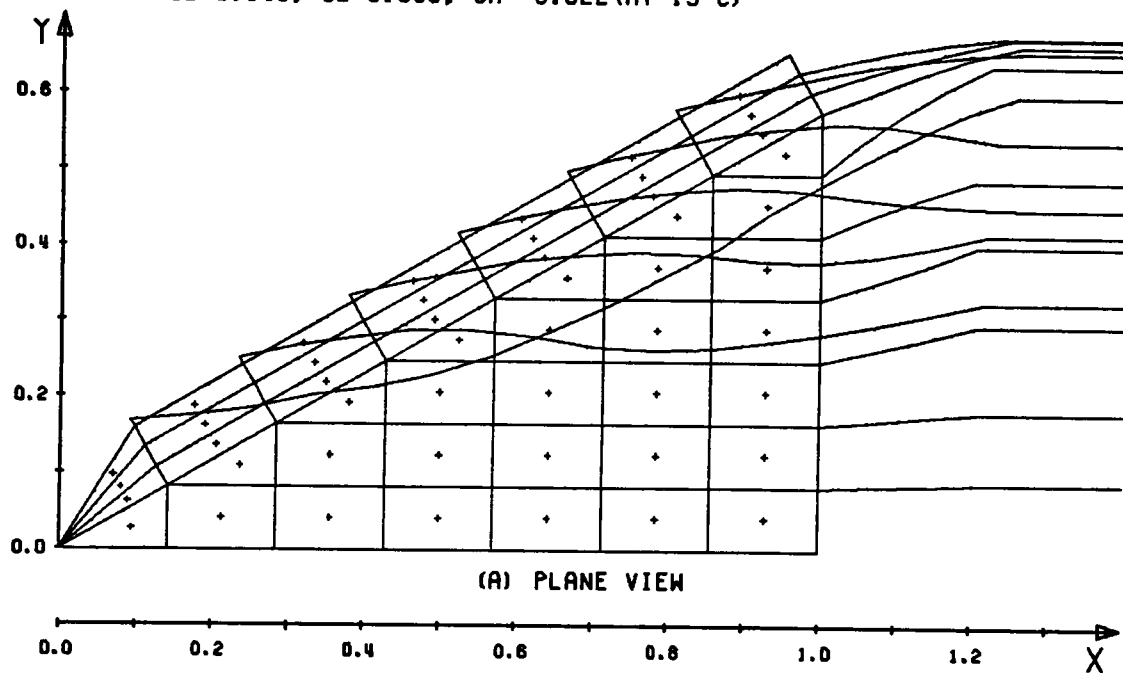


Fig. 68. Converged shape of free vortices at $\alpha=10^\circ$ with $\delta=20^\circ$

7X3, CONVERGED AT ITER=23, IW=0
 FEDG=0.030, DTC=0.060, AFACT=1.250
 T=115.22 SEC HO=0.0082 FVEND=1.20
 ALPHA= 10.0 DEG., DELTF= 90.0 DEG.
 CL=0.485, CD=0.039, CM=-0.028 (AT .5 C)

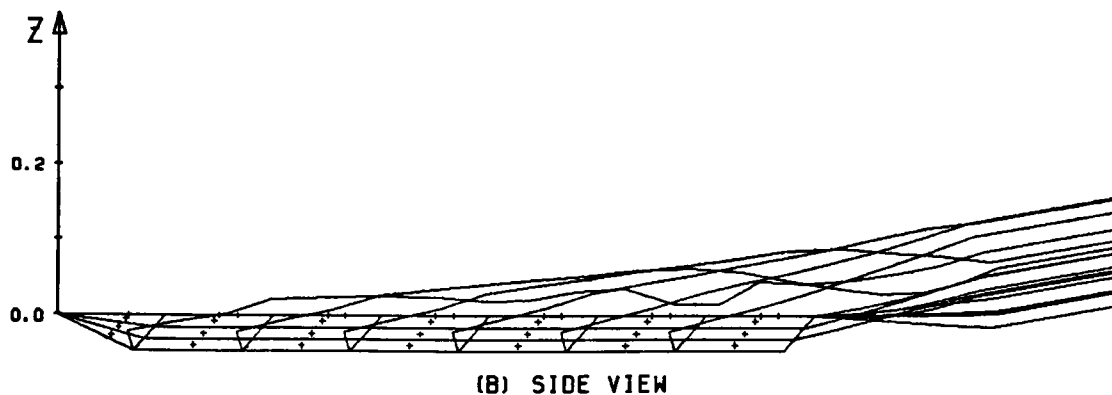
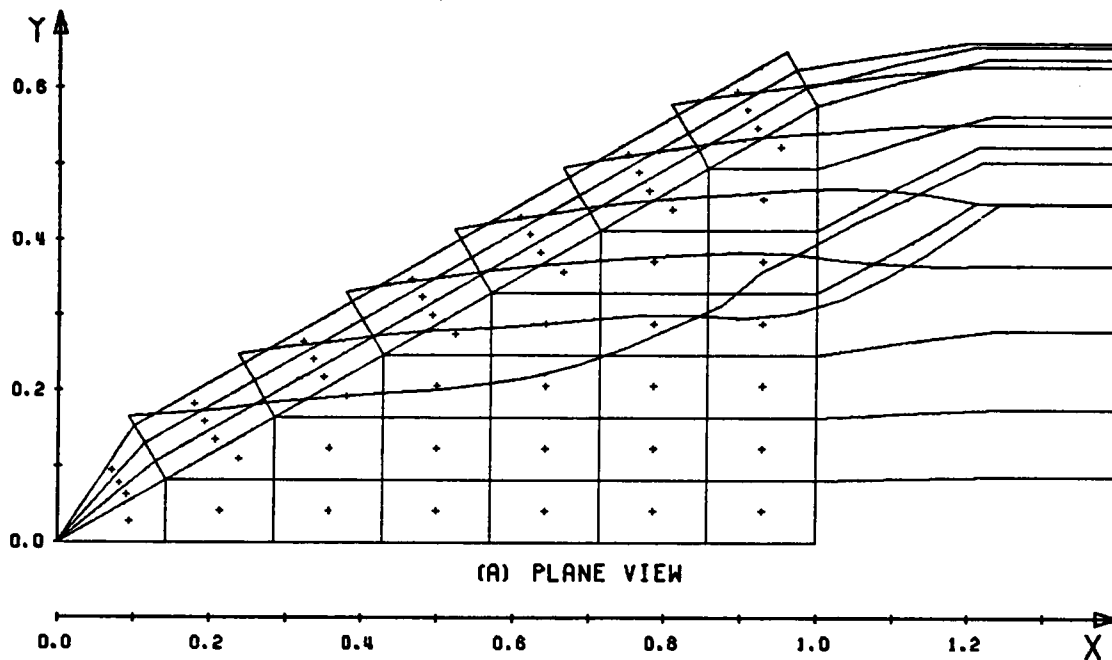


Fig. 69. Converged shape of free vortices at $\alpha=10^\circ$ with $\delta=30^\circ$

7X9, CONVERGED AT ITER= 7. IW=0
 FEDG=0.030, DTC=0.070, AFACT=1.250
 T= 29.91 SEC HO=0.0082 FVEND=1.20
 ALPHA= 10.0 DEG., DELTF= 40.0 DEG.
 CL=0.376, CD=0.019, CM=-0.022 (AT .5 C)

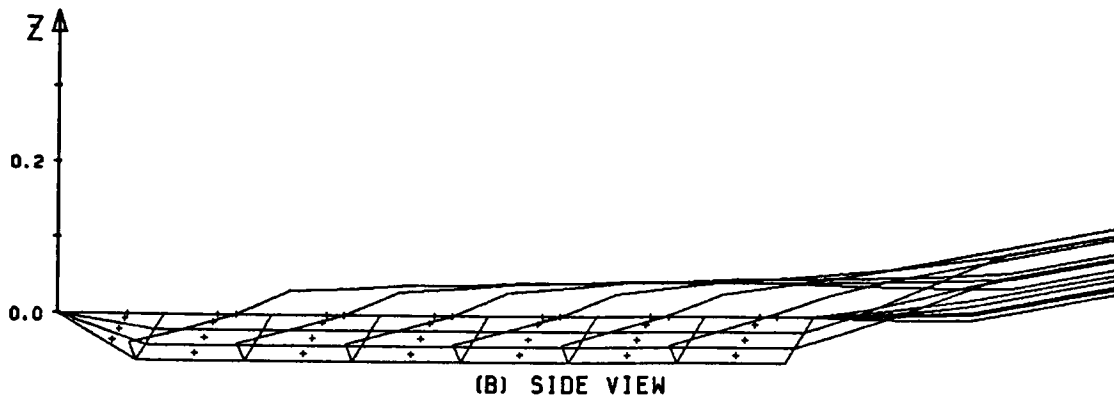
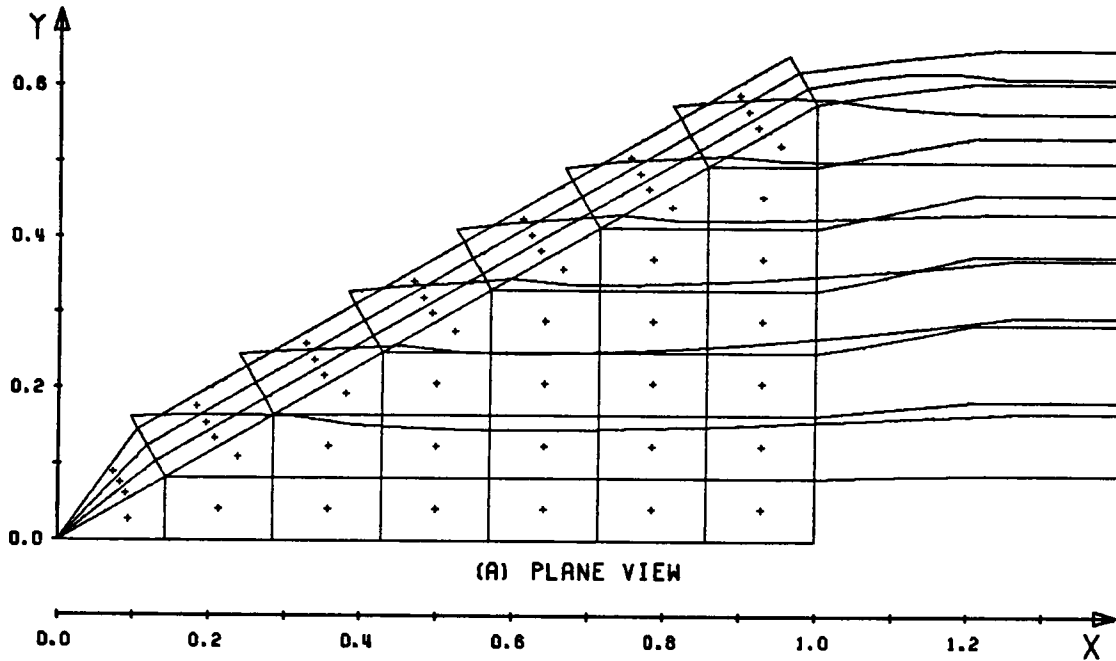


Fig. 70. Converged shape of free vortices at $\alpha=10^\circ$ with $\delta=40^\circ$

7X9, CONVERGED AT ITER= 7, IW=0
 FEDG=0.030, DTC=0.080, AFACT=1.250
 T= 26.22 SEC HO=0.0082 FVEND=1.20
 ALPHA= 5.0 DEG., DELTF= 20.0 DEG.
 CL=0.202, CD=0.005, CM=-0.011 (AT .5 C)

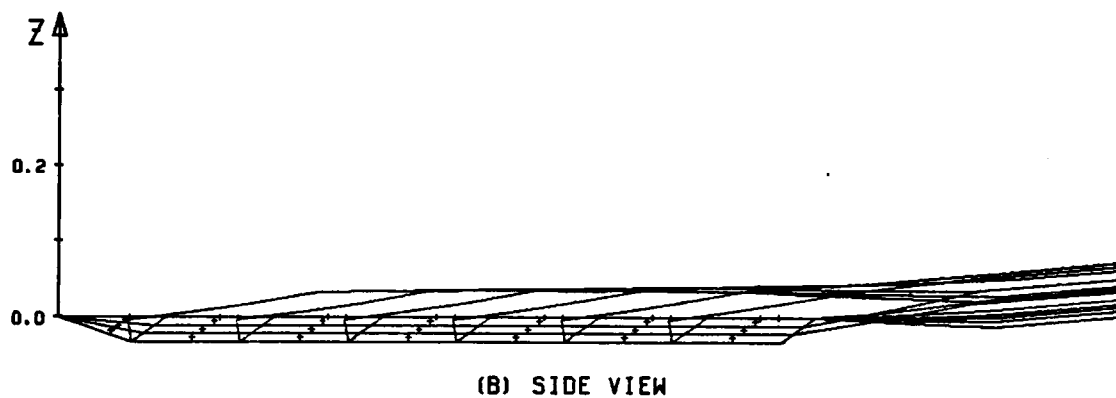
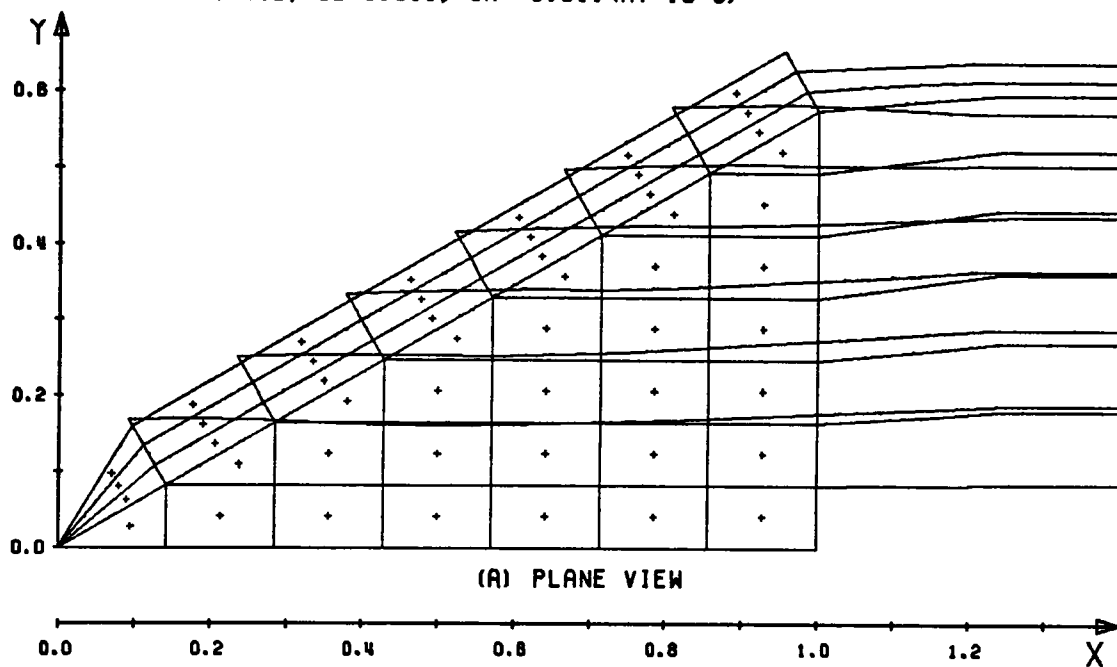


Fig. 71. Converged shape of free vortices at $\alpha=5^\circ$ with $\delta=20^\circ$

□ $\alpha=10.0$ $\delta=0.0$ 7 X 3

◇ $\alpha=10.0$ $\delta=0.0$ EXPERIMENT

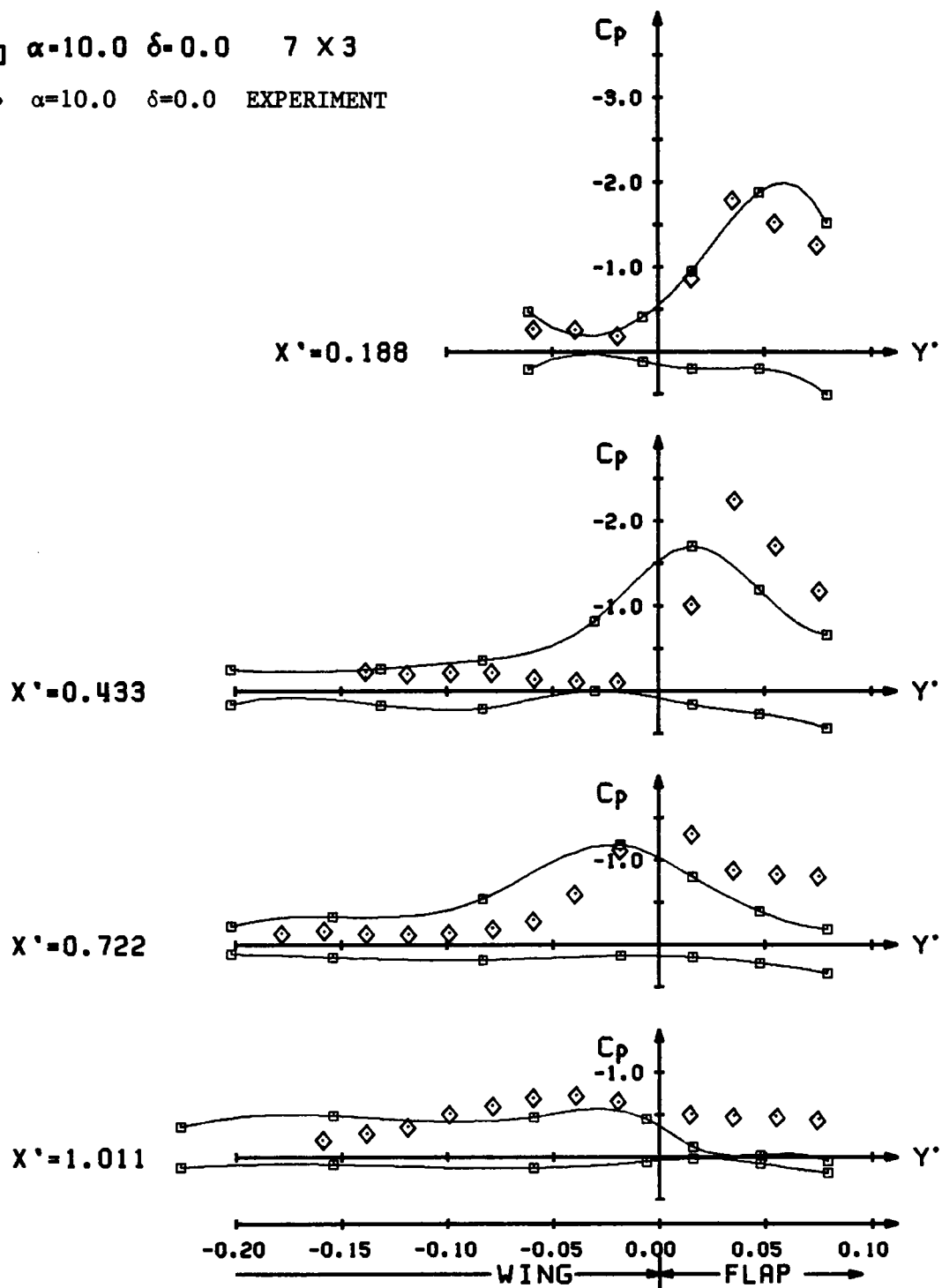


Fig. 72. Comparison of pressure distribution on a 60° delta wing with leading edge flap at $\alpha=10^\circ$ with $\delta=0^\circ$.

□ $\alpha=10.0$ $\delta=10.0$ 7 X 3

◇ $\alpha=10.0$ $\delta=10.0$ EXPERIMENT

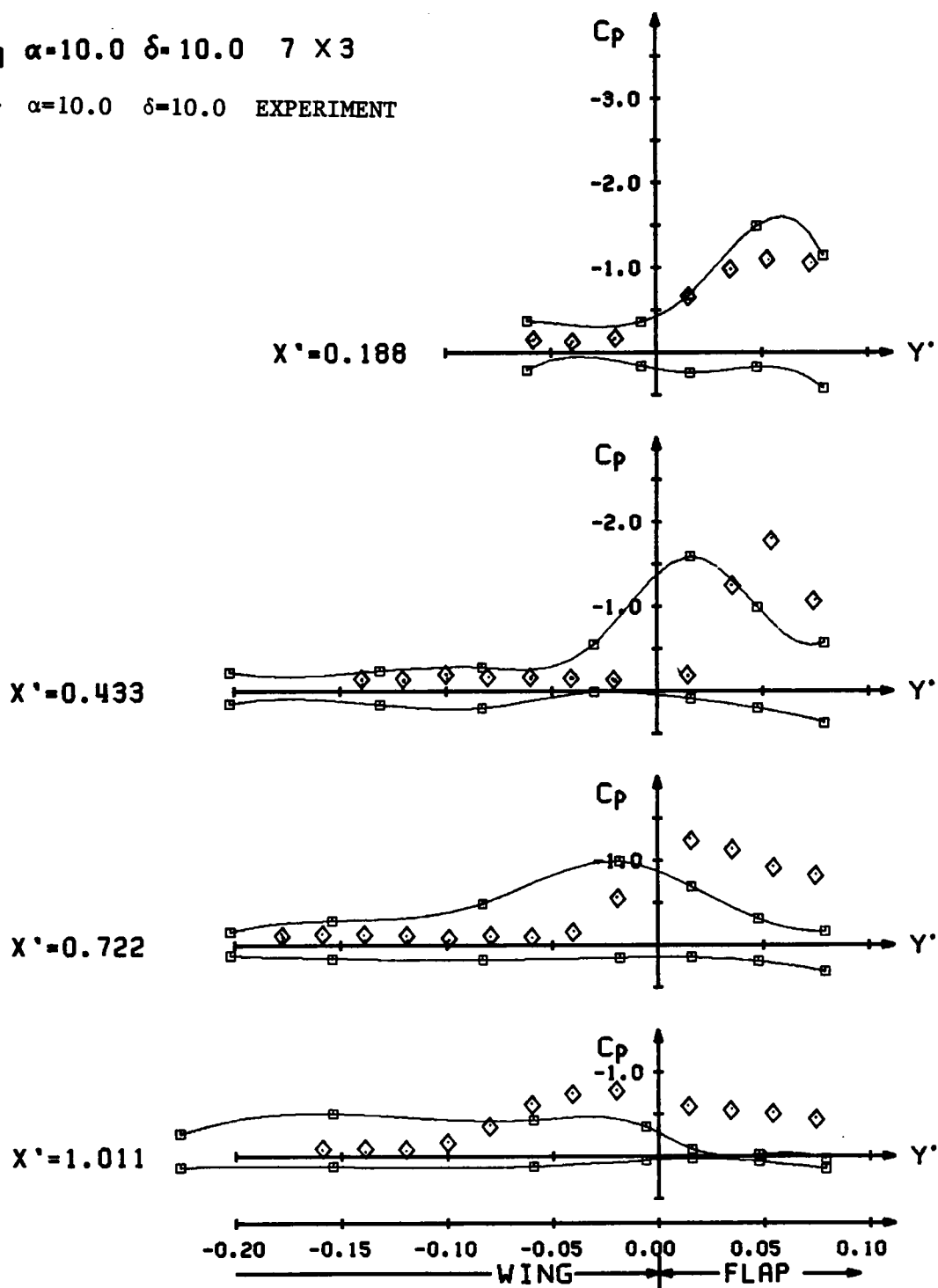


Fig. 73. Comparison of pressure distribution on a 60° delta wing with leading edge flap at $\alpha=10^\circ$ with $\delta=10^\circ$.

□ $\alpha=10.0$ $\delta=20.0$ 7 X 3

◇ $\alpha=10.0$ $\delta=20.0$ EXPERIMENT

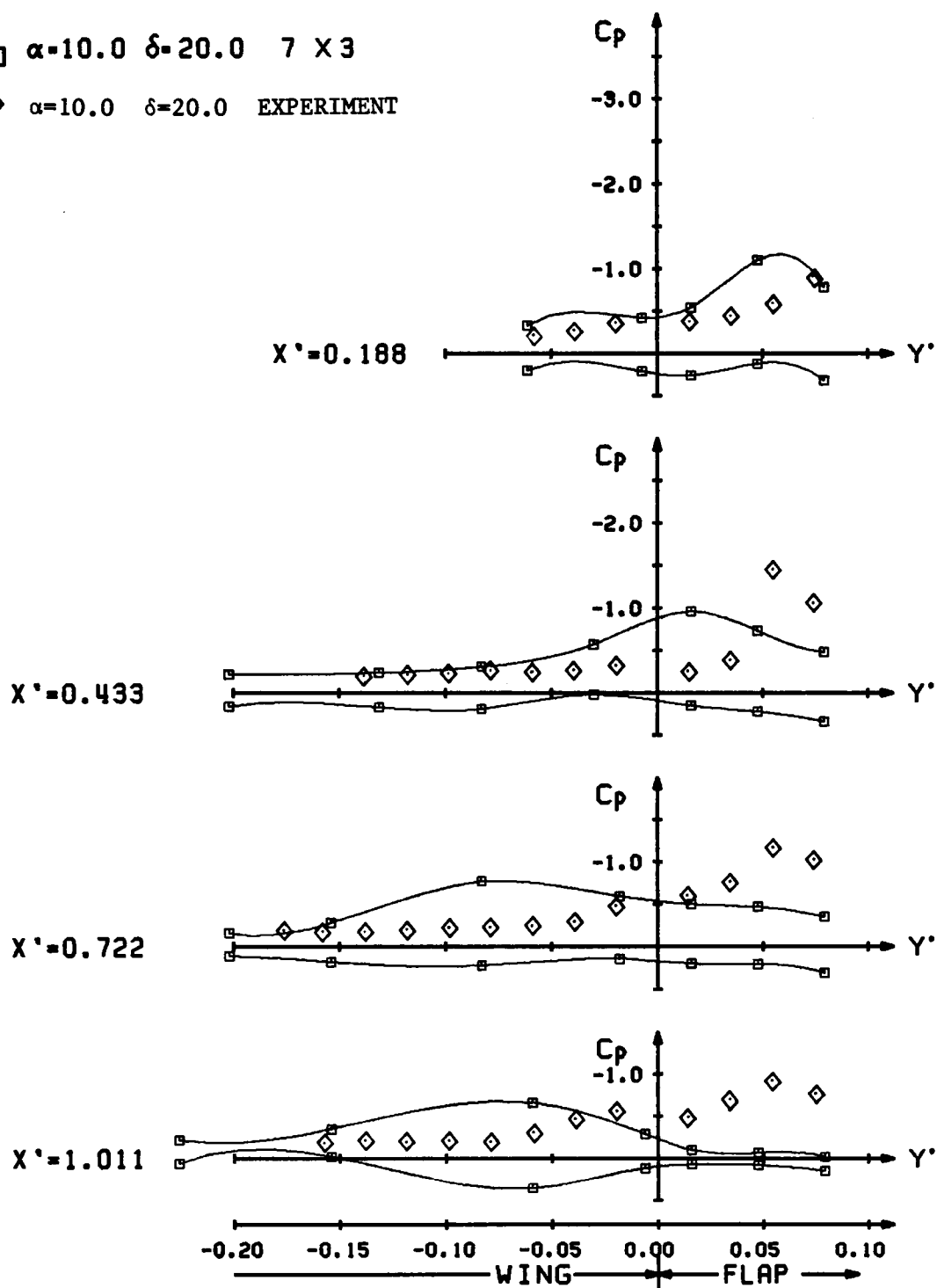


Fig. 74. Comparison of pressure distribution on a 60° delta wing with leading edge flap at $\alpha=10^\circ$ with $\delta=20^\circ$.

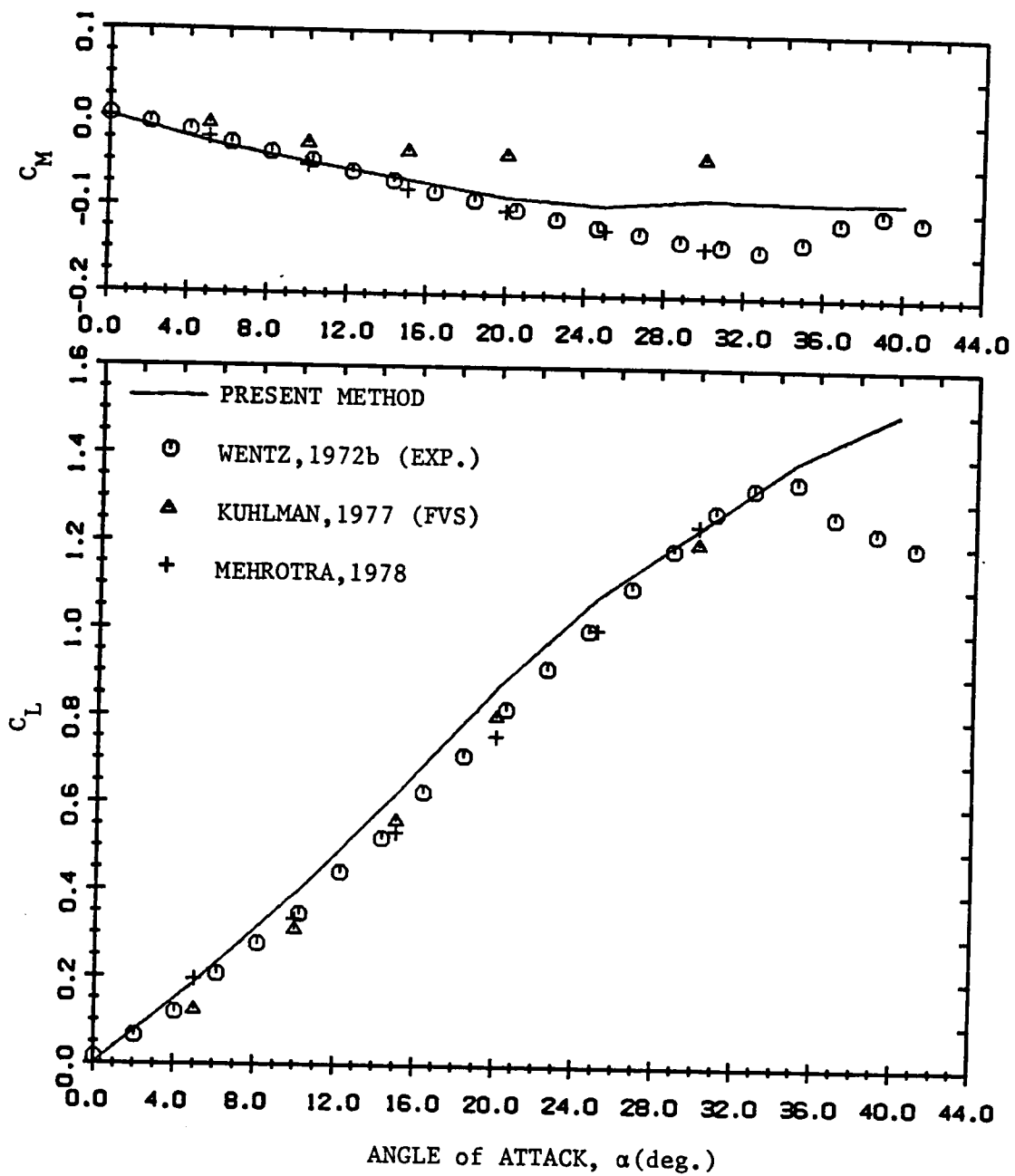


Fig. 75.a Comparison of longitudinal aerodynamic load characteristics for a 74° delta wing.

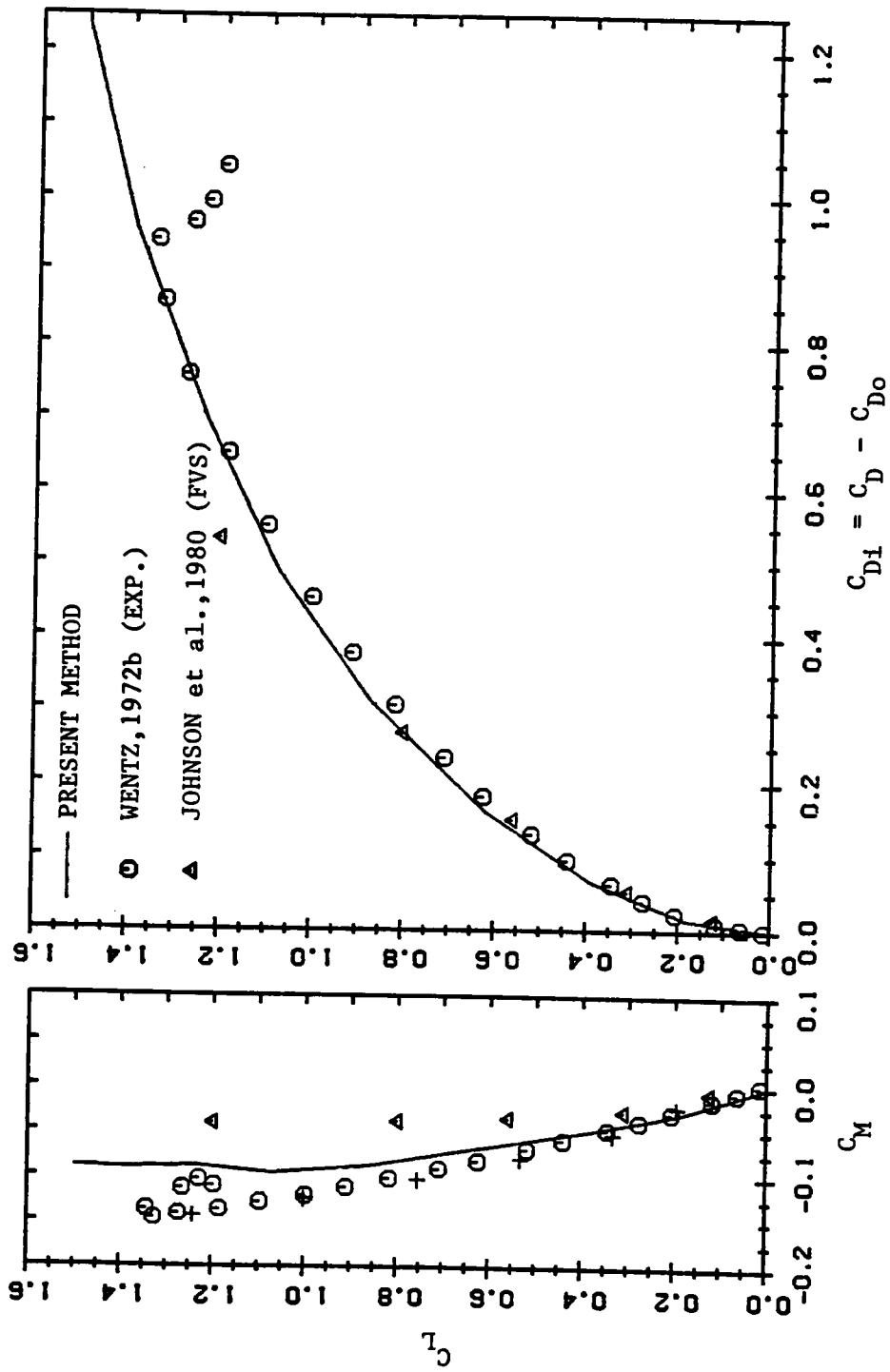


Fig. 75.b Concluded.

9X2, CONVERGED AT ITER=12
 FEDG=0.010, DTC=0.070, AFACT=1.250
 T= 72.83 SEC HO=0.0040 FVEND=1.20
 ALPHA= 15.0 DEG., DELTF= 7.0 DEG.
 CL=0.621, CD=0.161, CM=-0.069 (AT .5 C)

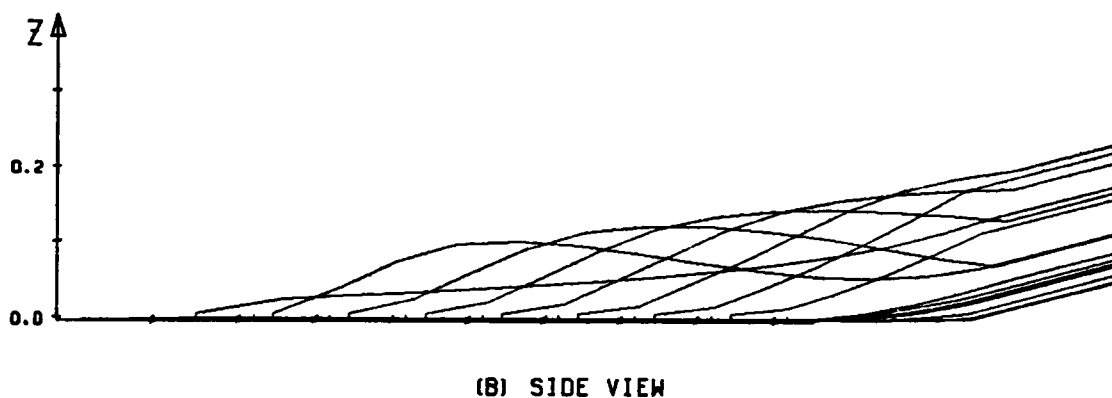
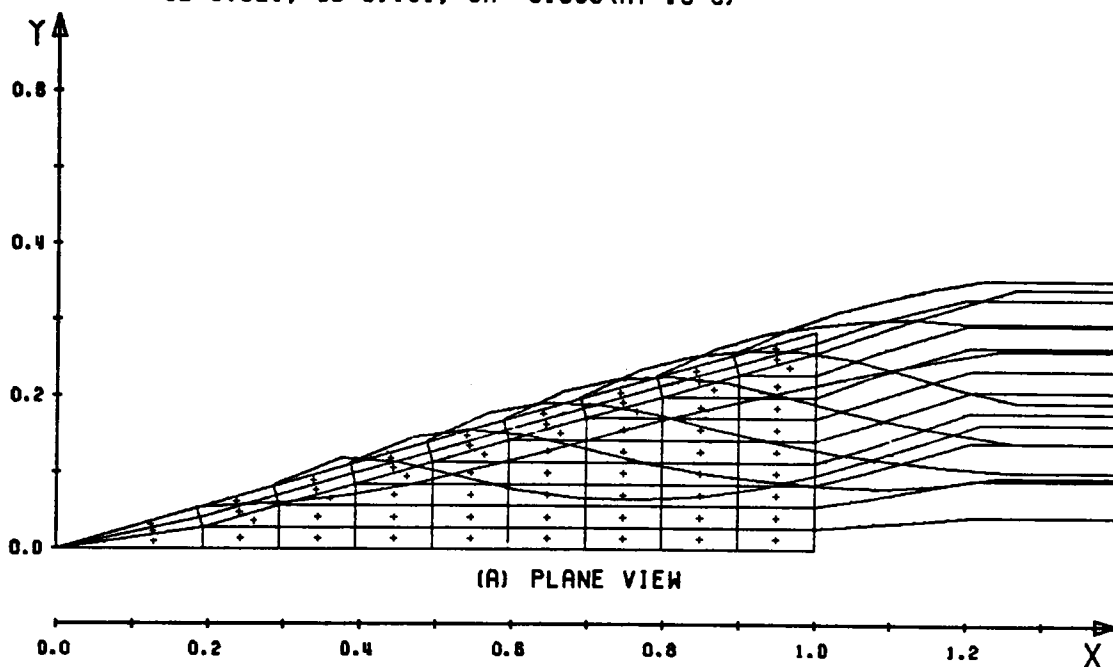


Fig. 76. Typical converged shape of free vortex filaments for a plain 74° delta wing.

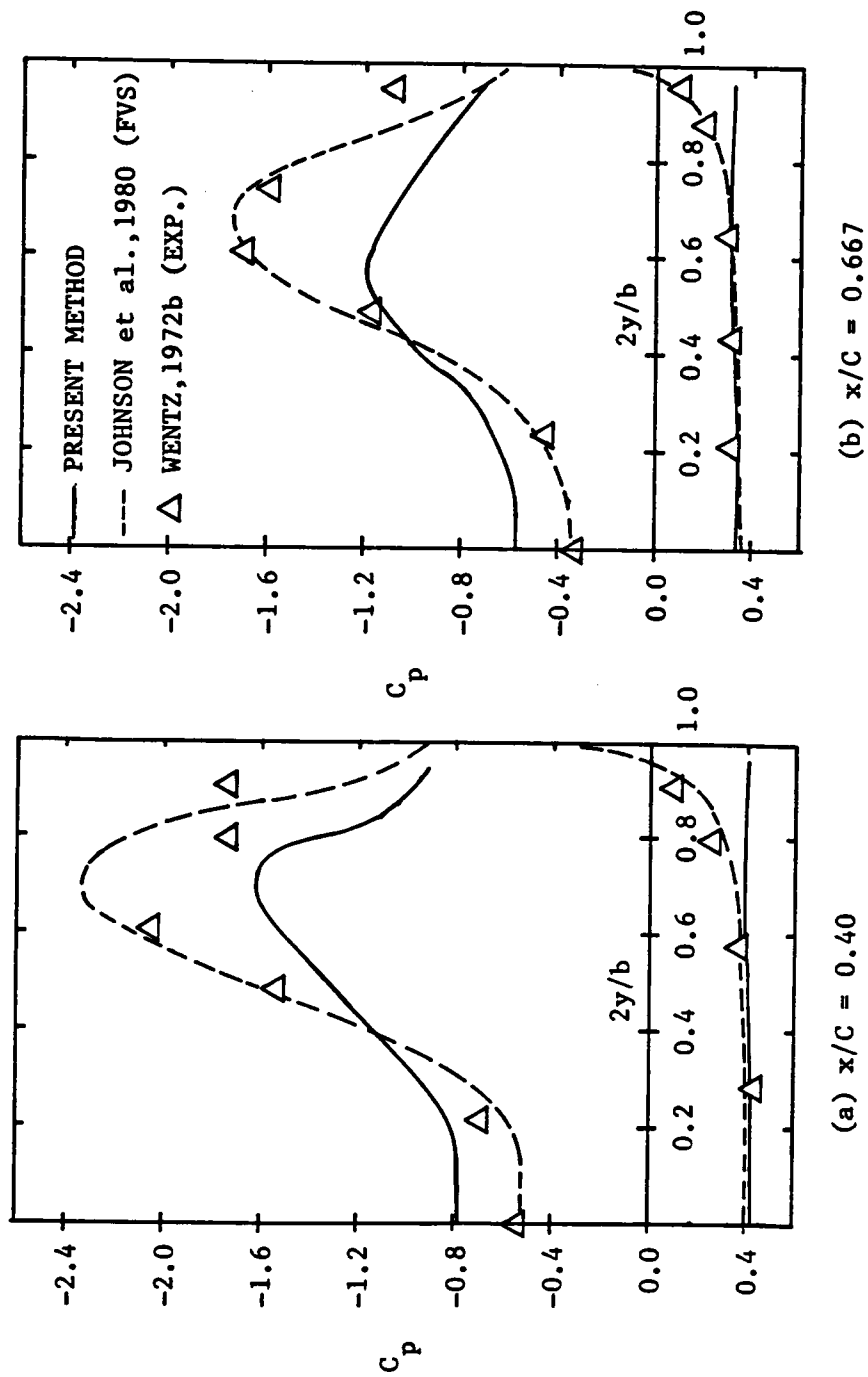


Fig. 77. Comparison of pressure distributions for a 74° delta wing.

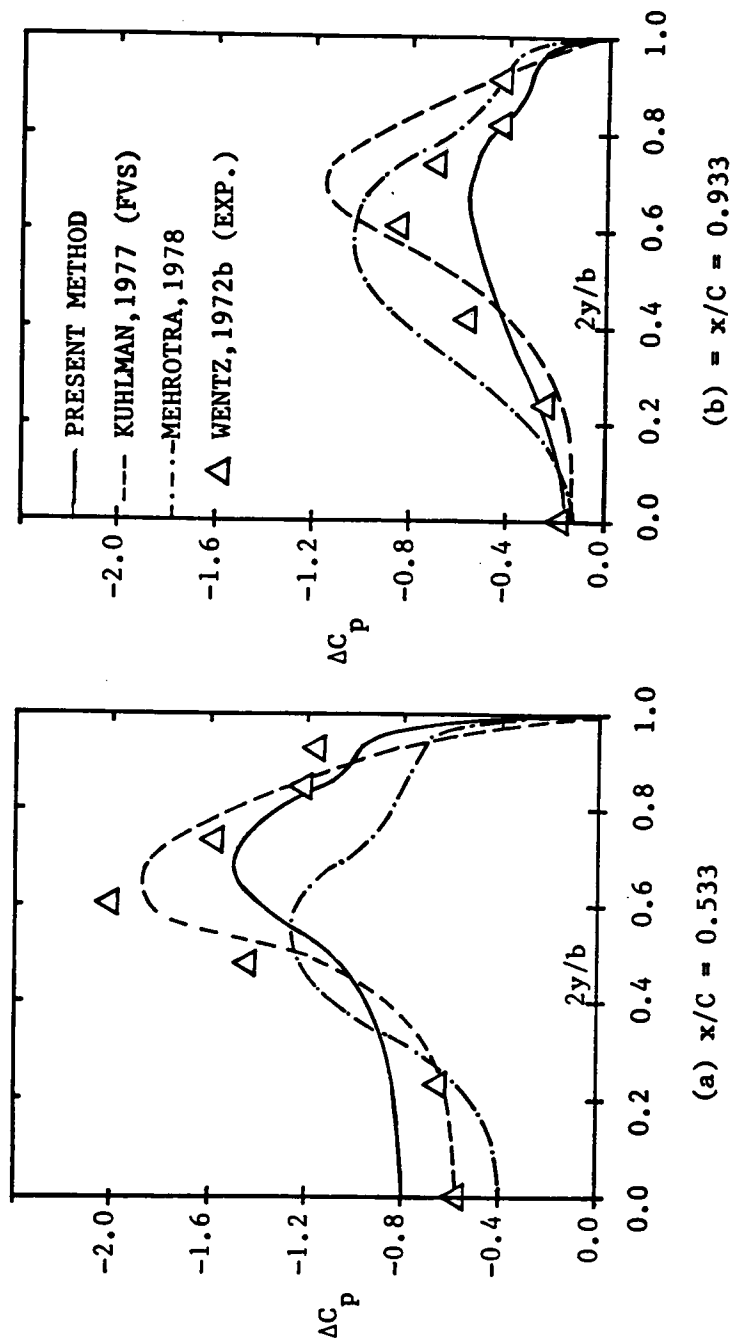


Fig. 78. Comparison of pressure difference distributions for a 74° delta wing.

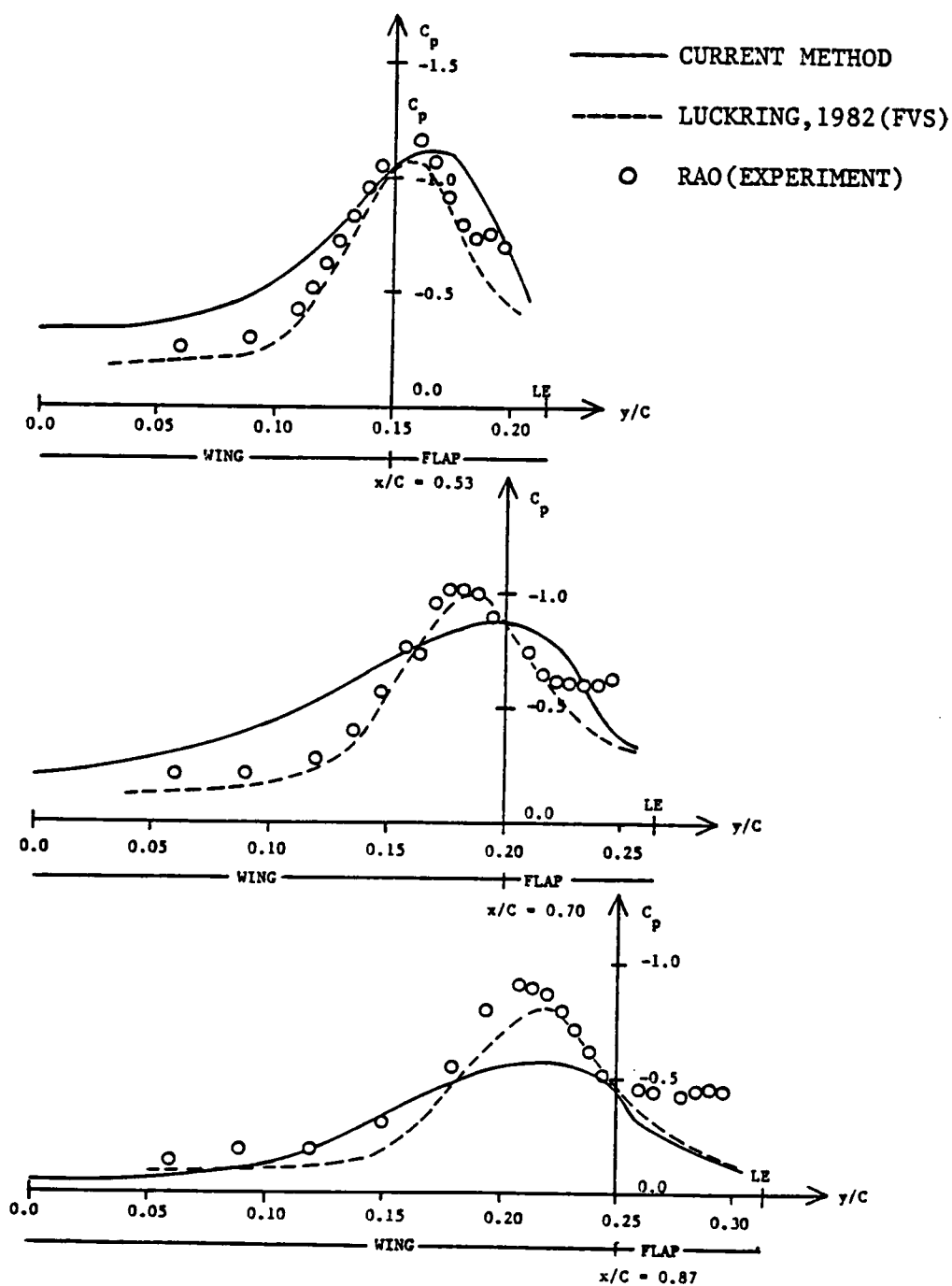


Fig. 79. Pressure distribution on a 74° delta wing with leading edge flap at $\alpha=14^\circ$ with $\delta=0^\circ$.

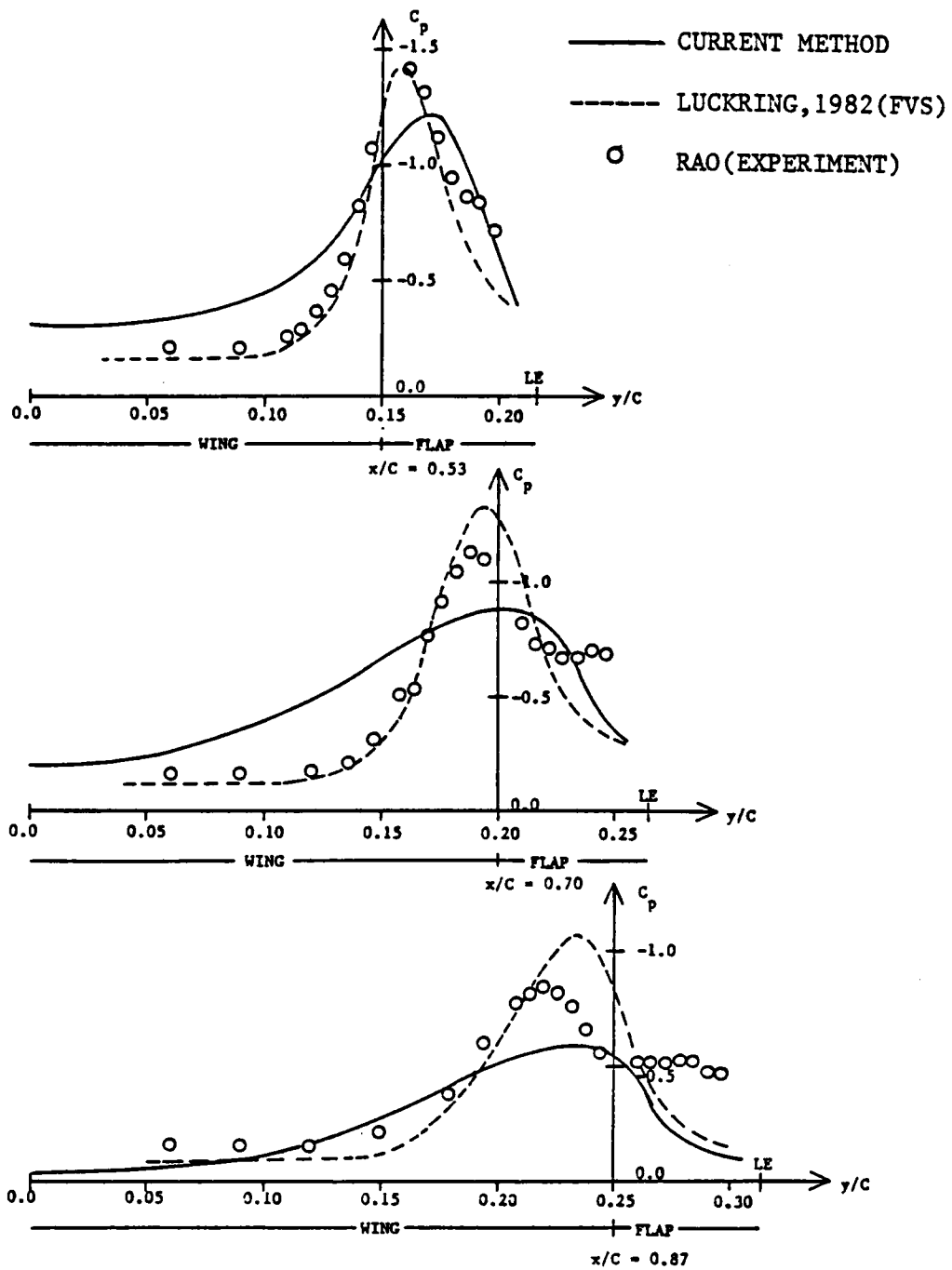


Fig. 80. Pressure distribution on a 74° delta wing with leading edge flap at $\alpha=14^\circ$ with $\delta=10^\circ$.

7X4, CONVERGED AT ITER=13
 FEDG=0.020, DTC=0.030, AFACT=1.250
 T=157.08 SEC HO=0.0041 FVEND=1.20
 ALPHA= 14.0 DEG., DELTF= 0.0 DEG.
 CL=0.719, CD=0.179, CM=-0.002 (AT .5 C)

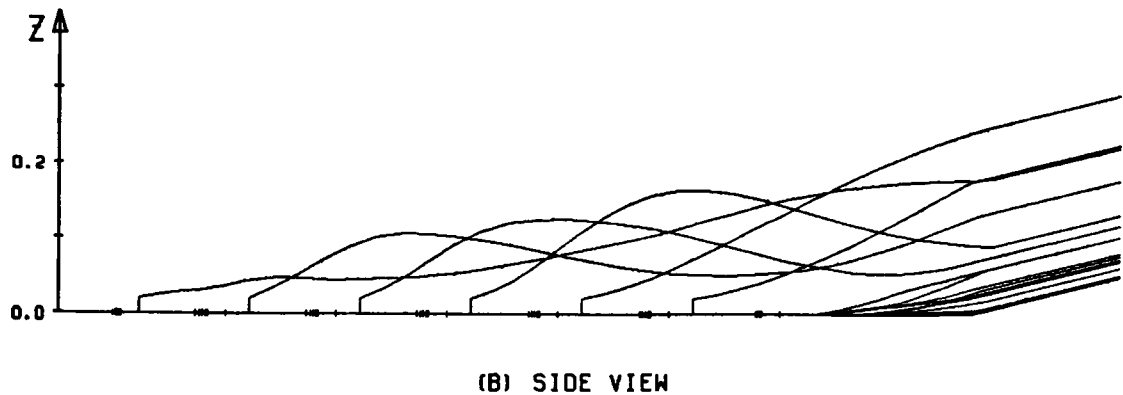
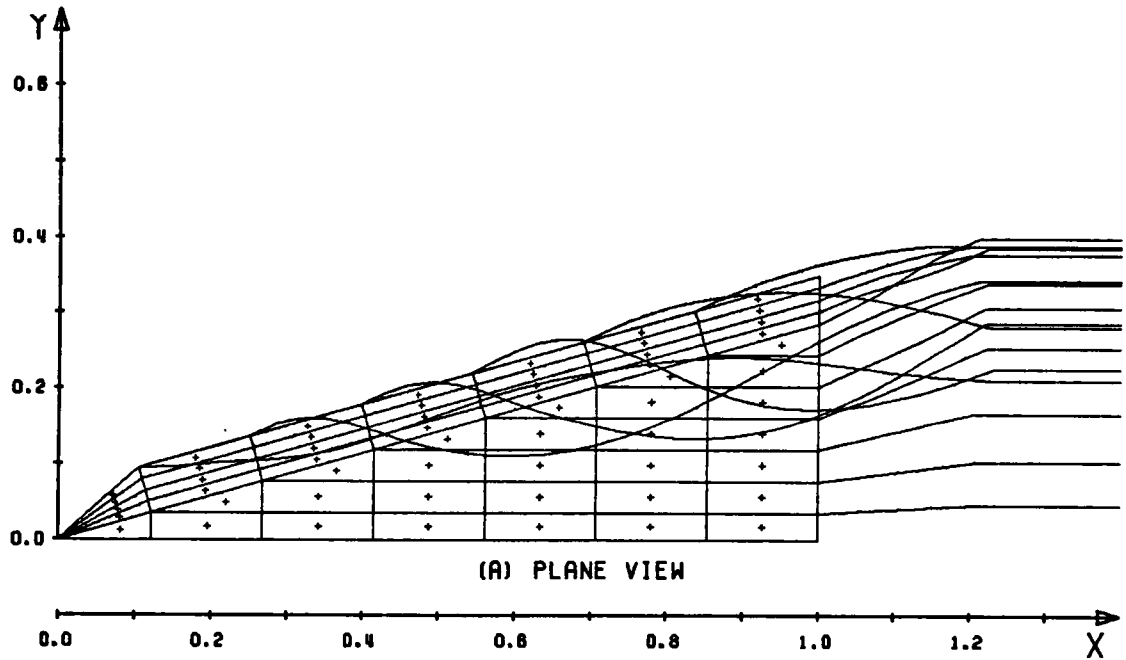


Fig. 81.a Converged shape of free vortices for a 74° delta wing with leading edge flap.

7X4, CONVERGED AT ITER=15
 FEDG=0.020, DTC=0.030, AFACT=1.250
 T=184.10 SEC HO=0.0041 FVEND=1.20
 ALPHA= 14.0 DEG., DELTF= 10.0 DEG.
 CL=0.670, CD=0.151, CM= 0.005 (AT .5 C)

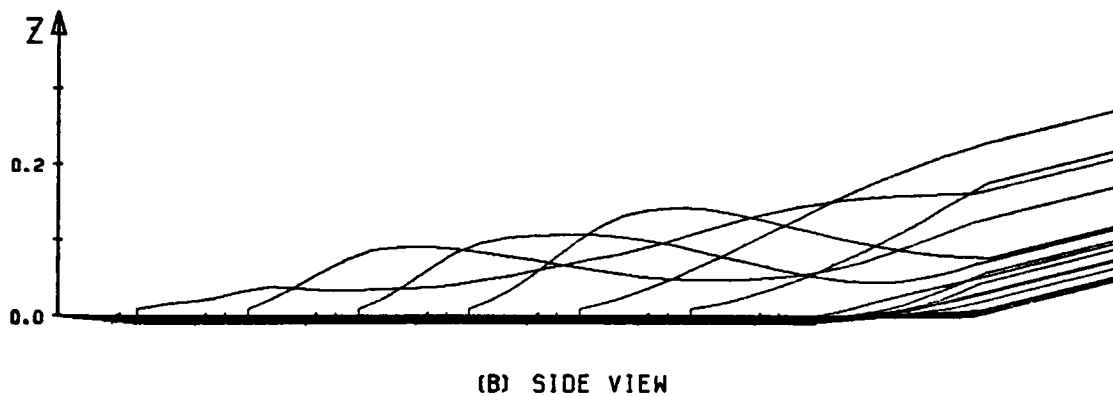
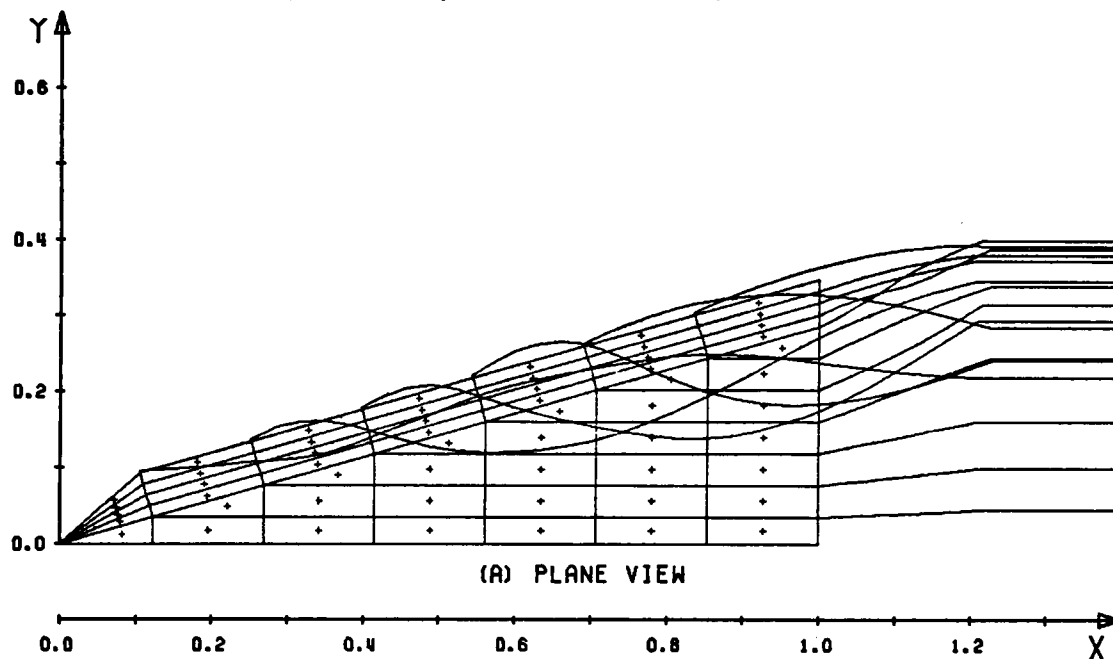


Fig. 82. Converged shape of free vortices for a 74° delta wing with leading edge flap at $\alpha=14^\circ$ with $\delta=10^\circ$.

**The vita has been removed from
the scanned document**